

Thermodynamic properties of new multiferroic and linear magnetoelectric crystals

Inaugural-Dissertation
zur
Erlangung des Doktorgrades
der Mathematisch-Naturwissenschaftlichen Fakultät
der Universität zu Köln

vorgelegt von
Matthias Ackermann
aus Göttingen

Köln 2014

Berichterstatter: Prof. Dr. Ladislav Bohatý
Priv.-Doz. Dr. Thomas Lorenz

Tag der mündlichen Prüfung: 20.10.2014

Contents

1	Introduction	1
2	Theory	5
2.1	Ferroic ordering phenomena	5
2.1.1	Symmetry conditions for primary ferroic effects	7
2.2	Multiferroics	8
2.2.1	Multiferroics of type I	9
2.2.2	Multiferroics of type II	12
2.3	The magnetoelectric effect	17
2.3.1	Phenomenological description	18
2.3.2	Microscopic origin and theoretical description	19
2.4	Ferrotoroidicity	20
3	Experimental	23
3.1	Experimental environment	23
3.2	Dielectric investigations	25
3.2.1	The spontaneous electric polarization	25
3.2.2	The magnetoelectrically induced electric polarization	27
3.2.3	The relative dielectric constant	28
3.2.4	Sample preparation	30
3.2.5	Measuring apparatus: high-temperature measurements	31
3.2.6	Measuring apparatus: low-temperature measurements	34
3.2.7	Data analysis: background currents and noise	36

3.2.8	Data analysis: background-current correction and integration	37
4	The pyroxenes $A\text{Fe}X_2\text{O}_6$ ($A = \text{Na, Li}$; $X = \text{Si, Ge}$)	41
4.1	Introduction	41
4.2	Experimental details	45
4.3	$\text{LiFeSi}_2\text{O}_6$	47
4.3.1	Magnetic properties	47
4.3.2	Dielectric properties	48
4.3.3	Magnetoelectric effect	51
4.3.4	Influence of electrode-area mismatch on the results of the dielectric investigations	54
4.3.5	Polarized-light microscopy	60
4.3.6	Thermal expansion and magnetostriction	61
4.3.7	Toroidal moment	65
4.3.8	Phase diagrams and conclusion	66
4.4	$\text{NaFeGe}_2\text{O}_6$	68
4.4.1	Magnetic properties	68
4.4.2	Dielectric properties	70
4.4.3	Thermal expansion and magnetostriction	73
4.4.4	Phase diagrams and conclusion	75
5	The erythrosiderite-type family $A_2[\text{FeCl}_5(\text{H}_2\text{O})]$ ($A = \text{K, Rb, Cs, NH}_4$)	79
5.1	Introduction	79
5.2	Experimental details	82
5.3	$(\text{NH}_4)_2[\text{FeCl}_5(\text{H}_2\text{O})]$	84
5.3.1	Phase transitions in zero magnetic field	84
5.3.2	Magnetic properties	87
5.3.3	Dielectric properties	90
5.3.4	Thermal expansion and magnetostriction	93
5.3.5	Phase diagrams and conclusion	96

5.4	$A_2[\text{FeCl}_5(\text{H}_2\text{O})]$ with $A = \text{K, Rb, Cs}$	100
5.4.1	Magnetic properties	100
5.4.2	Dielectric properties	102
5.4.3	Magnetoelectric effect	105
5.4.4	Phase diagrams and conclusion	110
6	Explorative studies of potential multiferroic compounds	113
6.1	$\text{NaFe}(\text{WO}_4)_2$	113
6.1.1	Introduction	113
6.1.2	Experimental details	114
6.1.3	Thermal expansion and magnetostriction	115
6.1.4	Dielectric properties	119
6.1.5	Conclusion	121
6.2	CuBr_2	122
6.2.1	Introduction	122
6.2.2	Experimental details	122
6.2.3	Dielectric properties	123
6.2.4	Conclusion	124
6.3	$\text{Mn}_3\text{Al}_2(\text{GeO}_4)_3$	125
6.3.1	Introduction	125
6.3.2	Experimental details	125
6.3.3	Dielectric properties	126
6.4	Tb_3TaO_7	127
6.4.1	Introduction	127
6.4.2	Experimental details	127
6.4.3	Results and discussion	128
7	Summary	131
	Appendix	135

A	Tensor formalism for the description of macroscopic physical properties of crystals	135
B	Transformation properties of axial vectors	136
C	Linear optical properties of crystals	137
D	Continuous-flow cryostat for dielectric investigations in a temperature range of 100-580 K	139
D.1	The measuring apparatus	139
D.2	Measuring process	141
D.3	Test measurements	141
E	Pyroelectric-current measurements	143
E.1	$\text{LiFeSi}_2\text{O}_6$	143
E.2	$\text{NaFeGe}_2\text{O}_6$	145
E.3	$(\text{NH}_4)_2[\text{FeCl}_5(\text{H}_2\text{O})]$	147
E.4	$A_2[\text{FeCl}_5(\text{H}_2\text{O})]$, ($A = \text{K, Rb, Cs}$)	149
E.5	CuBr_2	152
E.6	$\text{Mn}_3\text{Al}_2(\text{GeO}_4)_3$	153
F	Comparison of magnetic-susceptibility data of natural aegirine and synthetic $\text{NaFeSi}_2\text{O}_6$	154
G	Symmetry aspects of magnetoelectric phenomena	155
G.1	Forms of the linear magnetoelectric tensor	155
G.2	Magnetoelectric types of order	156
H	Engineering drawings	159
H.1	New sample holder for VTI-measurement insert	159
H.2	Continuous-flow cryostat	163
Bibliography		171
Abstract		183
Kurzzusammenfassung		185
Danksagung		187

Publications and conference contributions	189
Curriculum vitae	190
Offizielle Erklärung	191

Chapter 1

Introduction

The study of magnetoelectric coupling phenomena originated in 1888 with Wilhelm Conrad Röntgen's discovery of an induced magnetization in a dielectric, which moved in the presence of an electric field [1]. Some years later in 1894 Pierre Curie conjectured about the existence of materials, that may develop an electric polarization in a magnetic field or a magnetization in an electric field, a phenomenon, which was later called magnetoelectric effect [2]. Its "elastoelectric" analogue, the piezoelectric effect had been discovered already in 1880 also by Pierre Curie and his brother Jacques Curie [3]. The experimental proof for the existence of the magnetoelectric effect had to wait, however, about 60 years until in 1960 D. N. Astrov found in the antiferromagnetic compound Cr_2O_3 an electric-field induced magnetization [4]. This was the starting shot for intense research activities in the field of magnetoelectricity and subsequently many more other magnetoelectric materials were found [5].

Over the years, the concept of magnetoelectric behaviour was generalized by the idea that apart from strong cross-couplings of electric and magnetic responses also electric and magnetic types of ferroic order could coexist in one material. According to H. Schmid, the combined presence of ferroelectricity and one type of magnetic order is called nowadays magnetoelectric multiferroicity and since the pioneering work at the end of the 1950s a lot of multiferroic materials were found. In general, the microscopic mechanisms leading to ferroelectricity or a magnetic order are quite different and therefore the coupling between the corresponding order parameters is rather weak. But already at the end of the 1960s first thoughts came up whether distinctive magnetic structures may induce the occurrence of ferroelectricity [6, 7]. The experimental proof followed some years later with the investigation of Cr_2BeO_4 , demonstrating the presence of ferroelectricity induced by a cycloidal spin structure [8, 9]. Curiously, this idea was not further pursued in the following decades and therefore it took over twenty years until in 2003 with TbMnO_3 another spin-driven multiferroic was discovered [10]. In this context, for the first time a huge magnetoelectric coupling between

the magnetic and electric order parameter could be demonstrated (the electric polarization could be rotated by 90° , by applying a magnetic field). Subsequently, intense research activities started to further investigate the phenomenon of spin-driven multiferroicity and the magnetoelectric coupling phenomena present in this class of materials [11]. This was probably also driven by the great potential of multiferroics with strong magnetoelectric couplings for technical applications, especially in the field of data storage. Consequently, a lot of other spin-driven multiferroics were found and investigated in detail during the last decade, and also some theoretical models were developed to explain the microscopic mechanisms [11]. Anyhow, there are still a lot of open questions in the field of spin-driven multiferroics and multiferroicity in general and still new multiferroic materials are needed to enlarge the playground for experimental and theoretical work.

Therefore, the objective of the present work was the search for new multiferroic or magnetoelectric crystals, with strong magnetoelectric couplings and their basic characterization by investigating their thermodynamic properties. In the search for new multiferroics of particular importance are those materials, which possess a large variety of different compositions with (nearly) isomorphous structures because they open the possibility to study the impact of slight crystal-chemical modifications on their magnetoelectric properties. A better understanding of these cross-correlations is essential to enable perhaps in the future the fabrication of multiferroics with tuned properties, such as higher transition temperatures, larger electric polarizations and stronger magnetoelectric couplings. With the pyroxenes, such a class of multiferroic and magnetoelectric materials was discovered some years ago [14, 15]. The mineral aegirine of the composition $\text{Na}_{1.04}\text{Fe}_{0.83}\text{Ca}_{0.04}\text{Mn}_{0.02}\text{Al}_{0.01}\text{Ti}_{0.08}\text{Si}_2\text{O}_6$ was identified as multiferroic, while $\text{LiFeSi}_2\text{O}_6$ and $\text{LiCrSi}_2\text{O}_6$ were proved to be linear magnetoelectrics. Interestingly, multiferroicity in $\text{Na}_{1.04}\text{Fe}_{0.83}\text{Ca}_{0.04}\text{Mn}_{0.02}\text{Al}_{0.01}\text{Ti}_{0.08}\text{Si}_2\text{O}_6$ could arise only due to the natural dopants in this compound. Synthetic $\text{NaFeSi}_2\text{O}_6$ apparently has a modified magnetic structure compared to aegirine indicating that it could be only linear magnetoelectric [16]. Although in the years after the pioneering work of S. Jodlauk et al. [14, 15] intense research activities set in to find more examples of multiferroic materials within the pyroxene family, at the beginning of the present work only some more linear magnetoelectrics were known [17, 18]. Therefore, the search for new multiferroics and linear magnetoelectrics was continued within the pyroxene family in this work. In this context, $\text{NaFeGe}_2\text{O}_6$ could be characterized as first synthetic multiferroic within the pyroxene family.¹ In addition, the linear magnetoelectric properties of $\text{LiFeSi}_2\text{O}_6$ and their anisotropy were investigated and analysed in detail. Furthermore, with the erythrosiderite-type compounds $A_2[\text{FeCl}_5(\text{H}_2\text{O})]$ ($A = \text{K}, \text{Rb}, \text{Cs}, \text{NH}_4$) a new family of non-oxide multiferroic and linear magnetoelectric materials was discovered and systematically examined. The influence of the ionic radii

¹Parallel to the investigations in the present work, multiferroicity in $\text{NaFeGe}_2\text{O}_6$ was also found by another research group in polycrystalline samples [12].

of the *A*-site elements and of their stereochemical properties on the magnetic and magnetoelectric properties of the erythrosiderite-type compounds could be studied. The experimental results prove in analogy to the pyroxenes that already slight crystal-chemical modifications suffice to strongly modify the magnetoelectric properties.

The discovery of spin-driven multiferroicity in the compound MnWO_4 [14, 19–21] some years ago, led to the search for other multiferroic materials in the tungstate family following the aforementioned approach studying the impact of crystal-chemical modifications on the magnetoelectric properties [14]. In this context, first evidence was found that $\text{NaFe}(\text{WO}_4)_2$ could be a multiferroic with a new underlying microscopic mechanism [14]. Detailed investigations of this compound in the present work, however, revealed that the claim of multiferroicity is apparently wrong. In addition to the experimental work within the pyroxene, the erythrosiderite-type and tungstate family, more explorative work led to the discovery of multiferroicity in CuBr_2 with a relative high transition temperature in the vicinity of the boiling point of liquid nitrogen.² Furthermore, with $\text{Mn}_3\text{Al}_2(\text{GeO}_4)_3$ a new perfectly antisymmetric linear magnetoelectric was found, which could be interesting for the study of the so-called toroidal moment, that is discussed for some years in the community of multiferroic research. Finally, among the group of rare-earth tantalates with Tb_3TaO_7 another potential multiferroic was discovered.

The thesis is organized as follows. In the first chapter a short introduction into the field of ferroic ordering phenomena with the focus on multiferroicity, the magnetoelectric effect and ferrotoroidicity is given. In the second chapter the experimental background is explained, including the basic principles, measurement techniques and experimental apparatuses, which are important for this work. In the following chapters, the experimental results arranged according to the investigated crystals are presented, discussed and analysed. In the appendix the tensor formalism for the description of macroscopic physical properties of crystals is shortly introduced, including a definition of the crystal-physical reference system. The transformation properties of axial vectors under space-time coordinate transformations are summarized and a short introduction to the linear optical properties of crystals is given. Then, the functionality of the continuous-flow cryostat, which was developed during the present work, is explained and engineering detail drawings of developed sample holders are presented. Furthermore, the raw data of the pyroelectric-current measurements are summarized. Finally for the present work important symmetry aspects of magnetoelectric coupling phenomena are given.

²As in the case of $\text{NaFeGe}_2\text{O}_6$, parallel to the investigations in the present work, multiferroicity in CuBr_2 was also found by another research group in polycrystalline samples [13].

Chapter 2

Theory

2.1 Ferroic ordering phenomena

According to K. Aizu, a ferroic crystal may be regarded as a slight distortion (lowering of symmetry) of a certain non-ferroic ideal crystal, which is referred to as the prototype of that ferroic crystal [22]. In general, the structure of a ferroic crystal and all of its physical properties are related to the crystallographic system (or the crystal-physical system) of the high-symmetry prototypic phase. Two or more energetically degenerate orientation states (domain states) are generated due to the lowering of symmetry at a ferroic phase transition. In general, the degeneracy can be lifted by applying one of the "driving forces" magnetic field $\mathbf{H} = [H_i]$, electric field $\mathbf{E} = [E_i]$, mechanical stress $\tilde{\sigma} = [\sigma_{ij}]$ or a combination of these. Consequently, one orientation state can be transferred into another one. The point group G_f of an orientation state of the ferroic phase is a subgroup of the point group G_p of the prototypic phase. Therefore, $|G_p| - |G_f|$ symmetry elements are lost during a ferroic phase transition.¹ The orientation states of a ferroic phase can be transferred into each other by applying these lost symmetry elements. Their number is determined by the ratio $|G_p|/|G_f|$ [22]. There are 773 possible symmetry-lowering paths of ferroic phase transitions. They can be characterized by the associated pairs $G_p F G_f$, which are known as Aizu species. In the presence of the driving forces $\mathbf{H} = [H_i]$, $\mathbf{E} = [E_i]$ and $\tilde{\sigma} = [\sigma_{ij}]$ the stability of an orientation state of a ferroic crystal can be described by the density of the free enthalpy $g = g(\tilde{\sigma}, \mathbf{E}, \mathbf{H}, T)$ with the total increment [23, 24]

$$dg = s dT - \epsilon_{ij} d\sigma_{ij} - P_i dE_i - \mu_0 M_i dH_i. \quad (2.1)$$

Here, s denotes the density of entropy, T the temperature, $[\epsilon_{ij}]$ the mechanical strain tensor, $[P_i]$

¹ $|G_p|$ and $|G_f|$ denote the order of the point group of the prototypic phase and of the ferroic phase, respectively.

the electric polarization and $[M_i]$ the magnetization. All tensor properties are related to the crystal-physical system of the prototypic phase of the considered ferroic crystal. A short introduction of tensors and their transformation properties under transformation of coordinates is given in appendix A. In addition, the crystal-physical reference system is defined and its relation to the crystallographic reference system is introduced. In the following discussion, isothermal conditions are assumed. Therefore, the density of entropy is not considered further. The other quantities are expanded in McLaurin series² (see equations 2.2-2.4).

$$\epsilon_{ij} = \epsilon_{ij}^{(S)} + s_{ijkl}\sigma_{kl} + Q_{kij}H_k + d_{kij}E_k + \dots \quad (2.2)$$

$$P_i = P_i^{(S)} + \varepsilon_0\chi_{ij}^{(el)}E_j + \alpha_{ij}H_j + d_{ijk}\sigma_{jk} + \frac{1}{2}\beta_{ijk}H_jH_k + \gamma_{jki}H_jE_k + \dots \quad (2.3)$$

$$\begin{aligned} \mu_0 M_i = & \mu_0 M_i^{(S)} + \mu_0\chi_{ij}^{(mag)}H_j + \alpha_{ji}E_j + Q_{ijk}\sigma_{jk} \\ & + \beta_{jki}E_jH_k + \frac{1}{2}\gamma_{ijk}E_jE_k + \dots \end{aligned} \quad (2.4)$$

As zero-order terms of the expansions of $[\epsilon_{ij}]$, $[P_i]$ and $[M_i]$ the spontaneous mechanical strain $[\epsilon_{ij}^{(S)}]$, the spontaneous electric polarization $[P_i^{(S)}]$ and the spontaneous magnetization $[M_i^{(S)}]$ are obtained, respectively. Furthermore, the expansions contain elastic, magnetostrictive, electrostrictive, magnetoelectric, piezomagnetic and piezoelectric contributions, which are induced by applied mechanical stress, electric or magnetic fields or combinations of these. The mediating physical quantities are the elastic compliance tensor $[s_{ijkl}]$, the piezoelectric tensor $[d_{ijk}]$, the piezomagnetic tensor $[Q_{ijk}]$, the tensor of the electric and magnetic susceptibility $[\chi_{ij}^{(el)}]$ and $[\chi_{ij}^{(mag)}]$, respectively, the magnetoelectric tensor $[\alpha_{ij}]$ and finally the tensors of the quadratic and bilinear magnetoelectric effects $[\beta_{ijk}]$ and $[\gamma_{ijk}]$, respectively. The insertion of the terms from equations 2.2-2.4 for the mechanical strain $[\epsilon_{ij}]$, the electric polarization $[P_i]$ and the magnetization $[M_i]$ into equation 2.1 and integration yields the following relation for the density of the free enthalpy g .

$$\begin{aligned} g = g_0 - & P_i^{(S)}E_i - \mu_0 M_i^{(S)}H_i - \epsilon_{ij}^{(S)}\sigma_{ij} \\ - & \frac{1}{2}\varepsilon_0\chi_{ij}^{(el)}E_iE_j - \frac{1}{2}\mu_0\chi_{ij}^{(mag)}H_iH_j - \frac{1}{2}s_{ijkl}\sigma_{ij}\sigma_{kl} \\ - & \alpha_{ij}E_iH_j - d_{ijk}E_i\sigma_{jk} - Q_{ijk}H_i\sigma_{jk} \\ - & \frac{1}{2}\beta_{ijk}E_iH_jH_k - \frac{1}{2}\gamma_{ijk}H_iE_jE_k - \dots \end{aligned} \quad (2.5)$$

Two arbitrary orientation states of a ferroic crystal, named as I and II, are described by the respec-

²McLaurin series: Taylor series $f(x) = \sum_{k=1}^{\infty} \frac{f^{(k)}(x_0)}{k!}(x - x_0)^k$ evaluated at the point $x_0 = 0$

tive densities of the free enthalpy g^I or g^{II} in the presence of the driving forces $\mathbf{H} = [H_i]$, $\mathbf{E} = [E_i]$ and $\tilde{\sigma} = [\sigma_{ij}]$. The energy difference $\Delta g = g^I - g^{II}$ between the two orientation states results to

$$\begin{aligned} \Delta g = & \Delta P_i^{(S)} E_i + \mu_0 \Delta M_i^{(S)} H_i + \Delta \epsilon_{ij}^{(S)} \sigma_{ij} \\ & + \frac{1}{2} \epsilon_0 \Delta \chi_{ij}^{(el)} E_i E_j + \frac{1}{2} \mu_0 \Delta \chi_{ij}^{(mag)} H_i H_j + \frac{1}{2} \Delta s_{ijkl} \sigma_{ij} \sigma_{kl} \\ & + \Delta \alpha_{ij} E_i H_j + \Delta d_{ijk} E_i \sigma_{jk} + \Delta Q_{ijk} H_i \sigma_{jk} \\ & + \frac{1}{2} \Delta \beta_{ijk} E_i H_j H_k + \frac{1}{2} \Delta \gamma_{ijk} H_i E_j E_k + \dots \end{aligned} \quad (2.6)$$

According to the non-zero terms in equation 2.6, which contribute to the energy difference $\Delta g \neq 0$, a classification of a multitude of ferroic ordering phenomena is possible.

Primary ferroic effects If one of the linear terms $\Delta P_i^{(S)}$, $\Delta M_i^{(S)}$ or $\Delta \epsilon_{ij}^{(S)}$ is non-zero and if the corresponding orientation states are switchable with the corresponding driving forces E , H or σ , the primary ferroic effects ferroelectricity, ferromagnetism or ferroelasticity are obtained, respectively [23]. The switching between two domain states can be regarded as an isothermal and isostructural phase transition of first order. It is therefore attended with a hysteresis loop [25].

Secondary ferroic effects If one of the quadratic terms $\Delta \chi_{ij}^{(el)}$, $\Delta \chi_{ij}^{(mag)}$, Δs_{ijkl} , $\Delta \alpha_{ij}$, Δd_{ijk} or ΔQ_{ijk} is unequal to zero and if the corresponding orientation states are switchable with the corresponding driving forces $E_i E_j$, $H_i H_j$, $\sigma_{ij} \sigma_{kl}$, $E_i H_j$, $E_i \sigma_{jk}$ or $H_i \sigma_{jk}$, the ferroic effects ferrobielectricity, ferrobimagnetism, ferrobielasticity, ferromagnetoelectricity, ferroelasto-electricity or ferromagnetoelasticity occur [23].

Ferroic effects of higher order Analogous to the effects of first and second order there exist also effects of third or even higher orders, but these higher-order effects will not be discussed further in this thesis.

2.1.1 Symmetry conditions for primary ferroic effects

The order parameters of the primary ferroic effects ferroelectricity, ferromagnetism and ferroelasticity differ in their behaviour with respect to time reversal and space inversion. The vector of the spontaneous electric polarization $[P_i^{(S)}]$ is space-antisymmetric and time-symmetric. Its limiting group is $\infty mm1'$ [26]. Thus, ferroelectricity can only occur in crystals with polar symmetry with a point group that is a subgroup of this limiting group. The resulting 31 ferroelectric point groups

are [27]:

$$1, 2, 3, 4, 6, 1', 2', 3', 4', 6', 21', 31', 41', 61', m, m', mm2, m'm'2, m'm'2', mm21', \quad (2.7)$$

$$3m, 3m', 3m1', 4mm, 4m'm', 4'mm', 4mm1', 6mm, 6m'm', 6'mm', 6mm1'$$

The vector of the spontaneous magnetization $[M_i^{(S)}]$ is space-symmetric and time-antisymmetric. Its symmetry can be described by the limiting group $\frac{\infty}{m} \frac{2'}{m'} \frac{2'}{m'}$ [26]. Therefore, the occurrence of ferromagnetism is constrained to crystals with a point group that is a subgroup of this limiting group. This constraint results in the following 31 ferromagnetic point groups [27]:

$$1, 2, 3, 4, 6, \bar{1}, \bar{2}, \bar{3}, \bar{4}, \bar{6}, 2', m', m'm'2', \frac{2}{m}, \frac{4}{m}, \frac{6}{m}, \frac{2'}{m'}, \bar{3}m', 6mm, 3m', \quad (2.8)$$

$$\bar{4}2'm', \frac{4}{m} \frac{2'}{m'} \frac{2'}{m'}, \bar{6}2'm', mm'm', \frac{6}{m} \frac{2'}{m'} \frac{2'}{m'}, 22'2', 42'2', 32', 62'2', 2m'm', 4m'm'$$

The symmetry of many antiferromagnetic spin configurations can also be described by the concept of magnetic point groups. In table 5 and 6 in appendix G, a listing of the 90 magnetic point groups, that allow an antiferromagnetic ordering, can be found. For more complex magnetic structures as, e.g., for helical spin structures this concept is limited, however. In such cases the magnetic symmetry may be described more reasonable in the framework of representation theory by irreducible representations of the respective crystallographic space group. Comprehensive contributions to the description of spin structures by magnetic point groups can be found, e.g., in [28, 29]. An introduction into the field of representation theory is given in [30, 31]. A comparison of both methods and their advantages and disadvantages, respectively, are discussed in [31, 32].

In contrast to the above-discussed cases of ferroelectricity and ferromagnetism, the symmetry analysis of the order parameter of ferroelasticity yields no constraints for its point-group symmetry. The tensor of the spontaneous mechanical strain $[\epsilon_{ij}^{(S)}]$ is space- and time-symmetric. The strain tensor at a transition from the prototypic into a ferroelastic phase must, however, gain at least one additional independent component compared to the prototypic phase to enable the onset of a spontaneous strain. That's why a change to another crystal system of lower symmetry has to occur at the transition. Therefore, cubic and hexagonal crystals cannot be ferroelastic.

2.2 Multiferroics

A material is called multiferroic if a phase exists with the combined presence of two or more primary ferroic effects [33]. In general, this definition is extended by the antiferroic forms of ordering such as, e.g., antiferromagnetism. In this section the focus will lie on magnetoelectric multiferroic-

ity, which means the simultaneous presence of ferroelectricity and some type of magnetic order.³ Apart from this term, in the older literature the terms ferroelectromagnetism or seignettomagnetism are used. In the field of magnetoelectric multiferroicity two different groups of materials are distinguished [34,35]. In the first group, such multiferroic materials are summarized (multiferroics of type I), in which the magnetic and ferroelectric order has different microscopic origins. Depending on the symmetry relation between prototypic phase and ferroic phase, a magnetoelectric coupling between magnetism and ferroelectricity is possible [36,37]. Because of the different microscopic mechanisms, however, that lead to a magnetic or ferroelectric order in this group, the coupling is usually very weak. In addition, the transition into the ferroelectric phase takes place in general at higher temperatures than the transition into the magnetically ordered phase. In the second group, multiferroic materials are summarized, in which the magnetic order is the reason for the occurrence of ferroelectricity (multiferroics of type II). In general, there exists a strong coupling between the magnetic and ferroelectric order in this group of materials.

2.2.1 Multiferroics of type I

The microscopic mechanisms, which lead to the occurrence of magnetic or ferroelectric ordering, are in general quite different. The microscopic origin for the occurrence of a magnetic order in electrically insulating materials lies actually always in localized spins, which are coupled via magnetic exchange interactions. Magnetic, electrically insulating materials therefore must contain elements with partly filled electronic shells. In contrast, there are multiple microscopic origins for the occurrence of ferroelectricity. A ferroelectric order can, for example, be generated by the alignment of already existing molecular groups with an electric dipole moment, the collective deformation of electronic orbitals with respect to the corresponding atomic nuclei or the collective shifting of some of the ions in the ionic lattice. Thus, multiferroics of type I differ, apart from possible differences in the magnetic order, particularly in the microscopic mechanisms, leading to the ferroelectric order. In the following, the most important of these mechanisms for multiferroics of type I will be explicated.

A lot of ferroelectric materials are members of the large family of perovskites ABO_3 , as, e.g., $BaTiO_3$ one of the most prominent ferroelectrics [38]. The A sites at the corners of the unit cell are often occupied by alkali or earth-alkali metals as well as by metals of the rare-earth group. The B sites at the centres of the unit cell are usually occupied by transition-metal ions. In the perovskite family, the transition to the ferroelectric phase is typically caused by a structural instability. This instability is responsible for the shift of the sixfold-coordinated B ions from their central positions towards one of the oxygen ions below the ordering temperature. Though there exists a multitude

³In the following, the term multiferroicity is always used for magnetoelectric multiferroicity. If another type of multiferroicity is meant, it will explicitly be mentioned.

of magnetic materials in the perovskite family [39], practically no perovskites, which are simultaneously magnetic and ferroelectric, are known.⁴ The reasons for that were intensely discussed in literature [34, 35, 40–42]. The most recent theory assumes that the occurrence of ferroelectricity is favoured by non-magnetic transition-metal ions with an empty d shell on the B site. The empty d shell enables the formation of a strong covalent bonding with one of the neighbouring oxygen ions by hybridization of the d states of the transition-metal ion with the 2p states of the corresponding oxygen ion. Therefore, an energy gain may arise for the non-centrosymmetric position of the B ion with respect to the original centrosymmetric one [43, 44]. In contrast, magnetic transition-metal ions on the B sites with partly filled d shells suppress the formation of such covalent bonding with the oxygen neighbours and are therefore stable at their centrosymmetric positions in the unit cell. At the beginning of the field of research of multiferroic ordering phenomena at the end of the 1950s, the search for multiferroic materials was initially focused on the group of perovskites, despite of the problems discussed above. Usually, ferroelectric compounds were selected and a part of the diamagnetic d^0 ions on the B sites was substituted by paramagnetic d^n ions, resulting in compounds of the formula $A(B_x^{d^0} B_{1-x}^{d^n})O_3$. After the synthesis of first polycrystalline ceramic samples, such as $Pb(Fe_{1/2}Nb_{1/2})O_3$, $Pb(Fe_{1/2}Ta_{1/2})O_3$ or $Pb(Fe_{2/3}W_{1/3})O_3$ [45, 46] a lot of other multiferroic perovskite compounds were synthesized in the same way [47–49]. Because of the relatively low concentration of paramagnetic ions in these mixed perovskites, the magnetic ordering temperatures are typically very low. In addition, the coupling between magnetism and ferroelectricity is very weak. The occurrence of ferromagnetic as well as antiferromagnetic order was observed.

At the beginning of the 1960s, $BiFeO_3$ was discovered as a perovskite-type multiferroic material that apparently represents an exception to the above discussed d^0 - d^n problem [50]. However, the ferroelectric order in this case is not caused by a shifting of the magnetic Fe^{3+} ions at the B sites from their centrosymmetric positions, but by the stereochemically-active ns^2 free electron pairs ("lone pair") of the Bi^{3+} ions at the A sites [51]. $BiFeO_3$ is up to date one of the most intensively studied multiferroics [52]. One of the reasons for these intensive investigations lies for sure in the very high ordering temperatures, significantly above room temperature. Below $T_C = 1143$ K, $BiFeO_3$ becomes ferroelectric with $P_S \simeq 1 \text{ Cm}^{-2}$ [53–55] and orders then at $T_N = 643$ K antiferromagnetically, forming an incommensurate cycloidal spin arrangement [54, 56]. Because of this complicated spin structure, $BiFeO_3$ takes a special position within the group of multiferroic materials with stereochemically-active ns^2 lone electron pairs as source of ferroelectricity. In $BiFeO_3$, there exists a considerable coupling between magnetism and ferroelectricity [61–64], in contrast

⁴This mutual exclusion principle for the perovskites applies only to proper ferroelectrics, where ferroelectricity is caused by a shift of the B ions in the ABO_3 structure. There exist other mechanisms, which lead in some magnetic perovskite-type compounds to ferroelectricity, see below.

to other members of this group as, e.g., BiMnO_3 [57, 58] or PbVO_3 [59, 60].

Also at the beginning of the 1960s, the hexagonal manganates RMnO_3 ($R = \text{Sc, Y, In, Ho, Er, Tm, Yb, Lu}$) were discovered to form an additional multiferroic family [65]. The hexagonal manganates show antiferromagnetic order between 70 K and 130 K by formation of non-collinear, planar spin arrangements [66, 67]. YMnO_3 was investigated very thoroughly and exemplarily to identify the reasons for the occurrence of ferroelectricity in this family of materials [68, 69]. The structure of YMnO_3 consists of densely packed layers of trigonal MnO_5 bipyramids, which are separated by layers of Y^{3+} ions. These bipyramids have the tendency to tilt in the structure, generating Y-O pairs with an electric dipole moment. Thus, the ferroelectric order is a consequence of a structural deformation and is therefore often designated as a geometrically induced ferroelectricity. This mechanism may most probably be assigned to the other members of the family of hexagonal manganates as well. Because the microscopic mechanisms of the magnetic and the ferroelectric order are very different to each other in the group of hexagonal manganates, only a weak direct coupling between the corresponding order parameters is present. Although, a series of interesting magnetoelectric coupling phenomena was discovered [70]. In the case of YMnO_3 , a coupling of magnetic and electric domains was observed as a consequence of a pinning of antiferromagnetic domain walls at the positions of the ferroelectric domain walls [71]. In the case of HoMnO_3 , it was discovered that the application of an external electric field modifies the spin structure of the Mn^{3+} and Ho^{3+} sublattices [72]. A geometrically induced ferroelectricity exists also in the multiferroic family of barium fluorides BaMF_4 ($M = \text{Mn, Fe, Co, Ni}$), which have been investigated intensively since the end of the 1960s [73, 74].

The family of the boracites $\text{M}_3\text{B}_7\text{O}_{13}\text{X}$ ($M = \text{bivalent metal ion, } X = \text{halide ion}$) constitutes an additional group of multiferroic materials. The majority of the boracites orders antiferromagnetically at temperatures between 5 K and 95 K, sometimes with a weak ferromagnetic moment [49]. First investigations of the magnetic and ferroelectric properties of some members of this group were performed in the mid of the 1960s [75, 76]. The detailed microscopic mechanism of ferroelectricity in the family of the boracites is not completely understood yet [40]. Nevertheless, the strong distinctive anisotropy in the mixed MO_4X_2 octahedra is assumed to favour an instability of the magnetic M^{2+} ion in its centrosymmetric position and thus leading to ferroelectricity [5]. $\text{Ni}_3\text{B}_7\text{O}_{13}\text{I}$ has an exceptional position among the group of multiferroic materials of type I. Ferroelectric and also magnetic order occur simultaneously below 61.5 K in this compound (together with ferroelasticity) and show a strong magnetoelectric coupling [77, 78]. The vector of the spontaneous, weak ferromagnetic magnetization \mathbf{M}_S is perpendicular to the vector of the spontaneous electric polarization \mathbf{P}_S . The reversal of polarity of \mathbf{P}_S is connected with a rotation of \mathbf{M}_S by 90° in the plane perpendicular to \mathbf{P}_S [77]. Thus, the vector of the magnetization can be switched by applying an electric field. In the other members of the boracite family, as in most of the other

multiferroics of type I, the coupling between magnetism and ferroelectricity is only weak.

Relatively new theoretical discussions have shown that distinctive forms of electric charge order can also lead to ferroelectricity in magnetically ordered systems [79,80]. In this context, the occurrence of multiferroicity was predicted for a whole series of charge-ordered materials by theoretical considerations, such as for the family of rare-earth nickelates $R\text{NiO}_3$ ($R = \text{Ho, Lu, Pr, Nd}$) [81] or for magnetite Fe_3O_4 [82]. For magnetite, this prediction could be experimentally confirmed recently, but apparently only a short-range charge order connected with a kind of relaxor ferroelectricity was observed [83]. In many cases of charge-ordered materials, however, an unambiguous experimental proof for their ferroelectric properties is lacking. The claim of charge-ordered multiferroicity in LuFe_2O_4 [84] was disproved recently. The in the original experiments detected pyroelectric currents as well as the found anomalous large dielectric constant could be attributed to the finite intrinsic conductivity of LuFe_2O_4 in combination with extrinsic effects of the geometry of the experiment [85,86].

Further information about multiferroic materials of type I can be found in a number of review articles [5, 11, 33, 47–49, 87–89].

2.2.2 Multiferroics of type II

After the discussion of the group of multiferroics of type I in the previous section with rather independent ferroelectric and magnetic orders, this chapter is dealing with the group of multiferroics of type II, in which the magnetic ordering itself is the source for ferroelectricity.

Already at the end of the 1960s first thoughts came up whether distinctive magnetic structures may induce ferroelectricity [6,7]. In principle, spin alignments are possible, which can change an initially centrosymmetric crystal into a polar one. In such a case, the occurrence of a polar vector as, e.g., the spontaneous electric polarization is allowed, see section 2.1.1. In figure 2.1, different spin arrangements with distinct symmetries are displayed. The symmetry of two adjacent magnetic ions with parallel aligned spins in the xz plane can be described by the centrosymmetric magnetic point group $\frac{2}{m} \frac{2'}{m'} \frac{2'}{m'}$, see figure 2.1 (a).⁵ Based on this arrangement, different symmetry-lowering paths can be realized by a tilting of both spins. A canting of the spins within the xz plane leads to a polar arrangement, which is described by the magnetic point group $2m'm'$, see figure 2.1 (b). In this case, parallel to the twofold rotation axis a spontaneous electric polarization could occur. The spin arrangement, which is formed after a canting of the spins within the xy plane, can be described by the magnetic point group $22'2'$, that is non-centrosymmetric but also non-polar, see figure 2.1 (c). Therefore, no electric polarization can occur here. But also this spin

⁵The transformation properties of axial vectors under application of different space-time symmetry operations are summarized in appendix B.

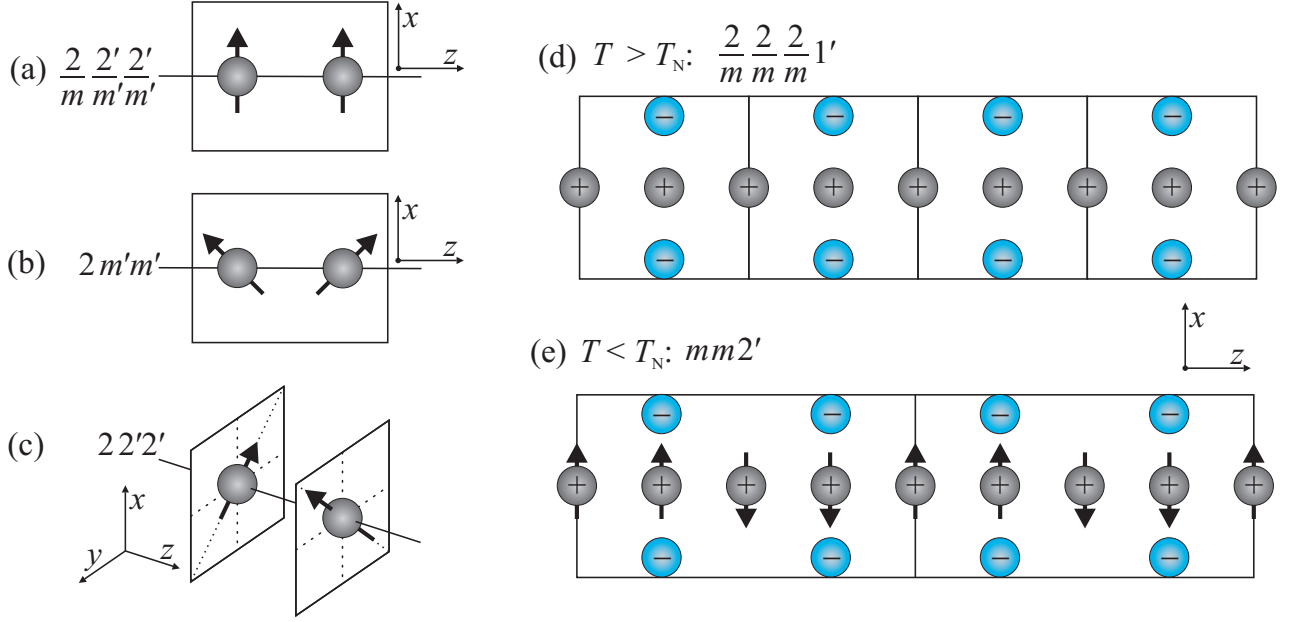


Figure 2.1: Schematic picture of different spin arrangements with their magnetic point-group symmetries. The transformation properties of axial vectors under application of different space-time symmetry operations are summarized in appendix B. (a) Centrosymmetric arrangement of two neighbouring spins. (b) Canted spin arrangement with a polar symmetry. (c) Canted spin arrangement with a non-centrosymmetric, non-polar symmetry. (d) Paramagnetic state of a hypothetical two-dimensional centrosymmetric crystal lattice above T_N (e) Collinear antiferromagnetically ordered state of the same two-dimensional crystal lattice below T_N with a polar symmetry.

arrangement as well as collinear spin structures, which are for themselves non-polar, can become polar in combination with a crystal lattice. This case is illustrated in figures 2.1 (d) and (e) using the example of a hypothetical two-dimensional, centrosymmetric crystal lattice, which becomes non-centrosymmetric and polar with the onset of an antiferromagnetic $\uparrow\downarrow\downarrow\uparrow$ order below T_N . At this transition the point group $\frac{2}{m} \frac{2}{m} \frac{2}{m} 1'$ of the paramagnetic structure transforms into the polar one $mm 2'$ of the antiferromagnetically ordered structure. Consequently, an electric polarization could develop parallel to the twofold rotation axis in this case.

Similar symmetry considerations, as illustrated above, led at the end of the 1970s to the identification of more than 30 potential multiferroics among the magnetic compounds known at this time [8]. One of these compounds, Cr_2BeO_4 , turned out to be indeed a multiferroic. Neutron-diffraction experiments revealed that Cr_2BeO_4 orders magnetically below 28 K by formation of a cycloidal spin structure and dielectric investigations proved that it becomes simultaneously ferroelectric [8, 9]. Thus, Cr_2BeO_4 was the first discovered multiferroic of type II. Despite the successful experimental proof that special magnetic structures as in Cr_2BeO_4 can induce ferroelectricity, this idea was not pursued in the following decades. Not until much later in 2003, with TbMnO_3 an additional multiferroic material of type II with a cycloidal spin arrangement below $T_C = 27$ K was discov-

ered [10,90]. The strong coupling between ferroelectric and magnetic order in this compound (an applied magnetic field rotates the electric polarization by 90°) led subsequently to an intensive search for additional multiferroics of type II. In the meantime, a large number of multiferroic materials of this class is known. Most of them show cycloidal spin structures, such as Cr_2BeO_4 or TbMnO_3 . But there exist also examples with spiral or collinear spin configurations as, for example, CuFeO_2 [91] or $\text{Ca}_3\text{CoMnO}_6$ [92]. Especially among magnetic frustrated systems, an exceptional large number of multiferroics of type II was found. Therefore, multiferroics of type II have usually very low magnetic ordering temperatures. Furthermore, the absolute values of the induced electric polarizations in this class of materials are typically some orders of magnitude smaller than in conventional ferroelectrics. For example, the electric polarization of TbMnO_3 reaches at 10 K a value of about $\sim 0.8 \text{ mC/m}^2$, whereas the electric polarization of the conventional ferroelectric BaTiO_3 amounts to $\sim 260 \text{ mC/m}^2$ at room temperature [10].

Parallel to the search for new multiferroics of type II and the experimental characterization of their properties, different models to explain the magnetically induced ferroelectricity were developed and discussed. These are partly based on exclusively electronic [93–96] and partly on exclusively ionic mechanisms [80, 97–100]. Recently, a generalized model to describe the spin-induced ferroelectricity was proposed, that combines the electronic as well as the ionic contributions [101]. Nevertheless, in many cases of known multiferroics of type II it is not yet clear which mechanisms are responsible for or dominate the magnetically induced ferroelectricity.

In the case of cycloidal spin structures, all discussed microscopic models unfold, at least qualitatively, the same prediction for the electric polarization, which is induced by the spin structure via

$$\mathbf{P} \propto \mathbf{e}_{ij} \times (\mathbf{S}^{(i)} \times \mathbf{S}^{(j)}). \quad (2.9)$$

Here, \mathbf{e}_{ij} denotes the unit vector along the connecting line of two adjacent spins $\mathbf{S}^{(i)}$ and $\mathbf{S}^{(j)}$. The magnitude of the corresponding proportionality constant is dependent on the dominating microscopic mechanisms of the spin-orbit coupling, the spin-exchange interactions and on the magnetoelastic coupling of the crystal lattice. The vector of the electric polarization is oriented perpendicular to \mathbf{e}_{ij} as well as to the spin rotation axis in accordance to the results of the symmetry considerations of different canted spin arrangements from above. Its sign depends on the helicity of the cycloid. Its absolute value is dependent on the magnitude of the proportionality constant and on the magnitude of the rotation angle between two adjacent spins of the cycloid.

The most prominent model for magnetically induced ferroelectricity in the case of cycloidal spin structures is based on the antisymmetric Dzyaloshinskii-Moriya interaction [97], which results from a relativistic correction to the usual super-exchange interaction. Originally, it was introduced

and discussed to explain the canting of antiferromagnetically ordered spins in materials, such as $\alpha\text{-Fe}_2\text{O}_3$ [102, 103]. Two adjacent spins $\mathbf{S}^{(i)}$ and $\mathbf{S}^{(j)}$ of a super-exchange chain can be described by the Hamiltonian

$$H_{\text{DM}} = \mathbf{D}_{ij} \cdot (\mathbf{S}^{(i)} \times \mathbf{S}^{(j)}). \quad (2.10)$$

The orientation of the so-called Moriya-vector \mathbf{D}_{ij} depends on the local symmetry of the crystal lattice [103]. This is illustrated in figure 2.2, which shows a schematic picture of two one-dimensional super-exchange chains of different local symmetry with a cycloidal spin arrangement. The orientation of the n -th spin within the cycloid can be described as follows:

$$\mathbf{S}^{(n)} = \begin{pmatrix} 0 \\ S_2^{(0)} \cos(n\theta + \varphi_2) \\ S_3^{(0)} \cos(n\theta + \varphi_3) \end{pmatrix} \quad (2.11)$$

The quantity θ denotes the rotation angle between two adjacent spins and $(\varphi_2 - \varphi_3)$ the phase shift between the two spin components $S_2^{(n)}$ and $S_3^{(n)}$. In the first case presented in figure 2.2 (a), the diamagnetic ions X^- are located at the centres between the magnetic ions M^+ . Therefore, at each X^- site an inversion centre is present, leading to a vanishing Dzyaloshinskii-Moriya interaction [103]. In the second case presented in figure 2.2 (b), the diamagnetic ions are shifted out of their centrosymmetric positions, leading to the formation of a zigzag chain. For each $\text{M}_n^+ - \text{X}^- - \text{M}_{(n+1)}^+$ molecule, a Dzyaloshinskii-Moriya interaction occurs with the Moriya-vector

$$\mathbf{D}_{n,n+1}(\mathbf{u}_n) = \gamma(\mathbf{e}_2 \times \mathbf{u}_n) \quad (2.12)$$

as a function of the respective shifting vector \mathbf{u}_n . The vector \mathbf{e}_2 designates the unit vector along the connecting line of two magnetic ions M_n^+ and $\text{M}_{(n+1)}^+$ and γ is a constant [97, 104]. Starting from the zigzag-chain configuration of figure 2.2 (b), the influence of small motions $\delta\mathbf{u}_{(n)}$ of the diamagnetic ions X^- on the Hamiltonian will be considered. According to [97], the part of the Hamiltonian, that depends on $\delta\mathbf{u}_{(n)}$, consists of the Dzyaloshinskii-Moriya interaction and a term of the elastic energy:

$$\begin{aligned} \delta H &= \sum_n \gamma(\mathbf{e}_2 \times \delta\mathbf{u}_{(n)}) \cdot (\mathbf{S}^{(n)} \times \mathbf{S}^{(n+1)}) + \sum_n \frac{\kappa}{2}(\delta u_{(n)1}^2 + \delta u_{(n)2}^2 + \delta u_{(n)3}^2) \\ &= \sum_n \gamma \delta\mathbf{u}_{(n)} \cdot (\mathbf{e}_2 \times (\mathbf{S}^{(n)} \times \mathbf{S}^{(n+1)})) + \sum_n \frac{\kappa}{2}(\delta u_{(n)1}^2 + \delta u_{(n)2}^2 + \delta u_{(n)3}^2) \end{aligned} \quad (2.13)$$

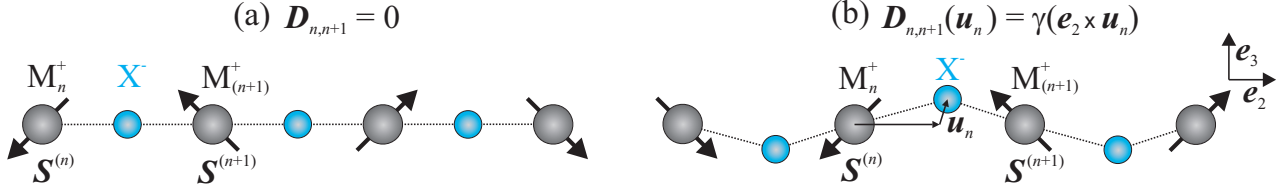


Figure 2.2: Schematic picture of two one-dimensional super-exchange chains of different local symmetry. Each chain consist of diamagnetic X^- and magnetic ions M^+ . (a) In the case of inversion centres, located at the X^- sites the Dzyaloshinskii-Moriya interaction vanishes. (b) A shifting of the X^- ions out of their centrosymmetric positions destroys the inversion centres. For each $M_n^+-X^- - M_{(n+1)}^+$ molecule, a Dzyaloshinskii-Moriya interaction occurs with the Moriya-vector $\mathbf{D}_{n,n+1}(\mathbf{u}_n) = \gamma(\mathbf{e}_2 \times \mathbf{u}_n)$ as a function of the respective shifting vector \mathbf{u}_n .

After inserting equation 2.11 into equation 2.13 and using a trigonometric identity⁶ the following expression for the Hamiltonian is obtained:

$$\delta H = \sum_n \left(\gamma S_2^{(0)} S_3^{(0)} \sin(\theta) \sin(\varphi_3 - \varphi_2) \delta u_{(n)3} + \frac{\kappa}{2} (\delta u_{(n)1}^2 + \delta u_{(n)2}^2 + \delta u_{(n)3}^2) \right) \quad (2.14)$$

By partial differentiation of equation 2.14 with respect to $\delta u_{(n)i}$ an energy minimum results for

$$\delta u_{(n)3} = -\frac{\gamma}{\kappa} S_2^{(0)} S_3^{(0)} \sin(\theta) \sin(\varphi_3 - \varphi_2), \quad \delta u_{(n)2} = \delta u_{(n)1} = 0. \quad (2.15)$$

Therefore, a collective displacement of the diamagnetic ions X^- parallel to \mathbf{e}_3 may occur generating an electric polarization in the same direction. This result is equivalent to the general prediction from equation 2.9 for the electric polarization induced by a cycloidal spin arrangement. The term of the elastic energy in the second line of equation 2.13 is always positive. In addition, the term of the Dzyaloshinskii-Moriya interaction $\mathbf{e}_2 \times (\mathbf{S}^{(n)} \times \mathbf{S}^{(n+1)})$ has the same value for all spin pairs of the cycloid. Therefore, the displacements $\delta \mathbf{u}_{(n)}$ of all diamagnetic ions X^- have to be oriented in the same direction, parallel or antiparallel to $\mathbf{e}_2 \times (\mathbf{S}^{(n)} \times \mathbf{S}^{(n+1)})$ in order to minimize the total energy. Consequently, the induced electric polarization can be expressed by the proportionality relation from equation 2.9.

In order to give an idea how ferroelectricity can be induced by collinear spin structures, the example of $\text{Ca}_3\text{CoMnO}_6$ will be discussed in the following. $\text{Ca}_3\text{CoMnO}_6$ has a quasi one-dimensional chain-like arrangement of magnetic Co^{2+} and Mn^{4+} ions. Below $T_N = 16$ K a polar, antiferromagnetic "up-up-down-down"-spin structure [92] (magnetic point group $2m'm'$) arises, see figure 2.3. This spin structure may be described by a frustrated Ising-spin chain with ferromagnetic exchange interactions between nearest neighbours (J_F) and antiferromagnetic exchange interactions between

⁶ $\sin(\alpha - \beta) = \sin(\alpha) \cos(\beta) - \cos(\alpha) \sin(\beta)$

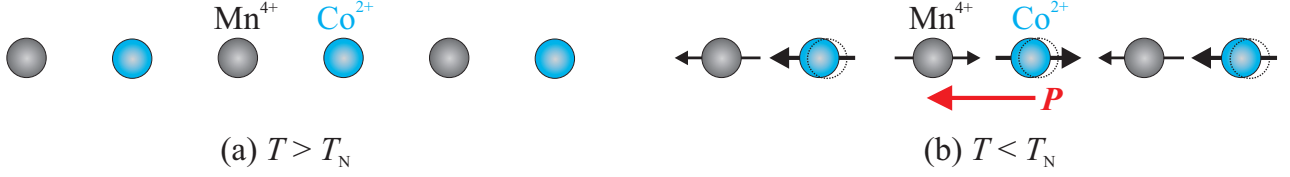


Figure 2.3: Schematic picture of the chain configuration in the (a) paramagnetic phase and (b) antiferromagnetically ordered phase of $\text{Ca}_3\text{CoMnO}_6$. Below the Néel temperature, a collective displacement of the Co^{2+} ions with respect to the Mn^{4+} ions occurs along the chain. Consequently, an electric polarization in the same direction arises [92].

next-nearest neighbours (J_{AF})

$$H = J_{\text{F}} \sum_i S_i^z S_{i+1}^z + J_{\text{AF}} \sum_i S_i^z S_{i+2}^z \quad \text{with } J_{\text{AF}} > 1/2 |J_{\text{F}}|. \quad (2.16)$$

If $\partial J_{\text{F}}/\partial x \neq 0$ and $\partial J_{\text{AF}}/\partial x \neq 0$, an energy gain can arise by shortening the bonds between ions with parallel spins. Consequently, an electric polarization along the chain is generated because of the different valencies of the Co^{2+} and Mn^{4+} ions.

2.3 The magnetoelectric effect

Coupling phenomena between magnetic and electric properties of solids, such as the coupling between magnetic and ferroelectric order in some multiferroics, are designated in general as magnetoelectric effects. The original definition for magnetoelectric effects is, however, interpreted considerably narrower and describes the generation of an electric polarization in a solid by an applied magnetic field or vice versa the generation of a magnetization by an applied electric field. In the following, magnetoelectric effects shall be discussed in this narrower sense. One can distinguish the linear magnetoelectric effect and effects of higher order.

Based on symmetry considerations, Pierre Curie predicted already in 1894 the possibility of magnetoelectric effects in solids [2], but it took another 60 years until the antiferromagnetic Cr_2O_3 was discovered to be the first linear magnetoelectric material [4, 105–109]. Cr_2O_3 certainly is the most intensively investigated and best understood magnetoelectric until today. Though, at the same time first magnetoelectrics of higher order were found [110, 111], most of the experimental and theoretical work in this field concentrated on the linear magnetoelectric effect. Subsequently, many more linear magnetoelectrics were discovered such as Ti_2O_3 [112] or GaFeO_3 [113]. A summary of a large number of known materials, which show the linear magnetoelectric effect, can be found in [114]. In addition, there exist a lot of review articles about the magnetoelectric effect [70, 115–117].

2.3.1 Phenomenological description

Phenomenologically, magnetoelectric effects may be described by an expansion of the density of the free enthalpy in analogy to equation 2.5, neglecting the terms of the mechanical strain [118]:

$$\begin{aligned}
 -g(\mathbf{E}, \mathbf{H}) = & -g_0 + P_i^{(S)} E_i + \mu_0 M_i^{(S)} H_i + \frac{1}{2} \varepsilon_0 \chi_{ij}^{(el)} E_i E_j + \frac{1}{2} \mu_0 \chi_{ij}^{(mag)} H_i H_j \\
 & + \alpha_{ij} E_i H_j + \frac{1}{2} \beta_{ijk} E_i H_j H_k + \frac{1}{2} \gamma_{ijk} H_i E_j E_k + \dots
 \end{aligned} \quad (2.17)$$

The magnetoelectric polarization and magnetization are obtained by differentiation of equation 2.17 with respect to \mathbf{E} or \mathbf{H} and by taking into account only the mixed terms of the second line.

$$P_i^{(ME)} = -\frac{\partial g}{\partial E_i} = \alpha_{ij} H_j + \frac{1}{2} \beta_{ijk} H_j H_k + \gamma_{jki} H_j E_k + \dots \quad (2.18)$$

$$\mu_0 M_i^{(ME)} = -\frac{\partial g}{\partial H_i} = \alpha_{ji} E_j + \beta_{jki} E_j H_k + \frac{1}{2} \gamma_{ijk} E_j E_k + \dots \quad (2.19)$$

The axial c tensor $[\alpha_{ij}]$ in equations 2.18 and 2.19 describes the linear magnetoelectric effect [119], the polar i tensor $[\beta_{ijk}]$ and the axial c tensor $[\gamma_{ijk}]$ characterize the bilinear and quadratic magnetoelectric effect, respectively [120, 121].⁷ The tensors $[\beta_{ijk}]$ as well as $[\gamma_{ijk}]$ are symmetric in their last two indices, whereas $[\alpha_{ij}]$ needs in general not to be symmetric. The linear magnetoelectric effect can occur only in magnetically ordered states, that do not contain the time-reversal symmetry element $1'$ as separate symmetry operation. In 58 of the 90 magnetic point groups the linear magnetoelectric effect is allowed. A summary of these point groups including the associated tensor forms can be found in appendix G. The magnetic point groups, which allow the bilinear or quadratic magnetoelectric effect, are summarized in appendix G in the tables 5 and 6. The associated tensor forms are in this case not specified but can be found, for example, in [122]. Apart from the SI-unit system, the rationalized or non-rationalized Gaussian CGS system is used frequently in the literature for the definition of the magnetoelectric tensors.⁸ The relation between the linear magnetoelectric tensor defined in these three unit systems can be described as follows [109, 117].

$$^c \alpha_{ij} = 4\pi \alpha_{ij}^{rG} = \alpha_{ij}^G \quad (2.20)$$

⁷The definition of polar and axial c and i tensors can be found in appendix A. The magnetoelectric effects of higher order, described by $[\beta_{ijk}]$ and $[\gamma_{ijk}]$ can be considered as magnetic-field and electric-field induced linear magnetoelectric effects, respectively. $[\beta_{ijk}]$ has the same symmetry restrictions as the piezoelectric effect and $[\gamma_{ijk}]$ the same as the piezomagnetic effect.

⁸In the present work, all magnetoelectric tensors are given in SI units.

Here, α^{rG} and α^{G} denote the linear magnetoelectric tensor in the rationalized and non-rationalized Gaussian CGS system, respectively, and c is the velocity of light in the vacuum.

In addition to the primary magnetoelectric effects, described by equations 2.18 and 2.19, secondary effects are also imaginable as, for example, the combination of the impact of magnetostrictive and piezoelectric or electrostrictive and piezomagnetic effects, respectively. Such secondary effects should in fact be considered when investigating and describing magnetoelectric effects, as is commonly done when dealing with the pyroelectric effect [123]. Nevertheless, this type of problems has hardly attracted any attention in the literature up to now.

According to the classification of ferroic effects in section 2.1, the linear as well as the bilinear and quadratic magnetoelectric effects are ferroic effects of higher order. Therefore, the general concepts, which were developed in this context to describe ferroic ordering phenomena, can also be applied to magnetoelectric effects. A higher-symmetric prototypic phase can be assigned to each magnetoelectric phase. Both are connected via a symmetry-lowering ferroic phase transition leading to the generation of magnetoelectric domains, which differ at least in one pair of the components of the respective magnetoelectric tensors. Thus, in the presence of the external fields \mathbf{E} and \mathbf{H} an energy difference between different domains results, which may be described as follows.⁹

$$\Delta g = \Delta\alpha_{ij}E_iH_j + \frac{1}{2}\Delta\beta_{ijk}E_iH_jH_k + \frac{1}{2}\Delta\gamma_{ijk}H_iE_jE_k + \dots \quad (2.21)$$

For the switching of magnetoelectric domains, an electric as well as a magnetic field is necessary then. The required mutual orientation of both of these fields results from the form of the magnetoelectric tensors.

2.3.2 Microscopic origin and theoretical description

In order to explain the temperature dependence of the linear magnetoelectric effect of Cr_2O_3 a microscopic, semi-empirical theory was developed, using a two-ion model [124]. Accordingly, the temperature dependence of the linear magnetoelectric tensor components for \mathbf{B} parallel (α_{\parallel}) and \mathbf{B} perpendicular (α_{\perp}) to the magnetic easy axis are characterized by the product of the corresponding magnetic susceptibilities $\chi_{\parallel}^{(\text{mag})}(T)$ and $\chi_{\perp}^{(\text{mag})}(T)$ with the sublattice magnetization $\bar{S}(T)$.

$$\alpha_{\parallel}(T) \propto \chi_{\parallel}^{(\text{mag})}(T) \cdot \bar{S}(T), \quad \alpha_{\perp}(T) \propto \chi_{\perp}^{(\text{mag})}(T) \cdot \bar{S}(T) \quad (2.22)$$

⁹See also equation 2.6 in section 2.1.

This theory was extended in the context of perturbation theory [125–128]. The modification of the single-ion anisotropy, the symmetric and antisymmetric superexchange interactions, the dipolar interactions and the Zeeman energy by an electric field were considered.

The perturbative nature of the microscopic mechanisms leading to the linear magnetoelectric effect also explains its relative weakness. An upper bound for the linear magnetoelectric effect is given by the relation [129]

$$\alpha_{ij}^2 < \chi_{ii}^{(\text{el})} \chi_{jj}^{(\text{mag})}, \quad (2.23)$$

where $\chi_{ii}^{(\text{el})}$ and $\chi_{jj}^{(\text{mag})}$ denote the electric and magnetic susceptibility, respectively. Thus, only in ferroelectric and/or ferromagnetic materials with large susceptibilities an appreciably large magnetoelectric effect can be expected.

2.4 Ferrotoroidicity

Certain antiferromagnetic spin orders with head to tail arrangements of spins forming spin vortices can be described by a time- and space-antisymmetric, axio-polar vector quantity \mathbf{t} (limiting group $\frac{\infty}{m'} \frac{2}{m} \frac{2}{m}$ [130]) called the toroidal moment.¹⁰ For the case of localized magnetic moments \mathbf{m}_α being positioned at the lattice sites \mathbf{r}_α , this quantity is defined as [131]

$$\mathbf{t} = \frac{1}{2} \sum_{\alpha} \mathbf{r}_\alpha \times \mathbf{m}_\alpha, \quad (2.24)$$

where the sum runs over all magnetic moments \mathbf{m}_α . A shift of the origin by the vector \mathbf{R} leads to

$$\mathbf{t}' = \frac{1}{2} \sum_{\alpha} (\mathbf{r}_\alpha + \mathbf{R}) \times \mathbf{m}_\alpha = \mathbf{t} + \frac{1}{2} \mathbf{R} \times \sum_{\alpha} \mathbf{m}_\alpha. \quad (2.25)$$

Because the sum $\sum_{\alpha} \mathbf{m}_\alpha$ in equation 2.25 over all magnetic moments will be non-zero in general, the definition of the toroidal moment in equation 2.24 is dependent on the choice of the origin within the crystal lattice. For many antiferromagnetic structures, however, $\sum_{\alpha} \mathbf{m}_\alpha$ vanishes and therefore the toroidal moment then is independent from the chosen origin.¹¹ Analogous to the definition of the magnetization \mathbf{M} as the density of the magnetic dipole moment the toroidization \mathbf{T} can be defined as the density of the toroidal moment [131]. For a bulk crystal containing N

¹⁰In table 5 and 6 of appendix G the 31 magnetic point groups, that allow the presence of a toroidal moment, are listed.

¹¹A detailed discussion about the origin dependence of the toroidal moment can be found in [131, 132].

identical unit cells of the volume V , this definition leads to

$$\mathbf{T} = \frac{1}{2NV} \sum_{\alpha} \mathbf{r}_{\alpha} \times \mathbf{m}_{\alpha} = \frac{1}{2V} \sum_i \mathbf{r}_i \times \mathbf{m}_i, \quad (2.26)$$

where the summation on the right side of equation 2.26 runs over all magnetic moments within one unit cell. In addition to the origin dependence of the toroidal moment, a multivaluedness problem arises for the toroidization due to the periodic boundary conditions in a bulk solid crystal. Therefore, only changes in the toroidization are well-defined quantities and are considered as physically measurable quantities [131, 132].

As will be shown in the following, the concept of the toroidal moment can also be set into relation to the linear magnetoelectric effect. According to [132, 133], the integral $I = - \int \mathbf{M}(\mathbf{r}) \mathbf{H}(\mathbf{r}) d^3r$ of a continuous magnetization distribution $\mathbf{M}(\mathbf{r})$ in an inhomogeneous magnetic field $\mathbf{H}(\mathbf{r})$ can be expanded in powers of field gradients, calculated at some arbitrary reference point $\mathbf{r} = 0$. Up to the first order this expansion leads to the following expression [132, 133]:

$$I = -\mathbf{m} \cdot \mathbf{H}(0) - a(\nabla \mathbf{H})_{\mathbf{r}=0} - \mathbf{t} \cdot [\nabla \times \mathbf{H}]_{\mathbf{r}=0} - q_{ij}(\partial_i H_j + \partial_j H_i)_{\mathbf{r}=0} - \dots \quad (2.27)$$

The zero-order term in equation 2.27 contains the magnetic dipole moment \mathbf{m} . The first-order terms are composed of the magnetoelectric monopole moment a , the toroidal moment \mathbf{t} and the magnetic quadrupole moment q_{ij} [133]. As can be seen in equation 2.27, the toroidal moment couples to the curl of the magnetic field. All these first-order terms are time- and space-antisymmetric and have therefore the same symmetry properties with respect to time reversal and spatial inversion as the linear magnetoelectric effect. The linear magnetoelectric tensor $[\alpha_{ij}]$ can be decomposed into a pseudoscalar \tilde{a} , a vector $[\tilde{t}_k]$ and a symmetric traceless tensor $[\tilde{q}_{ij}]$ [132]:

$$\alpha_{ij} E_i H_j = \tilde{a} E_i H_i + \tilde{t}_k \epsilon_{kij} E_i H_j + \tilde{q}_{ij} (E_i H_j + E_j H_i) \quad (2.28)$$

A comparison of equation 2.27 with equation 2.28 directly reveals that the presence of non-zero magnetic multipoles a , \mathbf{t} and q_{ij} contributes to the scalar, the antisymmetric and symmetric part of the magnetoelectric response, respectively. Therefore, non-zero components of the antisymmetric part of the linear magnetoelectric tensor are a necessary condition for the occurrence of a toroidal moment. However, it is difficult to give a general relation between the magnetic multipoles a , \mathbf{t} and q_{ij} and the corresponding components of the linear magnetoelectric tensor. In this sense, the presence of an antisymmetric part of the magnetoelectric response is not necessarily indicative for a toroidal moment [132]. There are spin structures, which do not give rise to a toroidal moment but nevertheless allow antisymmetric magnetoelectric responses, as, for example, in the compound

ZnCr_2Se_4 [132, 134, 135].

As was shown in section 2.1.1, the order parameters of the primary ferroic effects ferroelectricity, ferromagnetism and ferroelasticity can be classified in terms of spatial inversion and time reversal symmetry. In this sense, the spontaneous electric polarization is time-symmetric and space-antisymmetric, the spontaneous magnetization space-symmetric and time-antisymmetric and finally the spontaneous strain time- and space-symmetric. There is an ongoing debate in literature about the question if the toroidal moment, introduced above could complete this symmetry scheme being the order parameter of a fourth type of primary ferroic order (ferrotoroidicity), which breaks both time-reversal and space-inversion symmetry [25, 131–133, 136–138]. If ferrotoroidicity were a fourth primary ferroic effect, the expansion of the free enthalpy g in equation 2.5 could be extended by ferrotoroidic terms [25]:

$$g = g_0 - \dots T_i^{(S)} S_i - \frac{1}{2} \tau_{ij} S_i S_j - \theta_{ij} E_i S_j - \zeta_{ij} H_i S_j - g_{ijk} S_i \sigma_{jk} \quad (2.29)$$

Here, $[T_i^{(S)}]$ denotes the spontaneous toroidization, $[\tau_{ij}]$ the toroidic susceptibility, $[\theta_{ij}]$ the linear electrotoroidic effect, $[\zeta_{ij}]$ the linear magnetotoroidic effect and $[g_{ijk}]$ the piezotoroidic effect. The driving force for ferrotoroidic domain switching in this case would be a crossed electric and magnetic field $[S_i] = [(\mathbf{E} \times \mathbf{H})_i]$. But according to equation 2.27, an inhomogeneous magnetic field with a non-vanishing curl could also be used for domain switching and via the magnetoelectric effect also collinear magnetic and electric fields. Furthermore, in the case of ferrotoroidic domains with a ferromagnetic contribution in a canted spin structure even a magnetic field would be sufficient [25].

The extension of Aizu's classification of ferroic phase transitions to ferroic phases allowing a spontaneous toroidization, reveals that ferrotoroidic domains will always be identical with the corresponding antiferromagnetic domains [25, 136]. Furthermore, up to date no definite experimental proof exists that the toroidal moment can serve as a primary order parameter independent from an antiferromagnetic or structural ordering. Therefore, it is an open question if the concept of the toroidal moment describes new ordering phenomena or if it is only a different description of the already well-known magnetic or magnetoelectric types of ordering.

Chapter 3

Experimental

The experimental focus of this thesis lies on the investigation of the dielectric and magnetoelectric characteristics of new multiferroic or magnetoelectric materials. However, a lot of other thermodynamic properties were investigated in the present work as well, such as the thermal expansion or linear magnetostriction, the magnetic susceptibility and the specific heat. In addition, polarized-light microscopy was used to visualize ferroelastic domains and to detect phase transitions connected with a loss of symmetry. The experimental fundamentals of dielectric and magnetoelectric investigations, which are relevant for the present work, are discussed in detail in the following sections. The basics of the other above mentioned investigations are only briefly explained in section 3.1. However, in these cases references are given, where much more detailed informations can be found.

3.1 Experimental environment

Most of the measurements were performed in two different ^4He -bath cryostats (OXFORD Instruments, Cryogenic Ltd). Both are equipped with superconducting magnets and lambda stages. The maximal achievable magnetic fields at the basis temperature of 4.2 K amount to 14 T and 15 T, respectively and can be increased by 2 T using the lambda stages. More detailed information about the cryostats can be found, e.g., in [142, 143]. By inserting a variable temperature insert (VTI) (KONTI cryostat, CryoVac) into these cryostats, a temperature range of 1.8-300 K is covered for the experiments. A precise temperature control is achieved using a temperature controller (LS 340, LakeShore). The VTI was put into operation by S. Orbe during her diploma thesis and is described there in detail [144]. By operating a sorption-pumped ^3He insert (HelioxVL, OXFORD Instruments) within the cryostats, the experimental low-temperature limit can be expanded down to 0.25 K. A detailed description of his functionality can be found, e.g., in [145]. The temperature control is provided by a temperature controller (ITC-501, OXFORD Instruments). Via a filter box

different measurement devices can be connected to the Heliox insert [146]. The sample holder used in the Heliox insert for the dielectric investigations as well as the measuring insert used in the VTI are described in the following sections.

For the thermal-expansion and magnetostriction measurements in the Heliox system and in the VTI, two different home-built capacitance dilatometers were used. The dilatometer for the Heliox system was engineered by O. Heyer during his diploma thesis [147]. The dilatometer for the VTI was designed by S. Orbe during her diploma thesis [144]. Some of the thermal-expansion measurements in zero magnetic field were performed in a home-built apparatus, called "TADNull", which covers a temperature range of 4.2-200 K [148, 149], and some others in a commercial inductive dilatometer (Perkin Elmer TMA7) in a temperature range of 130-273 K. Some fundamentals of capacitance dilatometry are summarized in [150–152]. The thermal-expansion coefficients $\alpha_i = 1/L_i^0 \cdot \partial \Delta L_i / \partial T$ and the linear magnetostriction coefficients $\lambda_i = 1/L_i^0 \cdot \partial \Delta L_i / \partial B_i$ were obtained by numerically calculating the temperature and magnetic-field derivatives of the length changes ΔL_i , where L_i^0 denotes the respective sample length along the measured axis. In order to enlarge the available temperature range for dielectric investigations, a continuous-flow cryostat operated with cold nitrogen gas, which covers the temperature range 100-580 K, was designed and built with the help of the mechanical workshop of the II. Physikalisches Institut in the course of the present work. Two similar cryostats, designed by H. Schneeberger and E. Breidenbach [153, 154] during their PhD theses served as a guide for the design of the new cryostat. Magnetic fields cannot be applied in this apparatus. In the context of the master thesis of L. Anderson [155], the continuous-flow cryostat was tested and optimized by investigating different well-known pyroelectrics and ferroelectrics. However, during the actual work no new multiferroic material with an ordering temperature in the temperature range of the new cryostat was found. Therefore, the design and the mode of operation of this cryostat is not described here, but in appendix D. In addition, the results of some test measurements are presented and compared with the results of corresponding measurements in the VTI as well as with data from the literature. For the measurements of the magnetic susceptibility, two different commercial systems, a SQUID (MPMS, Quantum Design) and a vibrating-sample magnetometer (PPMS, VSM, Quantum Design), were used. All the measurements in the SQUID magnetometer were performed by S. Heijligen. The VSM allows measurements in a temperature range of 1.8-400 K and a magnetic-field range of 0-14 T, while the SQUID magnetometer covers a temperature range of 1.8-325 K and a magnetic-field range of 0-7 T. Both systems are described in detail in many PhD and diploma theses, see, e.g., [139–141]. For the detection of symmetry-lowering phase transitions as well as for the observation of ferroelastic domains, a polarized-light microscope (Orthoplan-Pol, Leitz), equipped with a continuous-flow cryostat (Microstat, OXFORD Instruments) with a temperature range 4-500 K was used. The temperature control is provided by a temperature controller (ITC-502, OXFORD Instruments). The

whole equipment stems from J.-P. Riv  ra from the department of inorganic and analytical chemistry at the Universit   de Geneve and was put into operation by M. Schalenbach during his bachelor thesis [156]. For the specific-heat measurements, a commercial calorimeter (PPMS, Quantum Design) with a temperature range of 1.8-400 K and a magnetic-field range of 0-14 T was used. The measurement principle is based on a thermal-relaxation method. The sample on the sample platform is weakly coupled to a surrounding heat reservoir with a constant temperature. Then, a well-defined heat pulse is applied to the sample platform leading to an exponential rise of the sample temperature proceeded by an exponential relaxation. From the time constants of temperature rise and relaxation the specific heat can be determined. More information about the used relaxation method and specific-heat measurements in general can be found, e.g., in [139, 145, 157]. X-ray powder-diffraction measurements were performed in the temperature range 5-300 K using a diffractometer (D-5000, Siemens), equipped with a home-built ^4He -flow cryostat. Si was added to the powder samples under investigation as an internal standard. T. Bardenheuer and J. Brand gave assistance during these measurements. Prof. Dr. P. Becker determined peak positions and intensities from the raw data by full-profile fitting, the patterns were indexed with the software TREOR and the lattice constants were refined by least-squares refinement (all implemented in WinXPOW suite [158]). More information about the diffractometer Siemens D-5000 and experimental details about powder-diffraction measurements can be found, e.g., in [159, 160].

3.2 Dielectric investigations

This section is organized as follows. First, the basic principles of pyroelectric- and magnetoelectric-current measurements as well as of measurements of the quasistatic relative dielectric constant are explained. Then, important techniques of crystal preparation are discussed and the experimental apparatus is presented. Finally, the techniques to analyse the experimental data including a discussion of possible error sources and their adequate consideration during the analysis are introduced.

3.2.1 The spontaneous electric polarization

The temperature dependence of the spontaneous electric polarization of a single-domain, ferroelectric/multiferroic crystal below the Curie temperature is described by the pyroelectric effect [161].

$$\Delta P_i = p_i(T) \Delta T \quad (3.1)$$

A temperature change ΔT causes a change of the spontaneous electric polarization $\Delta \mathbf{P}$. The derivative of the spontaneous electric polarization with respect to the temperature $p_i(T) = \partial P_i(T) / \partial T$ is referred to as the pyroelectric coefficient. It is dependent on the ther-

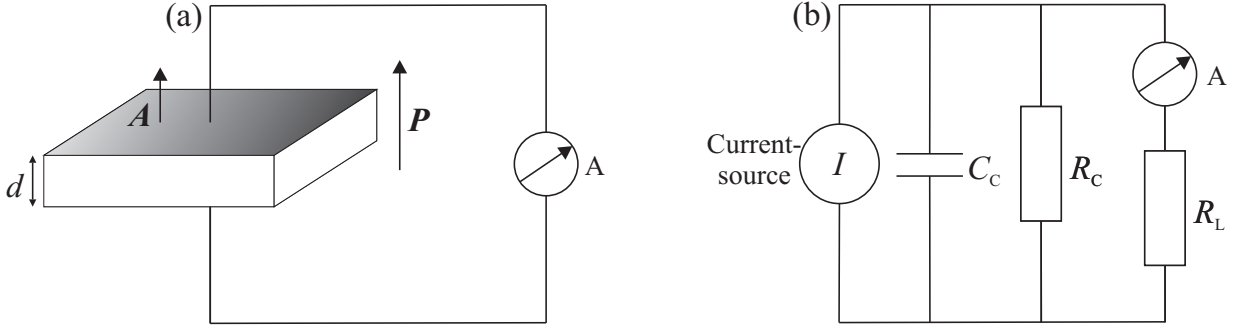


Figure 3.1: (a) Schematic picture of the experimental setup for pyroelectric-current measurements. (b) Equivalent circuit of the experimental setup. C_C denotes the capacity of the sample and R_C its electric resistivity, which can be composed of an intrinsic and extrinsic contribution. An extrinsic conductivity can, e.g., arise from contaminated sample edges leading to surface currents. R_L stands for the input resistivity of the amperemeter.

modynamic boundary conditions. The pyroelectric coefficient at constant mechanical strain ($[\epsilon_{ij}] = \text{const.}$) is different from the pyroelectric coefficient at constant mechanical stress ($[\sigma_{ij}] = \text{const.}$). In the second case, a thermal expansion of the sample under investigation can contribute via the piezoelectric effect to the change of polarization and thus to the pyroelectric coefficient. Further information about the pyroelectric effect can be found, for example, in [123, 161, 234].

The measurement principle applied in this work to determine the spontaneous electric polarization of a ferroelectric/multiferroic crystal is a slight modification of the principle proposed by R. L. Byer and C. B. Roundy [162] to investigate the pyroelectric effect.¹ In the following a mechanical free, plane-parallel sample with metallized surfaces with the area A is considered. The sample surfaces are short circuited via a high-sensitive amperemeter (picoamperemeter, electrometer) with an input resistance R_L , see figure 3.1. At the beginning the sample shall be in its paraelectric phase. A continuous change of the electric polarization will occur according to equation 3.1 below the Curie temperature during a cooling cycle with a constant rate dT/dt .² The resulting surface charges will be compensated through the amperemeter and the electric resistivity R_C of the sample. The corresponding pyroelectric current

$$I(T) = \frac{R_C}{R_L + R_C} Ap(T) \frac{dT}{dt} \quad (R_L \ll R_C) \quad Ap(T) \frac{dT}{dt}, \quad (3.2)$$

(which is registered by the amperemeter) is dependent on the ratio of the electric resistances R_C and R_L . Because the input resistance R_L of an amperemter is usually very small, the fac-

¹A summary about the basic principles of pyroelectric-current measurements is given in [163].

²At this point the simplifying assumption is made that at the transition into the ferroelectric phase only one ferroelectric domain is generated.

tor $R_C/(R_L + R_C)$ may be neglected for adequately well electrically insulating crystals. Solving equation 3.2 for the pyroelectric coefficient leads to

$$p(T) = \frac{1}{A} \frac{dt}{dT} I(T). \quad (3.3)$$

By integration of equation 3.3 with respect to the temperature the electric polarization $P(T)$ is obtained, disregarding the at first unknown integration constant $P(T_0)$:

$$P(T) = P(T_0) + \frac{1}{A} \int_{T_0}^T I(T(t)) dt \quad (3.4)$$

If T_0 is well above the Curie temperature, the integration constant $P(T_0)$ disappears and even the absolute value of the electric polarization is completely identified.

In reality, a poly-domain state emerges in general in a crystal at the transition into its ferroelectric phase. Therefore, a single-domain state has to be enforced by applying a sufficiently large electric poling field. The best results can be achieved by applying the electric field to the crystal in its paraelectric phase, succeeded by a cooling process in its ferroelectric phase because the necessary field strengths to pole the domains are minimal near the Curie temperature.

3.2.2 The magnetoelectrically induced electric polarization

The magnetic-field induced electric polarization in a linear magnetoelectric is temperature dependent as well as the spontaneous electric polarization of a ferroelectric or multiferroic. This temperature dependence is determined by that of the linear magnetoelectric effect and may be described as follows (see section 2.3.1).

$$\Delta P_i = \tilde{\alpha}_{ij}(T) H_j \Delta T \quad (3.5)$$

The tensor $\tilde{\alpha}_{ij}(T) = \partial \alpha_{ij}(T) / \partial T$ designates the derivative of the linear magnetoelectric tensor with respect to the temperature and the vector H_j stands for the applied magnetic field. In the following, the same measurement setup, which was already described in the previous section, is considered, see figure 3.1. Within the magnetoelectric phase of the sample under investigation a continuous temperature change with the rate dT/dt leads according to equation 3.5 to a magnetoelectric-current flow

$$I(T) = \frac{R_C}{R_L + R_C} A \tilde{\alpha}_{ij}(T) H_j \frac{dT}{dt} \stackrel{(R_L \ll R_C)}{=} A \tilde{\alpha}_{ij}(T) H_j \frac{dT}{dt} \quad (3.6)$$

recorded by the amperemeter.³ Analogous to equation 3.4, the magnetoelectrically induced electric polarization and its temperature dependence can be calculated by integration of the magnetoelectric current from equation 3.6. To achieve a single-domain magnetoelectric phase an electric and magnetic field with suitable mutual orientations have to be applied simultaneously to the crystal above its ordering temperature, see section 2.3.1. Afterwards, the crystal is cooled down in the presence of these applied fields.

The determination of the magnetic-field dependence of the electric polarization of linear magnetoelectric materials is based on the same measuring principle as the above-described temperature-dependent determination. A change of the magnetic field at a fixed temperature T_0 causes a change of the electric polarization because of the linear magnetoelectric effect:

$$\Delta P_i = \alpha_{ij}(T_0) \Delta H_j \quad (3.7)$$

At this point the same experimental setup, as already discussed for the temperature-dependent magnetoelectric investigations is considered. The sample under investigation shall be in its linear magnetoelectric phase with only one single domain. A continuous change of the magnetic field with a constant rate dH/dt at a constant temperature induces a continuous change of the magnetic-field induced electric polarization and therefore a continuous current flow

$$I(H) = \frac{R_C}{R_L + R_C} A \alpha_{ij}(T_0) \frac{dH_j}{dt} \quad (R_L \ll R_C) \quad A \alpha_{ij}(T_0) \frac{dH_j}{dt}. \quad (3.8)$$

Analogous to equation 3.4 the electric polarization and its magnetic-field dependence is obtained by integration of the magnetoelectric current in equation 3.8. Choosing the lower integration limit of the magnetic field to be zero the integration constant disappears because in zero field the electric polarization vanishes. To achieve a single-domain state, the crystal has to be poled again by applying suitable poling fields.

3.2.3 The relative dielectric constant

The capacitance of a plane-parallel crystal sample of the thickness d with metallized surfaces of the size A may be described by the following capacitor formula if boundary effects, which arise due to the finite size of the surfaces, are neglected.

$$C = \epsilon_0 \epsilon_r \frac{A}{d} \quad (3.9)$$

³Here, as in the previous section the simplifying assumption is made that at the transition into the magnetoelectric phase only one single domain is generated.

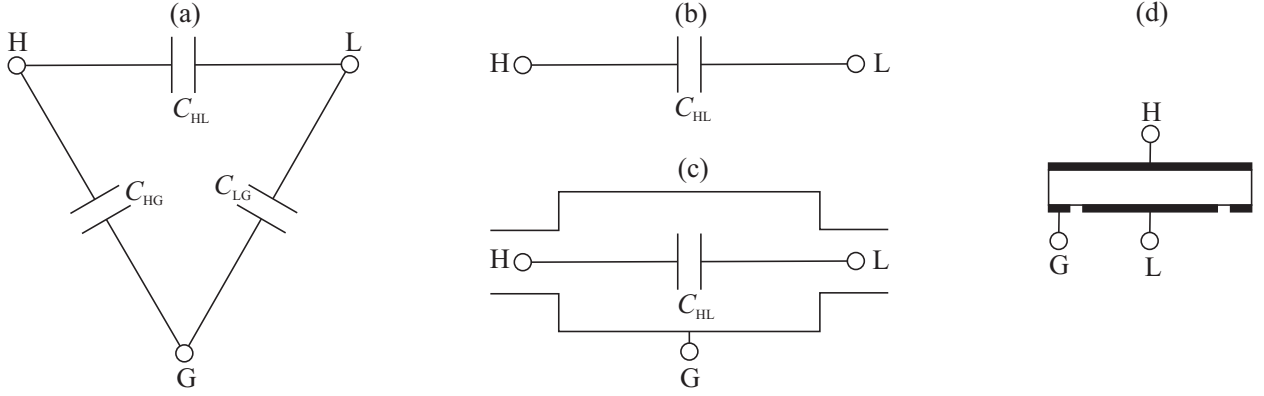


Figure 3.2: (a) Simple three-terminal capacitor model. C_{HL} denotes the direct capacity of the unknown capacitor, C_{HG} and C_{LG} designate the capacities between the capacitor plates (including the capacitor wiring) and the surrounding, such as the sample holder or other grounded objects. (b) Common two-terminal capacitor. (c) Ideal three-terminal capacitor. (d) Electrode configuration on a sample with grounded guarding electrode.

The quantity ϵ_r stands for the longitudinal effect of the relative dielectric tensor $[\epsilon_{ij}^r]$ parallel to the surface normal of the sample. Based on equation 3.9 the dielectric constant ϵ_r can be determined by measuring the capacitance by a capacitance bridge. Apart from its temperature dependence, the dielectric constant is of course also frequency dependent. In the present work, however, only quasi-static dielectric constants and their temperature and magnetic-field dependences were investigated at a fixed frequency of 1 kHz.

If the capacitor plates in a real experiment are simply connected with the high and low terminals of the capacitance bridge (two-terminal setup), the measured capacitance will be a superposition of the direct capacity C_{HL} of the unknown capacitor and of stray capacitances C_{HG} and C_{LG} to surrounding grounded objects, see figures 3.2 (a) and (b). In order to eliminate the influence of these undesired stray capacitances, the unknown capacitor including its wiring can be completely surrounded by a grounded shielding (three-terminal setup), see figure 3.2 (c) [164]. A further improvement of the setup can be achieved by a so-called guarding electrode, a ring-like electrode, which is mounted around one of the capacitor electrode areas and connected to ground, see figure 3.2 (d). This configuration leads to a homogeneous electric field between the proper electrodes of the capacitor and in addition stops eventually occurring surface currents. For very precise absolute measurements of dielectric constants, the so-called substitution method can be used [165–167]. It is based on a three-terminal setup and leads to a complete elimination of the geometric properties of the unknown capacitor, such as electrode areas and capacitor-plate distance. Detailed information about high-accuracy dielectric investigations can be found in [168].

In the present work, the main purpose of measuring the dielectric constant was to detect phase transitions and to complement the informations already revealed during the pyroelectric- and

magnetoelectric-current measurements. For the dielectric investigations, a slightly improved two-terminal setup was used. Instead of unshielded cables, two coaxial cables served as connection between the sample electrodes and the capacitance bridge. However, the samples under investigation as well as the first 2-3 cm of the contacting wires were not shielded.

3.2.4 Sample preparation

Most of the samples utilized in this work were oriented using well-developed morphological crystal faces, which served as reference planes in this case. In addition, polarized-light microscopy as well as X-ray diffraction in a Bragg arrangement were applied for the crystal orientation. All the preparations were done by Prof. Dr. L. Bohatý and Prof. Dr. P. Becker. For the dielectric investigations, plane-parallel discs with a thickness range of $\sim 0.8 - 1.5$ mm and surface areas of $\sim 10 - 40$ mm² were used.

The surfaces of the samples had to be coated by an electrically conducting layer without short circuiting them for the dielectric investigations. Already S. Jodlauk mentioned the importance of well-matched electrode areas to prevent the emergence of parasitic currents [14]. In the present work, a detailed analysis of such parasitic effects due to mismatched electrodes was performed in the context of the dielectric investigations of LiFeSi₂O₆, see section 4.3.4. The results of this analysis revealed that poorly matched electrode areas indeed can lead to significant parasitic contributions to pyroelectric and magnetoelectric currents. Therefore, a lot of care was taken to achieve congruently metallized sample surfaces. Different methods of metallization have been utilized. The simplest method is to apply conducting silver paint onto the surfaces of a sample (here conducting silver G3003A from Plano GmbH was used). However, this has an essential disadvantage: Only crystals, that are resistant against organic solvents, can be metallized by this method because the silver particles are suspended in a mixture of different organic solvents (here: propylenglycol-ether, ethanol, acetone, ethylacetate). Therefore, the surfaces of delicate samples were coated with a thin layer of gold or silver using a resistive evaporation system (MED 010, Balzers) or a sputtering system (Hummer, Anatech Ltd). Most of the samples were metallized using the resistive evaporation system because it offered faster evaporation rates than the sputtering system. Because the original sample holder of the resistive evaporation system had a very small heat capacity, it was removed by a massive copper sample holder, fabricated in the mechanical workshop of the Institut für Geologie und Mineralogie. This limited the heating of the samples during the metallization process, which proved to be important especially for delicate samples.

The rims of the samples had to be thoroughly covered before the metallization process to prevent their coating with silver or gold and thus the occurrence of a short circuit. At the beginning of this work, experiments with different types of screens to cover the rims were conducted, but

finally the use of vacuum grease (Baysilone paste from Bayer) proved to be the best applicable method for that purpose. With the grease as cover it was possible to metallize the sample surfaces completely, independent of their geometry, which led automatically to nearly perfectly-matched electrode areas. After the metallization process the grease could be removed very easily from the rims.

For the analysis of the dielectric measurements, the size of the metallized surfaces had to be determined as well as the thickness of the samples. For the determination of the size of the metallized area, a calibrated stereo microscope (Zeiss Stemi SV 11) with a microscope camera (Axio Cam ICc3) in connection with the software AxioVision 40AC was used. Photos, recorded by the camera could be loaded into the software and the margins of the metallized areas could be marked. From this information and the chosen magnification of the microscope the size of the metallized area is calculated by the software. The thickness of the samples was measured with a micrometer gauge.

3.2.5 Measuring apparatus: high-temperature measurements

As already mentioned in section 3.1, the dielectric investigations in the temperature regime 1.8-300 K were performed in a VTI (KONTI cryostat insertion, CryoVac). For these measurements, the same stick-like measurement insert, which was already used by S. Jodlauk during his PhD thesis [14], was employed, see figure 3.3 (a). It had been originally engineered by K. Berggold and was then modified and optimized by S. Jodlauk for dielectric measurements. The main part of the insert consists of a stainless steel tube, in which two miniature coaxial cables (type SS, LakeShore) and twelve 100 μm thin enamelled copper wires are fed through. At the one end, the stainless steel tube is terminated by a head with three vacuum flanges containing a 14-pin socket and two coaxial sockets for the connection with the different measurement devices. At its other end, three stainless steel capillary tubes are attached, equipped with radiation shields and terminated by a copper plate serving as thermal bath. Insulated pins are glued into the copper plate, which is connected with a copper sample platform.⁴ On the sample platform a Cernox thermometer (CX-1050-SD, LakeShore) is mounted. The surrounding space of the sample platform can be encased by a Teflon cup. An airlock is used for the installation of the measurement insert into the VTI to prevent air intrusion into its interior space. The sample under investigation can be positioned in the centre of the magnetic field with a spacer. The field direction points along the stick axis of the measurement insert. More detailed information about the measurement insert can be found in [14].

In the present work, a new sample holder was engineered for the above-described measurement insert. The main part consists of a gilded, rectangular copper disc ($15 \times 10 \times 3$ mm), supplied

⁴The copper plate is denoted in the following as pin disc.

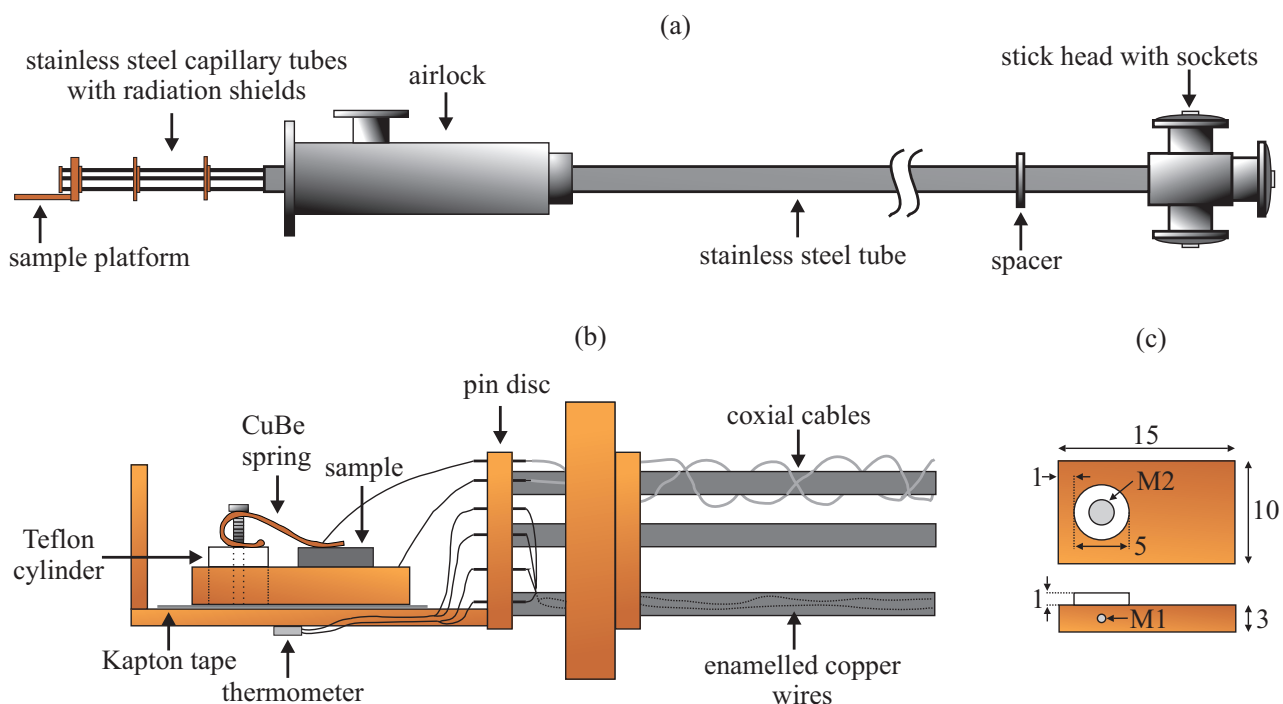


Figure 3.3: (a) Schematic picture of the measurement insert used for the dielectric investigations. (b) Enlarged picture of the sample platform of the measurement insert, including the used sample holder. (c) Dimensions in mm of the rectangular copper disc and the Teflon cylinder of the sample holder.

with a hole, see figure 3.3 (c). A Teflon cylinder with a screw thread (M2) is fitted into this hole and is fixed with a headless screw (M1). A gilded CuBe spring can be mounted on the Teflon cylinder via a stainless steel screw, as shown in the enlarged schematic picture of the lower part of the measurement insert including the new sample holder, see figure 3.3 (b). The samples are clamped between the spring and the rectangular copper disc and the sample holder is attached to the sample platform by using, e.g., instant adhesive. In order to achieve an electric insulation between the sample holder and the platform, kapton tape is used as intermediate layer between both, see figure 3.3 (b). Using drops of conducting silver paint, the CuBe spring as well as the rectangular copper disc of the sample holder are contacted with a $100\ \mu\text{m}$ thin enamelled copper wire. Both wires are then connected via two pins of the pin disc with the coaxial cables.

The kind of sample mounting in the new sample holder has some important advantages, compared to the method described by S. Jodlauk [14]. First of all, the clamping method is simpler and faster. Secondly, the copper wires need not to be attached directly on the sample surfaces, which proved to be important especially for delicate crystals, that are corroded by the solvents contained in the conducting silver paint. Thirdly, the clamped samples are free to expand in any direction, which can be important for crystals, that are sensitive to crack formation. Finally, the samples can be oriented very precisely by using the new sample holder, which is important when magnetic fields

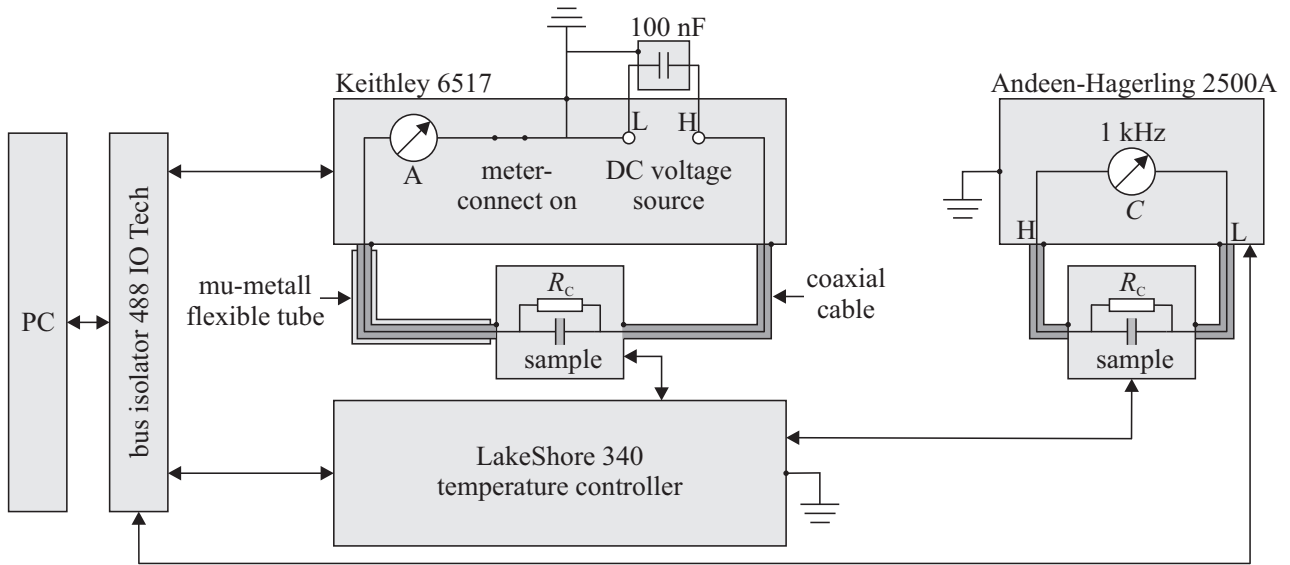


Figure 3.4: Schematic circuit diagram with the different measurement devices used for the dielectric investigations.

are applied.

In figure 3.4, a schematic circuit diagram is displayed with the different measurement devices used for the dielectric investigations. As already mentioned in section 3.1, the temperature within the VTI is controlled by a temperature controller (LS 340, LakeShore). Using both channels of the temperature controller, the platform thermometer and the VTI thermometer can be read out simultaneously. For the pyroelectric- and magnetoelectric-current measurements, a Keithley 6517 electrometer with integrated voltage source was used. The low terminal of the voltage source can be internally connected with the low terminal of the amperemeter unit of the electrometer. In order to stabilize the output of the voltage source it was shunted by a 100 nF capacitor. The two electrode areas of the sample under investigation were short circuited via the high terminal of the voltage source and the high terminal of the amperemeter unit by two RG58C/U coaxial cables. The coaxial cable to the high terminal of the amperemeter unit was additionally shielded by a flexible tube of mu metal. An extra noise shielding was achieved by the connection of the low terminals of the voltage source and of the amperemeter unit to ground, leading to a guarded configuration [169]. In addition, the guarding minimizes the occurrence of leakage currents in the measurement circuit. Furthermore, it is important to reduce mechanical vibrations to obtain a good signal to noise ratio. Therefore, the electrometer was positioned on a gel cushion and the coaxial cables to the measurement insert of the VTI were installed vibration free as well. For the capacitance measurements, a capacitance bridge (AH 2500A, Andeen-Hagerling, 1 kHz) was used, see right side of figure 3.4. All measurement devices were connected via an IEEE-488 bus and an intermediate bus isolator (Isolator488, IO Tech) to a computer.

The measurement is controlled by a software, called kSR-Sweeper, which is written in LabVIEW. The software has been developed by C. Zobel in the II. Physikalisches Institut and was then advanced by K. Berggold and G. Kolland [146, 170]. One of the main functions of the kSR-Sweeper is to set the external parameters during the measurement process, such as magnetic field, temperature, poling voltage. With another function of the software the control temperature can be swept with a constant rate at a fixed magnetic field or the magnetic-field strength at a stabilized temperature, while recording continuously data points (time, magnetic-field strength, control temperature, sample temperature, current/capacity). Typically, about one data point per second is recorded and saved in a text file. For the pyroelectric-current measurements, a precise temperature control is essential to achieve smooth temperature ramps, which are important for the proceeding calculation of the electric polarization by integration, see section 3.2.8. The typical process for the pyroelectric-current measurements is as follows. At first, a magnetic field of desired field strength is set and a static electric poling field of at least $\pm 200 \text{ Vmm}^{-1}$ is applied to the sample under investigation well above the ordering temperature.⁵ Due to the electric capacity of the sample an exponentially decreasing charging current occurs. After the decay of this current flow, the crystal is cooled with constant cooling rates between $0.5 - 4 \text{ Kmin}^{-1}$ to base temperature ensuring a single-domain state. After the removal of the poling field and the decay of the corresponding discharging current, the sample is heated again with constant heating rates between $0.5 - 4 \text{ Kmin}^{-1}$ to the paraelectric phase. Both, during the heating and cooling cycle the pyroelectric currents are recorded. For the magnetoelectric-current measurements, the same field-cooled poling process of the crystals is performed and the magnetoelectric currents are registered, while sweeping the magnetic field with rates between $0.1 - 0.5 \text{ Tmin}^{-1}$ at stabilized temperatures. The electric capacity was measured either with temperature-sweep rates of 0.5 Kmin^{-1} or with magnetic-field sweep rates of 0.1 Tmin^{-1} .

3.2.6 Measuring apparatus: low-temperature measurements

In the present work, the temperature range for dielectric investigations was extended down to 300 mK by engineering an adequate sample holder for the ^3He insert, already mentioned in section 3.1. The usual temperature control of the Heliox system proved to be inappropriate for pyroelectric-current measurements, since it does not allow to sweep the temperature satisfactorily smoothly and linearly. Therefore, a second temperature control loop to control the sample temperature independently from that of the Heliox system had to be integrated. In figure 3.5, a schematic picture of the sample holder is displayed. Its design is essentially the same as that of the already established sample holder for transport measurements in the Heliox system, which was

⁵Due to the helium atmosphere within the VTI, the maximal applicable voltage without the occurrence of flashovers is about 250 V.

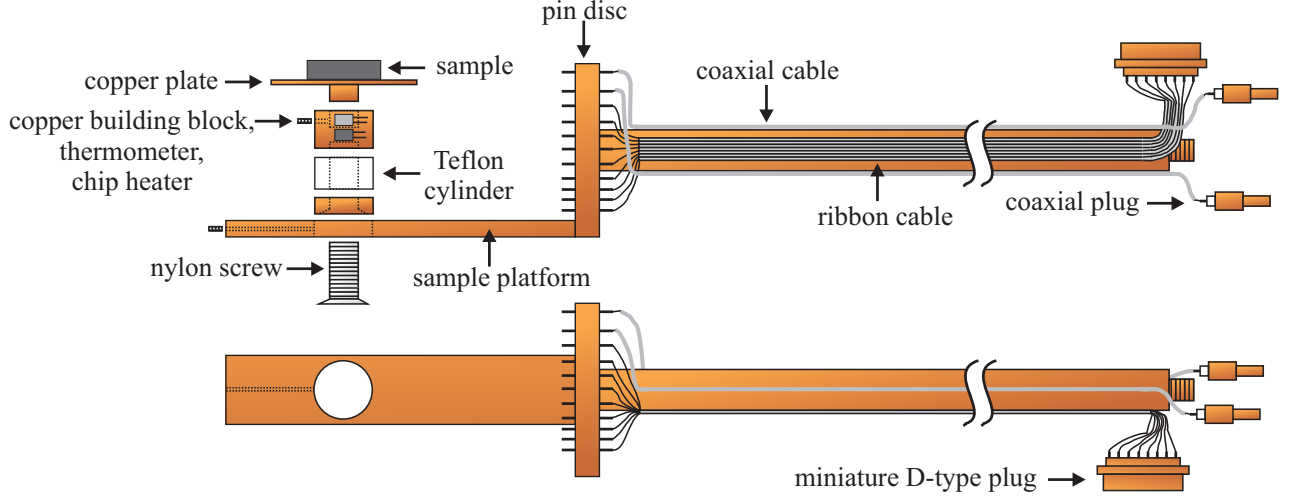


Figure 3.5: Schematic picture of the sample holder used for the dielectric investigations in the Heliox system.

constructed by G. Kolland and O. Breunig. Only two additional pins in the so-called pin disc are added for the coaxial cables, which are necessary for the dielectric investigations. The actual alteration is the implementation of a second sample platform, which is thermally decoupled from the original one and on which the samples under investigation are mounted. This new sample platform consists of a gilded copper plate, which is fitted into a gilded copper building block and fixed by a headless screw, see figure 3.5. On the side of the copper building block a Cernox thermometer (CX-1030-SD, serial number: X75096, LakeShore) and two shunted SMD-chip heaters (SMD 102, 1 k Ω , 0.25 W) are mounted. The copper building block is screwed together with two cylinders, one made of Teflon and one made of copper, respectively, using a nylon screw. Finally, the copper cylinder is fitted into the hole of the original sample platform and fixed by a headless screw.

The Teflon cylinder thermally decouples the new sample platform from the original one. The original sample platform serves as a heat sink for the new one and is usually kept at the base temperature of the ^3He pot of the Heliox system. Both, the base temperature and the sample temperature are controlled independently. The base temperature control of the Heliox system is provided by a temperature controller (ITC-501, OXFORD Instruments). The sample temperature, which is read out by an AC resistance bridge (LS 370, LakeShore), is controlled by a virtual LabVIEW PID controller driving the SMD-chip heaters on the copper building block via a current source (Knick DC-Calibrator J152 or Keithley precision current source 6220). The optimum PID settings for the virtual PID controller turned out to be $K_p = 3$, $T_i = 0.15$ min and $T_d = 0.005$ min at a maximum output current of 3 mA. Because of the thermal decoupling, the lowest achievable sample temperature is $\simeq 300$ mK. The sample temperature can be swept very smoothly and linearly with

rates up to 4 K/min while the base temperature is stabilized (for example at 0.25 K). The power of the chip heaters suffices to achieve sample temperatures well above the base temperature. Differences in temperature of about 30 K are possible, without the occurrence of strong drifts of the base temperature.

The samples under investigation can be attached by a drop of conducting silver paint on the sample platform and are contacted in the same way with two 100 μm thin manganin wires. For the dielectric investigations in the Heliox system, the same measurement devices are used as for the investigations in the VTI, see figure 3.4, and also the measurement process is the same, see section 3.2.5.

3.2.7 Data analysis: background currents and noise

The electric polarization of multiferroic or linear magnetoelectric compounds is typically very small. Therefore, pyroelectric or magnetoelectric-current measurements in these classes of materials are typically in the range of 0.1-100 pA.⁶ In this low-current regime, the accuracy of current measurements can be strongly influenced and degraded by leakage and offset currents. Leakage currents are generated by stray-resistance paths within the measurement circuit in connection with a voltage source. They can be reduced by guarding the high-impedance lead of the measurement circuit [171], as was explained in the context of figure 3.4. In addition, there exists a multitude of different offset currents. First of all, there is always a constant input offset of the used electrometer (here: $\simeq 0.03$ pA), which is, however, less important because it is nearly time independent and rather small. Secondly, the used coaxial cables can be a source for offset currents as well due to the so-called triboelectric effect [171]. Vibrations or the motion of the coaxial cables can lead to frictions between conductor and insulator and therefore to the creation of charge imbalances, which are then compensated by a current flow. This explains the importance of the reduction of vibrations of the whole measurement apparatus. Especially at the beginning of a measurement directly after the motion of the coaxial cables, relatively large offset currents emerge due to the triboelectric effect. Thirdly, a finite electric conductivity of the sample under investigation in connection with small input offset voltages of the voltage source of the electrometer as well as thermo or contact voltages in the measurement circuit can be a further source of offset currents.⁷ Finally, charge carriers can be trapped within the samples during the cooling cycles of the pyroelectric-current measurements with applied electric poling fields due to the decrease of thermal energy with decreasing temperature. These trapped charge carriers then are released again during the

⁶The noise level during the pyroelectric-current measurements amounted in this current range to about 0.01 pA in the present work.

⁷The electric conductivity can either be intrinsic or extrinsic. Extrinsic contributions to the conductivity of a sample can, e.g., be caused by contaminated sample edges in the case of hygroscopic compounds.

heating cycles with increasing temperature and cause additional offset currents. Such currents can be distinguished from real pyroelectric currents because they occur only during the heating cycles. In contrast, real pyroelectric currents arise both during the heating and cooling cycles, whenever the electric polarization changes. More information about some of the offset currents mentioned above can be found in [14], where also some measurements to exemplify their characteristics are presented.

3.2.8 Data analysis: background-current correction and integration

In order to analyse pyroelectric- and magnetoelectric-current measurements it is essential to separate the background currents from the real pyroelectric or magnetoelectric currents. This is, however, often difficult because the temperature or magnetic-field dependence of the background currents usually cannot be determined independently from the pyroelectric or magnetoelectric signals. A further problem arises due to the fact that the background signals often drift with time and are thus not reproducible. Therefore, the exact temperature or magnetic-field dependence of the background currents is unknown in general. Nevertheless, in most of the cases an adequate correction can be achieved by one of the following methods.

- (1) Constant offset currents:** In the non-pyroelectric, paraelectric phase of a multiferroic/magnetoelectric material a temperature change should in general not lead to a current flow. Detected current signals in the paraelectric phase can therefore be attributed to the present offset currents. If these are assumed to be temperature independent, the real pyroelectric current is obtained by subtraction of the constant current signal detected in the paraelectric phase.

$$I^{\text{real}}(T) = I^{\text{meas}}(T) - I_{\text{const}}^{\text{offs}} \quad (3.10)$$

For pyroelectric/magnetoelectric signals, which are large with respect to the background currents, this method leads to an adequate correction even in the case of temperature-dependent offset currents.

- (2) Completely invertible electric polarization:** If the electric polarization of a magnetoelectric or multiferroic material is completely invertible and if the present background currents do not drift strongly with time, another correction method can be applied. In general, the background signals are independent from the poling direction of the electric polarization. Therefore, they can be eliminated by subtracting the detected current signals of opposite poling directions. The division by a factor of two finally leads to the average real pyroelectric-

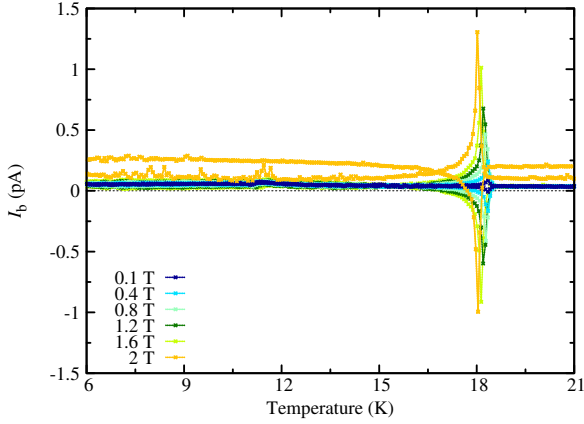


Figure 3.6: Temperature dependences of pyroelectric-current signals of $\text{LiFeSi}_2\text{O}_6$ along the b axis for magnetic fields applied along c . A constant heating rate of about 4 K/min was chosen and the electrode surface areas amounted to about 10 mm^2 . More information about the results of the dielectric investigations of $\text{LiFeSi}_2\text{O}_6$ can be found in chapter 4.

current signal.

$$I^{\text{real}}(T) = \frac{1}{2} (I_{E^+}^{\text{meas}}(T) - I_{E^-}^{\text{meas}}(T)) \quad (3.11)$$

(3) Magnetic-field induced electric polarization: For linear magnetoelectric materials, no pyroelectric-current signal occurs in zero magnetic field. In this case, the background currents and their temperature dependence can be determined. If the background currents do not drift strongly with time and if they are independent from the magnetic field, the real magnetic-field induced pyroelectric-current signal is obtained by subtraction of the zero-field background currents.

$$I_{B \neq 0}^{\text{real}}(T) = I_{B \neq 0}^{\text{meas}}(T) - I_{B=0}^{\text{offs}} \quad (3.12)$$

The above described correction methods were implemented in the course of the present work in an analysis software written in LabVIEW. The different data files can be loaded into the software and the best correction method is chosen and applied. After the adequate correction of the pyroelectric/magnetoelectric-current data the corresponding electric polarizations and their temperature or magnetic-field dependences can be calculated by numerical integration, based on the expression in equation 3.4. For that purpose, a second analysis software was written in LabVIEW. Using the so-called trapezoidal rule

$$\int_a^b f(x) dx \approx \frac{f(a) + f(b)}{2} (b - a) \quad (3.13)$$

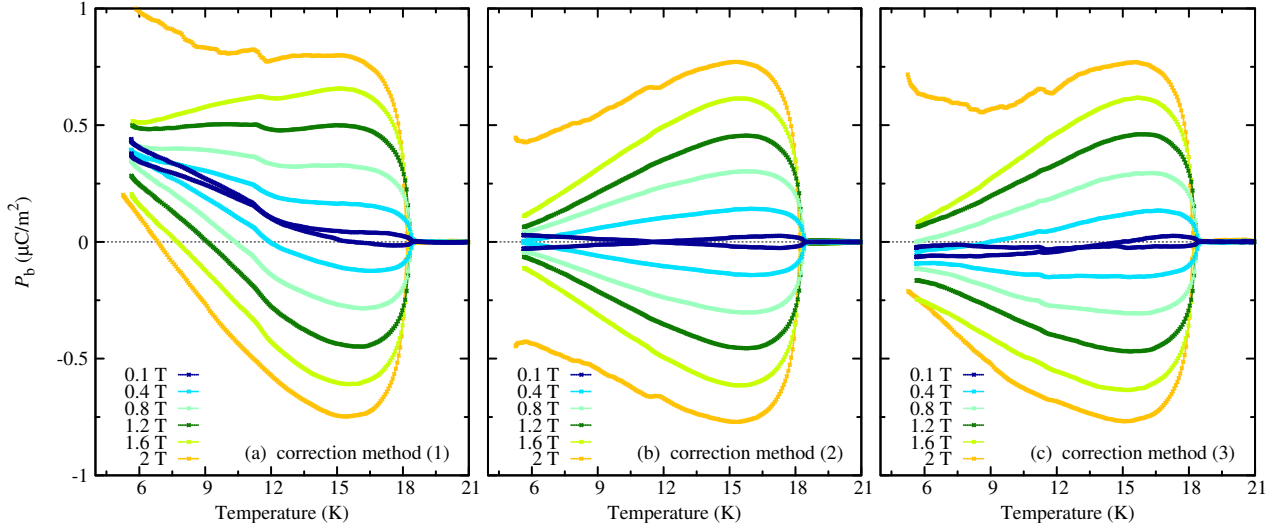


Figure 3.7: Temperature dependences of the electric polarization of $\text{LiFeSi}_2\text{O}_6$ along b for magnetic fields applied along c . Different correction methods were applied before the integration process. (a) Subtraction of a constant background current from the pyroelectric-current data. (b) Subtraction of the pyroelectric-current signals of opposite poling directions divided by a factor of two. (c) Subtraction of the current signals in zero magnetic field from the pyroelectric-current data in magnetic fields.

for the numerical integration, the following algorithm was implemented in the integration software.

$$P\left(\frac{t_{i+2} - t_{i+1}}{2}\right) = P\left(\frac{t_{i+1} - t_i}{2}\right) + \frac{1}{A} \frac{I(t_{i+2}) + I(t_{i+1})}{2} (t_{i+2} - t_{i+1}) \quad (3.14)$$

Here, t_i denotes the i -th time entry in the input data file, which is used for the integration, and $I(t_i)$ the corresponding current entry. The variable A denotes the surface area of the sample electrodes. The average time $\frac{t_{i+2} - t_{i+1}}{2}$ is assigned to the calculated polarization value P . Each time entry t_i can be related to a corresponding sample temperature T_i . Therefore, after the integration process, which leads to a time versus polarization array $\left\{\frac{t_{i+2} - t_{i+1}}{2}, P\left(\frac{t_{i+2} - t_{i+1}}{2}\right)\right\}$, the temperature dependence of the electric polarization is easily obtained by calculating $\frac{T_{i+2} - T_{i+1}}{2}$ for each polarization value $P\left(\frac{t_{i+2} - t_{i+1}}{2}\right)$. The resulting temperature-time-polarization array $\left\{\frac{T_{i+2} - T_{i+1}}{2}, \frac{t_{i+2} - t_{i+1}}{2}, P\left(\frac{t_{i+2} - t_{i+1}}{2}\right)\right\}$ is finally saved by the software in a result file.

To conclude this section, the problems of an adequate data correction, especially for very small pyroelectric/magnetoelectric-current signals will be further discussed using the example of the linear magnetoelectric compound $\text{LiFeSi}_2\text{O}_6$, one of the investigated materials in the present work. As example, the temperature dependences of the pyroelectric-current signals detected along the b axis for magnetic fields applied along c with field strengths up to 2 T were chosen, see figure 3.6. The non-zero current signals above the ordering temperature $\simeq 18$ K can be attributed to the background currents. As can be seen in figure 3.6, they seem to be temperature indepen-

dent at least within the paraelectric phase of $\text{LiFeSi}_2\text{O}_6$. The current signals at 2 T are, however, shifted with respect to the other ones, which indicates a drift of the background currents with time. All three correction methods, described above, are applied to the measured raw data $I(T)$ and the corresponding polarization $P(T)$ is calculated by integration. In figure 3.7, the resulting temperature-dependent electric polarizations are summarized. The subtraction of a constant background current from the pyroelectric-current data causes a strong asymmetry between the different poling directions of the resulting electric polarization data, see figure 3.7(a). Therefore, the assumption of a constant background current is apparently not justified in this case. The subtraction of the pyroelectric-current signals of opposite poling directions yields a better result, as can be seen in figure 3.7(b). The obtained polarization P is fully antisymmetric with respect to the poling field by construction. Thus, this antisymmetry cannot be used as a criterion to test the data quality. In the present case, the $P(T)$ data at the lowest field ($B = 0.1$ T) seem to change sign, which appears rather unphysical. The third correction method with a subtraction of the current signals in zero magnetic field from the pyroelectric-current data in magnetic fields also leads to an acceptable result, see figure 3.7(c). However, here as well a slight asymmetry between the temperature dependences of the electric polarization of opposite poling directions is visible, indicating a not sufficiently adequate correction of the background currents. In conclusion, one can state that an adequate correction of the pyroelectric/magnetoelectric-current signals is crucial to obtain acceptable and reliable results of the electric polarization.

Chapter 4

The pyroxenes $A\text{Fe}X_2\text{O}_6$ ($A = \text{Na, Li}$; $X = \text{Si, Ge}$)

4.1 Introduction

The family of pyroxenes with the general formula $AMX_2\text{O}_6$ (A = mono- or divalent metal, M = di- or trivalent metal and X = tri- or tetravalent cation) is a very important group of minerals. More than 20 vol% of the earth's crust and upper mantle down to about 400 km consists of pyroxene minerals. For that reason, they were intensively studied in geoscience for decades, e.g., [199–203]. A large variety of different compositions exists in the pyroxene family. The A site can, for example, be occupied by Li^+ , Na^+ , Ca^{2+} , Mg^{2+} , Mn^{2+} or Fe^{2+} and the M site by numerous transition-metal elements such as Ti^{3+} , V^{3+} , $\text{Cr}^{3+}/\text{Cr}^{2+}$, $\text{Mn}^{2+}/\text{Mn}^{3+}$, $\text{Fe}^{2+}/\text{Fe}^{3+}$, Co^{2+} or Ni^{2+} . This variety is further enlarged by different possible X -site elements, such as Si^{4+} or Ge^{4+} . Depending on the composition, the pyroxenes crystallize in orthorhombic or monoclinic symmetries. The members of the subgroup of monoclinic pyroxenes are called clinopyroxenes. The typical clinopyroxene crystal structure is displayed in figure 4.1 (a) using the example of $\text{NaFeSi}_2\text{O}_6$. It consists of one-dimensional zigzag chains of edge-sharing $[\text{MO}_6]$ octahedra, which are connected by chains of $[\text{XO}_4]$ tetrahedra within the (110) and $(\bar{1}10)$ planes. Both chain systems are running along the c axis. For the case of magnetic M^{2+}/M^{3+} cations, there are three relevant magnetic exchange interactions J_1 , J_2 and J_3 , see figure 4.1 (b) [14, 15]. On the one hand, J_1 connects neighbouring M^{2+}/M^{3+} sites within the zigzag chains via $M\text{--O--}M$ super-exchange pathways. On the other hand, the super-exchange interactions J_2 and J_3 connect M^{2+}/M^{3+} sites of different chains via one or two $[\text{XO}_4]$ tetrahedra, respectively. In this context, the M^{2+}/M^{3+} elements form triangular lattices within the (110) and $(\bar{1}10)$ planes, which can give rise to a magnetic frustration potential if one exchange is antiferromagnetic and the others are both either ferromagnetic

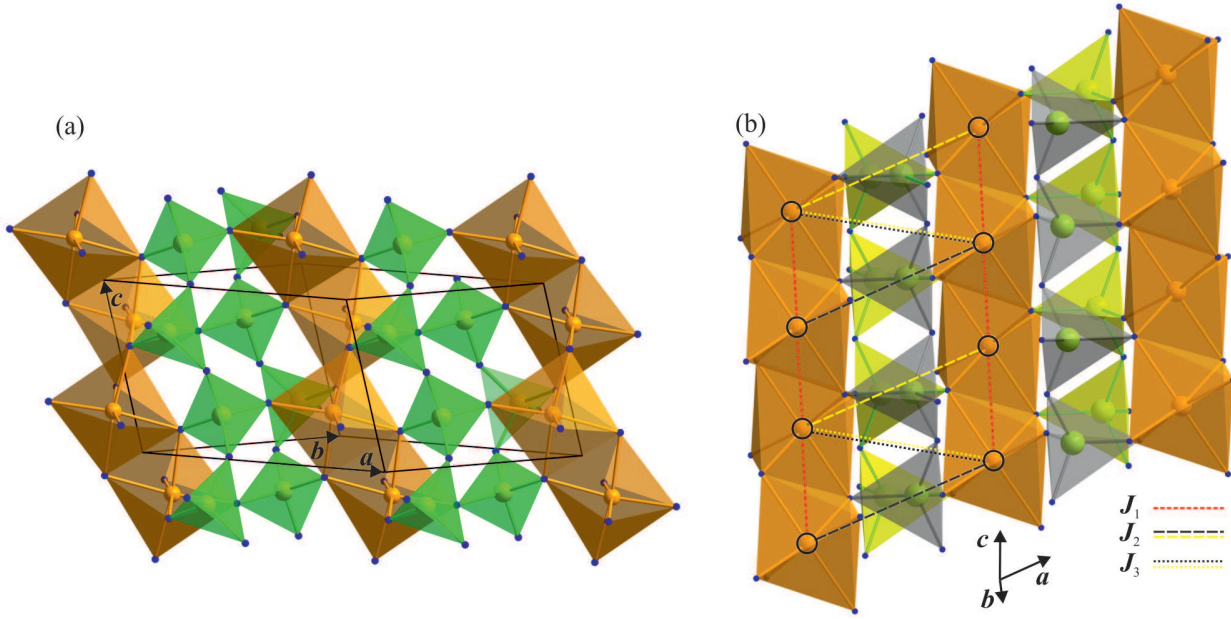


Figure 4.1: (a) General room-temperature crystal structure of the clinopyroxenes using the example of $\text{NaFeSi}_2\text{O}_6$. (b) Magnetic interaction pathways for the case of magnetic M^{2+}/M^{3+} ions. J_1 runs along the *c* axis and connects M^{2+}/M^{3+} sites within the zigzag chains. J_2 and J_3 connect M^{2+}/M^{3+} sites of different chains via one or two $[XO_4]$ tetrahedra, respectively. Hence, J_1 , J_2 and J_3 form a triangular magnetic subsystem. The yellow pathways run along the yellow tetrahedra in the back, while the black ones run along the grey tetrahedra in the front.

or antiferromagnetic, see figure 4.1 (b). Up to date only two pyroxene compounds are known (aegirine of the composition $\text{Na}_{1.04}\text{Fe}_{0.83}\text{Ca}_{0.04}\text{Mn}_{0.02}\text{Al}_{0.01}\text{Ti}_{0.08}\text{Si}_2\text{O}_6$ and $\text{NaFeGe}_2\text{O}_6$), which show a spiral magnetic ordering [204–207]. In general, most of the pyroxenes show collinear antiferromagnetic orders [17, 204, 208, 209], but there are also exceptions, such as $\text{NaCrGe}_2\text{O}_6$, which shows a ferromagnetic order [210]. In table 4.1, the room-temperature space groups, lattice parameters and magnetic ordering temperatures of some members of the clinopyroxene family are summarized. An extensive compilation of magnetic and structural data on clinopyroxenes can be found in [211].

A few years ago, the pyroxene compound $\text{NaFeSi}_2\text{O}_6$ was identified as multiferroic material [14, 15]. In the same publication, $\text{LiFeSi}_2\text{O}_6$ and $\text{LiCrSi}_2\text{O}_6$ were proved to be linear magnetoelectrics. This was the starting point for intense and systematic investigations of the magnetic and dielectric properties of plenty of compounds of the pyroxene family to clarify the mechanisms of multiferroicity and linear magnetoelectricity in this class of materials [17, 18, 204, 206, 208–210]. As will be seen in the following discussion, it is important to note that all the primary investigations of $\text{NaFeSi}_2\text{O}_6$ reported in [14, 15] were performed on a natural single crystal from Mount Malosa (Malawi) with the composition $\text{Na}_{1.04}\text{Fe}_{0.83}\text{Ca}_{0.04}\text{Mn}_{0.02}\text{Al}_{0.01}\text{Ti}_{0.08}\text{Si}_2\text{O}_6$. The mineral

crystal	space group	$a / b / c$ (Å)	β (°)	T_N (K)	references
$\text{NaFeSi}_2\text{O}_6$	$C2/c$	9.658 / 8.795 / 5.294	107.42	8	[14, 15, 212]
$\text{NaFeGe}_2\text{O}_6$	$C2/c$	10.01 / 8.94 / 5.25	108	13	[207]
$\text{LiFeSi}_2\text{O}_6$	$C2/c \xrightarrow{(230 \text{ K})} P2_1/c$	9.675 / 8.668 / 5.297	110.22	18.5	[14, 15, 212, 213]
$\text{LiFeGe}_2\text{O}_6$	$C2/c \xleftarrow{(789 \text{ K})} P2_1/c$	9.893 / 8.836 / 5.379	108.83	20	[214–216]

Table 4.1: Room-temperature lattice constants, space groups and Néel temperatures of $\text{NaFeSi}_2\text{O}_6$, $\text{NaFeGe}_2\text{O}_6$, $\text{LiFeSi}_2\text{O}_6$ and $\text{LiFeGe}_2\text{O}_6$.

name aegirine is used for the natural compound of this composition in the rest of the present work to distinguish it from the synthetic one. Magnetic-susceptibility measurements on this natural compound revealed the onset of an antiferromagnetic order at 8 K, followed by a second magnetic transition at 6 K. Dielectric investigations gave evidence for the occurrence of a spontaneous electric polarization along the monoclinic b axis ($P_b \simeq 13 \mu\text{C}/\text{m}^2$) below this second transition. Magnetic fields applied within the ac plane suppress the electric polarization along b completely around 4 T. Instead, a smaller electric polarization along c is induced [14, 15]. Based on a series of single-crystal and powder neutron-diffraction measurements, the magnetic structure of aegirine could be resolved [204].¹ Below the first transition at 8 K the magnetic structure forms an incommensurate transverse spin-density wave with the moments lying within the ac plane. At the second transition at 6 K the magnetic structure transforms into an elliptical helix with the incommensurate propagation vector $\mathbf{k} = (0, 0.77, 0)$ and the spin rotation axis being oriented along b [204]. As shown in [204], the onset of ferroelectricity in aegirine below 6 K can be understood by a symmetry analysis of the helical spin structure analogous to the Curie principle. The symmetry of a helical spin arrangement can be described by the magnetic point group $22'2'$, see section 2.2.2. Therefore, the occurrence of the elliptical helix in the present case of aegirine leads to a lowering of symmetry from $C2/c1'$ to $C2'$, which explains the simultaneous onset of the spontaneous electric polarization along b .²

Several investigations on synthetic powder samples of $\text{NaFeSi}_2\text{O}_6$ gave evidence that the magnetic properties of synthetic $\text{NaFeSi}_2\text{O}_6$ are different from those of the natural compound aegirine [16, 204, 206, 217, 218]. Specific-heat and muon-spin-relaxation measurements revealed that synthetic $\text{NaFeSi}_2\text{O}_6$ seems to undergo only a single transition at about 7 K [16]. This result

¹The samples for the neutron-diffraction experiments were all cut from the same natural single crystal from Mount Malosa, Malawi, which was used for the primary measurements reported in [14, 15].

²This symmetry is obtained by intersecting the magnetic point group $22'2'$ of the helical spin structure with that, $2/m1'$ of the paramagnetic phase of aegirine.

is consistent with comparative magnetic-susceptibility measurements of polycrystalline powder samples of aegirine and synthetic $\text{NaFeSi}_2\text{O}_6$ performed in the present work, see appendix F. Neutron powder-diffraction measurements gave evidence for a second commensurate magnetic structure in addition to the incommensurate magnetic structures already observed in aegirine below 8 K [204, 206, 217]. The proposed commensurate propagation vectors are, however, contradictory. In conclusion, one may speculate that multiferroicity in aegirine could be caused by the natural dopants present in that compound. In contrast, synthetic $\text{NaFeSi}_2\text{O}_6$ could be linear magnetoelectric only. However, a definite proof of this speculation is still missing because of the difficulties in growing large synthetic single crystals of $\text{NaFeSi}_2\text{O}_6$.

Apart from aegirine, up to date only one other multiferroic compound could be identified within the pyroxene family, namely $\text{NaFeGe}_2\text{O}_6$ [12]. The vast majority of the investigations of this compound, reported in literature so far, were performed on polycrystalline powder samples [12, 206, 207, 219, 220]. Measurements of the magnetic susceptibility revealed the occurrence of low-dimensional magnetic correlations around 33 K, succeeded by the onset of a three-dimensional antiferromagnetic order below 13 K [12, 206, 207]. Previous results of magnetic-susceptibility and Mössbauer-spectroscopy measurements had indicated a slightly higher Néel temperature of about 15 K [219, 220]. Among the group of Fe^{3+} -based pyroxenes, $\text{NaFeGe}_2\text{O}_6$ exhibits the most pronounced low-dimensional magnetic characteristics [206]. Specific-heat measurements revealed a further phase transition at about 11.8 K [207]. Dielectric investigations on sintered polycrystalline pellets proved that this second transition coincides with the onset of a spontaneous polarization of about $13 \mu\text{C}/\text{m}^2$, whose absolute value can be decreased with increasing magnetic-field strength [12]. Two different neutron-diffraction experiments on powder as well as on single-crystal samples of $\text{NaFeGe}_2\text{O}_6$ are reported in literature [205–207]. The results of both studies indicate that the magnetic structure of $\text{NaFeGe}_2\text{O}_6$ forms an incommensurate cycloidal spin arrangement below the second transition at 11.8 K with the spins lying mainly within the ac plane. The reported propagation vectors $\mathbf{k} = (0.3357, 0, 0.0814)$ [205, 207] and $\mathbf{k}' = (0.323, 1.0, 0.080)$ [206], however, are contradictory within the crystallographic space group $C2/c$. The magnetic structure between 11.8 K and 13 K has not been resolved yet.

$\text{LiFeSi}_2\text{O}_6$ is the best investigated linear magnetoelectric among the pyroxenes. It undergoes a structural phase transition at about 230 K with a lowering of translational symmetry from $C2/c$ to $P2_1/c$ [213]. Several neutron-diffraction studies have been performed to resolve the magnetic structure of $\text{LiFeSi}_2\text{O}_6$ [204, 216, 221]. The results of these studies imply that $\text{LiFeSi}_2\text{O}_6$ orders antiferromagnetically below 18.5 K. The more recent studies identify $P2_1/c'$ as the most probable magnetic space group [204, 216]. The spins form a canted antiferromagnetic structure with the magnetic moments being oriented mainly along the c axis. The spins are ordered ferromagnetically within each of the zigzag chains along c , while the spins of neighbouring chains are

ordered antiferromagnetically. The reported magnetic moments $\mathbf{M} = (0.52, 0.05, 4.83)$ [216] and $\mathbf{M}' = (0.58, 0.69, 3.91)$ [204], both given in the crystallographic coordinate system of $\text{LiFeSi}_2\text{O}_6$, are contradictory. The magnetic space group $P2_1/c'$ is in accordance with the form of the linear magnetoelectric tensor of $\text{LiFeSi}_2\text{O}_6$, which was determined by detailed dielectric investigations [14, 15].³ At 14 K the absolute value of the largest tensor component of $\text{LiFeSi}_2\text{O}_6$ amounts to $\alpha_{33} = 4.86 \text{ ps/m}$, which corresponds to a magnetic-field induced electric polarization of $\simeq 18 \mu\text{C/m}^2$ in an applied magnetic field of 6 T [14]. Apart from the tensor components, which are allowed in the magnetic space group $P2_1/c'$, also some for that symmetry forbidden components were found to be non-zero. These "forbidden" magnetoelectric components were attributed to experimental imperfections, as slightly misoriented sample surfaces or small misalignments of the applied magnetic fields. Additionally, the possibility of parasitic effects due to not perfectly-matched electrode areas was discussed in this context [14].

4.2 Experimental details

All crystals of $\text{LiFeSi}_2\text{O}_6$ and $\text{NaFeGe}_2\text{O}_6$ investigated in the present work were grown by Prof. Dr. P. Becker-Bohatý from high-temperature solutions using a top-seeded solution-growth process. For growing $\text{LiFeSi}_2\text{O}_6$ crystals, a melt solution of the system $\text{Li}_2\text{MoO}_4\text{--LiVO}_3$ was used and for the growth of $\text{NaFeGe}_2\text{O}_6$ crystals, a melt-solution of the system $\text{Na}_2\text{MoO}_4\text{--NaVO}_3$. The morphological faces, which were indexed via X-ray diffraction, were used as reference planes for the sample orientation. Samples with faces perpendicular to $\mathbf{b} \times \mathbf{c}$, \mathbf{b} and \mathbf{c} were prepared.

In the course of the present work, the interpretation of some results of the study of the magnetoelectric properties of $\text{LiFeSi}_2\text{O}_6$, reported in the PhD thesis of S. Jodlauk [14] were doubted. As mentioned above, a strong linear magnetoelectric effect was detected with the components α_{11} , α_{13} , α_{31} and α_{33} in accordance with the magnetic space group $P2_1/c'$ proposed in [204, 216]. But in addition, finite tensor components α_{21} , α_{12} , α_{23} and α_{32} were also observed with about one to two orders of magnitude smaller absolute values compared to those of α_{11} , α_{13} , α_{31} and α_{33} . These latter results are inconsistent with the magnetic space group $P2_1/c'$. However, they were attributed to experimental imperfections and therefore not taken into account [14]. A first hint that $\text{LiFeSi}_2\text{O}_6$ could be actually triclinic below $T_N \simeq 18.5 \text{ K}$ was found by M. Baum in his PhD thesis [204]. He poled the antiferromagnetic domains of $\text{LiFeSi}_2\text{O}_6$ via the linear magnetoelectric effect by applying different combinations of electric and magnetic fields and visualized the poling characteristics via neutron diffraction. The antiferromagnetic domains could be poled not only via the components α_{11} , α_{13} , α_{31} and α_{33} as expected, but also via the components α_{12} and α_{32} forbidden for the monoclinic symmetry, which suggests an actual triclinic symmetry. However, because sample

³The experimentally determined tensor form of $\text{LiFeSi}_2\text{O}_6$ corresponds to the form (B) in appendix G.

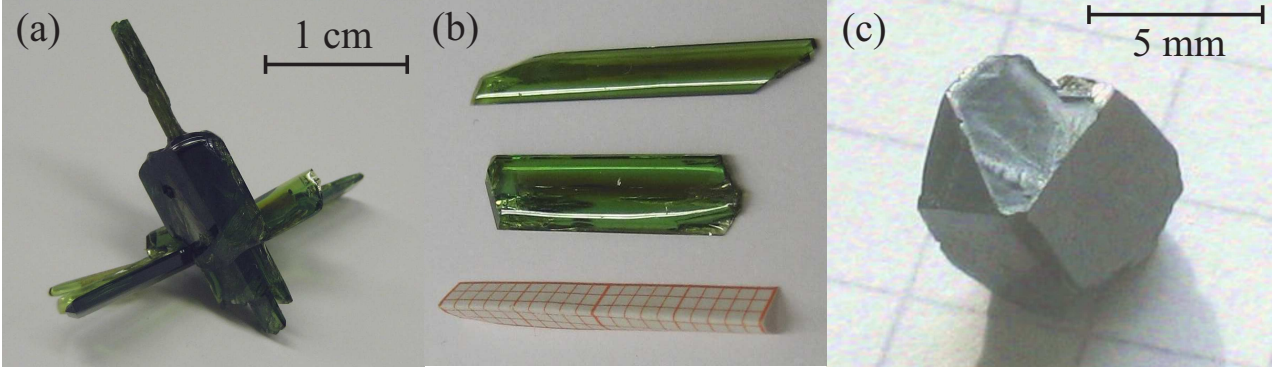


Figure 4.2: (a)-(b) Crystals of $\text{LiFeSi}_2\text{O}_6$ (c) Crystal of $\text{NaFeGe}_2\text{O}_6$

misalignments with respect to the applied magnetic fields could not be excluded, the possibility of a triclinic symmetry of the antiferromagnetic phase of $\text{LiFeSi}_2\text{O}_6$ was not considered further.

In the present work, the magnetoelectric properties of $\text{LiFeSi}_2\text{O}_6$ were reinvestigated with a higher accuracy and the focus on minimizing the extrinsic error sources reported in [14]. For that purpose, the sample surfaces were completely metallized with silver by evaporation for the dielectric investigations to assure very well-matched electrode areas. Additionally, possible misalignments of the samples with respect to applied magnetic fields could be minimized to the order of 1° . Furthermore, the influence of non-identical electrodes on the results of pyroelectric-current measurements were systematically investigated using samples of the well-known pyroelectric compounds $\text{Sr}[\text{Sb}_2\{(+)\text{-C}_4\text{H}_2\text{O}_6\}_2 \cdot 2\text{H}_2\text{O}]$ and $\text{Li}_2\text{SO}_4 \cdot \text{H}_2\text{O}$.

The high-accuracy dielectric measurements reveal unambiguously that all magnetoelectric tensor components apart from α_{22} are present in the antiferromagnetically ordered phase of $\text{LiFeSi}_2\text{O}_6$. This implies that the low-temperature phase of $\text{LiFeSi}_2\text{O}_6$ cannot be monoclinic with the magnetic point group $2/m'$ as proposed in [204, 216], but has to be triclinic with the magnetic point group $\bar{1}'$. The transition from $2/m1'$ to $\bar{1}'$ at $\simeq 18.5$ K could directly be observed with a polarized-light microscope in zero magnetic field, see section 4.3.5. In addition, a new magnetoelectric phase was discovered for magnetic fields along c above $\simeq 6$ T and was further investigated by thermal-expansion and magnetostriction measurements.⁴ Apart from these fundamental findings, the temperature dependence of all components of the magnetoelectric tensor was determined. Finally, magnetic-field versus temperature phase diagrams were derived.

The multiferroic properties of $\text{NaFeGe}_2\text{O}_6$ and their anisotropy were characterized by dielectric investigations, magnetic-susceptibility, thermal-expansion and magnetostriction measurements.⁵ The magnetic-susceptibility measurements reveal that $\text{NaFeGe}_2\text{O}_6$ orders antiferromagnetically at

⁴The thermal-expansion and magnetostriction measurements were performed together with L. Andersen.

⁵Parallel to the experiments in the present work, $\text{NaFeGe}_2\text{O}_6$ was proved to be multiferroic in a dielectric study of polycrystalline pressed pellets [12].

$T_N \simeq 13 \text{ K}$ with the spins being oriented mainly along $b \times c$. At $T_C \simeq 11.6 \text{ K}$, a second transition occurs with a spin reorientation after that the spins are lying mainly within the ac plane. The second transition coincides with the onset of an electric polarization ($P \simeq 32 \mu\text{C}/\text{m}^2$) lying mainly within the ac plane with a small component along b . Detailed magnetic-field versus temperature phase diagrams are derived. Depending on the direction of the magnetic field, up to three different multiferroic phases are identified, which are separated by a magnetically ordered, but non-ferroelectric phase from the paramagnetic phase.

4.3 $\text{LiFeSi}_2\text{O}_6$

In the following, the investigations of the compound $\text{LiFeSi}_2\text{O}_6$ summarized in section 4.2 are presented, analysed and discussed in detail.

4.3.1 Magnetic properties

The results of the magnetic-susceptibility measurements of $\text{LiFeSi}_2\text{O}_6$ adopted from the PhD thesis of S. Jodlauk [14] are repeated and shortly explained in this section as far as they are important for the present work.

The temperature-dependent magnetic susceptibilities of $\text{LiFeSi}_2\text{O}_6$ for magnetic fields up to 14 T (applied along the $b \times c$, b and c axis) are displayed in figures 4.3 (a)-(c). The low-field curves signal magnetic ordering at $T_N \simeq 18.5 \text{ K}$. While $\chi_c(T)$ shows a well-defined kink at T_N and subsequently decreases with decreasing temperature, $\chi_{b \times c}(T)$ and $\chi_b(T)$ hardly change below T_N indicating that the spins are oriented mainly along the c axis. Towards larger fields, the decrease of $\chi_c(T)$ for $T < T_N$ systematically vanishes, and finally around 8 T the principal behaviour of $\chi_c(T)$ is almost identical to that of $\chi_{b \times c}(T)$ and $\chi_b(T)$, see figure 4.3 (c). This suggests that for $\mathbf{B} \parallel \mathbf{c}$ a spin-flop transition occurs, which is also visible in the low-temperature measurements of the magnetization as a function of the magnetic field, see figure 4.3 (d). The spin-flop field amounts at $T = 5 \text{ K}$ to $\simeq 6 \text{ T}$ and is nearly constant with increasing temperature, see the inset in figure 4.3 (d).

The inverse susceptibilities $1/\chi_i$ follow a Curie-Weiss behaviour from about 40 K up to room temperature, which is illustrated for $1/\chi_b$ in figure 4.3 (e) for a magnetic field of 1 T. Linear fits to the data of $1/\chi_i$ for $T > 100 \text{ K}$ yield a negative Weiss temperature $\theta \simeq -24 \text{ K}$ and an effective magnetic moment $\mu_{\text{eff}} \simeq 5.9 \mu_B$. The negative Weiss temperature signals a net antiferromagnetic exchange interaction and the effective magnetic moment is close to the expected value $\mu_{\text{eff}} = g\mu_B\sqrt{S(S+1)} = 5.92 \mu_B$ of Fe^{3+} with $S = 5/2$ and $g = 2$.

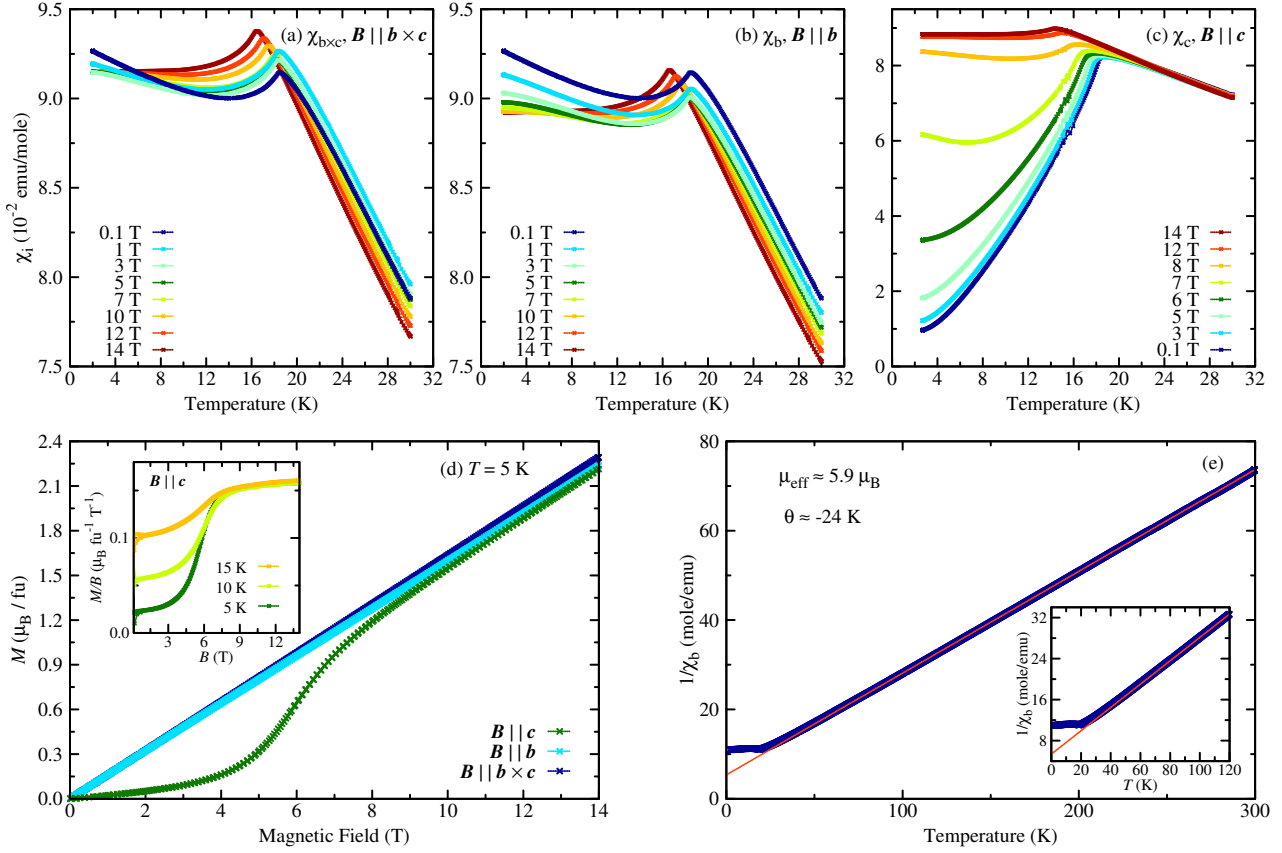


Figure 4.3: (a)-(c) Temperature dependences of the magnetic susceptibility $\chi_{b \times c}$, χ_b and χ_c of LiFeSi₂O₆ for different magnetic fields. (d) Magnetization at 5 K as functions of the magnetic field applied parallel to $b \times c$, b and c ; the inset shows M/B for $B \parallel c$ at different temperatures. (e) Temperature dependence of the inverse susceptibility $1/\chi_b$ together with a Curie-Weiss fit (line) in the temperature range from 100 K to 300 K (the inset shows a magnification of the low-temperature range). All plots are adopted from [14].

4.3.2 Dielectric properties

Figure 4.4 summarizes the temperature-dependent measurements of the electric polarization $P_{b \times c}$, P_b and P_c of LiFeSi₂O₆ in magnetic fields applied along $b \times c$, b and c . The respective pyroelectric-current densities can be found in appendix E.1. The data of $P_c(T)$ for applied magnetic fields along $b \times c$ and c in figures 4.4 (g) and (i) were not achieved in the present work, but are adopted from [14].

In zero magnetic field, no electric polarization occurs below $T_N \simeq 18.5$ K. Applied magnetic fields along $b \times c$, b or c , however, induce an electric polarization, which linearly increases with increasing magnetic field for small field strengths confirming the presence of a linear magnetoelectric effect in LiFeSi₂O₆ in accordance to [14]. The transition temperature slightly decreases with increasing magnetic-field strength. Apart from $P_{b \times c}$, which exhibits apparently a preferred direction, all components were completely invertible by reversing the electric poling field. In figure 4.4, only

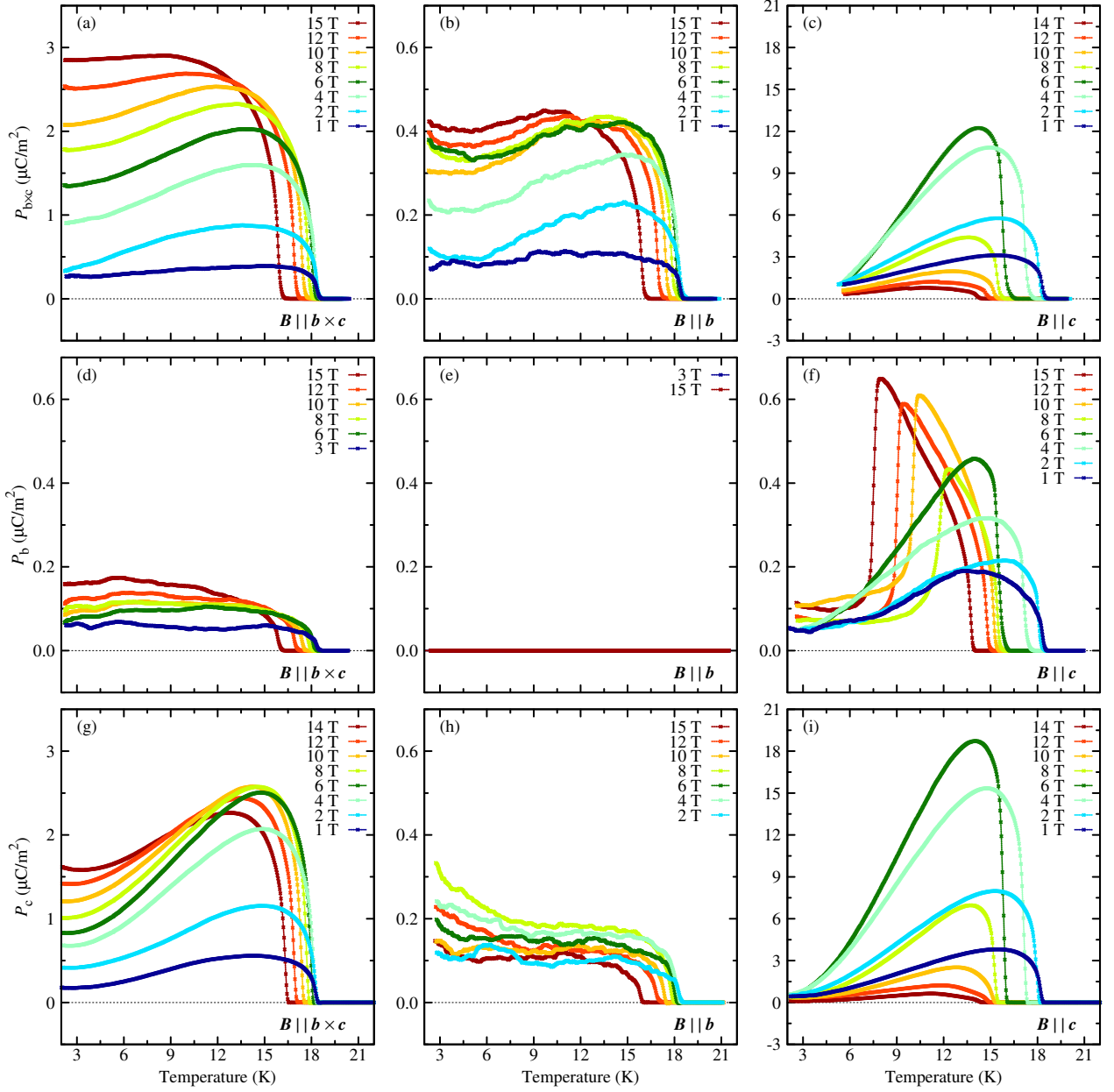


Figure 4.4: Temperature dependences of the electric polarization $P_{b \times c}$, P_b and P_c (top to bottom) of $\text{LiFeSi}_2\text{O}_6$ for magnetic fields applied parallel to the $b \times c$, b or c axis (left to right). The electric polarization was completely invertible by changing the sign of the electric field in all the cases, apart from $P_{b \times c}$. Only one direction of the electric polarization is shown. The data in panel (g) and (i) are adopted from [14].

one poling direction is displayed for each polarization component. For $B || b \times c$ and $B || c$, the induced electric polarization is mainly lying within the ac plane with a small component along b . The maximum absolute values of $P^{B_{b \times c}}$ and P^{B_c} amount to $\simeq 3.8 \mu\text{C}/\text{m}^2$ and $\simeq 22.5 \mu\text{C}/\text{m}^2$, respectively, at a magnetic field of 6 T. The induced polarization for $B || b$ is one or two orders of magnitude smaller than that for the other two field directions with a maximum absolute value of

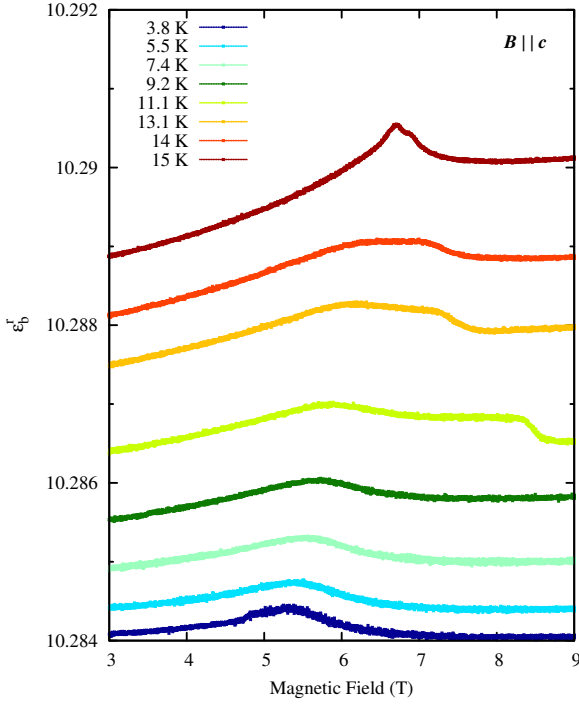


Figure 4.5: Magnetic-field dependences of the component ϵ_b^r of the dielectric tensor for $B||c$ at representative temperatures. The single anomalies for temperatures below 9.2 K can be attributed to the spin-flop transition. There are two anomalies at higher temperatures, which correspond to the spin-flop transition and to the suppression of P_b for magnetic fields applied along c , respectively.

about $P^{B_b} = 0.45 \mu\text{C}/\text{m}^2$ at a field of 6 T. It is exclusively confined to the ac plane.

For $B||c$, the magnetic-field induced electric polarization reaches a broad maximum below T_N and approaches zero for $T \rightarrow 0$ K, see figures 4.4(c), (f) and (i). In the vicinity of the spin-flop transition around 6 T, both components $P_{b \times c}$ and P_c reach maximum values and then decrease continuously with further increasing magnetic-field strength. In contrast, P_b proceeds to enlarge also above 6 T with increasing magnetic fields. Interestingly, unlike $P_{b \times c}$ and P_c , this component is sharply suppressed in that field range for lower temperatures indicating the presence of a phase transition, which has not been reported in literature yet, see figure 4.4(f). This phase transition curiously could not be observed in the magnetization data, see figure 4.3(d). Only the spin-flop transition occurring around 6 T is visible. The emergence of this new phase transition could be confirmed, however, by magnetic-field dependent measurements of the component ϵ_b^r of the dielectric tensor for $B||c$, see figure 4.5.⁶ For low temperatures, a single anomaly is visible in the magnetic-field dependent data of ϵ_b^r coinciding with the spin-flop transition, already discussed in the context of figure 4.3. Above 11.1 K, a second anomaly occurs, which coincides with the suppression of $P_b(T)$ and thus can be attributed to the corresponding phase transition. With increasing temperatures both anomalies converge.

For magnetic fields applied perpendicular to the magnetic easy axis, the temperature dependences

⁶Temperature-dependent measurements of the longitudinal components ϵ_i^r ($i = b \times c, b, c$) of the dielectric tensor were not performed in the present work, but can be found in [14]

of all polarization components are very similar, see figure 4.4. Below T_N , they first grow and then saturate more or less for lower temperatures. The present deviations from this characteristics, as, for example, the strong increase of $P_c^{B_b}(T)$ for $T \rightarrow 0$ K at high magnetic-field strengths, see figure 4.4(h), are probably not real physical effects. Instead, they obviously reflect the general problem in considering the background currents properly before the calculation of the electric polarization, especially for very small pyroelectric-current signals.⁷

The results of the dielectric investigations reveal unambiguously the presence of $P_{b \times c}^{B_b}$, $P_b^{B_{b \times c}}$, $P_b^{B_c}$ and $P_c^{B_b}$. Extrinsic error sources, such as mismatched electrode areas or sample misalignments, which could have led to parasitic contributions to the determined electric polarizations, could be eliminated as far as possible.⁸ All four components are one or two orders of magnitude smaller than $P_{b \times c}^{B_{b \times c}}$, $P_c^{B_{b \times c}}$, $P_{b \times c}^{B_c}$ and $P_c^{B_c}$. Interestingly, the component $P_b^{B_b}$ seems to be completely zero. The presence of $P_{b \times c}^{B_b}$, $P_b^{B_{b \times c}}$, $P_b^{B_c}$ and $P_c^{B_b}$ is in contradiction with the monoclinic space group $P2_1/c$ proposed in literature [14,204,216] and indicates that at least in applied magnetic fields the symmetry of $\text{LiFeSi}_2\text{O}_6$ below T_N is actually triclinic. Consequently, four magnetic space groups are in principle possible, namely $P\bar{1}'$, $P\bar{1}$, $P1$ or $P1'$. The two space groups $P\bar{1}$ and $P1'$ can be excluded because they do not allow a linear magnetoelectric effect, see appendix G. The space group $P1$ can be (almost certainly) excluded as well because it would allow the occurrence of an electric polarization in zero magnetic field. Therefore, only $P\bar{1}'$ remains to describe the triclinic phase of $\text{LiFeSi}_2\text{O}_6$ correctly. In order to investigate if the triclinicity is already present in zero magnetic field, the dielectric investigations were extended to very low magnetic-field strengths in the millitesla range.⁹ The corresponding results give no hint at possibly existing threshold fields, see, e.g., figure 4.6(f). This is confirmed by the findings of a series of investigations with a polarized-light microscope.¹⁰

4.3.3 Magnetoelectric effect

All the components of the electric polarization of $\text{LiFeSi}_2\text{O}_6$ are depending linearly on the magnetic-field strength for small magnetic fields, as mentioned in section 4.3.2. This indicates that $\text{LiFeSi}_2\text{O}_6$ is linear magnetoelectric. The linear field dependence of the electric polarization of $\text{LiFeSi}_2\text{O}_6$ is illustrated in figure 4.6 by plotting the components P_i ($i = b \times c, b, c$) as functions of the magnetic field along $b \times c$, b and c at representative temperatures. The data points were obtained from the results of the temperature-dependent measurements of the electric polarization, displayed in figure 4.4. Linear fits to the magnetic-field dependent electric polarization data yield

⁷For more informations about these problems see section 3.2.7.

⁸In section 4.3.4, parasitic effects due to mismatched electrode areas are discussed and analysed in detail.

⁹The magnetic-field strengths in this low-field regime were determined by a Hall sensor (LHP-NU, Arepoc).

¹⁰The results of these measurements are discussed in detail in section 4.3.5.

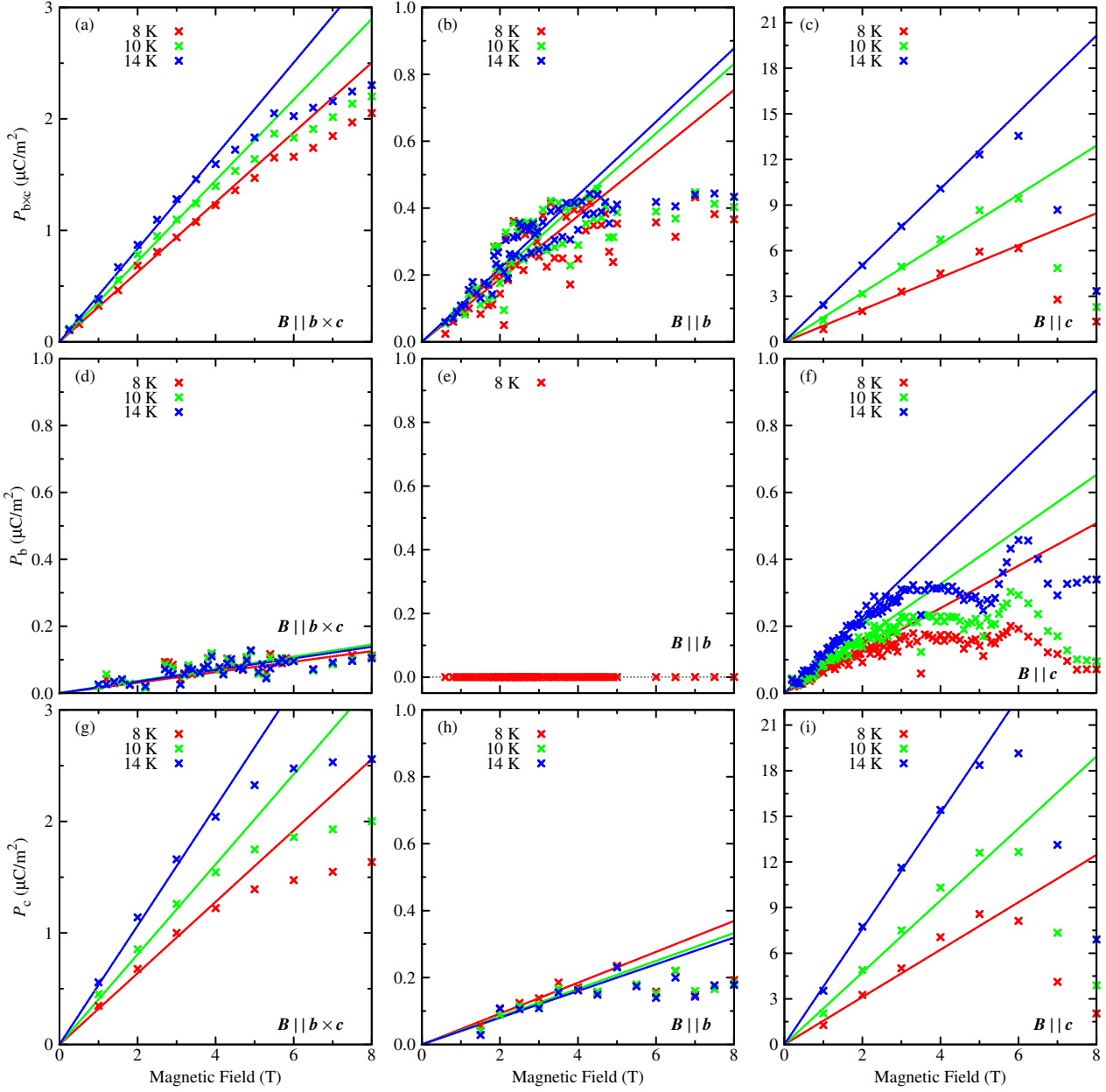


Figure 4.6: Magnetic-field dependences of the electric polarization of $\text{LiFeSi}_2\text{O}_6$ at representative temperatures for applied magnetic fields along $\mathbf{b} \times \mathbf{c}$, \mathbf{b} or \mathbf{c} . The field-dependent data, presented here, were obtained by resorting the temperature-dependent data of figure 4.4. For panel (g) and (i) the temperature-dependent data from [14] were used. The solid lines indicate linear fits to the data for small magnetic-field strengths.

the linear magnetoelectric tensor components $\alpha_{ij}(T) = \partial \mu_0 P_i(T) / \partial B_j$ in SI units, see figure 4.7. For the representative temperatures, presented in figure 4.6, the fitted linear functions are displayed as solid lines.

The absolute values of α_{12} , α_{21} and α_{32} as well as their exact temperature behaviour, see figure 4.7 (b), (d) and (h), have to be considered with some caution. The corresponding components

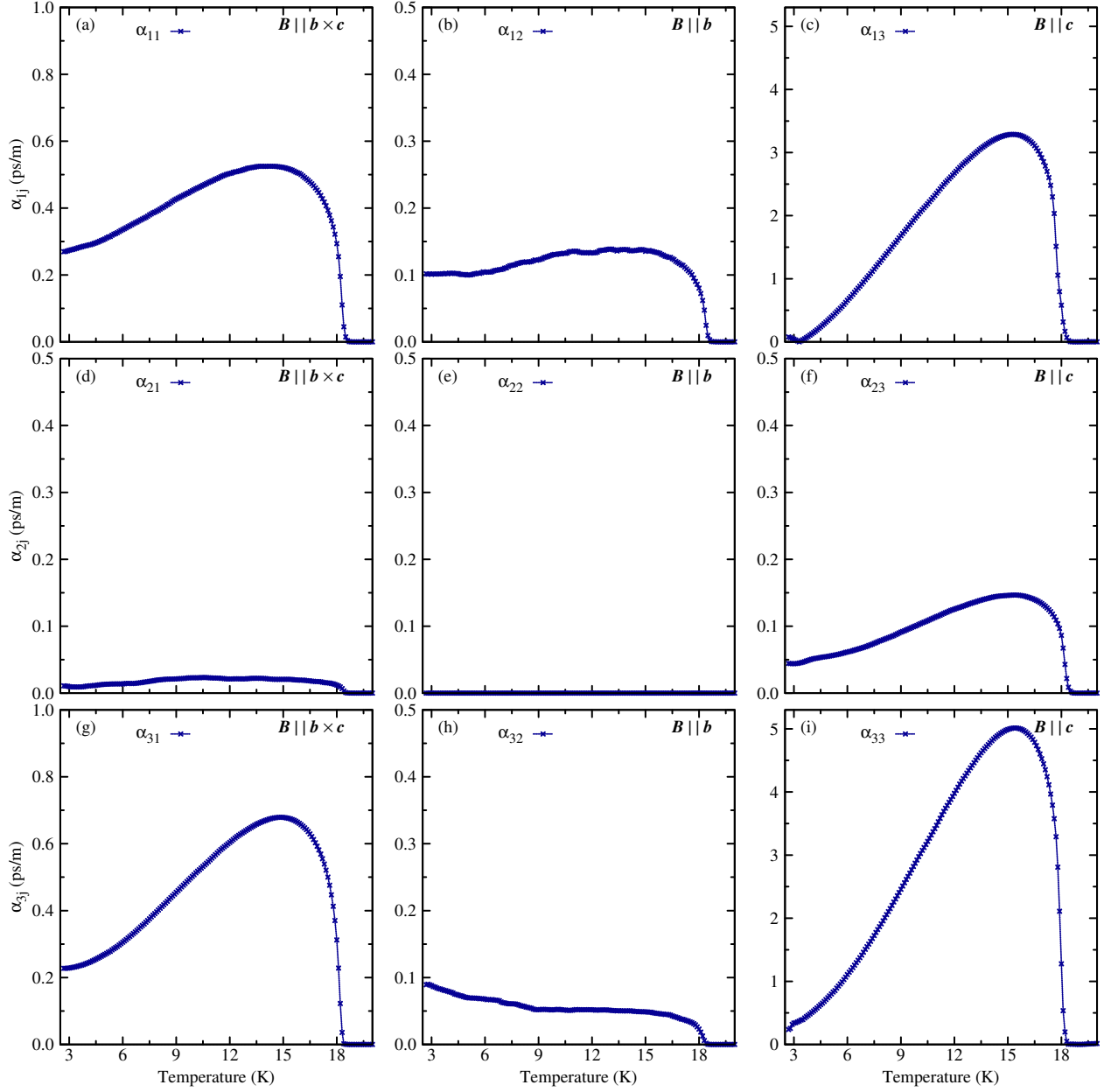


Figure 4.7: Temperature dependences of the components of the linear magnetoelectric tensor of $\text{LiFeSi}_2\text{O}_6$. Within the experimental uncertainty α_{22} is zero. All the other components have finite values.

of the magnetic-field induced electric polarization are very small and hence noisy, see figure 4.6 (b), (d) and (h). Therefore, the determination of the magnetoelectric tensor components in these directions by fitting linear functions to the field-dependent data is linked to significant errors. In equation 4.1, the components of the linear magnetoelectric tensor of $\text{LiFeSi}_2\text{O}_6$ at 14 K are displayed. The components α_{11} , α_{12} , α_{31} and α_{33} are within the experimental uncertainties in accordance with those determined in [14]. The components α_{12} , α_{21} , α_{23} and α_{32} are one or two orders of

magnitude smaller, than the components α_{11} , α_{12} , α_{31} and α_{33} .

$$[\alpha_{ij}^{\text{SI}}](14 \text{ K}) = \begin{bmatrix} 0.52 & 0.14 & 3.44 \\ 0.02 & 0 & 0.14 \\ 0.67 & 0.05 & 4.78 \end{bmatrix} \frac{\text{ps}}{\text{m}} \quad (4.1)$$

4.3.4 Influence of electrode-area mismatch on the results of the dielectric investigations

In the context of the study of the magnetoelectric properties of $\text{LiFeSi}_2\text{O}_6$, S. Jodlauk already described the problem of parasitic currents due to mismatched electrode areas [14]. However, he did not analysed the problem in much detail. During the reinvestigation of the magnetoelectric properties of $\text{LiFeSi}_2\text{O}_6$ in the present work the problem of such parasitic currents was investigated and analysed systematically to permit the discrimination between true magnetoelectric and parasitic effects. In the course of the present dielectric study it turned out that even small misalignments of electrode areas strongly influence the resulting pyroelectric or magnetoelectric currents. This is illustrated for two different series of pyroelectric-current measurements performed on a sample of $\text{LiFeSi}_2\text{O}_6$ with the surface normal oriented along \mathbf{b} and a magnetic field applied parallel to \mathbf{c} .

In the first series of measurements the sample surfaces were partly metallized by silver paint taking care of well-matched electrode areas. The resulting temperature dependences of the electric polarization are displayed in figure 4.8 (a) for opposite poling directions of the applied electric fields.¹¹ For small magnetic fields, the electric polarization grows linearly with increasing field strength and then reaches a maximum value of about $1.6 \mu\text{C}/\text{m}^2$ at 6 T. In the low-field range a slight asymmetry between opposite poling directions is visible. Above 6 T, the electric polarization decreases and for very high magnetic fields a relative brought anomaly occurs at lower temperatures. In addition, the asymmetry disappears in the high-field range.

In the second series of measurements the sample surfaces were completely metallized by silver by evaporation, leading to nearly perfectly-matched electrode areas. The resulting temperature dependences of the electric polarization are displayed in figure 4.8 (b) again for both poling directions of the applied electric fields.¹¹ The electric polarization in this case is about a factor of three smaller than that for the not perfectly-matched electrode areas. As before, it increases linearly with increasing magnetic-field strength up to a maximum value of about $0.45 \mu\text{C}/\text{m}^2$ at 6 T. Obviously, the asymmetry observed before has vanished here. In addition, the electric polarization behaves completely different above 6 T. First of all, it does not decrease with increasing magnetic field and

¹¹The corresponding pyroelectric-current densities are presented in figure 7 in appendix E.1.

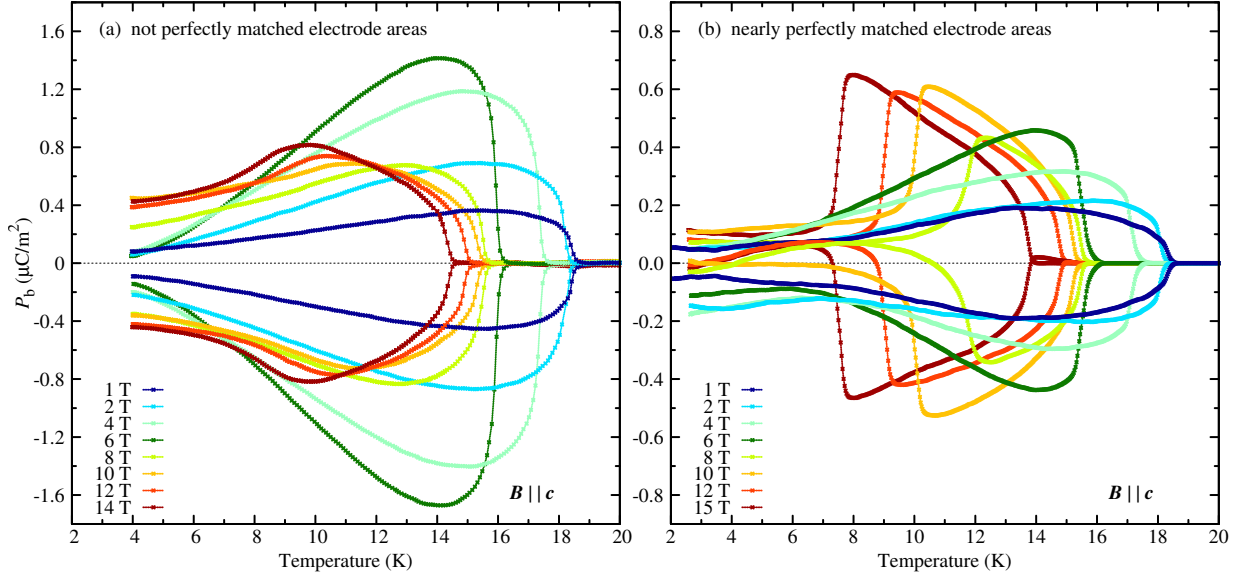


Figure 4.8: Temperature dependences of the polarization component P_b of $\text{LiFeSi}_2\text{O}_6$ for an applied magnetic field parallel to the c axis. Both poling directions of P_b are displayed. The presented temperature dependences of P_b in (a) resulted from measurements performed on a sample with not perfectly-matched electrode areas, while those presented in (b) are based on measurements performed on a sample with nearly perfectly-matched electrode areas. Note the different scales of P_b .

secondly instead of the broad anomalies described above, sharp drops occur at lower temperatures. The different results of the two series of measurements described above can be qualitatively understood as follows. For the nearly perfectly-matched electrode areas, the measurements reveal the real magnetic-field induced polarization along \mathbf{b} (P_b^{pure}), see figure 4.8 (b). In the case of the not perfectly-matched electrode areas, this true electric polarization along \mathbf{b} is superposed by fractions of the two other components $P_{b \times c}$ and P_c . Compared to the pure value P_b^{pure} , both $P_{b \times c}$ and P_c are about two orders of magnitude larger for magnetic fields below 6 T. Therefore, already small fractions of $P_{b \times c}$ and P_c suffice to enlarge the apparent polarization P_b^{wrong} detected along \mathbf{b} . The preferred direction of the polarization along $\mathbf{b} \times \mathbf{c}$, mentioned in section 4.3.2 probably leads to the observed asymmetry of P_b^{wrong} for the not perfectly-matched electrode areas. For magnetic fields above 6 T, the real component P_b^{pure} slightly further increases with increasing field strength, while $P_{b \times c}$ and P_c strongly decrease. Finally above 12 T, all three polarization components have the same order of magnitude, see figure 4.9. Hence, the influence of $P_{b \times c}$ and P_c on P_b^{wrong} diminishes in the high-field range, which explains the disappearance of its asymmetry there. The broadening and weakening of the sharp drop, which is visible in the pure polarization data along \mathbf{b} in the high-field range, can also be attributed to the influence of $P_{b \times c}$ and P_c . Adding $P_b^{\text{pure}}(T)$ and fractions of $P_{b \times c}(T)$ and $P_c(T)$ for a magnetic field of, e.g., 12 T would indeed lead to a broad maximum comparable to that observed in the polarization data of figure 4.8 (a) for that field strength. Similar

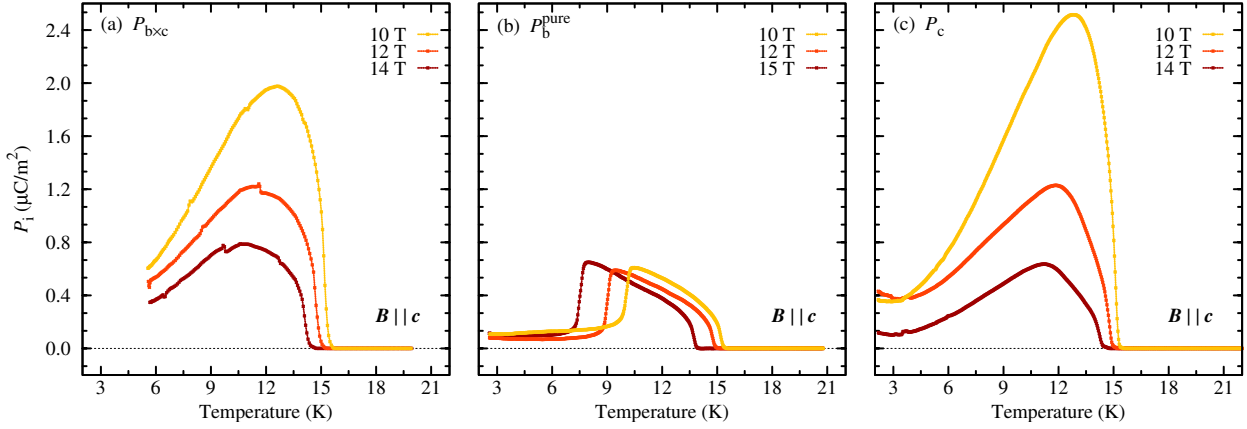


Figure 4.9: (a)-(c) Temperature dependences of the three polarization components $P_{b \times c}$, P_b^{pure} and P_c of LiFeSi₂O₆ for an applied magnetic field parallel to the c axis above 10 T.

effects to those discussed above were also observed for other components of the magnetic-field induced electric polarization of LiFeSi₂O₆ such as for $P_{b \times c}^{B_b}$ or $P_b^{B_{b \times c}}$, whenever an electrode-area mismatch was present.

The problem of parasitic pyroelectric currents due to mismatched electrode areas was further studied by investigating two well-known pyroelectrics Sr[Sb₂{(+)-C₄H₂O₆}₂·2H₂O] and Li₂SO₄·H₂O. The pyroelectric effect of both compounds was examined in detail by H. Schneeberger in his PhD thesis [153]. Sr[Sb₂{(+)-C₄H₂O₆}₂·2H₂O] crystallizes at room temperature in the space group $P6_4$. Consequently, its pyroelectric vector is oriented parallel to the sixfold rotation axis. At room temperature and at constant mechanical stress its absolute value amounts to $5.3 \mu\text{Cm}^{-2}\text{K}^{-1}$ [153]. Li₂SO₄·H₂O crystallizes at room temperature in the space group $P2_1$. Therefore, its pyroelectric vector is oriented parallel to the twofold rotation axis. At room temperature and at constant mechanical stress its absolute value amounts to $87.3 \mu\text{Cm}^{-2}\text{K}^{-1}$ [153]. Furthermore, it has a sign change in the low-temperature range at around 110 K. For test purposes of the continuous-flow cryostat developed during the present work and presented in appendix D, the pyroelectric effect of Li₂SO₄·H₂O was reinvestigated down to a temperature of 4 K.¹² For the study of parasitic pyroelectric currents due to mismatched electrode areas, a (100) Sr[Sb₂{(+)-C₄H₂O₆}₂·2H₂O] sample and a (10 $\bar{1}$) Li₂SO₄·H₂O sample were used. Because the pyroelectric vector is parallel to the sample surfaces in both cases, no pyroelectric effect should be detectable. While Li₂SO₄·H₂O was investigated in detail, Sr[Sb₂{(+)-C₄H₂O₆}₂·2H₂O] was examined more qualitatively. Therefore, in the following the results of Li₂SO₄·H₂O are presented in more detail. The data of Sr[Sb₂{(+)-C₄H₂O₆}₂ qualitatively confirm the findings of Li₂SO₄·H₂O.

There are three principal electrode-area configurations, which are presented in figure 4.10 and dis-

¹²The corresponding results are presented in appendix D as well.

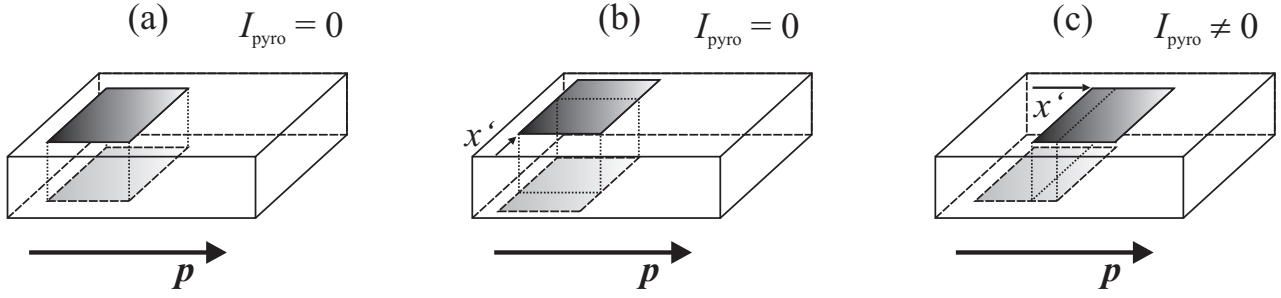


Figure 4.10: Schematic picture of different electrode-area configurations for a plate-like sample with the pyroelectric vector \mathbf{p} lying within the surface. (a) Perfectly-matched electrode areas. (b) Misaligned electrode areas perpendicular to \mathbf{p} . (c) Misaligned electrode areas parallel to \mathbf{p} .

cussed in the following. First of all, the electrode areas can match perfectly, see figure 4.10 (a). As expected, no pyroelectric effect was detected in that case, neither for $\text{Sr}[\text{Sb}_2\{(+)\text{-C}_4\text{H}_2\text{O}_6\}_2 \cdot 2\text{H}_2\text{O}]$ nor for $\text{Li}_2\text{SO}_4 \cdot \text{H}_2\text{O}$, see figure 4.11 (a). Secondly, the electrode areas can be misaligned perpendicular to the pyroelectric vector \mathbf{p} , see figure 4.10 (b). No pyroelectric effect was detected in that case again (not shown here). An electrode-area mismatch parallel to \mathbf{p} , see figure 4.10 (c), finally led to the occurrence of a parasitic pyroelectric effect $p_b^{\text{parasitic}}$. It was investigated in detail for different strong misalignments of the electrodes parallel to \mathbf{p} . The emerging parasitic pyroelectric currents during the heating and cooling cycles were recorded and the corresponding coefficients $p_b^{\text{parasitic}}$ were calculated, see red and black data points in figure 4.11 (b), (c) and (d). The dashed lines in the same figures represent the temperature dependence of the real pyroelectric effect p_b^{real} of $\text{Li}_2\text{SO}_4 \cdot \text{H}_2\text{O}$ scaled on the parasitic effects.¹³

For a 30% electrode-area mismatch, the temperature dependence of the parasitic effect during the cooling cycle (in black) coincides well with the scaled real effect $0.19 \cdot p_b^{\text{real}}(T)$ above 110 K, see figure 4.11 (b). Around 110 K, however, $p_b^{\text{parasitic}}(T)$ does not change its sign as $p_b^{\text{real}}(T)$ does, but has a kink and then follows $-0.05 \cdot p_b^{\text{real}}(T)$. In the vicinity of 90 K, the parasitic effect then relaxes back on the $0.19 \cdot p_b^{\text{real}}$ curve with further decreasing temperature and finally essentially follows this curve until the experimental low-temperature limit is reached. A similar anomalous hysteretic behaviour arises during the heating cycle. Below 30 K, $p_b^{\text{parasitic}}(T)$ first follows the $-0.05 \cdot p_b^{\text{real}}$ curve and then at higher temperatures relaxes back on the $0.19 \cdot p_b^{\text{real}}$ curve. As in the cooling cycle the parasitic effect does not change its sign around 110 K, but first follows again the $-0.05 \cdot p_b^{\text{real}}$ curve, proceeded at higher temperatures by a relaxation back on the $0.19 \cdot p_b^{\text{real}}$ curve. The anomalous hysteretic behaviour of the parasitic effect in the vicinity of 4 K and 110 K grows in intensity with increasing electrode-area mismatch, in the other temperature regions the parasitic effect decreases, see figures 4.11 (c) and (d).

¹³The temperature dependence of the real pyroelectric effect of $\text{Li}_2\text{SO}_4 \cdot \text{H}_2\text{O}$ can be found in figure 5 in appendix D.

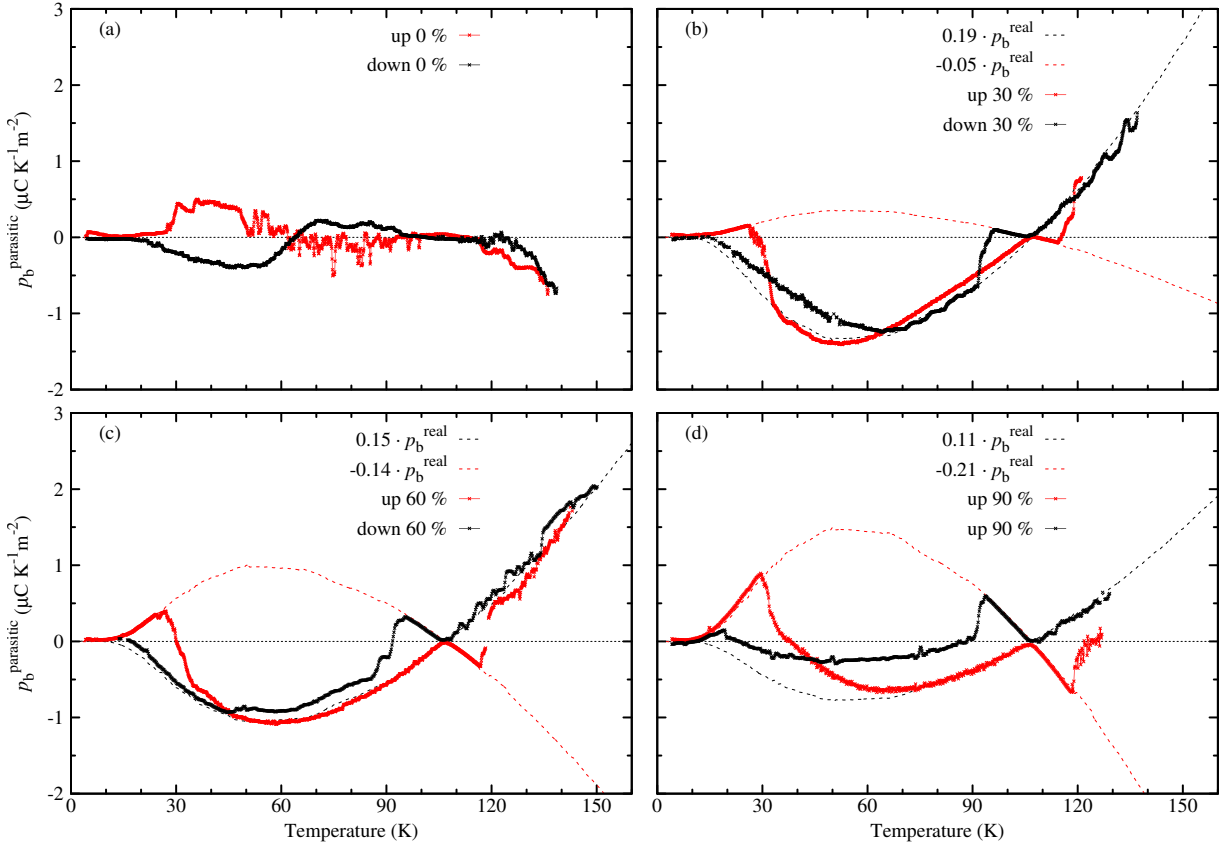


Figure 4.11: Temperature dependences of the parasitic pyroelectric coefficient of $\text{Li}_2\text{SO}_4 \cdot \text{H}_2\text{O}$ for electrode-area configurations with different misalignments parallel to the real pyroelectric effect. 30%, e.g., denotes an electrode-area mismatch, where 30% of the areas do not overlap. For more details see text.

In the following, a simple theoretical model for the occurrence of parasitic pyroelectric currents for mismatched electrode areas according to the configuration in figure 4.10(c) will be developed. Assuming that the sample with mismatched electrodes may be at the beginning at a constant temperature, the electric polarization will be compensated by free electric charges on the sample surfaces and therefore the internal electric field will be zero. A continuous temperature change with the rate $\frac{dT}{dt}$ leads via the pyroelectric effect to a continuous change of the electric polarization

$$\frac{dP}{dt} = p^{\text{real}} \frac{dT}{dt} \quad (4.2)$$

oriented parallel to the sample surface. Accordingly, an internal electric field E_{pol} in the same direction builds up with a continuous change

$$\frac{dE_{\text{pol}}}{dt} = \frac{p^{\text{real}}}{\epsilon_0} \frac{dT}{dt} \quad (4.3)$$

leading to an electric-potential difference $U = \Phi_1 - \Phi_2$ between the edges of the considered

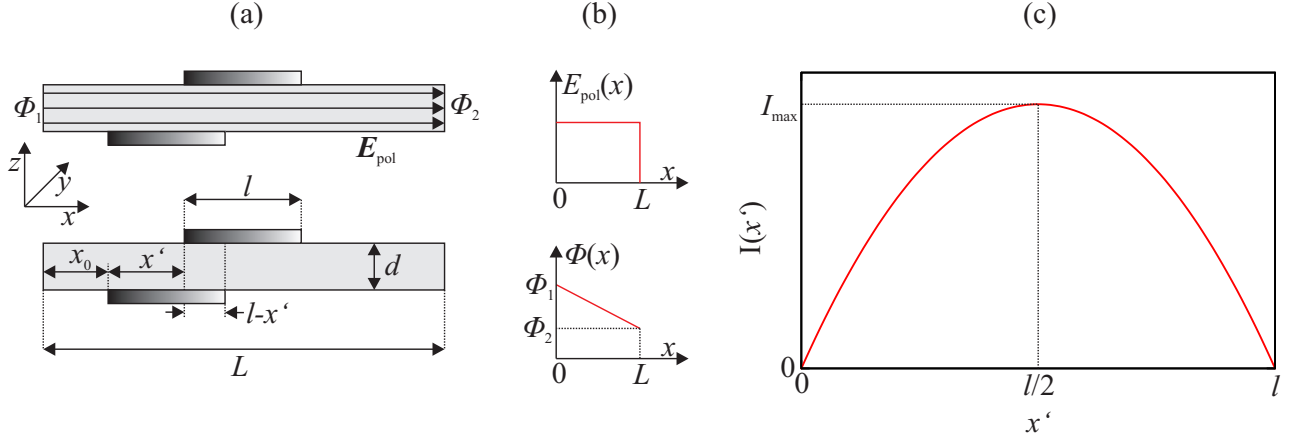


Figure 4.12: (a) Schematic picture of a pyroelectric sample with mismatched electrode areas parallel to the pyroelectric vector. A temperature change leads via the pyroelectric effect to the occurrence of an internal electric field and an electric-potential difference between the sample edges. (b) Dependence of the internal electric field and the internal electric potential with respect to the coordinate x in the idealized picture of a parallel-plate capacitor. (c) Parasitic pyroelectric current and its dependence on the electrode-area misalignment x' .

sample, see figure 4.12 (a). In the idealized picture of a parallel-plate capacitor, the internal electric field is constant everywhere in the sample and the electric potential changes linearly with x , see figure 4.12 (b). The shift x' of the mismatched electrode areas with respect to each other causes an electric-potential difference $U_{\text{parasitic}} = E_{\text{pol}}x'$ between both electrodes, which depends linearly on the shift x' . Due to the continuous temperature change this electric-potential difference changes continuously according to

$$\frac{dU_{\text{parasitic}}}{dt}(x') = \frac{p^{\text{real}}}{\epsilon_0} \frac{dT}{dt} x'. \quad (4.4)$$

The overlapping part of the electrode areas forms a second parallel-plate capacitor with the capacitance $C = \frac{\epsilon_0 \epsilon_r}{d} (l - x') y_0$. Therefore, the parasitic pyroelectric current

$$I_{\text{parasitic}}(x') = \frac{p^{\text{real}} \epsilon_r}{d} \frac{dT}{dt} y_0 x' (l - x') \quad (4.5)$$

flows to charge the capacitor as long as the electrode areas partly overlap. The parasitic current in equation 4.5 grows with increasing electrode-area mismatch x' up to a maximum value at half overlapping electrodes, see figure 4.12 (c). With further increasing mismatch the parasitic current decreases again and reaches finally zero at zero overlap of the electrode areas.

In accordance to the above-developed model, the real pyroelectric effect of $\text{Li}_2\text{SO}_4 \cdot \text{H}_2\text{O}$ can be scaled on the parasitic effect, see figure 4.11. Furthermore, the parasitic effect first grows with

increasing electrode-area mismatch and then decrease again. But according to the model the parasitic effect for the 60% electrode mismatch should be larger than that for the 30% electrode mismatch, which is not reflected by the experimental data, see figure 4.11. Furthermore, the observed parasitic effect for the 90% electrode mismatch is too large. The reason for the hysteretic anomalous behaviour in the vicinity of the vanishing pyroelectric effect observed in the experiments of $\text{Li}_2\text{SO}_4 \cdot \text{H}_2\text{O}$ is unclear as well. Therefore, further contributions to the parasitic effect apparently exist, which are not contained in the present model. Nevertheless, at least qualitatively it seems to be appropriate for the description of the parasitic effects observed in the present work.

4.3.5 Polarized-light microscopy

As discussed in section 4.3.2, the dielectric investigations of $\text{LiFeSi}_2\text{O}_6$ indicate that the symmetry of its antiferromagnetically ordered phase is triclinic. Therefore, a symmetry-lowering phase transition from the monoclinic to the triclinic system has to occur. $\text{LiFeSi}_2\text{O}_6$ is an optically biaxial crystal in the monoclinic phase above 18.5 K. Its indicatrix forms a triaxial ellipsoid with three different principal axes $n_\gamma > n_\beta > n_\alpha$.¹⁴ The semi axis n_β corresponds in this case to $n_{(2)}^0$ and is therefore fixed to the \mathbf{b} axis by the monoclinic symmetry. For a (100) sample, n_β coincides with one of the semi axes of the corresponding elliptic section. Consequently, the orientation of the elliptic section is fixed as long as the monoclinic symmetry is maintained. Two different polished $\sim 100 \mu\text{m}$ thin, plate-like (100) samples were investigated with a polarized-light microscope in zero magnetic field. Polariser and analyser of the microscope were adjusted parallel to the semi axes of the elliptic section of the optical indicatrix. Above $T_N \simeq 18.5 \text{ K}$, the orientation of the elliptic section was found to be fixed as expected for the monoclinic symmetry, but in the vicinity of T_N it started to rotate continuously about the $\mathbf{b} \times \mathbf{c}$ axis with decreasing temperature, which is schematically shown in figure 4.13 (a). At the experimental low-temperature limit $\simeq 4 \text{ K}$ the elliptical section was rotated by about 2° with respect to the \mathbf{b} axis, see figure 4.14. This result unambiguously proves that a symmetry-lowering phase transition from the monoclinic to the triclinic system occurs at 18.5 K in accordance to the results of the dielectric investigations, presented in section 4.3.2. The transition from the monoclinic to the triclinic system was additionally visualized by using the polarized-light microscope with the conoscopic technique for a (001)^e sample. For this sample orientation, one of the two optic axes of $\text{LiFeSi}_2\text{O}_6$ and the temperature evolution of its orientation could be observed, see figure 4.13 (b). The optic axes of $\text{LiFeSi}_2\text{O}_6$ are confined to the ac plane in the monoclinic phase because n_β corresponds to $n_{(2)}^0$. Above $T_N \simeq 18.5 \text{ K}$, the orientation of the optic axis only changed within the ac plane as expected for the monoclinic symmetry. Below T_N the orientation of the optic axis then shifted out of that plane, which is only possible for a triclinic symmetry.

¹⁴A short introduction to the linear optical properties of crystals is given in appendix C.

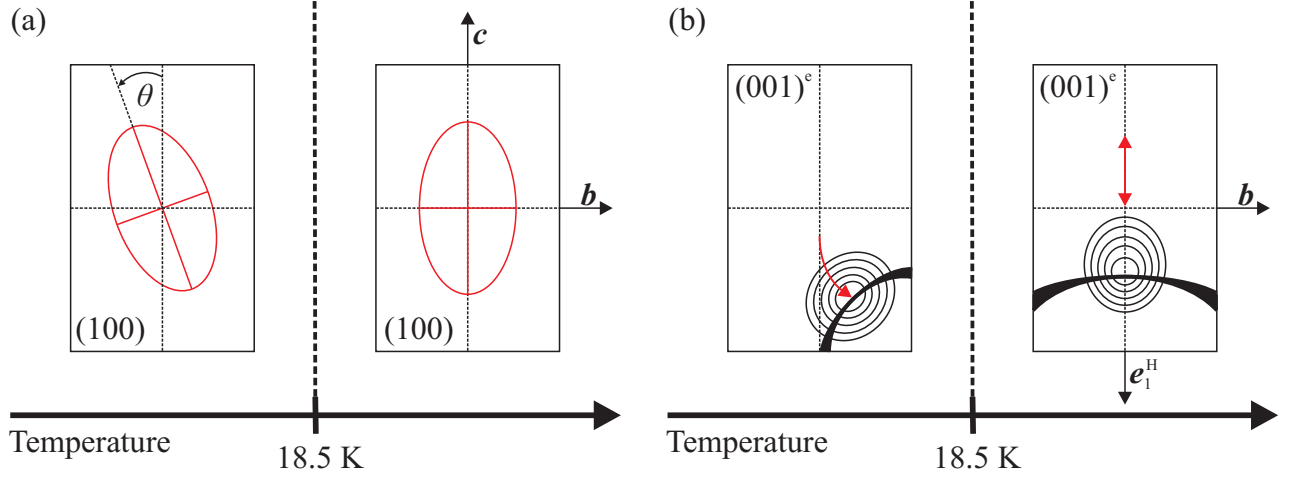


Figure 4.13: (a) Schematic picture of the elliptic section of the optical indicatrix in a plate-like (100) sample of $\text{LiFeSi}_2\text{O}_6$ below and above 18.5 K. (b) Schematic conoscopic interference picture of a (001)^e sample of $\text{LiFeSi}_2\text{O}_6$ with one of the optic axes below and above 18.5 K.

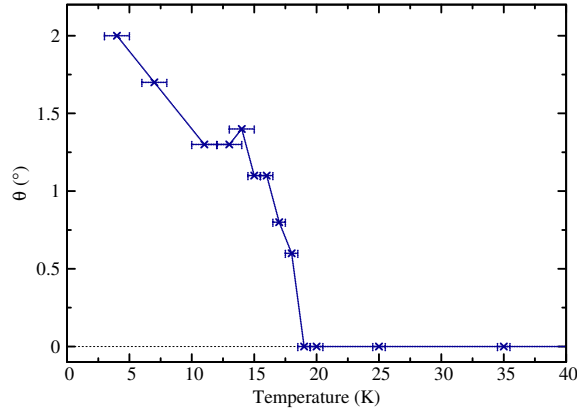


Figure 4.14: Temperature dependence of the rotation angle θ of the elliptic section of a plate-like (100) sample of $\text{LiFeSi}_2\text{O}_6$.

Summing up the results of the polarized-light microscopy and those of the dielectric investigations one can state that in zero magnetic field $\text{LiFeSi}_2\text{O}_6$ transforms from the monoclinic space group $P2_1/c1'$ to the triclinic one $P\bar{1}'$ at $T_N = 18.5$ K. Surprisingly, in none of the investigated samples ferroelastic domains could be observed below T_N , although $P2_1/c' \rightarrow P\bar{1}'$ is a ferroelastic phase transition. This indicates that in all cases only a single ferroelastic domain formed during the transition.

4.3.6 Thermal expansion and magnetostriction

As discussed in section 4.3.2, the component P_b of the magnetic-field induced electric polarization of $\text{LiFeSi}_2\text{O}_6$ shows an anomalous temperature dependence for a magnetic field parallel to c in the high-field regime above 6 T, see figure 4.4. In this high-field regime $P_b(T)$ is sharply suppressed at lower temperatures, which suggests the presence of a phase transition, that has not been reported

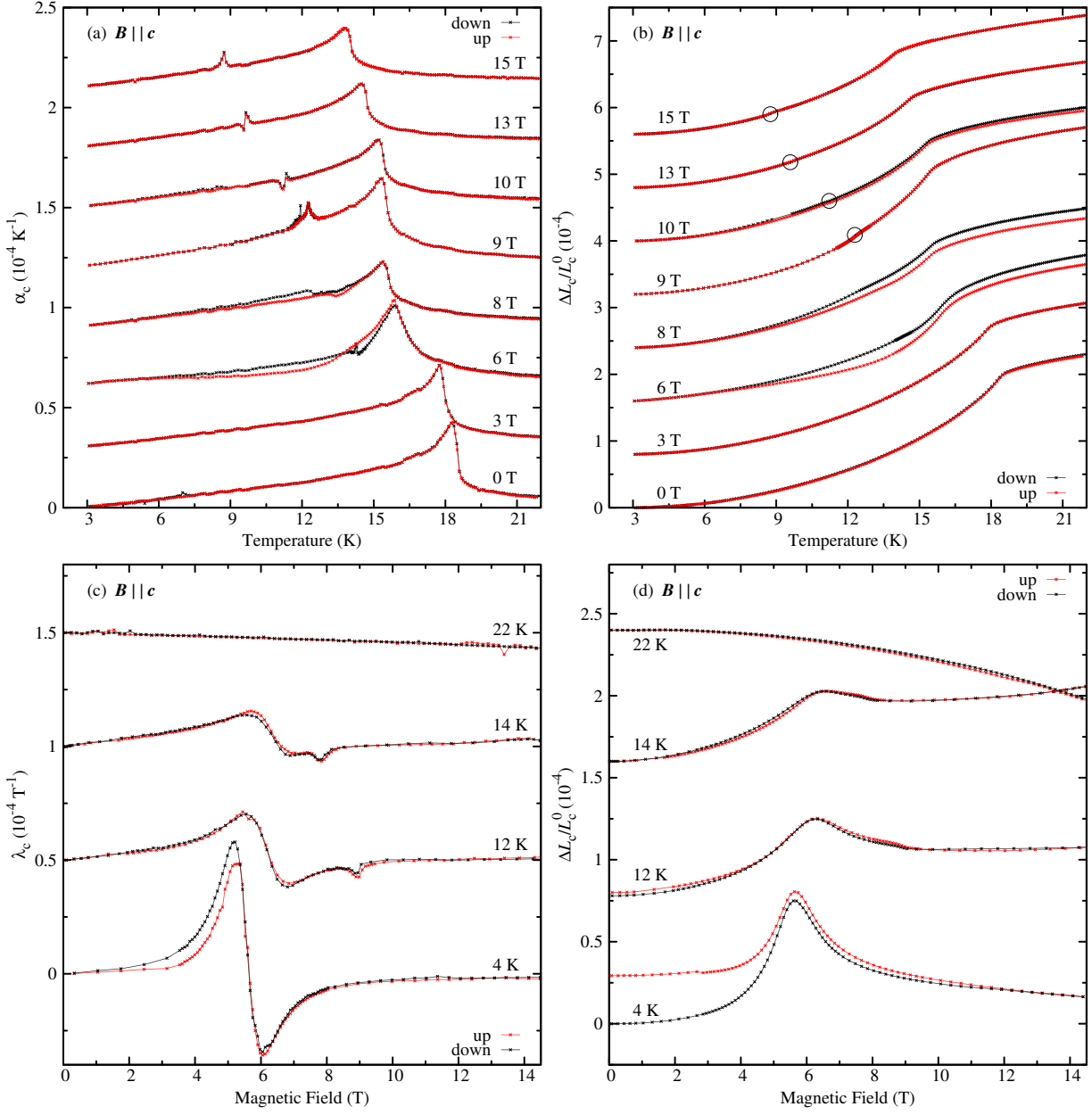


Figure 4.15: Longitudinal thermal expansion and magnetostriction of LiFeSi₂O₆ along the c direction for a magnetic field applied parallel to c . In (a) and (b), the temperature dependences of the thermal-expansion coefficient α_c and of the corresponding relative length changes $\Delta L_c/L_c^0$ are displayed for various magnetic-field strengths. The weak anomalies due to the new transition already observed during the dielectric investigations are well resolved in the α_c curves, but are hardly visible in the $\Delta L_c/L_c^0$ curves. Therefore, they are marked by open circles. In (c) and (d), the magnetic-field dependences of the magnetostriction coefficient λ_c and of the corresponding relative length changes $\Delta L_c/L_c^0$ are displayed for various temperatures. For clarity, the curves are shifted with respect to each other with increasing field strength and temperature, respectively, by constant offsets of $0.3 \times 10^{-4} \text{ K}^{-1}$ in (a), 0.8×10^{-4} in (b), $0.5 \times 10^{-4} \text{ T}^{-1}$ in (c) and 0.8×10^{-4} in (d).

in literature yet. Interestingly, it is not visible for the other components $P_{b \times c}(T)$ and $P_c(T)$. Also in the magnetization data presented in figure 4.3 (d) it could not be observed. However, anomalies were detected in the magnetic-field dependent data of the component ϵ_b^r of the dielectric tensor, which coincide with the suppression of $P_b(T)$, see figure 4.5, supporting the presence of the phase transition. In order to achieve a better understanding of the phase transition, detailed studies of the thermal expansion and of the magnetostriction for a magnetic field along c were performed. In a first series of measurements, the longitudinal thermal expansion along c and the longitudinal magnetostriction in the same direction were investigated.

The thermal-expansion measurements performed with increasing and decreasing temperature at constant magnetic fields are summarized in figure 4.15 (a) and (b). The transition at $T_N \simeq 18.5$ K in zero field causes an anomaly in the thermal-expansion data and shifts continuously towards lower temperatures with increasing field strength. In the vicinity of the spin-flop transition between 6-8 T a weak temperature hysteresis occurs. For even larger fields, the hysteresis disappears again and instead an additional anomaly arises, which is well resolved in the $\alpha_c(T)$ data, but hardly visible in the $\Delta L_c(T)/L_c^0$ curves.¹⁵ It can probably be attributed to the transition already found in the dielectric investigations. However, there is a systematic discrepancy of about 1 K between the dielectric and thermal-expansion data with respect to the transition temperature. In contrast, the onset of the antiferromagnetic order in $\text{LiFeSi}_2\text{O}_6$ is detected at the same temperature in the dielectric investigations and the thermal-expansion measurements. Therefore, the systematic temperature discrepancy of the new transition cannot be explained by the differences of applied cooling and heating rates or by the different thermometers used. At present, the origin of the temperature discrepancy has not been understood yet.

In figure 4.15 (c) and (d), the magnetostriction measurements performed with increasing and decreasing field strength at constant temperatures are summarized. For the lowest temperature $T = 4$ K, the magnetostriction curves show an anomaly around 6 T, which can be attributed to the spin-flop transition occurring in this field range. The corresponding length change $\Delta L_c/L_c^0$ is quite unusual, see figure 4.15 (d). One would expect that the spin-flop transition should cause either an elongation ($\Delta L > 0$) or a contraction ($\Delta L < 0$). Here, however, ΔL shows a local maximum at the spin-flop field.¹⁶ Additionally, there is a large discrepancy between the up and down measurement in this case. With increasing temperature the spin-flop field stays nearly constant and the local maxima of the corresponding length changes $\Delta L_c/L_c^0$ reduce. Besides, the discrepancy between the up and down measurement disappears. At 12 K a second anomaly occurs in the high-

¹⁵The corresponding temperatures are marked by open circles in the $\Delta L_c(T)/L_c^0$ curves.

¹⁶Different measurements in the course of the present work showed that samples of $\text{LiFeSi}_2\text{O}_6$ with the c axis parallel to the magnetic field tend to rotate away from that orientation in the vicinity of the spin-flop field. This rotation could cause an additional, apparent positive length change in the magnetostriction measurements in this field range.

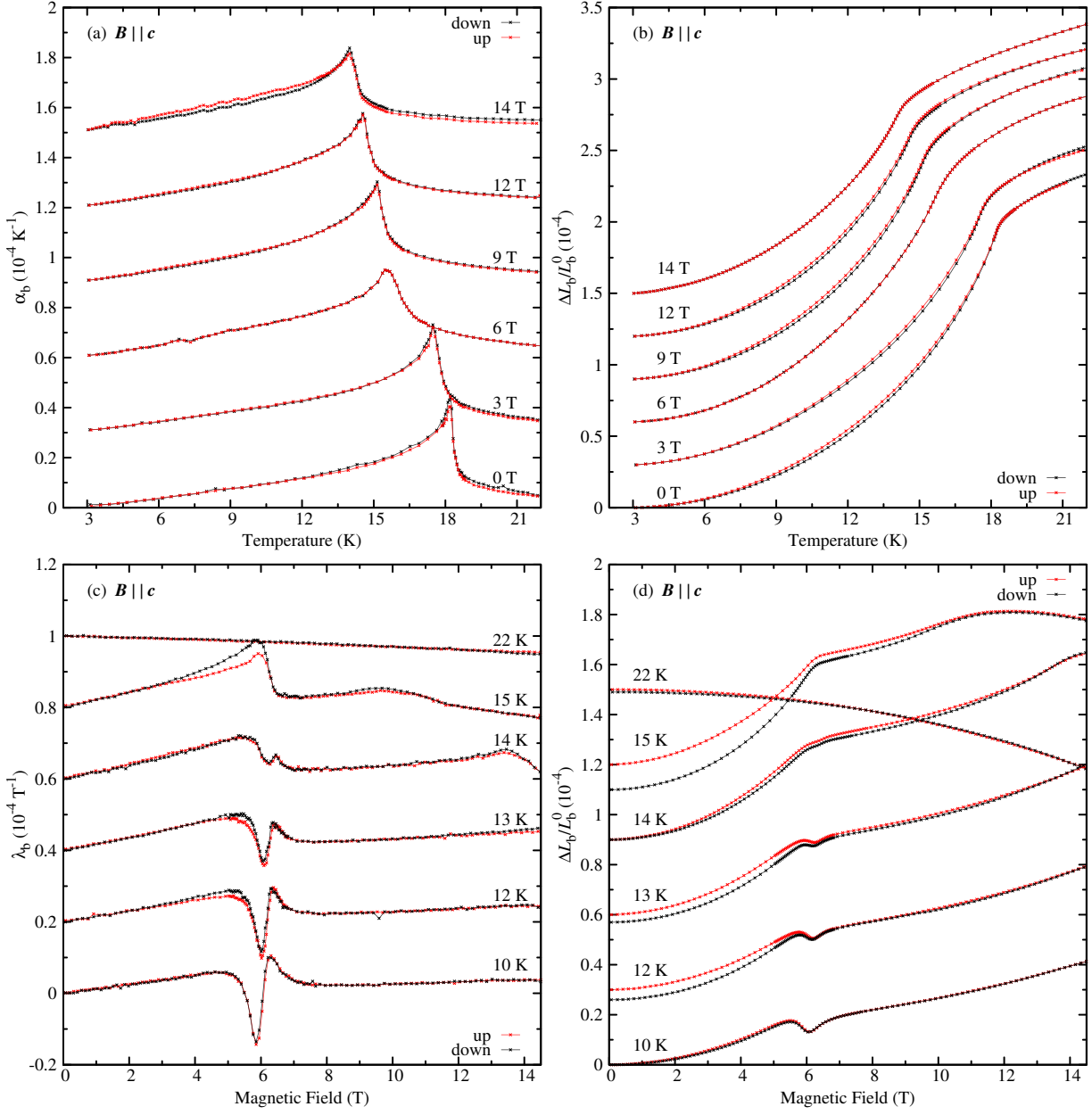


Figure 4.16: Transversal thermal expansion of LiFeSi₂O₆ along **b** for a magnetic field applied parallel to **c**. In (a), the temperature dependences of the thermal-expansion coefficient α_b and in (b) those of the corresponding relative length changes $\Delta L_b/L_b^0$ are displayed for different magnetic-field strengths. Only the transition in the antiferromagnetic phase of LiFeSi₂O₆ is visible. In (c) and (d), the magnetic-field dependences of the magnetostriction coefficient λ_b and of the corresponding relative length changes $\Delta L_c/L_c^0$ are displayed for various temperatures. For clarity, the curves are shifted with respect to each other with increasing field strength and temperature, respectively, by constant offsets of $0.3 \times 10^{-4} \text{ K}^{-1}$ in (a), (b) and (d) and $0.2 \times 10^{-4} \text{ T}^{-1}$ in (c).

field regime, which can probably be attributed to the new transition already found in the dielectric investigations. The systematic discrepancy between the dielectric and thermal-expansion data with

respect to the transition temperature mentioned above is also observed between the dielectric and magnetostriction data with respect to the transition field. The transition fields found in the magnetostriction data are systematically about 1 T lower than those observed in the dielectric data. Well above T_N at 22 K, no anomalies are observed in the magnetostriction curves as expected, see figure 4.15 (c) and (d). There, the magnetostriction depends quadratically over the entire field range on the magnetic-field strength, which is typical for materials with a linear field dependence of the magnetization. In conclusion, the results of the longitudinal thermal-expansion and magnetostriction measurements seem to confirm the presence of a novel phase transition in $\text{LiFeSi}_2\text{O}_6$ for an applied magnetic field $B > 6$ T along c . However, the origin of the observed discrepancies of the transition temperatures and transition fields found in the thermal-expansion and the magnetostriction measurements on the one hand and the dielectric investigations on the other hand has not been understood yet.

In the dielectric investigations the new transition could be only observed for a transversal field configuration, hence in the electric polarization component P_b and the component ϵ_b^r of the dielectric tensor for $\mathbf{B} \parallel \mathbf{c}$. Therefore, in a second series of measurements the transversal thermal expansion and magnetostriction along \mathbf{b} for a magnetic field applied parallel to \mathbf{c} was investigated. The thermal-expansion data in figure 4.16 (a) and (b) again show distinct anomalies below $T_N \simeq 18.5$ K coinciding with the transition to the antiferromagnetically ordered phase of $\text{LiFeSi}_2\text{O}_6$. Curiously, the second transition, which is visible in the longitudinal thermal-expansion data at higher magnetic fields, could not be detected in the transversal configuration of the thermal-expansion measurements. Also in the magnetostriction curves of the transversal configuration displayed in figure 4.16 (c) and (d) this transition is not visible. Only the spin-flop transition, which occurs around 6 T, is reflected by anomalies similar to those of the longitudinal configuration. Again the corresponding length changes $\Delta L_c/L_c^0$ are quite unusual, see figure 4.16 (d). Additionally, discrepancies occur between the up and down measurement at lower magnetic fields for 12 K, 13 K and 15 K. At 22 K the magnetostriction depends again quadratically on the magnetic-field strength over the entire field range, as expected.

4.3.7 Toroidal moment

As discussed in section 2.4, certain antiferromagnetic spin orders with head-to-tail arrangements of spins forming spin vortices can be described by a time and space antisymmetric, axio-polar vector quantity \mathbf{t} called the toroidal moment. All the magnetic point groups of spin arrangements, which allow a toroidal moment, are summarized in the tables 5 and 6 in appendix G. A toroidization oriented along the monoclinic \mathbf{b} axis with an absolute value of $T = 0.00025(3) \mu_B/\text{\AA}^2$ was calculated for $\text{LiFeSi}_2\text{O}_6$ in the framework of the monoclinic space group $P2_1/c'$ [138,204]. For this calculation, the centrosymmetric phase of $\text{LiFeSi}_2\text{O}_6$ above $\simeq 229$ K with the space group $C2/c$ served as

prototype phase. However, as discussed in the previous sections, the dielectric investigations and the observations with a polarized-light microscope in the present work reveal that the symmetry of the antiferromagnetic phase of LiFeSi₂O₆ is actually not monoclinic but triclinic with the space group $P\bar{1}$.¹⁷ Therefore, the toroidization will have components along all crystallographic axes. Although the deviation from the monoclinic symmetry will probably be small, the toroidization cannot be derived in the framework of the triclinic symmetry before the exact triclinic structure is known. The switching of the antiferromagnetic domains of LiFeSi₂O₆ via the linear magnetoelectric effect was investigated by a spherical neutron-polarization analysis for different combinations of electric and magnetic fields [138, 204]. In this context, the antiferromagnetic domain switching was interpreted as control of the corresponding toroidal domains. But as mentioned in section 2.4, the extension of Aizu's classification to ferroic phases, that allow a spontaneous toroidization, reveals that ferrotoroidic domains will always be identical with the corresponding antiferromagnetic domains [25, 136]. Therefore, the introduction of a toroidal moment in the case of LiFeSi₂O₆ is, at least at the macroscopic level, only an alternative way to describe the antiferromagnetic order. Thus, a possible distinction between the toroidal and the antiferromagnetic order as primary effect would require the search for differences on the microscopic scale.

4.3.8 Phase diagrams and conclusion

Based on the results of different neutron-diffraction studies, the monoclinic space group $P2_1/c'$ was proposed for the antiferromagnetic phase of LiFeSi₂O₆ in literature [204, 216]. In contradiction to this proposal, the results of the present investigations reveal that LiFeSi₂O₆ transforms at $T_N \simeq 18.5$ K from the monoclinic space group $P2_1/c1'$ actually to the triclinic one $P\bar{1}$. The reinvestigation of the magnetoelectric effect of LiFeSi₂O₆ proves that all components of the linear magnetoelectric tensor are present below $T_N \simeq 18.5$ K apart from the component α_{22} . The induced electric polarization components $P_{b \times c}^{B_b}$, $P_b^{B_{b \times c}}$, $P_b^{B_c}$ and $P_c^{B_b}$ are one or two orders of magnitude smaller than $P_{b \times c}^{B_{b \times c}}$, $P_c^{B_{b \times c}}$, $P_{b \times c}^{B_c}$ and $P_c^{B_c}$, which would be allowed already for a monoclinic symmetry. A detailed analysis of the parasitic currents generated by mismatched electrode areas shows the importance of well-matched electrodes, especially in the case of only small pyroelectric or magnetoelectric effects. A simple model for the description of parasitic pyroelectric currents could be derived. As discussed in the previous section, the antiferromagnetic spin structure of LiFeSi₂O₆ can be described in principle by the definition and calculation of a toroidization. On the macroscopic level this is, however, only an alternative way to describe the antiferromagnetic order. A discrimination of the toroidal and antiferromagnetic order would perhaps be possible on the microscopic scale.

¹⁷The space group $P\bar{1}$ allows the presence of a toroidal moment as well, see tables 5 and 6 in appendix G.

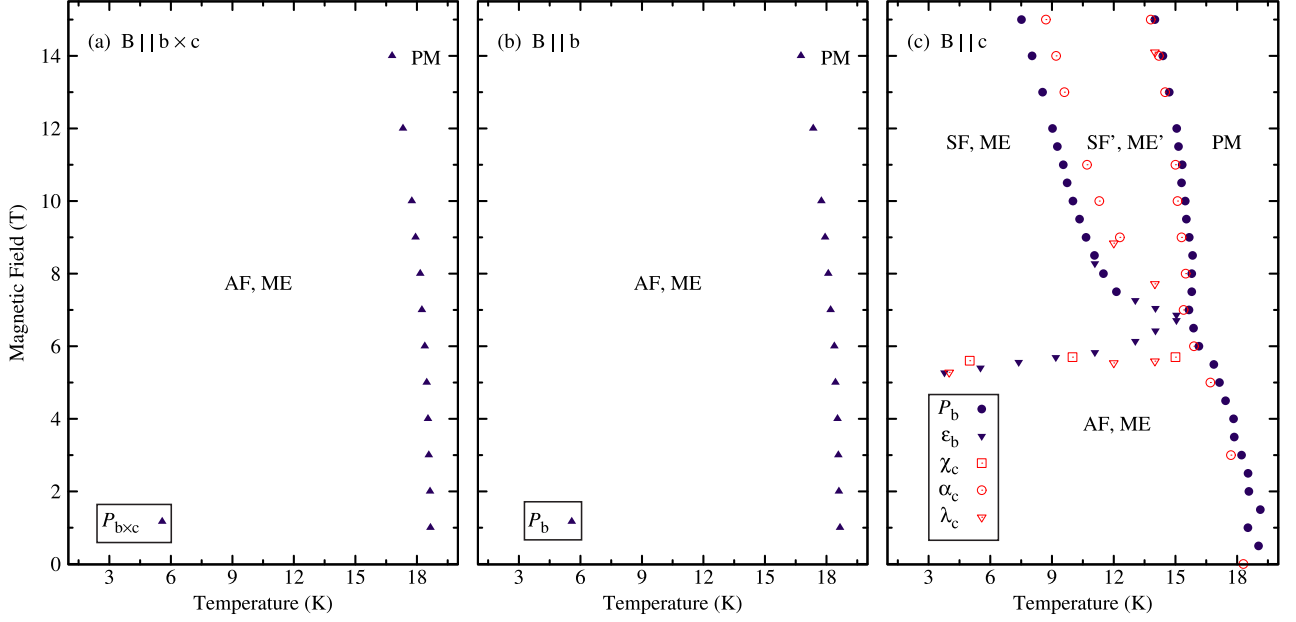


Figure 4.17: Magnetic-field versus temperature phase diagrams of $\text{LiFeSi}_2\text{O}_6$ for \mathbf{B} parallel to $\mathbf{b} \times \mathbf{c}$, \mathbf{b} or \mathbf{c} . The phase boundaries are based on the results of the dielectric investigations (P_b, ϵ_b^T), on the results of the thermal-expansion (α_c) and magnetostriction (λ_c) measurements and on the results of the magnetization measurements (χ_c).

By combining all the investigations of the present work, detailed magnetic field versus temperature phase diagrams could be derived for \mathbf{B} parallel to $\mathbf{b} \times \mathbf{c}$, \mathbf{b} and \mathbf{c} , see figure 4.17. On temperature decrease in zero magnetic field $\text{LiFeSi}_2\text{O}_6$ undergoes a phase transition at $T_N \simeq 18.5$ K from a paramagnetic monoclinic phase (PM) to an antiferromagnetically ordered triclinic and linear magnetoelectric phase (AF,ME). As shown in figure 4.17 (a) and (b), there is little influence of magnetic fields $\mathbf{B} \parallel \mathbf{b} \times \mathbf{c}$ or $\mathbf{B} \parallel \mathbf{b}$, which only cause a weak simultaneous decrease of the corresponding transition temperature $T_N(\mathbf{B})$. As expected for these field directions perpendicular to the magnetic easy axis, the magnetization linearly increases with the field, see figure 4.3, as well as the magnetic-field induced electric polarization ($P \propto B$), see figure 4.4.

A magnetic field applied along \mathbf{c} induces transitions to other magnetoelectric phases (SF,ME/SF',ME'), see figure 4.17 (c). With increasing field strength, a transition to a spin-flop phase (SF,ME) occurs at about 6 T in the low-temperature range, which extends up to the experimental magnetic high-field limit of 15 T. Curiously, towards higher temperatures above $\simeq 12$ K the course of the corresponding phase boundary, obtained from the dielectric investigations (in blue) systematically differs from that, obtained from the magnetostriction and magnetization measurements (in red). Below the spin-flop transition all components of the magnetic-field induced electric polarization increase linearly with increasing field strength. Above 6 T, the characteristics of the magnetic-field induced electric polarization changes. On temperature decrease in the

high-field regime between 7.5 T and 15 T, a further narrow magnetoelectric phase (SF',ME') occurs around 18 K with a temperature width of about 6 K, which has not been known in literature yet. Leaving that phase at lower temperatures causes a sharp suppression of the electric polarization component P_b , while the other two components are not affected, see figure 4.17 (c) and figure 4.4. This phase transition is also connected with distinct anomalies in the thermal-expansion and magnetostriction data, see figure 4.15. However, the exact course of the phase boundary, which separates the magnetoelectric phase (SF',ME') from the magnetoelectric phase (SF,ME), is not unique. The phase boundary based on the results of the dielectric investigations (in blue) is systematically shifted by about 1 K to lower temperatures with respect to that based on the results of the thermal-expansion/magnetostriction and magnetization measurements (in red). In addition, all phase boundaries, which are based on the dielectric investigations, seem to cross in one single point at about (16.5 K, 7.5 T). In contrast, considering only the phase boundaries based on the thermal-expansion/magnetostriction and magnetization measurements a small magnetic-field window between $\simeq 6$ T and $\simeq 8$ T seems to exist, where a direct transition from the paramagnetic (PM) to the spin-flop phase (SF,ME) takes place. The observed discrepancies of the phase boundaries in the phase diagram of LiFeSi₂O₆ for $B||c$ cannot be explained at the moment. Besides it is unclear, why the transition to the phase (SF',ME') could not be observed in the transverse thermal-expansion and magnetostriction measurements. Therefore, more investigations of the phase (SF',ME') are needed to clarify the open questions. In addition, the neutron-diffraction data of [204, 216] should be reanalysed in order to refine the nuclear and magnetic structure within the triclinic symmetry.

4.4 NaFeGe₂O₆

In the following, the measurements of the compound NaFeGe₂O₆ summarized in section 4.2 are presented, analysed and discussed in detail.

4.4.1 Magnetic properties

The temperature-dependent magnetic-susceptibility measurements of NaFeGe₂O₆ for magnetic fields up to 14 T (applied along the $b \times c$, b and c axis) are summarized in figures 4.18 (a)-(c).¹⁸ The low-field curves are consistent with previous results [12, 206, 207] and signal the onset of magnetic ordering at $T_N \simeq 13$ K proceeded by a second transition at $T_C \simeq 11.6$ K, where apparently a spin reorientation occurs. While $\chi_{b \times c}(T)$ shows a pronounced kink at T_N and subsequently decreases with decreasing temperature in the temperature interval $[T_C, T_N]$, $\chi_b(T)$ and $\chi_c(T)$ hardly change in this interval below T_N indicating that the spins are oriented at first mainly along the $b \times c$ axis,

¹⁸The magnetic measurements presented in this section were performed in a VSM magnetometer, see chapter 3.1.

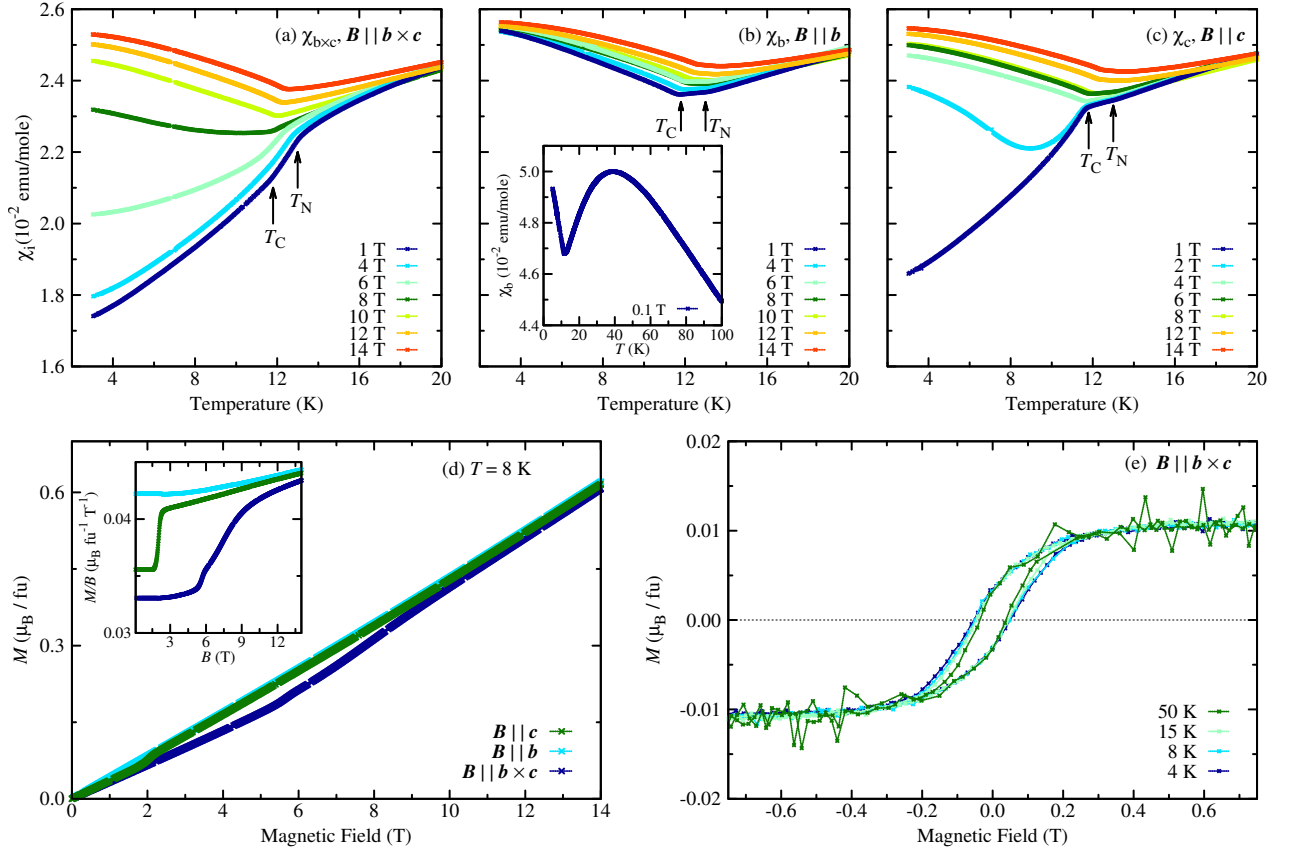


Figure 4.18: (a)-(c) Temperature dependences of the magnetic susceptibility $\chi_{b \times c}$, χ_b , and χ_c of $\text{NaFeGe}_2\text{O}_6$ for different magnetic fields. The inset in (b) shows χ_b , measured at 0.1 T in a wider temperature range. (d) Magnetization at 8 K as functions of the magnetic field applied parallel to $\mathbf{b} \times \mathbf{c}$, \mathbf{b} , and \mathbf{c} ; the inset shows M/B for all magnetic-field directions at the same temperature. (e) Observed hysteresis of the magnetization exemplified for $\mathbf{B} \parallel \mathbf{b} \times \mathbf{c}$ at different temperatures.

which thus forms a magnetic easy axis. At the second transition at $T_C \simeq 11.6$ K, the magnetic susceptibilities in all three directions show further kinks. Below the transition, $\chi_b(T)$ increases slightly with decreasing temperature whereas $\chi_{b \times c}(T)$ and $\chi_c(T)$ both decrease indicating that after the reorientation the spins are lying in the ac plane. The fact that $\chi_{b \times c}$ and χ_c of $\text{NaFeGe}_2\text{O}_6$ behave very similar and none of them approaches zero for $T \rightarrow 0$ K implies that there is no magnetic easy axis within the ac plane below T_C . Thus, the spins of $\text{NaFeGe}_2\text{O}_6$ show an XY anisotropy in the low-temperature regime with the ac plane as magnetic easy plane. This result is in accordance with two different neutron-diffraction studies, which revealed that the spin structure of $\text{NaFeGe}_2\text{O}_6$ forms an incommensurate cycloid within the ac plane below 5 K [205–207]. The magnetic structure between 11.6 K and 13 K has not been resolved yet. $\chi_b(T)$ is presented up to 100 K in the inset of figure 4.18 (b). At around 35 K, a broad maximum is visible indicating that the antiferromagnetic ordering in $\text{NaFeGe}_2\text{O}_6$ at $T_N \simeq 13$ K is preceded by low-dimensional magnetic correlations in agreement to [206].

Towards larger fields the decrease of both $\chi_{b \times c}(T)$ and $\chi_c(T)$ for $T < T_C$ systematically vanishes and finally above about 9 T the principal behaviour of $\chi_i(T)$ is almost identical for all three field directions, see figures 4.18 (a)-(c). This suggests that spin-flop transitions occur for either $\mathbf{B} \parallel \mathbf{b} \times \mathbf{c}$ or $\mathbf{B} \parallel \mathbf{c}$ with a change of the spin orientation from lying within the easy ac plane to lying within the plane that is perpendicular to the respective magnetic-field direction. These spin-flop transitions can also be seen in the low-temperature measurements of the magnetization as a function of the magnetic field, see figure 4.18 (d). The spin-flop fields are $\simeq 2$ T and $\simeq 5$ T at $T = 8$ K for $\mathbf{B} \parallel \mathbf{b} \times \mathbf{c}$ and $\mathbf{B} \parallel \mathbf{c}$, respectively. As will be seen in the following sections, the spin-flop transitions are related to structural changes and as well to reorientations of the electric polarization. The fact that the transition field is larger for $\mathbf{B} \parallel \mathbf{b} \times \mathbf{c}$ than for $\mathbf{B} \parallel \mathbf{c}$ and that the transition for $\mathbf{B} \parallel \mathbf{c}$ is much sharper illustrates that the magnetic properties of NaFeGe₂O₆ are not completely isotropic within the easy ac plane. Around 0 T, the magnetization $M(B)$ shows a hysteretic behaviour for all magnetic-field directions, which is exemplary illustrated in figure 4.18 (e) for $\mathbf{B} \parallel \mathbf{b} \times \mathbf{c}$ at different temperatures. It is present in a wide temperature range also well above the magnetic ordering temperature of NaFeGe₂O₆ and the widths of the hysteresis is nearly temperature independent. This indicates that the flux-grown NaFeGe₂O₆ crystals contain an impurity phase, probably maghemite γ -Fe₂O₃, which is ferrimagnetic. From the observed saturation magnetization of $0.01 \mu_B$ a contamination in the order of some 10^{-3} can be deduced. The magnetic-susceptibility and magnetization data in figure 4.18 is corrected by the ferromagnetic background.

4.4.2 Dielectric properties

Figure 4.19 summarizes the temperature-dependent measurements of the electric polarization $P_{b \times c}$, P_b and P_c of NaFeGe₂O₆ in magnetic fields applied along $\mathbf{b} \times \mathbf{c}$, \mathbf{b} and \mathbf{c} . The respective pyroelectric-current densities can be found in appendix E.2. The electric polarization was completely invertible by inverting the electric poling fields. In figure 4.19 one poling direction is displayed. NaFeGe₂O₆ becomes ferroelectric below $T_C \simeq 11.6$ K in zero magnetic field and develops a spontaneous electric polarization with the components $P_{b \times c} \simeq 27 \mu\text{C}/\text{m}^2$, $P_b \simeq 2 \mu\text{C}/\text{m}^2$ and $P_c \simeq 17 \mu\text{C}/\text{m}^2$ at 3 K. Thus, the spontaneous electric polarization has an absolute value of $\simeq 32 \mu\text{C}/\text{m}^2$ and is mainly lying within the ac plane with a small component along \mathbf{b} . It is about a factor of 2.5 larger than the spontaneous electric polarization of aegirine (Na_{1.04}Fe_{0.83}Ca_{0.04}Mn_{0.02}Al_{0.01}Ti_{0.08}Si₂O₆), the second known multiferroic compound within the pyroxene family [14, 15]. Assuming a point group symmetry $2/m$ (with cell setting unique axis \mathbf{b}) for the prototypic phase, see section 4.1, the crystallographic symmetry of the considered ferroelectric phase would be triclinic 1. The fact that the polarization is apparently not confined to the ac plane is inconsistent with the results of the magnetic investigations of the present work and with those reported in literature [205–207] if the standard theoretical model $\mathbf{P} \propto \mathbf{e}_{ij} \times (\mathbf{S}^{(i)} \times \mathbf{S}^{(j)})$

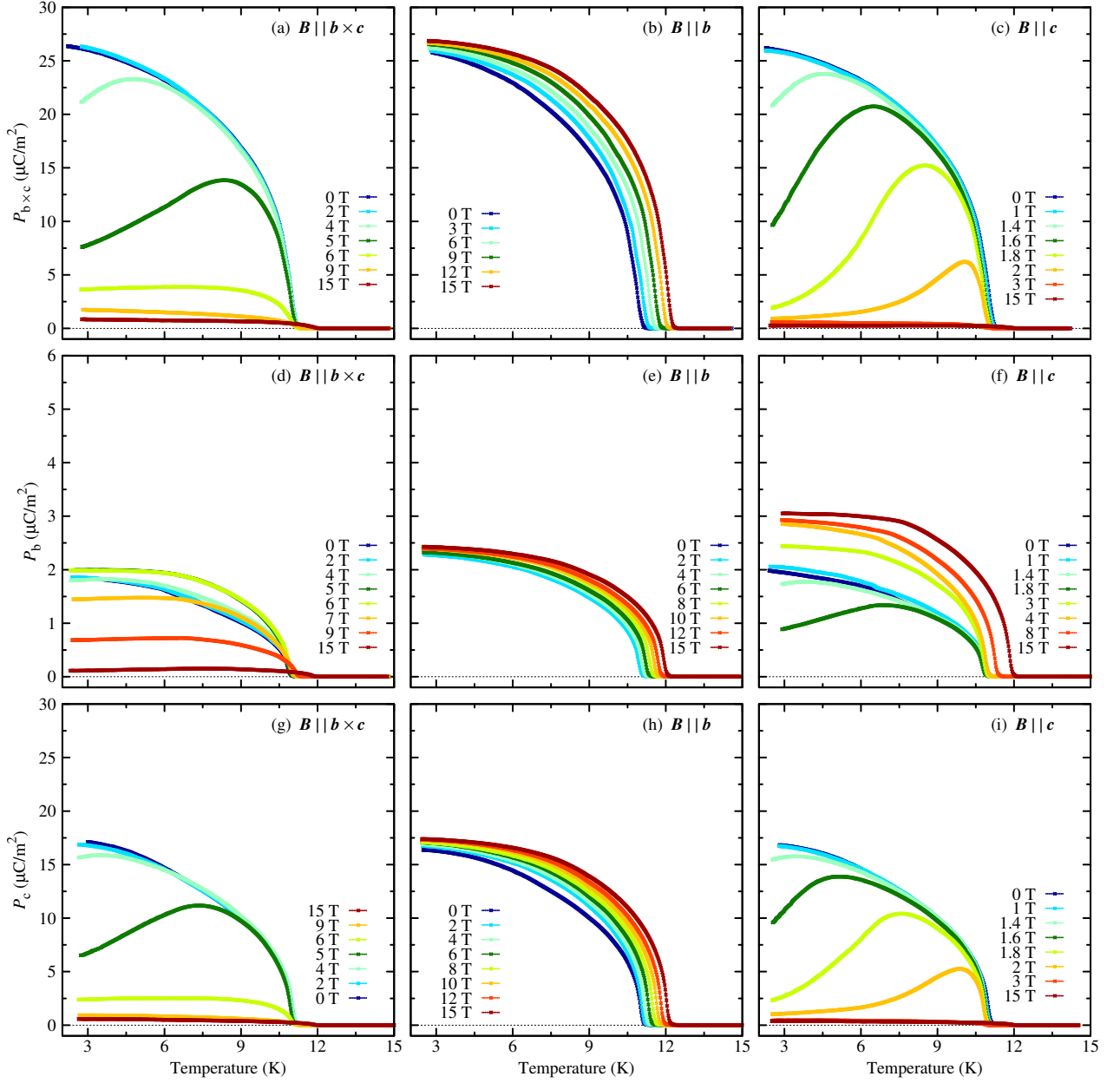


Figure 4.19: Temperature dependences of the electric polarization $P_{b \times c}$, P_b and P_c (top to bottom) of $\text{NaFeGe}_2\text{O}_6$ for magnetic fields applied parallel to the $b \times c$, b or c axis (left to right).

according to equation 2.9 for an electric polarization induced by a cycloidal spin structure is applied. Either the spins in the cycloidal phase of $\text{NaFeGe}_2\text{O}_6$ need to have a finite component along b , which was at least not excluded in [207], or the simple standard-theoretical model cannot be applied in this case. Another possible explanation for the observed inconsistency would be an erroneous sample orientation of the (010) sample. A deviation of 3.5° from (010) would explain the observed polarization of $\simeq 2 \mu\text{C}/\text{m}^2$ along b . However, this is unlikely because the electric

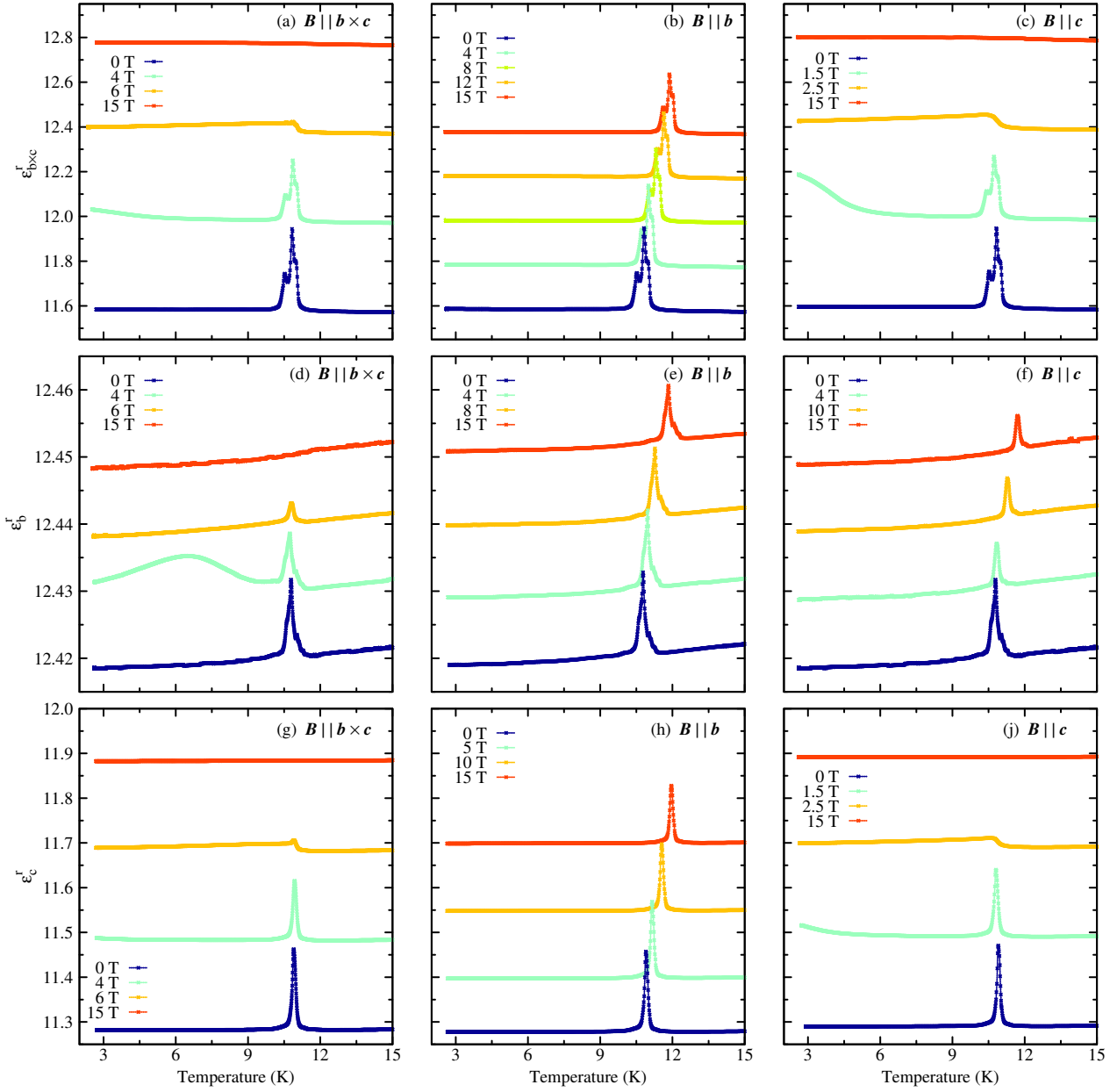


Figure 4.20: Representative temperature dependences of the longitudinal components of the dielectric tensor ϵ_i^r ($i = b \times c, b, c$ from top to bottom) of NaFeGe₂O₆ for different magnetic fields parallel to $b \times c$, b or c (from left to right). For clarity, the curves are shifted with respect to each other with increasing field strength by constant offsets of 0.01 in (d), (e) and (f), 0.15 in (h), 0.2 in (b), (g) and (j), 0.4 in (a) and (c).

polarization along b was examined on two different (010) samples, which revealed absolute values for P_b , that only differed by $0.2 \mu\text{C}/\text{m}^2$ from each other.

A magnetic field applied parallel to b causes a weak systematic increase of the transition temperature $T_C \simeq 11.6 \text{ K}$ and also slightly enlarges the magnitude of the electric polarization, but leaves its orientation almost unchanged. In contrast, magnetic fields applied either along $b \times c$ or c have a

much stronger influence on the electric polarization. Obviously, magnetic fields in both directions cause a strong suppression of both components $P_{b \times c}$ and P_c in the vicinity of the respective spin-flop fields $B_{\text{SF}} \simeq 5 \text{ T}$ or $B_{\text{SF}} \simeq 2 \text{ T}$. For $\mathbf{B} \parallel \mathbf{b} \times \mathbf{c}$, the component P_b is strongly suppressed in the high-field range as well. However, this suppression seems to be shifted to slightly larger magnetic fields compared to the other two components. In the vicinity of the spin-flop field for $\mathbf{B} \parallel \mathbf{c}$, the component P_b is first slightly suppressed as well, but then grows with increasing field up to a maximum value of $P_b \simeq 3 \mu\text{C}/\text{m}^2$ at 15 T. In summary, the magnetic-field dependent (re-)orientations of the electric polarization of $\text{NaFeGe}_2\text{O}_6$ can be described as follows: In zero magnetic field the spontaneous electric polarization is mainly lying within the ac plane with a small component along b . A magnetic field applied along $\mathbf{b} \times \mathbf{c}$ causes a strong suppression of all polarization components above $B_{\text{SF}} \simeq 5 \text{ T}$. For a magnetic field along \mathbf{c} , the polarization is rotated towards the \mathbf{b} axis in the vicinity of $B_{\text{SF}} \simeq 2 \text{ T}$. This rotation is accompanied by a strong decrease of the polarization by about 90%. A magnetic field along \mathbf{b} do not cause any reorientation of the electric polarization. The transitions to the ferroelectric phase also cause distinct anomalies in the temperature dependences of the corresponding longitudinal components ϵ_i^r of the dielectric tensor. This is shown in figure 4.20, which displays representative measurements of the temperature dependences of ϵ_i^r ($i = b \times c, b, c$). Below the spin-flop transitions all components ϵ_i^r show spiky anomalies in the temperature range between 9 K and 12 K. For $\mathbf{B} \parallel \mathbf{b} \times \mathbf{c}$, the anomalies of all components ϵ_i^r essentially vanish above $B_{\text{SF}} \simeq 5 \text{ T}$. For $\mathbf{B} \parallel \mathbf{c}$, the anomalies of $\epsilon_{b \times c}^r$ and ϵ_c^r vanish above $B_{\text{SF}} \simeq 2 \text{ T}$ as well, while those of ϵ_b^r stay present in the whole magnetic-field range. For $\mathbf{B} \parallel \mathbf{b}$ finally, the spiky anomalies of all components ϵ_i^r are present in the whole magnetic-field range. Interestingly, the anomalies of $\epsilon_{b \times c}^r$ have two maxima. An explanation for that behaviour is, however, still missing. From the data of the dielectric constants together with the polarization data above, it can be concluded that the spikes signal the corresponding transition temperatures to the ferroelectric phase with a spontaneous polarization lying either mainly within the ac plane or being oriented nearly along the \mathbf{b} axis.

4.4.3 Thermal expansion and magnetostriction

In order to map out the temperature versus magnetic-field phase diagrams of $\text{NaFeGe}_2\text{O}_6$ thermal-expansion and magnetostriction measurements along \mathbf{c} for magnetic fields applied parallel to $\mathbf{b} \times \mathbf{c}$, \mathbf{b} or \mathbf{c} were performed. Figure 4.21 displays a representative selection of $\alpha_c(T) = 1/L_c^0 \cdot \partial \Delta L_c / \partial T$ curves measured as a function of increasing or decreasing temperature at constant magnetic fields. Magnetic fields applied either along \mathbf{b} or \mathbf{c} have only little influence. In both cases the two transitions occurring at $T_N \simeq 13 \text{ K}$ and $T_C \simeq 11.6 \text{ K}$ in zero field are just continuously shifted towards higher temperatures with increasing field. Interestingly, the anomaly at $T_C \simeq 11.6 \text{ K}$ grows in intensity with increasing magnetic fields compared to the first anomaly

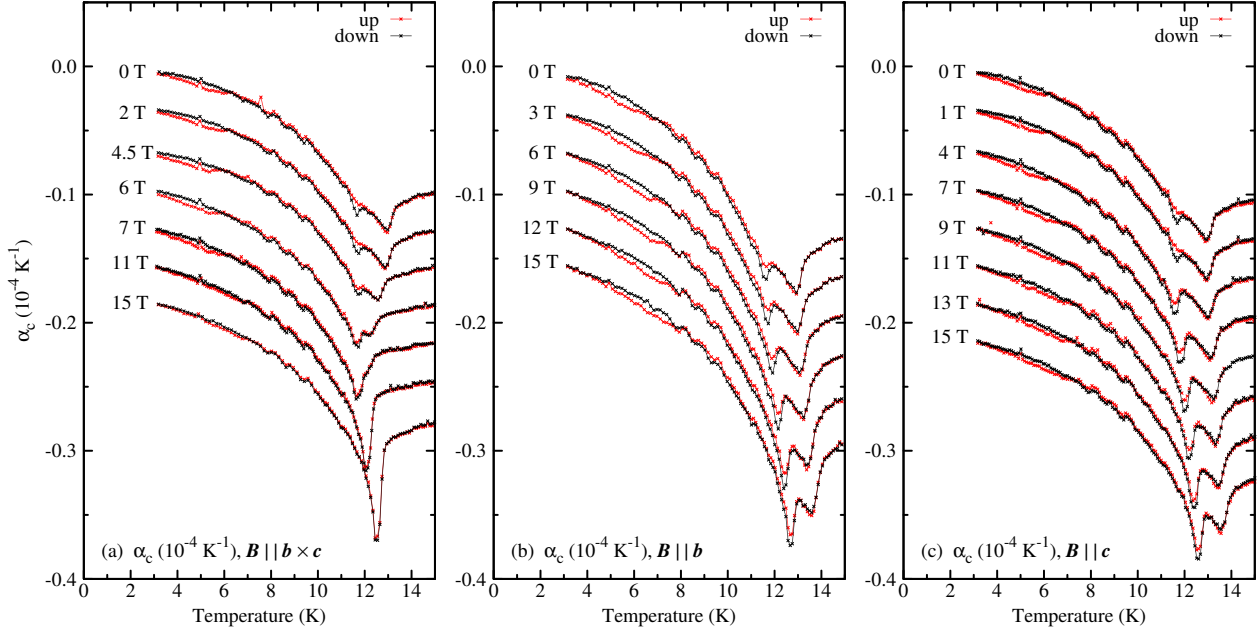


Figure 4.21: Thermal expansion of NaFeGe₂O₆ along c for magnetic fields applied parallel to $\mathbf{b} \times \mathbf{c}$, \mathbf{b} or \mathbf{c} . For clarity, the curves are shifted with respect to each other with increasing field strengths by constant offsets of $0.03 \cdot 10^{-4} \text{ K}^{-1}$ in (a), (b) and (c). Measurements with increasing and decreasing temperature are plotted as red and black symbols, respectively.

at $T_N \simeq 13 \text{ K}$. The two transitions occurring at T_N and T_C in zero field for $\mathbf{B} \parallel \mathbf{b} \times \mathbf{c}$ converge with increasing field strength until above 7 T only one transition remains, see figure 4.21 (a). The corresponding anomaly gets stronger with further increasing magnetic field.

Figure 4.22 summarizes representative magnetostriction measurements along c for magnetic fields parallel to $\mathbf{b} \times \mathbf{c}$, \mathbf{b} or \mathbf{c} , respectively. In this case, the relative length changes $\Delta L_c(T_0, \mathbf{B})/L_c^0$ for the three magnetic-field directions are displayed. Note that although most of the data have been studied up to a maximum field of 15 T, the field scales of figure 4.22 have been limited to 10 T because there are no further anomalies at higher fields. For $\mathbf{B} \parallel \mathbf{b}$, there is a quadratic magnetostriction ($\Delta L_b/L_b^0 \propto B^2$) in the entire field range, see figure 4.22 (b), which is typical for materials with a linear field dependence of the magnetization. For $\mathbf{B} \parallel \mathbf{c}$, the corresponding spin-flop transition around $B_{\text{SF}} \simeq 2 \text{ T}$ coincides with positive, almost discontinuous length changes of $\Delta L_c/L_c^0$ indicating that the spin-flop transition is of first-order. With increasing temperature, the transition shifts towards higher magnetic-field strength and the intensity of the length changes decrease. For $\mathbf{B} \parallel \mathbf{b} \times \mathbf{c}$, there is a phase transition with a blurred, positive length change $\Delta L_c/L_c^0$ at 3 K, which again coincides with the corresponding spin-flop transition at $B_{\text{SF}} \simeq 5 \text{ T}$, see figures 4.22 (b) and 4.18. Already the magnetization as well as the electric polarization data indicated that the spin-flop transition for this field direction is not very sharp. There is a slight discrepancy between the up and the down measurements. With increasing temperature the transition shifts

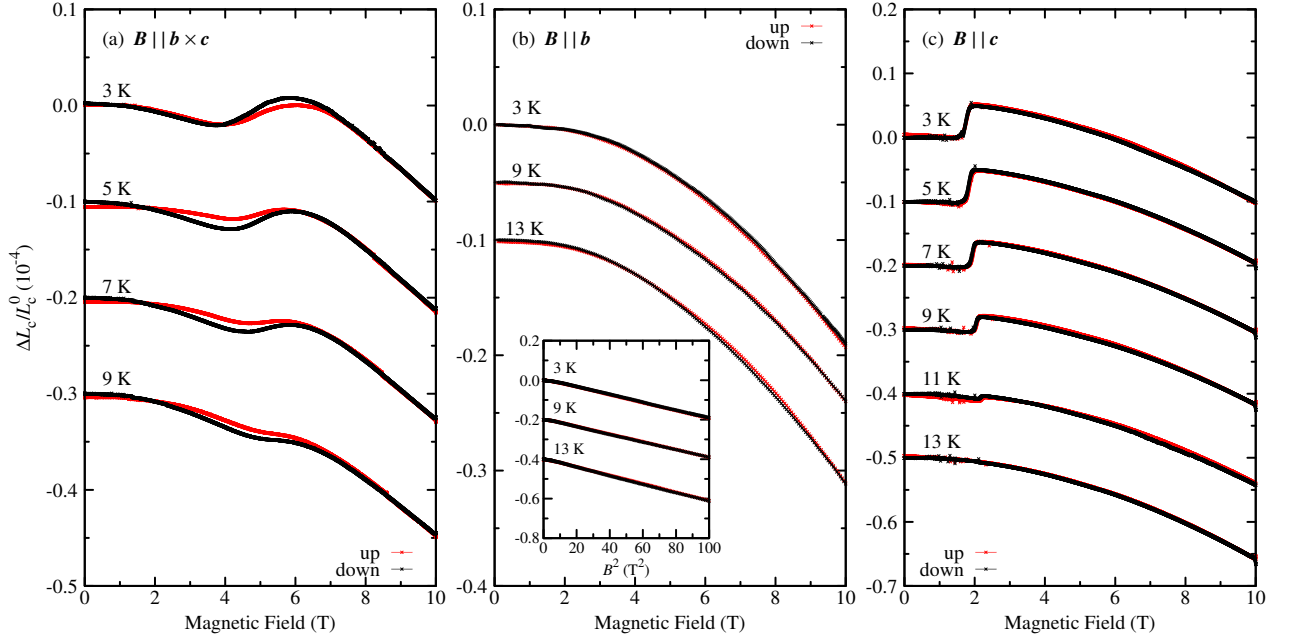


Figure 4.22: Magnetostriction of $\text{NaFeGe}_2\text{O}_6$ along c for magnetic fields applied parallel to $b \times c$, b or c . For clarity, the curves are shifted with respect to each other with increasing temperature by constant offsets of $0.1 \cdot 10^{-4}$ in (a), (b) and (c). Measurements with increasing and decreasing magnetic field are plotted as red and black symbols, respectively.

towards higher magnetic fields and the corresponding length changes decrease in intensity.

4.4.4 Phase diagrams and conclusion

By combining all the investigations of the present work, detailed magnetic-field versus temperature phase diagrams are derived for B parallel to $b \times c$, b and c , see figure 4.23. The critical fields and temperatures are based on the anomalies in $\Delta L_c(T, B)/L_c^0$ from the thermal-expansion and magnetostriction measurements, while the dielectric and magnetic properties of the various phases are inferred from the electric-polarization and magnetization data. The polarization and magnetization measurements show anomalies for most of the detected phase transitions as well and their positions agree within the experimental uncertainties with the anomalies of $\Delta L_c(T, B)/L_c^0$. On temperature decrease, $\text{NaFeGe}_2\text{O}_6$ undergoes a phase transition at $T_N \simeq 13$ K in zero magnetic field from its paramagnetic and non-ferroelectric phase to an antiferromagnetically ordered, non-ferroelectric phase. The magnetic-susceptibility measurements indicate a collinear spin structure with the spins being oriented mainly along the $b \times c$ axis in this phase, see figure 4.18. On further cooling, a spin reorientation occurs at $T_C \simeq 11.6$ K leading to an XY anisotropy and to the onset of ferroelectricity. The ferroelectric phase extends down to the experimental low-temperature limit of 2.5 K. The spontaneous polarization of this ferroelectric phase I has an absolute value of $\simeq 32 \mu\text{C}/\text{m}^2$ and is mainly lying within the ac plane with a small component along b . Based

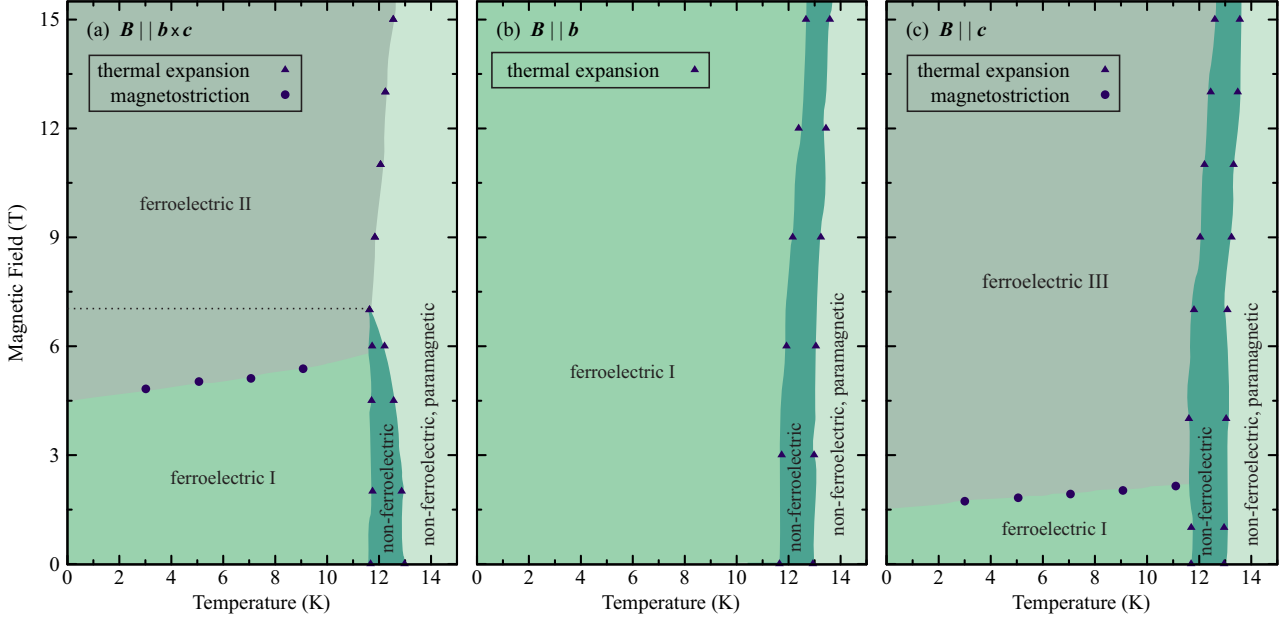


Figure 4.23: Magnetic-field versus temperature phase diagrams of NaFeGe₂O₆ for \mathbf{B} parallel to $\mathbf{b} \times \mathbf{c}$, \mathbf{b} or \mathbf{c} . The phase boundaries are based on the thermal-expansion (α_c) and magnetostriction (λ_c) measurements.

on two different neutron-diffraction studies, a cycloidal spin structure with the spins lying within the ac plane characterized by two inconsistent propagation vectors of $\mathbf{k} = (0.3357, 0, 0.0814)$ or $\mathbf{k}' = (0.323, 1.0, 0.080)$ was proposed for that phase [205–207].

Compared to aegirine (Na_{1.04}Fe_{0.83}Ca_{0.04}Mn_{0.02}Al_{0.01}Ti_{0.08}Si₂O₆) the second multiferroic compound among the pyroxenes, there are some clear differences in NaFeGe₂O₆. First of all, the spin structure of the multiferroic phase of aegirine forms a spiral with a propagation vector along the monoclinic \mathbf{b} axis [204]. In contrast, in the multiferroic phase of NaFeGe₂O₆ the spins apparently form a cycloid within the ac plane [205–207]. Secondly, the presence of all three components of the electric polarization in NaFeGe₂O₆ indicate a triclinic symmetry 1 for its multiferroic phase. The symmetry of the multiferroic phase of aegirine is monoclinic 2. Finally, the electric polarization of NaFeGe₂O₆ is about a factor of 2.5 larger than the spontaneous electric polarization of aegirine.

As shown in figure 4.23 (b), there is little influence of a magnetic field $\mathbf{B} \parallel \mathbf{b}$, which only causes a weak simultaneous increase of both transition temperatures $T_C(\mathbf{B})$ and $T_N(\mathbf{B})$. As expected for this field direction perpendicular to the magnetic easy plane, the magnetization linearly increases with field, see figure 4.18. Moreover, a weak increase of the electric polarization can be inferred from figures 4.19 (b), (e) and (h).

Magnetic fields applied either along $\mathbf{b} \times \mathbf{c}$ or \mathbf{c} induce transitions, which are accompanied by strong modifications of the electric polarization. In the vicinity of the spin-flop transition at $B_{\text{SF}} \simeq 5$ T

for $\mathbf{B} \parallel \mathbf{b} \times \mathbf{c}$ the electric polarization is continuously suppressed with increasing magnetic-field strength. Interestingly, the suppression of P_b starts at a slightly higher field strength around 7 T as that of the other two components. In the vicinity of that field strength also the intermediate antiferromagnetically ordered, non-ferroelectric phase vanishes, which is illustrated by the horizontal dashed line in figure 4.23 (a). At the experimental high-field limit of 15 T the polarization amounts to $\simeq 1 \mu C/m^2$. For $\mathbf{B} \parallel \mathbf{c}$, only the electric polarization within the ac plane is continuously suppressed in the vicinity of the corresponding spin-flop transition at $B_{SF} \simeq 2$ T, while the polarization along \mathbf{b} slightly grows with increasing field strength. Thus, the electric polarization is rotated by nearly 90° from mainly lying within the ac plane towards an orientation pointing nearly along \mathbf{b} for that field direction. This rotation is accompanied by a strong decrease of the polarization by about one order of magnitude. The intermediate antiferromagnetically ordered, non-ferroelectric phase stays present for the whole investigated magnetic-field range. The general orientation of the electric polarization found in this work indicates the presence of a more complex spin structure as reported in [205–207] with a finite spin component along \mathbf{b} within the ferroelectric phase I. In order to clarify the microscopic mechanisms leading to multiferroicity in $NaFeGe_2O_6$ and in order to resolve the inconsistencies discussed above, more detailed information about the magnetic structure are needed. Therefore, as a future task neutron-diffraction experiments should be performed on single crystals of $NaFeGe_2O_6$.

Chapter 5

The erythrosiderite-type family

$A_2[\text{FeCl}_5(\text{H}_2\text{O})]$ ($A = \text{K, Rb, Cs, NH}_4$)

5.1 Introduction

The family of erythrosiderite-type compounds $A_2[\text{FeCl}_5(\text{H}_2\text{O})]$, where A stands for an alkali metal or ammonium ion, forms a series of antiferromagnets with Néel temperatures ranging from 6 K to 15 K [172]. The room-temperature crystal structures of $A_2[\text{FeCl}_5(\text{H}_2\text{O})]$ are orthorhombic with the space group $Pnma$ for $A = (\text{NH}_4)$, K, Rb and $Cmcm$ for $A = \text{Cs}$, respectively [173–179]. Both structure types are closely related but not isomorphic, see figures 5.1 (a) and (b). In both cases the structure consists of isolated A^+ units and isolated complex groups $[\text{FeCl}_5(\text{H}_2\text{O})]^{2-}$ of sixfold octahedrally coordinated iron(III). The unit cells contain eight symmetrically equivalent A^+ cations and four $[\text{FeCl}_5(\text{H}_2\text{O})]^{2-}$ octahedra. Besides ionic bonds between the structural building blocks, there is a H-bonding (via O–H–Cl) between neighbouring $[\text{FeCl}_5(\text{H}_2\text{O})]^{2-}$ octahedra, which further stabilizes the crystal structures. These H-bonded octahedra form zigzag chains, which run along b for $A = (\text{NH}_4)$, K, Rb or along c for $A = \text{Cs}$. Along these chains the Fe–O bonds of adjacent octahedra are oriented mutually antiparallel to each other [176, 177, 180]. For $A = (\text{NH}_4)$, K, Rb, the Fe–O bonds of the octahedra are approximately lying parallel to the ac plane with alternating angles in the order of $\pm 40^\circ$ relative to the a axis. For $A = \text{Cs}$, these bonds are oriented parallel to b . Taking the zigzag chains as the dominant feature of the two crystal-structure types, the axes $\{a, b, c\}$ in the $Pnma$ structure corresponds to the axes $\{b, c, a\}$ in the $Cmcm$ structure, see figures 5.1 (a) and (b). The lattice constants are summarized in table 5.1.

The magnetic ordering phenomena in the $A_2[\text{FeCl}_5(\text{H}_2\text{O})]$ series have been subject of various investigations in the past. In this context, Néel temperatures ranging from 6 K to 15 K have been derived from measurements of the magnetic susceptibility [176, 180], see table 5.1. There are

5.1 Introduction

crystal:	$(\text{NH}_4)_2[\text{FeCl}_5(\text{H}_2\text{O})]$	$\text{K}_2[\text{FeCl}_5(\text{H}_2\text{O})]$	$\text{Rb}_2[\text{FeCl}_5(\text{H}_2\text{O})]$	$\text{Cs}_2[\text{FeCl}_5(\text{H}_2\text{O})]$
a (Å):	13.706	13.75	13.825	7.426
b (Å):	9.924	9.92	9.918	17.306
c (Å):	7.024	6.93	7.100	8.064
Ref.:	[175]	[173]	[176]	[177]
T_N (K):	7.25	14.06	10.05	6.5
Ref.:	[180]	[180]	[176]	[176]

Table 5.1: Room-temperature lattice constants and Néel temperatures of $A_2[\text{FeCl}_5(\text{H}_2\text{O})]$ with $A = (\text{NH}_4)$, K, Rb, Cs.

some clear differences between $(\text{NH}_4)_2[\text{FeCl}_5(\text{H}_2\text{O})]$ and the corresponding alkali-based compounds with $A = \text{K}, \text{Rb}, \text{Cs}$. Susceptibility data of the alkali-based compounds identify the \mathbf{a} axis as the magnetic easy axis, while no easy axis can be derived from the susceptibility data of $(\text{NH}_4)_2[\text{FeCl}_5(\text{H}_2\text{O})]$ [176, 180]. Moreover, heat-capacity measurements reveal a second phase transition at $T_C \simeq 6.87$ K for $(\text{NH}_4)_2[\text{FeCl}_5(\text{H}_2\text{O})]$ [180]. In contrast, for the alkali-based compounds only single transitions are reported [180, 181]. These observations led to the suggestion of a canted antiferromagnetic spin structure for $(\text{NH}_4)_2[\text{FeCl}_5(\text{H}_2\text{O})]$ with some kind of spin rearrangement at 6.87 K. Later on, there was some debate about the proposed spin canting and the occurrence of a structural phase transition around 240 K was suggested [182, 183]. However, no evidence for such a structural transition has been found in Mössbauer spectroscopy and powder X-ray diffraction experiments within the relevant temperature range [184]. The Mössbauer spectra also led to the suggestion of a more complex spin arrangement in $(\text{NH}_4)_2[\text{FeCl}_5(\text{H}_2\text{O})]$ because the interpretation of the spectra below T_N was inconsistent with a simple canted spin structure [184]. A determination of the magnetic structure of $(\text{NH}_4)_2[\text{FeCl}_5(\text{H}_2\text{O})]$ is still missing. In contrast, the magnetic structures of the alkali-based compounds with $A = \text{K}, \text{Rb}$ were determined via neutron scattering [185, 186]. The antiferromagnetically ordered phases of both compounds are described by the magnetic space group $Pn'm'a'$. The spin direction alternates between $\pm\mathbf{a}$ along the zigzag chains of the $[\text{FeCl}_5(\text{H}_2\text{O})]^{2-}$ octahedra running along \mathbf{b} and the spins of neighbouring chains are in phase. The magnetic structure is illustrated, in figure 5.1 (c), where the spins in two planes at $y = 0.25\mathbf{b}$ (grey octahedra) and $y = 0.75\mathbf{b}$ (yellow octahedra) are displayed and the five most relevant magnetic-exchange interaction paths $J_1 - J_5$ are sketched [185, 186]. These magnetic-exchange interactions are also important for the ammonium-based compound $(\text{NH}_4)_2[\text{FeCl}_5(\text{H}_2\text{O})]$ because its crystal structure is isomorphic to those of $\text{K}_2[\text{FeCl}_5(\text{H}_2\text{O})]$ and $\text{Rb}_2[\text{FeCl}_5(\text{H}_2\text{O})]$.

The J_1 -exchange interaction runs along the H-bonded zigzag chains of $[\text{FeCl}_5(\text{H}_2\text{O})]^{2-}$ octahedra parallel to \mathbf{b} via super-exchange paths $\text{Fe}-\text{O}-\text{H} \cdots \text{Cl}-\text{Fe}$. In addition to this intrachain-exchange interaction J_1 , there are four other interchain-exchange interactions $J_2 - J_5$. The interchain-exchange interactions J_2 and J_3 connect iron ions of $[\text{FeCl}_5(\text{H}_2\text{O})]^{2-}$ octahedra in different \mathbf{b}

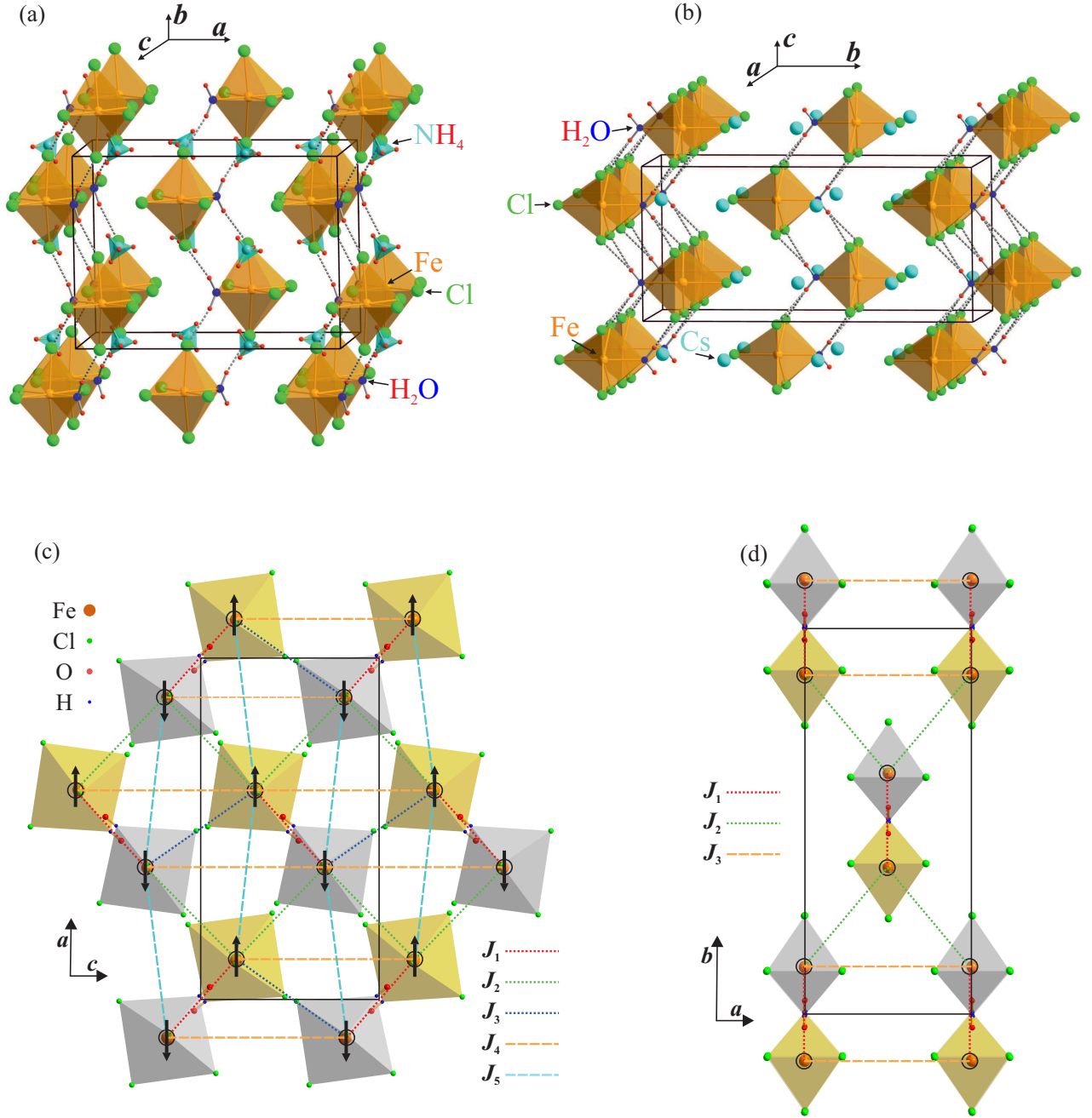


Figure 5.1: Room-temperature crystal structures of (a) $(\text{NH}_4)_2[\text{FeCl}_5(\text{H}_2\text{O})]$ and (b) $\text{Cs}_2[\text{FeCl}_5(\text{H}_2\text{O})]$. The crystal structures of $A_2[\text{FeCl}_5(\text{H}_2\text{O})]$ with $A = (\text{NH}_4), \text{K}, \text{Rb}$ are isomorphic. (c) Magnetic-exchange interaction paths and spin arrangement of $\text{K}_2[\text{FeCl}_5(\text{H}_2\text{O})]$ and $\text{Rb}_2[\text{FeCl}_5(\text{H}_2\text{O})]$ [185, 186]. The exchange-interaction paths for $(\text{NH}_4)_2[\text{FeCl}_5(\text{H}_2\text{O})]$ are the same. (c) Magnetic-exchange interaction paths of $\text{Cs}_2[\text{FeCl}_5(\text{H}_2\text{O})]$ [189].

planes via super-exchange paths $\text{Fe}-\text{Cl} \cdots \text{Cl}-\text{Fe}$, while the interchain-exchange interactions J_4 and J_5 connect iron ions of $[\text{FeCl}_5(\text{H}_2\text{O})]^{2-}$ octahedra within the same b plane via the super-exchange paths $\text{Fe}-\text{Cl} \cdots \text{Cl}-\text{Fe}$ and $\text{Fe}-\text{O} \cdots \text{Cl}-\text{Fe}$. For $\text{K}_2[\text{FeCl}_5(\text{D}_2\text{O})]$, fits to measured magnon

dispersion curves revealed for the exchange-interaction constants $J_1 \simeq -1.55$ K, $J_2 \simeq -0.71$ K, $J_3 \simeq -0.16$ K, $J_4 \simeq -0.24$ K and $J_5 \simeq -0.28$ K [186]. The intrachain-exchange interaction J_1 is the strongest one and all magnetic-exchange interactions are antiferromagnetic. This gives rise to a frustration potential, since J_4 and J_5 would favour antiferromagnetic order within the b planes, but cannot compete against the other three exchange interactions. Another interesting point is the strong spin-density delocalization from the iron ion towards its ligand atoms in $\text{K}_2[\text{FeCl}_5(\text{H}_2\text{O})]$ and $\text{Rb}_2[\text{FeCl}_5(\text{H}_2\text{O})]$ [172, 185]. This leads to the relatively strong super-exchange paths in these two compounds although they are very long in the order of 7-8 Å including two diamagnetic intermediaries.

Based on Mössbauer investigations, a structural phase transition at about 151.5 K was proposed for $\text{Cs}_2[\text{FeCl}_5(\text{H}_2\text{O})]$ [188], but no further investigations followed to confirm this. Besides, as for $(\text{NH}_4)_2[\text{FeCl}_5(\text{H}_2\text{O})]$, the magnetic structure of $\text{Cs}_2[\text{FeCl}_5(\text{H}_2\text{O})]$ is still unknown. In figure 5.1 (d) the relevant magnetic-exchange interaction paths between the iron ions of different $[\text{FeCl}_5(\text{H}_2\text{O})]^{2-}$ octahedra are displayed [189]. The grey octahedra are lying in planes at $z = 0.25c$ and the yellow ones in planes at $z = 0.75c$. The J_1 -exchange interaction runs along the H-bonded zigzag chains of $[\text{FeCl}_5(\text{H}_2\text{O})]^{2-}$ octahedra parallel to c via super-exchange paths of the type Fe-O-H...Cl-Fe. The exchange interaction J_2 connects iron ions of $[\text{FeCl}_5(\text{H}_2\text{O})]^{2-}$ octahedra in different c planes, while the exchange interaction J_3 connects iron ions of $[\text{FeCl}_5(\text{H}_2\text{O})]^{2-}$ octahedra within the same c plane. In both cases the super-exchange paths are of the type Fe-Cl...Cl-Fe.

5.2 Experimental details

All crystals of the erythrosiderite-type family $A_2[\text{FeCl}_5(\text{H}_2\text{O})]$ ($A = \text{K}, \text{Rb}, \text{Cs}, \text{NH}_4$) investigated in the present work were grown by Prof. Dr. L. Bohatý from aqueous solution of ACl and FeCl_3 with a surplus of HCl by controlled evaporation of the solvent. The growth temperatures as well as the starting compositions of the growth solutions for the different compounds are summarized in table 5.2. After typical growth periods of 6-8 weeks optically clear, red single crystals with dimensions up to about $40 \times 30 \times 20 \text{ mm}^3$ and well-developed flat morphological faces were obtained, see figure 5.2. Using the morphological faces as reference planes, oriented samples with faces perpendicular to the a , b or c axis were prepared. For all magnetic compounds of the erythrosiderite-type family with space group $Pnma$, isomorphous, diamagnetic In(III) analogues exist [180]. One of these compounds, namely $(\text{NH}_4)_2[\text{InCl}_5(\text{H}_2\text{O})]$ was grown by Prof. Dr. L. Bohatý in an analogue way to the other erythrosiderite-type compounds. The starting composition of the growth solution can be found in table 5.2 as well.

The crystals of the erythrosiderite-type family are hygroscopic and disintegrate in contact with a multitude of solvents. In order to clean the crystal surfaces isopropanol was used. Although

crystal	growth temperature	starting composition of growth solution
$(\text{NH}_4)_2[\text{FeCl}_5(\text{H}_2\text{O})]$	311 K	$1\text{NH}_4\text{Cl} + 2\text{FeCl}_3$ (non-stoichiometric ratio)
$\text{K}_2[\text{FeCl}_5(\text{H}_2\text{O})]$	311 K	$1\text{KCl} + 2.5\text{FeCl}_3$ (non-stoichiometric ratio)
$\text{Rb}_2[\text{FeCl}_5(\text{H}_2\text{O})]$	323 K	$2\text{RbCl} + 1\text{FeCl}_3$ (stoichiometric ratio)
$\text{Cs}_2[\text{FeCl}_5(\text{H}_2\text{O})]$	323 K	$2\text{CsCl} + 1\text{FeCl}_3$ (stoichiometric ratio)
$(\text{NH}_4)_2[\text{InCl}_5(\text{H}_2\text{O})]$	307 K	$2\text{NH}_4\text{Cl} + \text{InCl}_3$ (stoichiometric ratio)

Table 5.2: Parameters for crystal growth from aqueous solution of AlCl_3 and FeCl_3 (InCl_3 , respectively) with a surplus of HCl by controlled evaporation of the solvent; growth period: 8-12 weeks.

they can be stored some time in silicone oil, their surfaces are damaged after some weeks in contact with it, as well. $(\text{NH}_4)_2[\text{FeCl}_5(\text{H}_2\text{O})]$ and $\text{K}_2[\text{FeCl}_5(\text{H}_2\text{O})]$ are even more damageable than $\text{Rb}_2[\text{FeCl}_5(\text{H}_2\text{O})]$ and $\text{Cs}_2[\text{FeCl}_5(\text{H}_2\text{O})]$, probably also because they dissolve in H_2O non-stoichiometrically. Besides, all four compounds are predispositioned to crack formation, when cooled to temperatures far below room temperature. Metallizing the crystal surfaces with silver or gold electrodes by evaporation is difficult, too. It turned out that silver electrodes adhere better than gold electrodes on the crystal surfaces. In summary, the crystals of the erythrosiderite-type family have to be handled with a lot of care. A lot of practice was necessary until adequate measurements could be performed.

All compounds were characterized by dielectric investigations and measurements of the magnetic susceptibility. The results of these measurements establish $(\text{NH}_4)_2[\text{FeCl}_5(\text{H}_2\text{O})]$ as a new multi-ferroic material with coupled magnetic and electric order below $\simeq 6.9$ K. $(\text{NH}_4)_2[\text{FeCl}_5(\text{H}_2\text{O})]$ was further investigated by measurements of thermal expansion, magnetostriction and specific heat. During the thermal-expansion and magnetostriction measurements the temperature and the magnetic field were varied continuously with rates of ± 0.05 to ± 0.1 K/min or ± 0.1 T/min, respectively. These measurements were partially performed by D. Brünig during his bachelor thesis [157]. Combining all data from the different examinations, detailed magnetic-field versus temperature phase diagrams are derived. Depending on the direction of the magnetic field up to three different multiferroic phases are identified, which are separated by a magnetically ordered, but non-ferroelectric phase from the paramagnetic phase. Besides these low-temperature transitions, an additional phase transition at $\simeq 79$ K was observed, which probably is of structural origin. To gather more information about this phase transition, temperature-dependent powder X-ray diffraction measurements as well as measurements with a polarized-light microscope were performed. Furthermore the In analogue of $(\text{NH}_4)_2[\text{FeCl}_5(\text{H}_2\text{O})]$ was investigated to obtain more information about its structural properties independently from the magnetic ones.

The results of the dielectric and magnetic measurements of the alkali-based compounds $A_2[\text{FeCl}_5(\text{H}_2\text{O})]$ with $A = \text{K}, \text{Rb}, \text{Cs}$ prove that they are, in contrast to $(\text{NH}_4)_2[\text{FeCl}_5(\text{H}_2\text{O})]$ only linear magnetoelectrics. For each compound, all the linear magnetoelectric tensor components and

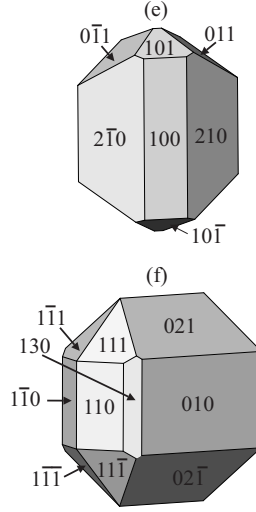


Figure 5.2: Crystals of (a) $(\text{NH}_4)_2[\text{FeCl}_5(\text{H}_2\text{O})]$, (b) $\text{K}_2[\text{FeCl}_5(\text{H}_2\text{O})]$, (c) $\text{Rb}_2[\text{FeCl}_5(\text{H}_2\text{O})]$, (d) $\text{Cs}_2[\text{FeCl}_5(\text{H}_2\text{O})]$. Typical morphology of (e) $\text{A}_2[\text{FeCl}_5(\text{H}_2\text{O})]$ with $\text{A} = (\text{NH}_4), \text{K}, \text{Rb}$, (f) $\text{Cs}_2[\text{FeCl}_5(\text{H}_2\text{O})]$. The well-developed morphology was used for the preparation of oriented samples.

their temperature dependences were determined from the experimental data. A symmetry analysis of the magnetoelectric effect of the Cs-based compound allows to determine the magnetic point group mmm' and to develop a model for its magnetic structure. In addition detailed magnetic-field versus temperature phase diagrams are derived.

5.3 $(\text{NH}_4)_2[\text{FeCl}_5(\text{H}_2\text{O})]$

In the following, the results of the measurements of $(\text{NH}_4)_2[\text{FeCl}_5(\text{H}_2\text{O})]$, summarized in section 5.2 are presented, analysed and discussed in detail. Most of these results were already published in [190]. Therefore, apart from some complements this chapter, including the figures, is basically adopted from this publication.

5.3.1 Phase transitions in zero magnetic field

By measuring the heat capacity of $(\text{NH}_4)_2[\text{FeCl}_5(\text{H}_2\text{O})]$, the occurrence of the magnetic phase transitions at $\simeq 6.9$ K and $\simeq 7.3$ K already reported in literature [180] could be confirmed, see figure 5.3 (a). In addition, the heat capacity data reveal a third phase transition at $T_{\text{HT}} \simeq 79$ K. These three phase transitions are also seen in the measurements of all three thermal-expansion coefficients α_i , see figures 5.3 (e) and (f). However, neither the specific-heat data nor the $\alpha_i(T)$ curves give any hint to a phase transition around 240 K, where the occurrence of a structural phase transition had been supposed for $(\text{NH}_4)_2[\text{FeCl}_5(\text{H}_2\text{O})]$ [183]. The fact that no anomalies were found in the magnetic-susceptibility measurements around T_{HT} (see below, Fig. 5.5 (e)) led to the conjecture that the transition around 79 K might be of structural origin. Therefore, temperature-dependent X-ray powder diffraction measurements were performed, but surprisingly the patterns above and below T_{HT} are identical within the experimental uncertainty. Particularly, no peak split-

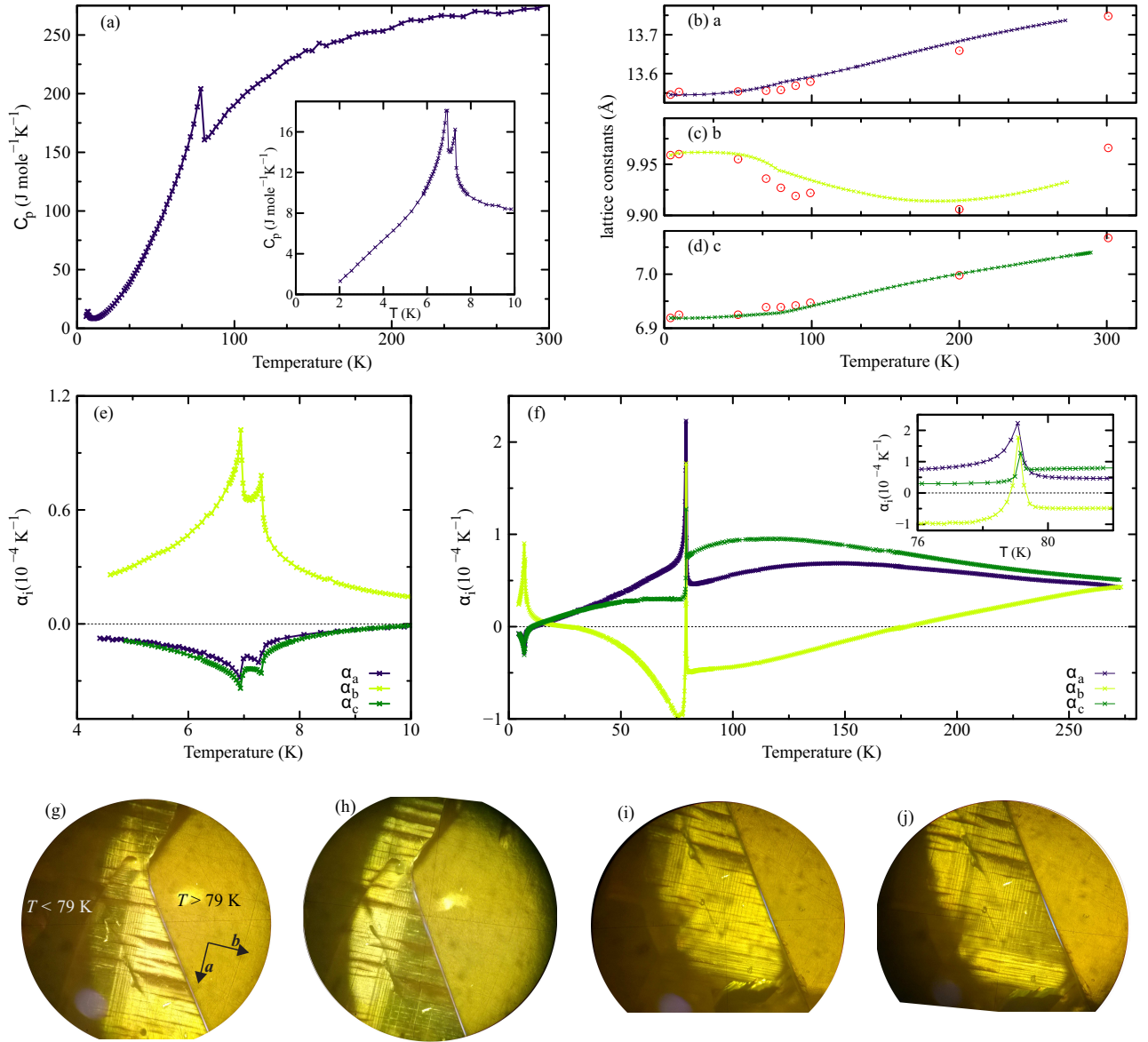


Figure 5.3: (a) Heat capacity of $(\text{NH}_4)_2[\text{FeCl}_5(\text{H}_2\text{O})]$ in a wide temperature range; the inset is a magnification of the low-temperature region. (b)-(d) Temperature dependences of the lattice constants a , b , and c obtained by X-ray powder diffraction measurements (circles) in comparison to the respective macroscopic length changes (lines) measured by capacitance dilatometry. (e) and (f) Thermal-expansion coefficients α_i along all three axes a , b and c below 10 K and over the entire temperature range, where the inset shows an expanded view around the transition at $\simeq 79 \text{ K}$. (g)-(j) Ferroelastic domains, which were observed for a plate-like sample with faces oriented perpendicular to c below the transition at $\simeq 79 \text{ K}$ indicating the occurrence of a ferroelastic phase transition.

tings or violations of systematic extinctions of the space group $Pnma$ of the high-temperature phase could be found below T_{HT} . In the figures 5.3 (b)-(d) the temperature-dependent lattice constants obtained from the X-ray diffraction are compared with the corresponding results obtained from the measured macroscopic length changes via capacitance dilatometry. There is an overall agreement

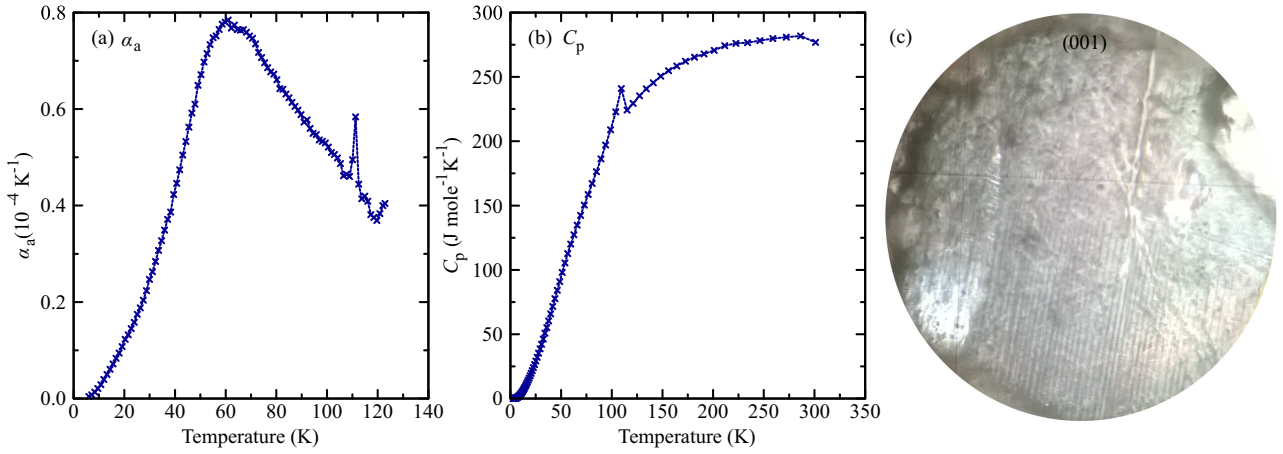


Figure 5.4: (a) Thermal-expansion coefficient α along the a axis of $(\text{NH}_4)_2[\text{InCl}_5(\text{H}_2\text{O})]$ in the temperature range 4-120 K. (b) Heat capacity of $(\text{NH}_4)_2[\text{InCl}_5(\text{H}_2\text{O})]$ in the temperature range 2-300 K. (c) Ferroelastic domains, which were observed for a plate-like sample with faces oriented perpendicular c , below the transition at $\simeq 110$ K, indicating the occurrence of a ferroelastic phase transition.

between both methods over the entire temperature range, see e.g. the anomalous negative thermal expansion of the b axis. The shape of the specific-heat anomaly at T_{HT} suggests a second-order phase transition, but the thermal-expansion curves, which have been studied with a much higher temperature resolution around T_{HT} , clearly show rather sharp peaks of positive signs, which are present for all three directions, see the inset of figure 5.3 (f). Integrating over these peaks reveals an almost discontinuous length change $\Delta L/L^0$ of all three directions a , b and c of $\simeq 0.5 - 1.5 \cdot 10^{-3}$, indicating that the transition at T_{HT} is of first order.

In order to get more information about the transition at T_{HT} thin, plate-like samples of thicknesses of $\sim 100 \mu\text{m}$ with polished surfaces, oriented perpendicular to a , b and c were examined with a polarized-light microscope. For the samples with faces perpendicular to c the occurrence of ferroelastic domains with two different domain states was observed below the transition at T_{HT} , indicating that it is a ferroelastic transition, see figures 5.3 (g)-(j). In all cases the polariser and analyser of the microscope were adjusted parallel to the semi-principal axis of the elliptic section of the optical indicatrix of one of these two present domain states, leading to stripe-like dark-bright domain patterns. The dark domain stripes in figure 5.3 (g) correspond to the bright ones in figure 5.3 (h). The same holds true for figures 5.3 (i) and (j). In all pictures presented, a temperature gradient was present due to a large crack, which divided the sample under investigation into two parts. In each picture, the temperature of the left part, where a domain pattern with two different domain states is visible, was below 79 K and the temperature of the right part without a domain pattern was above 79 K. For the samples with faces perpendicular to a or b no ferroelastic domains were observed. The domain walls, visible in figure 5.3 (g)-(j) are running along a and b and in company with the ferroelastic transition a crack system, with the cracks oriented mainly

parallel to the bc plane occurred (in the right part of the sample above 79 K no cracks arose). These cracks arise probably due to the distortions connected with the ferroelastic transition. Combining the informations about the ferroelastic domains, one can conclude that the orthorhombic crystal structure of $(\text{NH}_4)_2[\text{FeCl}_5(\text{H}_2\text{O})]$ with the space group $P\frac{2_1}{m}\frac{2_1}{n}\frac{2_1}{a}$ transforms at T_{HT} via a ferroelastic transition to a monoclinic one with the space group $P11\frac{2_1}{a}$ (species $mmm1'F2/m1'$). The crystal structure of $(\text{NH}_4)_2[\text{FeCl}_5(\text{H}_2\text{O})]$ was redetermined independently by Dr. P. Held¹ and by Dr. M. Fleck² at room temperature, to clarify the question if the orientation of the (NH_4) groups within the crystal structure is fixed or not. Both investigations gave strong evidence for a random orientation of the (NH_4) groups. Therefore, the monoclinic distortion below T_{HT} is probably small and only caused by a reorientation of the NH_4 groups (disorder-order transition).

These interpretations are further supported by the results of thermal-expansion and heat-capacity measurements, performed on the isomorphic, diamagnetic In(III) analogue $(\text{NH}_4)_2[\text{InCl}_5(\text{H}_2\text{O})]$ in combination with observations by polarized-light microscopy. The results are summarized in figure 5.4. Both the temperature-dependent specific-heat and thermal-expansion data show pronounced anomalies at $T_{\text{HT}}^{\text{In}} = 110$ K, see figure 5.4 (a), (b). Besides, such as in $(\text{NH}_4)_2[\text{FeCl}_5(\text{H}_2\text{O})]$, ferroelastic domains with two different domain states could be observed below $T_{\text{HT}}^{\text{In}}$ in samples with surface normals oriented parallel to c , while for samples with surface normals oriented parallel to a or b no domains could be detected, see figure 5.4 (c). Hence, $(\text{NH}_4)_2[\text{InCl}_5(\text{H}_2\text{O})]$ undergoes at $T_{\text{HT}}^{\text{In}} = 110$ K a structural phase transition from the orthorhombic system $P\frac{2_1}{m}\frac{2_1}{n}\frac{2_1}{a}$ to a monoclinic one with the space group $P11\frac{2_1}{a}$, as its Fe(III) analogue at $T_{\text{HT}}^{\text{Fe}} = 79$ K. The assumption that the structural transitions in $(\text{NH}_4)_2[\text{FeCl}_5(\text{H}_2\text{O})]$ and $(\text{NH}_4)_2[\text{InCl}_5(\text{H}_2\text{O})]$ are caused by an ordering of the orientation of the (NH_4) groups would also explain, why the powder X-ray data do not indicate a lowering of the orthorhombic symmetry to the monoclinic system. Consequently, the room-temperature crystal structure still can serve as a good approximation at lower temperatures, at least concerning the positions of the non-hydrogen atoms. Therefore, all results presented in the following sections are referred to the orthorhombic system.

5.3.2 Magnetic properties

The results of the temperature-dependent magnetic-susceptibility measurements of $(\text{NH}_4)_2[\text{FeCl}_5(\text{H}_2\text{O})]$ for magnetic fields up to 7 T (applied along the a , b and c axis) are summarized in the figures 5.5 (a)-(c), respectively³. The low-field curves are consistent with previous results [180] and signal magnetic ordering at $T_N \simeq 7.3$ K. While χ_a and χ_c show

¹Institut für Kristallographie, Universität zu Köln

²Institut für Mineralogie und Kristallographie, Universität Wien

³The magnetic measurements presented in this section were performed in a squid magnetometer, see section 3.1.

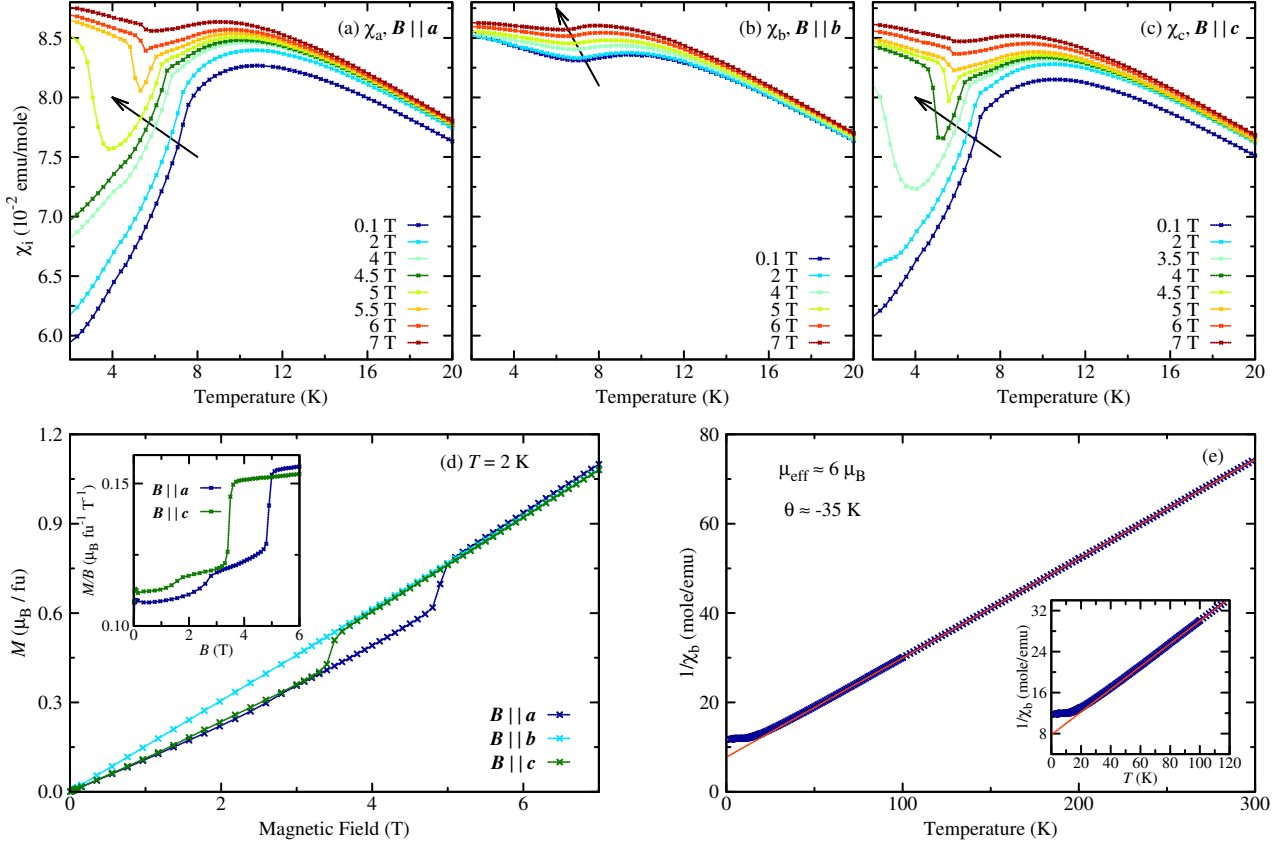


Figure 5.5: (a)-(c) Temperature dependences of the magnetic susceptibility χ_a , χ_b , and χ_c of $(\text{NH}_4)_2[\text{FeCl}_5(\text{H}_2\text{O})]$ for different magnetic fields. The arrows mark the direction of increasing field strength. (d) Magnetization at 2 K as functions of the magnetic field applied parallel to a , b and c ; the inset shows M/B for $B \parallel a$ and $B \parallel c$. (e) Temperature dependence of the inverse susceptibility $1/\chi_b$ together with a Curie-Weiss fit (line) in the temperature range from 100 K to 300 K (the inset shows a magnification of the low-temperature range).

well-defined kinks at T_N and subsequently decrease with decreasing temperature, $\chi_b(T)$ hardly changes below T_N , indicating that the spins are lying in the ac plane. The fact that χ_a and χ_c of $(\text{NH}_4)_2[\text{FeCl}_5(\text{H}_2\text{O})]$ behave very similar and none of them approaches zero for $T \rightarrow 0$ K implies that there is no magnetic easy axis within the ac plane. This is further supported by additional low-field susceptibility measurements (not shown) with magnetic fields along other directions within the ac plane. Thus, the spins of $(\text{NH}_4)_2[\text{FeCl}_5(\text{H}_2\text{O})]$ show an XY anisotropy with the ac plane as magnetic easy plane. As already mentioned in section 5.1, there have been different speculations about possible spin orientations within the ac plane earlier [180, 182–184], but no definite magnetic-structure determination has been reported until now.

Concerning the magnetic anisotropy, $(\text{NH}_4)_2[\text{FeCl}_5(\text{H}_2\text{O})]$ differs from the analogous potassium-based and rubidium-based compounds $A_2[\text{FeCl}_5(\text{H}_2\text{O})]$ ($A = \text{K}, \text{Rb}$). According to low-field susceptibility measurements [176, 180, 191], χ_a of both alkali-metal compounds approaches zero

for $T \rightarrow 0 \text{ K}$, while χ_b and χ_c hardly change, identifying \mathbf{a} as the magnetic easy axis.⁴ This is confirmed by magnetic-structure determinations of $\text{K}_2[\text{FeCl}_5(\text{D}_2\text{O})]$ and $\text{Rb}_2[\text{FeCl}_5(\text{D}_2\text{O})]$ by neutron-scattering investigations, which in addition revealed the magnetic space-group symmetry $Pn'm'a'$ for these compounds [185, 186]. These neutron studies also allowed to determine five relevant exchange couplings $J_1 - J_5$, which were explained in detail in section 5.1. They are all antiferromagnetic and the stronger ones ($J_1 - J_3$) enforce an antiferromagnetic ordering between the spins lying in neighbouring ac planes at $y = 0.25$ and $y = 0.75$. However, the spins lying in the same ac plane are ordered ferromagnetically, despite of the antiferromagnetic, but weaker exchange interactions J_4 and J_5 within these planes [185, 186]. Thus, there exists a certain degree of magnetic frustration in the $A_2[\text{FeCl}_5(\text{H}_2\text{O})]$ structure, which might be the reason for the more complex spin arrangement in the compound with $A = (\text{NH}_4)$, compared to those with $A = \text{K}, \text{Rb}$.

As shown in figure 5.5 (a) and (c), towards larger fields the decrease for $T < T_N$ of both, $\chi_a(T)$ and $\chi_c(T)$, systematically vanishes and finally above about 6 T the principal behaviour of $\chi_i(T)$ is almost identical for all three field directions. This suggests that for either $\mathbf{B}||\mathbf{a}$ or $\mathbf{B}||\mathbf{c}$, there are spin-flop transitions, with a change of spin orientation from lying within the easy ac plane to lying within the plane that is perpendicular to the respective magnetic-field direction. These spin-flop transitions can also be seen in the low-temperature measurements of the magnetization as a function of the magnetic field, see figure 5.5 (d). The spin-flop fields at $T = 2 \text{ K}$ are $\simeq 5 \text{ T}$ and $\simeq 3.5 \text{ T}$ for $\mathbf{B}||\mathbf{a}$ and $\mathbf{B}||\mathbf{c}$, respectively. Besides the spin-flop transitions, the magnetization curves display additional anomalies for both field directions, which are better resolved in a representation M/B versus B , see the inset of figure 5.5 (d). Corresponding anomalies can be seen in the temperature-dependent susceptibility data in figure 5.5 (a) and (c) for $B = 4 \text{ T}$ and 2 T , respectively. As will be seen in the following sections, both types of transitions are related to structural changes and as well to reorientations of the electric polarization. The fact that both transition fields are larger for $\mathbf{B}||\mathbf{a}$ than for $\mathbf{B}||\mathbf{c}$ illustrates that the magnetic properties of $(\text{NH}_4)_2[\text{FeCl}_5(\text{H}_2\text{O})]$ are not completely isotropic within the easy ac plane. This is supported by the slight, but systematic differences between the $\chi_a(T)$ and $\chi_c(T)$ curves in the intermediate field range, see figures 5.5 (a) and (c).

Figure 5.5 (e) displays the inverse susceptibility $1/\chi_b$ for a magnetic field of 0.1 T applied along \mathbf{b} , which follows a Curie-Weiss behaviour from above about 40 K up to room temperature. Here, only the data of χ_b are shown because almost identical values are obtained for χ_c in this high-temperature range, while χ_a is slightly larger ($\simeq 1 - 2 \%$). Almost isotropic high-temperature susceptibilities may be expected for a $3d^5$ high-spin configuration of the Fe^{3+} ions, as was already stated in [180]. Linear fits to the data of $1/\chi_i$ for $T > 100 \text{ K}$ yield a negative Weiss temperature $\theta \simeq -35 \text{ K}$ and an effective magnetic moment $\mu_{\text{eff}} \simeq 6 \mu_B$. The negative Weiss temperature

⁴The results of detailed magnetic-susceptibility measurements of both compounds, performed in the present work are presented in section 5.4.1.

signals a net antiferromagnetic-exchange interaction and the effective magnetic moment is close to the expected value $\mu_{\text{eff}} = g\mu_B\sqrt{S(S+1)} = 5.92\mu_B$ of Fe^{3+} with $S = 5/2$ and $g = 2$.

5.3.3 Dielectric properties

Figure 5.6 summarizes the results of the temperature-dependent measurements of the electric polarization P_a , P_b and P_c of $(\text{NH}_4)_2[\text{FeCl}_5(\text{H}_2\text{O})]$ in magnetic fields applied along \mathbf{a} , \mathbf{b} and \mathbf{c} . The respective pyroelectric-current densities can be found in appendix E.3. In zero magnetic field, $(\text{NH}_4)_2[\text{FeCl}_5(\text{H}_2\text{O})]$ becomes ferroelectric below $T_{\text{FE}} \simeq 6.9$ K and develops a spontaneous electric polarization, with the components $P_a \simeq 3\mu\text{C}/\text{m}^2$, $P_b \simeq 0.3\mu\text{C}/\text{m}^2$ and $P_c \simeq 0\mu\text{C}/\text{m}^2$ at 3 K. Thus, the spontaneous electric polarization is lying in the ab plane with an angle relative to the \mathbf{a} axis of $\angle(\mathbf{P}, \mathbf{a}) \simeq 7^\circ$. Assuming a point group symmetry $2/m$ (with cell setting unique axis \mathbf{c}) for the prototypic phase, see section 5.3.1, the probable crystallographic symmetry of the considered ferroelectric phase would be m or even triclinic, 1.

A magnetic field applied parallel to \mathbf{b} causes a weak systematic reduction of the transition temperature ($T_{\text{FE}}^{14\text{T}} \simeq 6$ K) and also slightly reduces the magnitude of the electric polarization, but leaves its orientation almost unchanged. In contrast, magnetic fields applied either along \mathbf{a} or \mathbf{c} have a much stronger influence on the electric polarization. Most obviously, for both directions a field of about 4–6 T causes a complete suppression of both components P_a and P_b , and simultaneously induces a finite polarization $\mathbf{P}||\mathbf{c}$, which continuously increases with further increasing magnetic field. In the figures 5.7 (a) and (b), these magnetic-field induced abrupt reorientations of \mathbf{P} for $\mathbf{B}||\mathbf{a}$ and $\mathbf{B}||\mathbf{c}$, respectively, are shown exemplarily for $T = 4.9$ K by plotting the components P_a , P_b and P_c as functions of the magnetic field.⁵ The open symbols are taken from the temperature-dependent polarization data of figure 5.6, while the solid lines were obtained by integrating the magnetoelectric currents during a magnetic-field sweep as described in section 3.2.1. For $P_a(\mathbf{B})$ and $P_c(\mathbf{B})$, the results of both methods agree to each other, while the polarization $P_b(\mathbf{B})$ is too small to induce large enough magnetoelectric currents, even if the magnetic-field sweep rate is increased to 1 T/min. A comparison of the $\mathbf{P}(\mathbf{B})$ data with the magnetization curves $\mathbf{M}(\mathbf{B})$ discussed above reveals that the magnetic-field dependent reorientations of the electric polarization coincide with the spin-flop transitions for both field directions $\mathbf{B}||\mathbf{a}$ and $\mathbf{B}||\mathbf{c}$. In addition, the data of figure 5.7 show that the electric polarization P_c above the critical field grows linearly with increasing magnetic field. At $B = 14$ T, $P_c \simeq 19\mu\text{C}/\text{m}^2$ or $\simeq 25\mu\text{C}/\text{m}^2$ is reached for $\mathbf{B}||\mathbf{a}$ or $\mathbf{B}||\mathbf{c}$, respectively, i.e., the absolute value of the polarization is enhanced by a factor of about 6 to 8 compared to its zero-field value. If the field-induced increase of the electric polarization above the transition is eliminated by linearly extrapolating $P_c(B > B_{\text{crit}})$ back to the critical field, the

⁵The respective magnetoelectric-current densities are presented in appendix E.3.

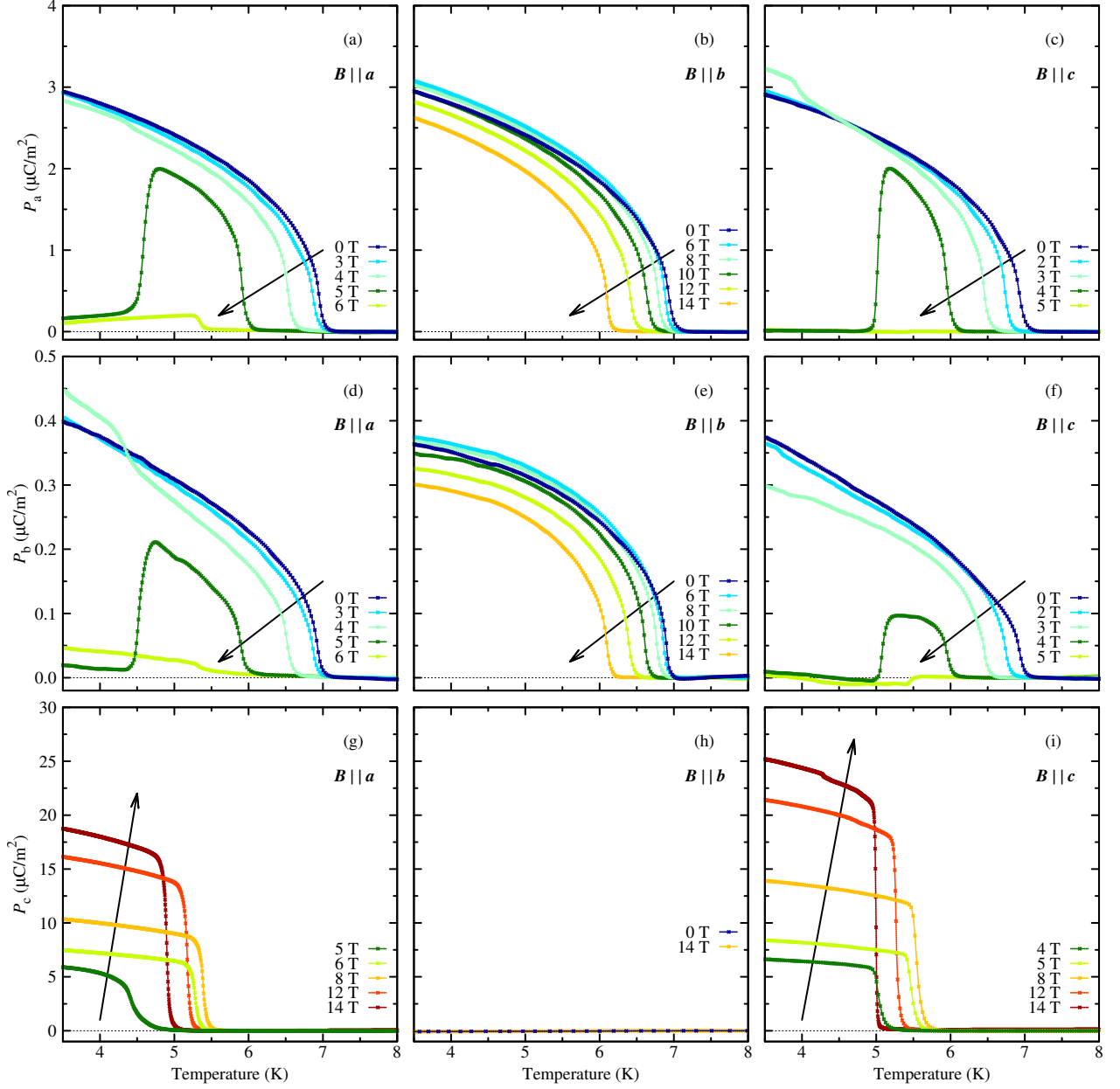


Figure 5.6: Temperature dependences of the spontaneous electric polarization P_a , P_b and P_c (top to bottom) of $(\text{NH}_4)_2[\text{FeCl}_5(\text{H}_2\text{O})]$ for magnetic fields applied parallel to the a , b or c axis (left to right). In all cases, single-domain phases were obtained by cooling the samples with an applied electric field of at least 200 V/mm. Besides the electric polarization is completely invertible by changing the sign of the electric field. The directions of increasing magnetic fields are marked by arrows.

absolute value of the polarization, e.g. at 4.9 K, changes from $|\mathbf{P}| \simeq P_a \simeq 2 \mu\text{C}/\text{m}^2$ below B_{crit} to $|\mathbf{P}| = P_c \simeq 5.2 \mu\text{C}/\text{m}^2$ for $\mathbf{B}||\mathbf{a}$ and to $|\mathbf{P}| = P_c \simeq 5.6 \mu\text{C}/\text{m}^2$ for $\mathbf{B}||\mathbf{c}$, respectively, above B_{crit} . As already discussed above, besides the spin-flop transition the magnetization data for both field directions, $\mathbf{B}||\mathbf{a}$ and $\mathbf{B}||\mathbf{c}$, signal another phase transition, which is located about 2 T below

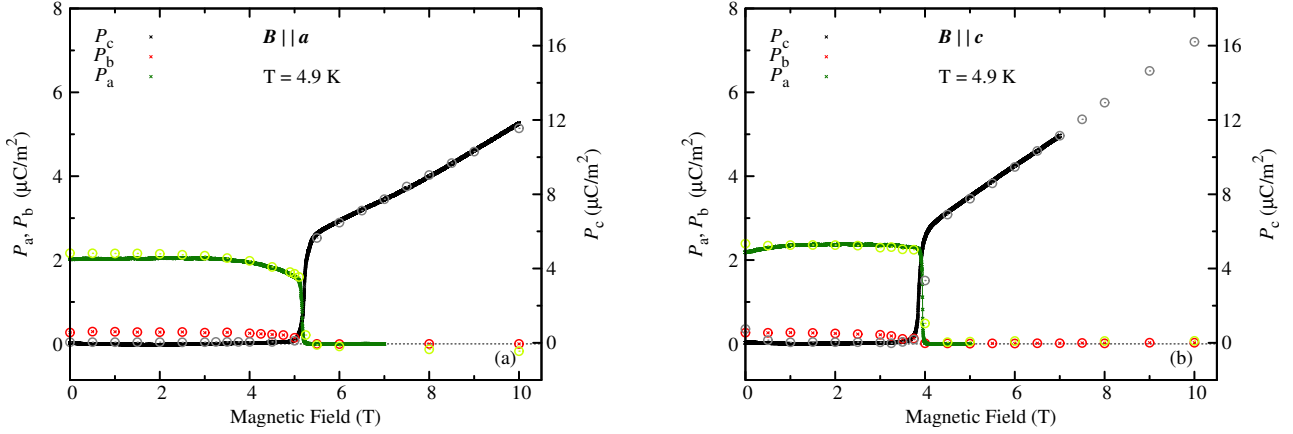


Figure 5.7: Representative magnetic-field dependences of the electric polarization P_a , P_b and P_c for magnetic fields applied along a (left) and c (right) at $T = 4.9$ K. Open symbols indicate data taken from the temperature-dependent polarization measurements shown in figure 5.6 and the solid lines indicate $P_a(B)$ and $P_c(B)$ obtained by integrating the magnetoelectric currents measured during magnetic-field sweeps. The latter method is not possible for $P_b(B)$ due to its small absolute value. Note the different scales used for P_i ($i = a, b$) and for P_c .

the spin-flop fields and is seen as small step-like increases of M/B , see the inset of figure 5.5 (d). These additional transitions also cause small changes in the electric polarization, which can be best seen by considering the turquoise curves in the figures 5.6(c) and (d). For $B = 3$ T along c , the polarization $P_a(T)$ shows a distinct increase around 4 K, while the polarization $P_b(T)$ has an additional increase around 4.5 K for $B = 4$ T along a .

In summary, the magnetic-field dependent (re-)orientations of the electric polarization of $(\text{NH}_4)_2[\text{FeCl}_5(\text{H}_2\text{O})]$ can be described as follows: In zero magnetic field the spontaneous polarization is lying in the ab plane and almost pointing along the a axis ($\angle(\mathbf{P}, \mathbf{a}) \simeq 7^\circ$). A magnetic field applied along a first (at $\simeq 4$ T) causes a slight reorientation of the polarization in the ab plane towards the b axis ($\angle(\mathbf{P}, \mathbf{a}) \sim 9^\circ$). At a larger field of about 5 T the polarization then completely rotates by 90° from the ab plane to the c axis. For a magnetic field along c , the first transition (at $\simeq 3$ T) causes a reorientation of the spontaneous polarization in the opposite sense ($\angle(\mathbf{P}, \mathbf{a}) \sim 5^\circ$), but is also followed by an analogous 90° change of the polarization to the c axis, occurring at about 4.5 T. For both field directions, the first transitions are accompanied by weak anomalies in the magnetization, while the 90° reorientations of the electric polarization from the ab plane to the c axis coincide with spin-flop transitions from the magnetic easy ac plane towards the plane perpendicular to the respective magnetic-field direction. Interestingly, for both magnetic-field directions the 90° reorientation of the electric polarization is accompanied by an abrupt, significant enhancement of its absolute value by about a factor of 2.5 and on further increasing the magnetic field the polarization linearly grows. Loosely speaking, a magnetic field $\mathbf{B}||\mathbf{c}$ has a "stronger effect" than a magnetic field $\mathbf{B}||\mathbf{a}$: The high-field slope $\partial P_c / \partial B_c \simeq 1.7 \cdot 10^{-6}$ A/V is larger than

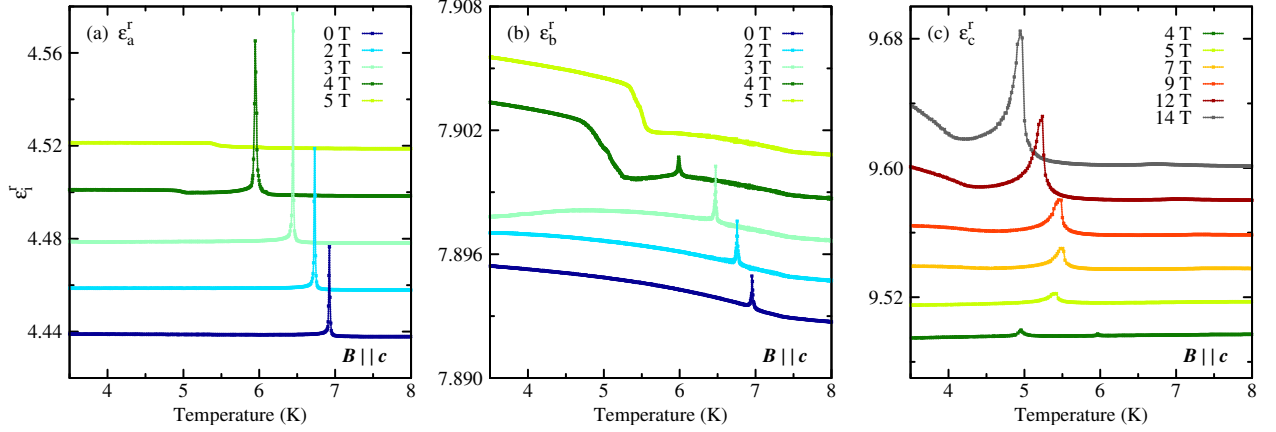


Figure 5.8: Representative temperature dependences of the longitudinal components of the dielectric tensor ϵ_i^r ($i = a, b, c$ from left to right) for different magnetic fields applied parallel to c . For clarity, with increasing field strength the curves are shifted with respect to each other by constant offsets of 0.02 in (a) & (c) and by 0.002 in (b).

$\partial P_a / \partial B_a \simeq 1.2 \cdot 10^{-6} \text{ A/V}$ and in order to induce the phase transition smaller field strengths are needed for $\mathbf{B} \parallel c$ than for $\mathbf{B} \parallel a$.

The transitions to the ferroelectric phases, discussed above, also cause distinct anomalies in the temperature and magnetic-field dependences of the corresponding longitudinal components ϵ_i^r of the dielectric tensor. This is shown exemplarily for $\mathbf{B} \parallel c$ in figure 5.8, which displays representative measurements of the temperature dependences of ϵ_i^r ($i = a, b, c$). Below 5 T, $\epsilon_a^r(T)$ and $\epsilon_b^r(T)$ show spiky anomalies in the temperature range between 6 K and 7 K, which essentially vanish for larger fields, while such spiky anomalies of growing intensity occur in $\epsilon_c^r(T)$ in this higher field range. From these results, together with the polarization data above, it can be concluded that these spikes signal the corresponding transition temperatures to the ferroelectric phases with a spontaneous polarization lying either in the ab plane or being oriented along the c axis. There are additional anomalies, e.g. the step-like increase in $\epsilon_b^r(T)$ for 4 T and 5 T, which are more difficult to interpret.

5.3.4 Thermal expansion and magnetostriction

The discussion in the sections above has mainly focused on the dielectric and magnetic properties of $(\text{NH}_4)_2[\text{FeCl}_5(\text{H}_2\text{O})]$, which are obviously most sensitive to transitions where either the polarization or the magnetization changes. In order to map out the temperature versus magnetic-field phase diagrams of this multiferroic material, it is more convenient to study thermodynamic properties, which are sensitive to both types of phase transitions, such as the specific heat or the thermal expansion, see figure 5.3. In the present case, detailed studies of the thermal expansion and of the magnetostriction for all three magnetic-field directions a , b and c were performed. As

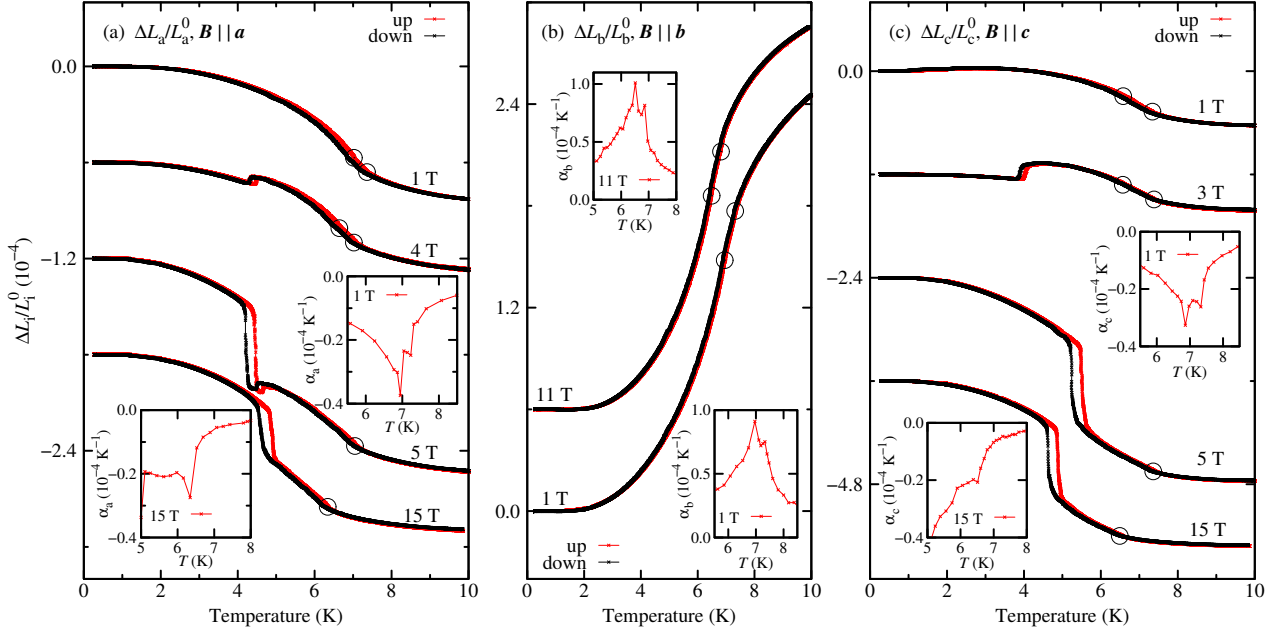


Figure 5.9: Thermal expansion of $(\text{NH}_4)_2[\text{FeCl}_5(\text{H}_2\text{O})]$ along the a , b and c direction for representative magnetic fields applied parallel to a , b and c , respectively. For clarity, with increasing field strengths the curves are shifted with respect to each other by constant offsets of $0.6 \cdot 10^{-4}$ in (a) & (b) and by $1.2 \cdot 10^{-4}$ in (c). Measurements with increasing and decreasing temperature are plotted as red and black symbols, respectively. The weak anomalies due to the continuous transitions at T_{FE} and T_{N} (see the zero-field data in figure 5.9) are hardly visible in the $\Delta L_i/L_i^0$ curves, but can be better seen in the thermal-expansion coefficients α_i shown in the insets. The corresponding transition temperatures are marked by open circles on the $\Delta L_i/L_i^0$ curves.

will be seen, $(\text{NH}_4)_2[\text{FeCl}_5(\text{H}_2\text{O})]$ shows various first-order phase transitions with rather large, almost discontinuous changes of the sample dimensions. Thus, in the following the relative length changes $\Delta L_i(T, \mathbf{B})/L_i^0$ with $\mathbf{B} \parallel L_i$ for $i = a, b$ and c will be presented. Figure 5.9 displays a representative selection of $\Delta L_i(T, \mathbf{B})/L_i^0$ curves measured as a function of increasing or decreasing temperature at constant magnetic fields. More results can be found in the bachelor thesis of D. Brünig [157]. For $\mathbf{B} \parallel b$, there is only little change. The two transitions occurring at $T_{\text{FE}} \simeq 6.9 \text{ K}$ and $T_{\text{N}} \simeq 7.3 \text{ K}$ in zero field are just continuously shifted towards lower temperatures with increasing field. As shown in the insets of figure 5.9 (b), the corresponding anomalies are resolved in the thermal-expansion coefficient α_b , but are only faintly visible in $\Delta L_b(T, \mathbf{B})/L_b^0$. Thus, these transitions are marked by open circles in the main panel of this figure. Additional anomalies occur for $\mathbf{B} \parallel a$ and for $\mathbf{B} \parallel c$. For both field directions, there is a sharp, almost discontinuous decrease of $\Delta L_i(T, \mathbf{B})/L_i^0$ on decreasing the temperature around 4 K in the field range of 3-4 T, indicating that the corresponding phase transition is of first order. Moreover, there is a weak temperature hysteresis, but its width partly arises also from the finite temperature sweep rate (see section 5.2). With a further increase of the field $\mathbf{B} \parallel a$ or $\mathbf{B} \parallel c$ above about 5 T, this discontinu-

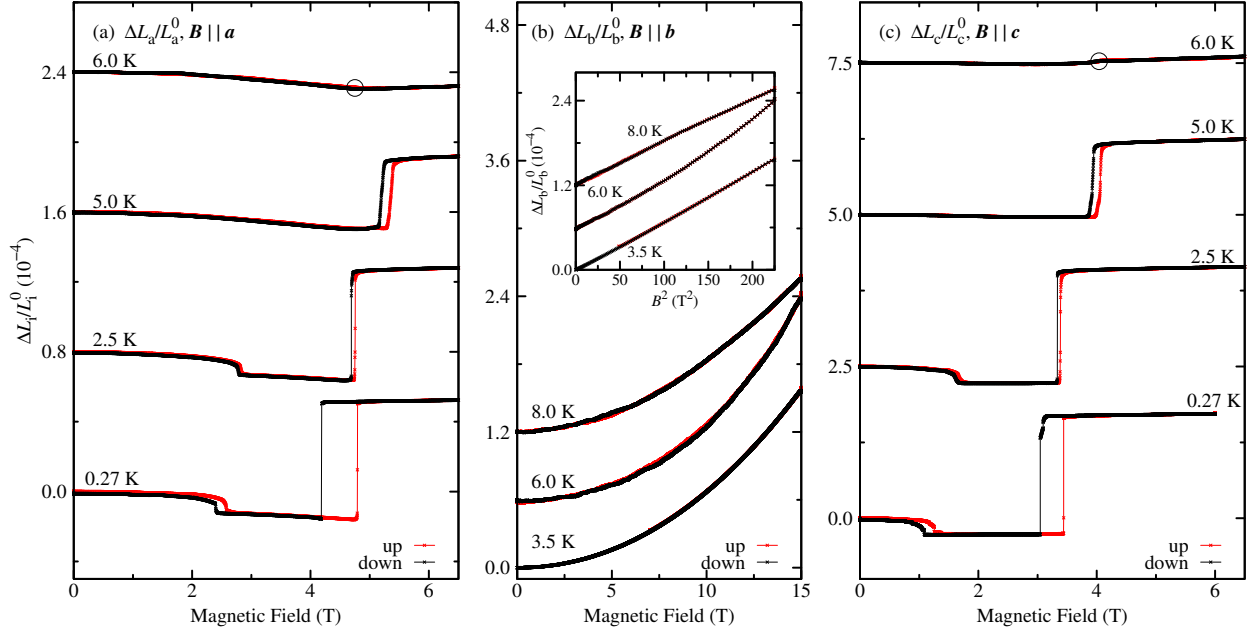


Figure 5.10: Magnetostriction of $(\text{NH}_4)_2[\text{FeCl}_5(\text{H}_2\text{O})]$ along the a , b or c direction for magnetic fields applied parallel to a , b and c , respectively. For clarity, with increasing temperature the curves are shifted with respect to each other by constant offsets of $0.8 \cdot 10^{-4}$, $0.6 \cdot 10^{-4}$ and $2.5 \cdot 10^{-4}$ in (a), (b) and (c), respectively. Measurements with increasing and decreasing magnetic field are plotted as red and black symbols, respectively. The open circles on the $\Delta L_i(B, T = 6 \text{ K})/L_i^0$ curves in (a) and (c) mark continuous phase transitions, which can better be seen in the corresponding derivatives with respect to B (not shown). The inset in (b) shows $\Delta L_b/L_b^0$ versus B^2 .

ous anomaly disappears again and also the continuous anomaly at the transition temperature T_{FE} vanishes, but another first-order phase transition occurs. This latter transition is characterized by a more pronounced hysteresis and a discontinuous length change $\Delta L_i(T, B)/L_i^0$, which is significantly larger and of the opposite sign than that of the discontinuous transition occurring below 5 T.

Figure 5.10 summarizes representative magnetostriction measurements along the a , b or c direction for magnetic fields applied parallel to a , b and c , respectively. As already mentioned above, more results can be found in the bachelor thesis of D. Br uning [157]. Again, the data for $B||a$ or $B||c$ are rather similar. At the lowest temperature ($T = 0.27 \text{ K}$) there are two hysteretic first-order phase transitions with (almost) discontinuous length changes $\Delta L_i/L_i^0$ of opposite signs for both directions a and c . Both transitions are also present at 2.5 K, but the hysteresis widths are considerably smaller. At an even higher temperature of 5 K, the transitions at the lower critical fields have vanished, while those at the larger fields are still present and their hysteresis widths are wider again. Finally at 6 K, the discontinuous length changes have vanished. Instead, there are kinks in $\Delta L_i/L_i^0$ around 4-5 T, which can be better seen in the corresponding derivatives with respect to B_i (not shown). These anomalies signal second-order phase transitions and are marked

by open circles on the $\Delta L_i/L_i^0$ curves. Note that although most of the data have been studied up to a maximum field of 15 T, the field scales of figures 5.10(a) and (c) have been limited to 6.5 T because there are no further anomalies in the higher field range. Figure 5.10(b) displays characteristic longitudinal magnetostriction curves for $\mathbf{B}||\mathbf{b}$. As can be inferred from the inset, in the paramagnetic/non-ferroelectric phase, i.e. above $T_N \simeq 7.3$ K, as well as in the multiferroic phase, i.e. well below $T_{\text{FE}} \simeq 6.9$ K, there is a quadratic magnetostriction ($\Delta L_b/L_b^0 \propto B^2$) in the entire field range studied, which is typical for materials with a linear field dependence of the magnetization. The curves taken at 6 K deviate from this simple quadratic field dependence above about 10 T, which is related to the fact that the field dependent phase boundary $T_{\text{FE}}(\mathbf{B})$ is approached.

5.3.5 Phase diagrams and conclusion

The B - T phase diagrams of $(\text{NH}_4)_2[\text{FeCl}_5(\text{H}_2\text{O})]$ for magnetic fields applied along \mathbf{a} , \mathbf{b} or \mathbf{c} are displayed in figure 5.11. The critical fields and temperatures are based on the anomalies in $\Delta L_i(T, \mathbf{B})/L_i^0$ from the thermal-expansion and magnetostriction measurements, while the dielectric and magnetic properties of the various phases are inferred from the electric-polarization and magnetization data. The polarization and magnetization measurements also show anomalies for most of the detected phase transitions and their positions agree well with the anomalies of $\Delta L_i(T, \mathbf{B})/L_i^0$ and also with those found in specific-heat measurements, which were performed for $\mathbf{B}||\mathbf{a}$ (not shown), see bachelor thesis of D. Br uning [157]. On temperature decrease in zero magnetic field, $(\text{NH}_4)_2[\text{FeCl}_5(\text{H}_2\text{O})]$ undergoes a phase transition at $T_N \simeq 7.3$ K from its paramagnetic and non-ferroelectric phase to an antiferromagnetically ordered non-ferroelectric phase. On further cooling, ferroelectricity occurs at $T_{\text{FE}} \simeq 6.9$ K. The ferroelectric phase extends down to the experimental low-temperature limit of 0.25 K. The spontaneous polarization of this ferroelectric phase I is oriented along the direction \mathbf{a}' in the ab plane with a small deviation from the \mathbf{a} axis of $\angle(\mathbf{a}, \mathbf{a}') \simeq 7^\circ$. The detailed magnetic structure of this phase (as well as of all the other phases) is not known, but from the magnetization data it can be concluded that the spins are lying within the ac plane without a magnetic easy axis. As mentioned above in section 5.1, neutron-scattering data revealed a certain frustration potential for the analogous compounds $A_2[\text{FeCl}_5(\text{D}_2\text{O})]$ with $A = \text{K}, \text{Rb}$ [185, 186]. Assuming similar magnetic-exchange interactions for $(\text{NH}_4)_2[\text{FeCl}_5(\text{H}_2\text{O})]$, one may speculate that small structural changes due to the substitution with $A = \text{NH}_4$ could further enhance this magnetic frustration and lead to the occurrence of spin spirals in the ac plane. This then could act as the underlying mechanism of multiferroicity of $(\text{NH}_4)_2[\text{FeCl}_5(\text{H}_2\text{O})]$ via the inverse Dzyaloshinskii-Moriya interaction [93, 97]. In this case, the fact that the spins are lying in the ac plane would imply a spin current $\mathbf{j}_s = \mathbf{S}_i \times \mathbf{S}_j$ along \mathbf{b} . Therefore, the observed electric polarization, pointing nearly along \mathbf{a} (in low magnetic fields) would require a propagation vector \mathbf{r} of the spin spiral (nearly) along \mathbf{c} due to $\mathbf{P} \sim \mathbf{r} \times \mathbf{j}_s$, see section 2.2.2.

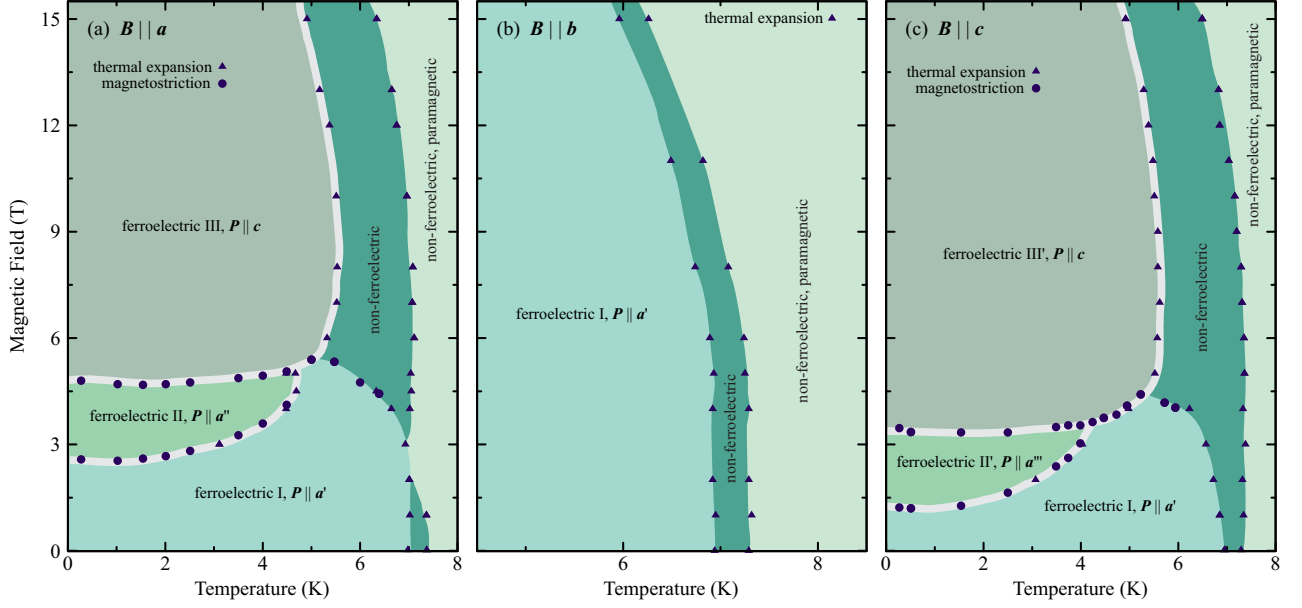


Figure 5.11: Magnetic-field versus temperature phase diagrams of $(\text{NH}_4)_2[\text{FeCl}_5(\text{H}_2\text{O})]$ for \mathbf{B} parallel to \mathbf{a} , \mathbf{b} and \mathbf{c} , respectively. The phase boundaries are based on the anomalies of the relative length changes $\Delta L_i(T, \mathbf{B})/L_i^0$ ($i = a, b$ or c) obtained from measurements of the thermal expansion (\triangle) or the magnetostriction (\circ) with increasing temperature or magnetic field, respectively. Almost discontinuous (and hysteretic) first-order phase transitions are marked by bold light-grey lines. For each of the different ferroelectric phases, the direction of the spontaneous electric polarization is denoted. All the vectors \mathbf{a}' , \mathbf{a}'' and \mathbf{a}''' lie within the ab plane with small deviations from the \mathbf{a} axis ($\angle(\mathbf{a}, \mathbf{a}') \simeq 7^\circ$, $\angle(\mathbf{a}, \mathbf{a}'') \simeq 9^\circ$, $\angle(\mathbf{a}, \mathbf{a}''') \simeq 5^\circ$).

As shown in figure 5.11 (b), there is little influence of a magnetic field $\mathbf{B}||\mathbf{b}$, which only causes a weak simultaneous decrease of both transition temperatures $T_{\text{FE}}(\mathbf{B})$ and $T_{\text{N}}(\mathbf{B})$. As expected for this field direction perpendicular to the magnetic easy plane, the magnetization linearly increases with field (see figure 5.5). Moreover, a weak decrease of the electric polarization can be inferred from figures 5.6 (b) and (e).

Magnetic fields applied either along \mathbf{a} or \mathbf{c} induce discontinuous transitions to other multiferroic phases. With increasing $\mathbf{B}||\mathbf{a}$ and at lowest temperatures, first a ferroelectric phase II is entered, in which the polarization tilts to $\mathbf{P}||\mathbf{a}''$ with $\angle(\mathbf{a}, \mathbf{a}'') \simeq 9^\circ$. At a larger field of about 4.5 T another discontinuous transition to a ferroelectric phase III occurs, where the spontaneous polarization increases by about a factor of 2.5 and rotates to $\mathbf{P}||\mathbf{c}$. The ferroelectric phase II only occurs below about 4.7 K, and in a small temperature window around 5 K direct discontinuous transitions between the ferroelectric phases I and III take place. Finally, above about 5.3 K continuous phase transitions between the ferroelectric phase I and the non-ferroelectric, antiferromagnetic phase are observed in the field range below about 5 T, while for higher fields discontinuous transitions between the non-ferroelectric, antiferromagnetic phase and the ferroelectric phase III take place. The transitions between the ferroelectric phases I and II cause rather weak anomalies in the magnetiza-

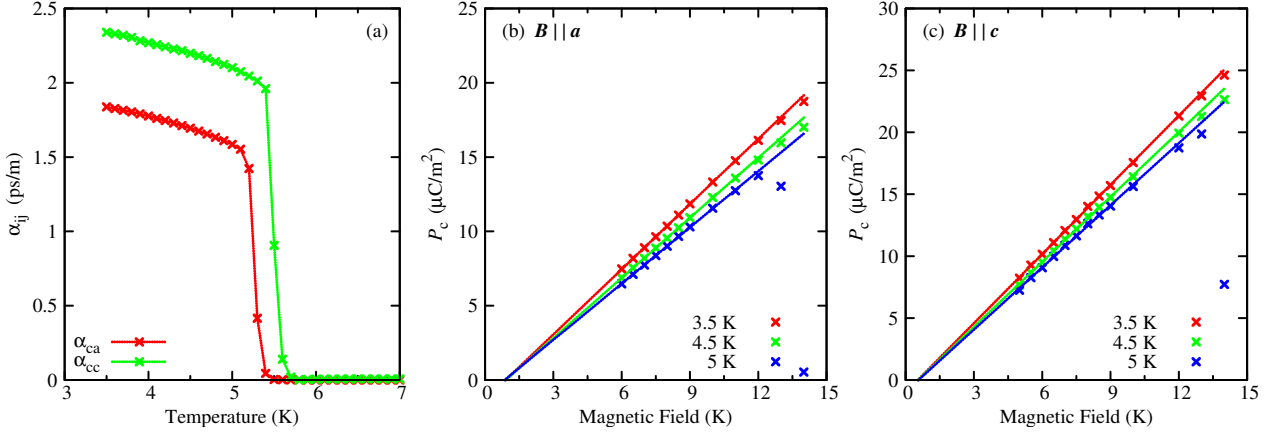


Figure 5.12: (a) Temperature dependence of the linear magnetoelectric coefficients α_{ca} and α_{cc} in SI units in the ferroelectric phases III and III' of $(\text{NH}_4)_2[\text{FeCl}_5(\text{H}_2\text{O})]$. (b)-(c) Magnetic-field dependences of the electric polarization of $(\text{NH}_4)_2[\text{FeCl}_5(\text{H}_2\text{O})]$ at representative temperatures for applied magnetic fields along a and c above the spin-flop transitions. The field-dependent data were obtained by resorting the temperature-dependent data of figure 5.6. The solid lines indicate linear fits to the data to determine the linear magnetoelectric coefficients.

tion, whereas those to the ferroelectric phase III are accompanied by a spin-flop transition. Most of the features described for $B \parallel a$ are also present for $B \parallel c$, but there are some significant differences. First of all, at the transition from the ferroelectric phase I to the intermediate phase II' the polarization rotates in the opposite sense to $P \parallel a'''$ with $\angle(a, a''') \simeq 5^\circ$. Secondly, the transition fields are somewhat smaller for $B \parallel c$ and the phase II'' only exists up to about 4 K. Consequently, the temperature window for a direct transition between the ferroelectric phases I and III' is wider than for $B \parallel a$. Finally, for $B \parallel c$, in the entire field range studied here, no direct transitions from the non-ferroelectric, paramagnetic phase to any of the multiferroic phases take place, whereas between 2 and 3 T for $B \parallel a$ there seems to be a small window for a direct transition to phase I. A direct transition of this type would require two different order parameters to be involved simultaneously. A similar case has been debated recently for CuO [192–194], where a direct transition from the non-ferroelectric, paramagnetic phase to the multiferroic phase had been reported originally. But more recently a sequence of two second-order phase transitions with very close critical temperatures, instead of one first-order phase transition was found in CuO [195, 196]. At present, it cannot be excluded that this might also be the case in $(\text{NH}_4)_2[\text{FeCl}_5(\text{H}_2\text{O})]$, but the actual data of both, thermal expansion and specific heat do not give any hint for the presence of two phase transitions in the field range of 2 to 3 T for $B \parallel a$.

Among all ferroelectric phases of the phase diagrams given in figure 5.11 the ferroelectric phases III and III' possess the most pronounced magnetoelectric effect, with a clear linear magnetic-field dependence of the polarization. From the slope $\partial P_i / \partial B_j = \mu_0 \alpha_{ij}$ derived in the context of figure 5.7, see section 5.3.3, the linear magnetoelectric coefficients $\alpha_{ca} \simeq 1.5$ ps/m and $\alpha_{cc} \simeq 2.1$ ps/m

result. For a comparison of these values with literature data of other magnetoelectric crystals it is more convenient to use dimensionless linear magnetoelectric coefficients α_{ij}^{G} as introduced by [109, 117], see section 2.3.1. Here, $\alpha_{ca}^{\text{G}} \simeq 4.6 \cdot 10^{-4}$ and $\alpha_{cc}^{\text{G}} \simeq 6.4 \cdot 10^{-4}$. According to equation 2.20, from these values the dimensionless rationalized Gaussian coefficients α_{ij}^{rG} can easily be determined:

$$\alpha_{ij}^{\text{rG}} = \frac{c}{4\pi} \alpha_{ij} = \frac{1}{4\pi} \alpha_{ij}^{\text{G}} \simeq \begin{cases} 3.7 \cdot 10^{-5}, & \text{for } ij = ca \\ 5.0 \cdot 10^{-5}, & \text{for } ij = cc \end{cases}$$

These values lie within the typical range of α^{rG} of 10^{-6} to 10^{-2} , as can be seen in a compilation of data given in [114]. The magnetoelectric effect of $(\text{NH}_4)_2[\text{FeCl}_5(\text{H}_2\text{O})]$ in the ferroelectric phases III and III' was also calculated for other temperatures, by fitting linear functions to the field-dependent polarization data between 3.5 K and 7 K. The resulting temperature dependences of the linear magnetoelectric coefficients α_{ca} and α_{cc} are presented in figure 5.12 (a). In figure 5.12 (b) and (c) the magnetic-field dependences of the electric polarization along a and c in the ferroelectric phases III and III' for representative temperatures are displayed, including linear fits to the data. Note that the non-ferroelectric, antiferromagnetic phase of $(\text{NH}_4)_2[\text{FeCl}_5(\text{H}_2\text{O})]$ shows no linear magnetoelectric effect, in contrast to $\text{K}_2[\text{FeCl}_5(\text{H}_2\text{O})]$, which is linear magnetoelectric in its antiferromagnetically ordered phase, see section 5.4. Consequently, the point group of the non-ferroelectric, antiferromagnetic phase of $(\text{NH}_4)_2[\text{FeCl}_5(\text{H}_2\text{O})]$ must be a non magnetoelectric subgroup of the point group $2/m$.

The results of the present investigations of a series of thermodynamic properties reveal that $(\text{NH}_4)_2[\text{FeCl}_5(\text{H}_2\text{O})]$ is a new multiferroic material. Multiferroicity in this compound arises at ~ 6.9 K, with preceding AFM ordering at ~ 7.3 K. While for low applied magnetic fields an electric polarization of about $3 \mu\text{C}/\text{m}^2$ is lying within the ab plane, it can be significantly enhanced and rotated to c for magnetic fields above about 5 T. The rather complex temperature versus magnetic-field phase diagrams of $(\text{NH}_4)_2[\text{FeCl}_5(\text{H}_2\text{O})]$ show several multiferroic/magnetoelectric phases, that differ in orientation and magnitude of the electric polarization and also in the orientation of the magnetic moments of iron. In order to characterize the different multiferroic/magnetoelectric phases of $(\text{NH}_4)_2[\text{FeCl}_5(\text{H}_2\text{O})]$ on the microscopic scale, and thus to enable an understanding of the underlying mechanism of multiferroicity of this compound, a detailed determination of the magnetic structures by means of neutron scattering is essential as a future investigation. However, because of the high content of hydrogen atoms (10 H per formula unit), this will require the use of the analogous deuterium compound $(\text{ND}_4)_2[\text{FeCl}_5(\text{D}_2\text{O})]$. Of course, a substantial influence of the isotope exchange on the relevant crystal properties is expected and will need a detailed investigation. Such studies could also help to clarify a possible influence of the system of hydrogen bonds on the phase transition at 79 K and on the mechanism of magnetoelectric multiferroicity in

$(\text{NH}_4)_2[\text{FeCl}_5(\text{H}_2\text{O})]$.

5.4 $A_2[\text{FeCl}_5(\text{H}_2\text{O})]$ with $A = \text{K}, \text{Rb}, \text{Cs}$

In the following, the results of the measurements of $A_2[\text{FeCl}_5(\text{H}_2\text{O})]$ with $A = \text{K}, \text{Rb}, \text{Cs}$ summarized in section 5.2 are presented, analysed and discussed in detail.

5.4.1 Magnetic properties

The magnetic-susceptibility measurements of $A_2[\text{FeCl}_5(\text{H}_2\text{O})]$ with $A = \text{K}, \text{Rb}, \text{Cs}$ are summarized in figure 5.13.⁶ The magnetic properties of all three compounds are rather similar. The low-field curves $\chi(T)$ show well-defined kinks at $T_N^K \simeq 14.3 \text{ K}$, $T_N^{\text{Rb}} \simeq 10.2 \text{ K}$ and $T_N^{\text{Cs}} \simeq 6.8 \text{ K}$ for $A = \text{K}, \text{Rb}$ and Cs , respectively, in agreement with previous results [176, 180, 185, 189, 191, 197]. In all three cases, χ_a decreases below T_N with decreasing temperature and approaches zero for $T \rightarrow 0 \text{ K}$, while χ_b and χ_c hardly change, indicating that the spins are oriented parallel to the \mathbf{a} axis, the magnetic easy axis. Note, however, that with respect to the zigzag chains of $[\text{FeCl}_5(\text{H}_2\text{O})]^{2-}$ octahedra the \mathbf{a} axis is oriented differently in the two structure types, see figure 5.1. Therefore, the magnetic easy axis in the Cs-based compound is perpendicular to that in the K-based and Rb-based compound. In the K-based and Rb-based compound T_N^K and T_N^{Rb} slightly decrease with increasing magnetic field independently from the field direction. In contrast, in the Cs-based compound T_N^{Cs} strongly decreases for all three field directions with increasing magnetic fields, which is in agreement with results of a Mössbauer study [198].

For larger magnetic fields parallel to \mathbf{a} , the decrease of $\chi_a(T)$ below T_N systematically vanishes for all compounds. Above the critical fields $B_{\text{SF}}^{\text{K}} \simeq 3.5 \text{ T}$, $B_{\text{SF}}^{\text{Rb}} \simeq 1.5 \text{ T}$ and $B_{\text{SF}}^{\text{Cs}} \simeq 1.2 \text{ T}$ the characteristics of $\chi_i(T)$ become nearly identical in all the compounds for all three magnetic-field directions \mathbf{a} , \mathbf{b} and \mathbf{c} , see figures 5.13 (a), (d) and (i), respectively. Therefore, spin-flop transitions occur at B_{SF}^A , with a rotation of the spins from being oriented along the \mathbf{a} axis to lying within the plane that is perpendicular to \mathbf{a} . These spin-flop transitions can also be seen in the low-temperature measurements of the magnetization as a function of the magnetic field, see the insets in figure 5.13 (a), (d), (i). Note that the field-dependent magnetization of the K-based compound was obtained by resorting the temperature-dependent magnetization data.

The inverse susceptibilities follow a Curie-Weiss behaviour from about 50 K up to room temperature for all three compounds, see the insets in figure 5.13 (b), (e), (g). Here, only the data of $1/\chi_b$ are displayed because the data of $1/\chi_a$ and $1/\chi_c$ for all the compounds are almost identical in the high-temperature regime. Linear fits to the data of $1/\chi_i^A$ for $T > 100 \text{ K}$ yield negative Weiss temperatures $\theta^A \simeq -39 \text{ K}$, -31 K , -12 K for $A = \text{K}, \text{Rb}$ and Cs , respectively, and an effec-

⁶The magnetic measurements presented in this section were performed in a squid magnetometer, see section 3.1.

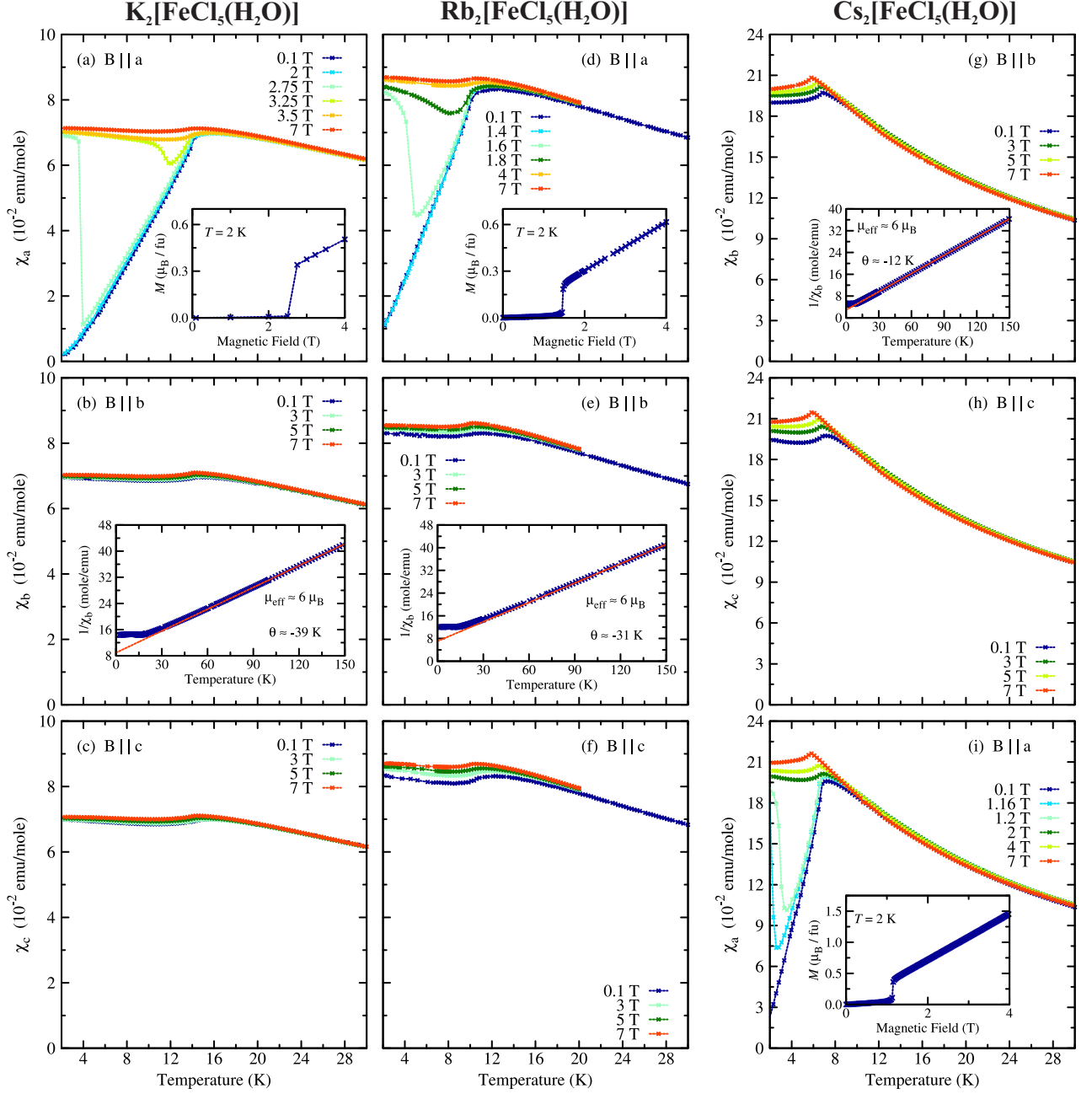


Figure 5.13: Temperature dependences of the magnetic susceptibility χ_a , χ_b , and χ_c of $A_2[\text{FeCl}_5(\text{H}_2\text{O})]$ for $A = \text{K}$ (a)-(c), $A = \text{Rb}$ (d)-(f), $A = \text{Cs}$ (g)-(i) for different magnetic fields parallel to a , b and c . The insets in (a), (d) and (i) show the magnetization at 2 K for a magnetic field parallel to a . The insets in (b), (e) and (g) show the temperature-dependent inverse susceptibility $1/\chi_b$ together with Curie-Weiss fits (lines) in the temperature range from 100 K to 300 K. Note that the $\{a, b, c\}$ axes in the $Pnma$ structure for $A = \text{K}, \text{Rb}$ correspond to the $\{b, c, a\}$ axes in the $Cmcm$ structure for $A = \text{Cs}$, see figure 5.1.

tive magnetic moment $\mu_{\text{eff}} \simeq 6 \mu_B$. The negative Weiss temperatures signal net antiferromagnetic exchange interactions, whose magnitude roughly scales with T_N . With increasing ionic radius of the alkali ions the sum of the exchange interactions diminishes, most probably due to the in-

creasing distance of the magnetic ions. The value of the effective magnetic moment lies close to $\mu_{\text{eff}} = g\mu_B\sqrt{S(S+1)} = 5.92\mu_B$, as expected for a $3d^5$ high-spin configuration of the Fe^{3+} ions and $g = 2$.

5.4.2 Dielectric properties

Figure 5.14 displays the temperature-dependent measurements of the electric polarization $\mathbf{P} = (P_a, P_b, P_c)$ of $A_2[\text{FeCl}_5(\text{H}_2\text{O})]$ with $A = \text{K}, \text{Rb}$ and Cs in magnetic fields applied parallel to \mathbf{a} , \mathbf{b} and \mathbf{c} . The corresponding pyroelectric currents can be found in appendix E.4. In none of the three compounds, an electric polarization arises below the corresponding Néel temperature in zero magnetic field. Applied magnetic fields, however, induce an electric polarization in all cases, which implies the presence of a magnetoelectric effect. The magnetic-field configurations, where no electric polarization is induced, are not presented here. The induced components of the electric polarization of $\text{K}_2[\text{FeCl}_5(\text{H}_2\text{O})]$ and $\text{Rb}_2[\text{FeCl}_5(\text{H}_2\text{O})]$ behave very similar with respect to their temperature and magnetic-field dependences. The induced electric polarization of $\text{Cs}_2[\text{FeCl}_5(\text{H}_2\text{O})]$ has slightly different characteristics.

As can be seen in figure 5.14 (a) and (d), P_a^K and P_a^{Rb} reach broad maxima around 12 K and 9 K, respectively, for $\mathbf{B}||\mathbf{a}$ and then approach zero for $T \rightarrow 0$ K. With increasing field strength the components P_a^K and P_a^{Rb} grow linearly in the low-field range until they are suppressed completely in the vicinity of the spin-flop fields at $B_{\text{SF}}^{\text{K}} = 3.5$ T and $B_{\text{SF}}^{\text{Rb}} = 1.5$ T, respectively. Above the spin-flop fields, electric polarizations P_c parallel to \mathbf{c} occur and then also grow linearly with further increasing magnetic fields, see figures 5.15 (a) and (b). For both compounds, the temperature dependences of P_b and P_c for $\mathbf{B}||\mathbf{b}$ and $\mathbf{B}||\mathbf{c}$, respectively, are very similar to each other, but different from P_a for $\mathbf{B}||\mathbf{a}$, see figure 5.14 (b), (c), (e) and (f). In both cases the induced polarizations depend again linearly on the field strength and P_c is about one order of magnitude larger than P_b .

In $\text{Cs}_2[\text{FeCl}_5(\text{H}_2\text{O})]$, a magnetic field parallel to \mathbf{a} induces an electric polarization along \mathbf{b} , while a magnetic field parallel to \mathbf{b} causes an electric polarization along \mathbf{a} , see figure 5.14 (g), (h). The temperature dependence of P_b^{Cs} for $\mathbf{B}||\mathbf{a}$ is very similar to that of P_a^K and P_a^{Rb} for $\mathbf{B}||\mathbf{a}$. It reaches a broad maximum around 5 K and then approaches zero for $T \rightarrow 0$ K. In the vicinity of the spin-flop field $B_{\text{SF}}^{\text{Cs}} = 1.2$ T, P_b^{Cs} is suppressed completely and instead an electric polarization with the components P_a^{Cs} and P_c^{Cs} arises, see figure 5.15 (c) and (d). For $\mathbf{B}||\mathbf{b}$, an electric polarization along \mathbf{a} is created, which saturates quickly with decreasing temperature and for $\mathbf{B}||\mathbf{c}$ no electric polarization at all emerges.

The occurrence of the magnetic-field induced electric polarizations for $T < T_N$ also causes anomalies in the temperature and magnetic-field dependences of the corresponding longitudinal components ϵ_i^r of the dielectric tensor. To illustrate this, representative measurements of the temperature-

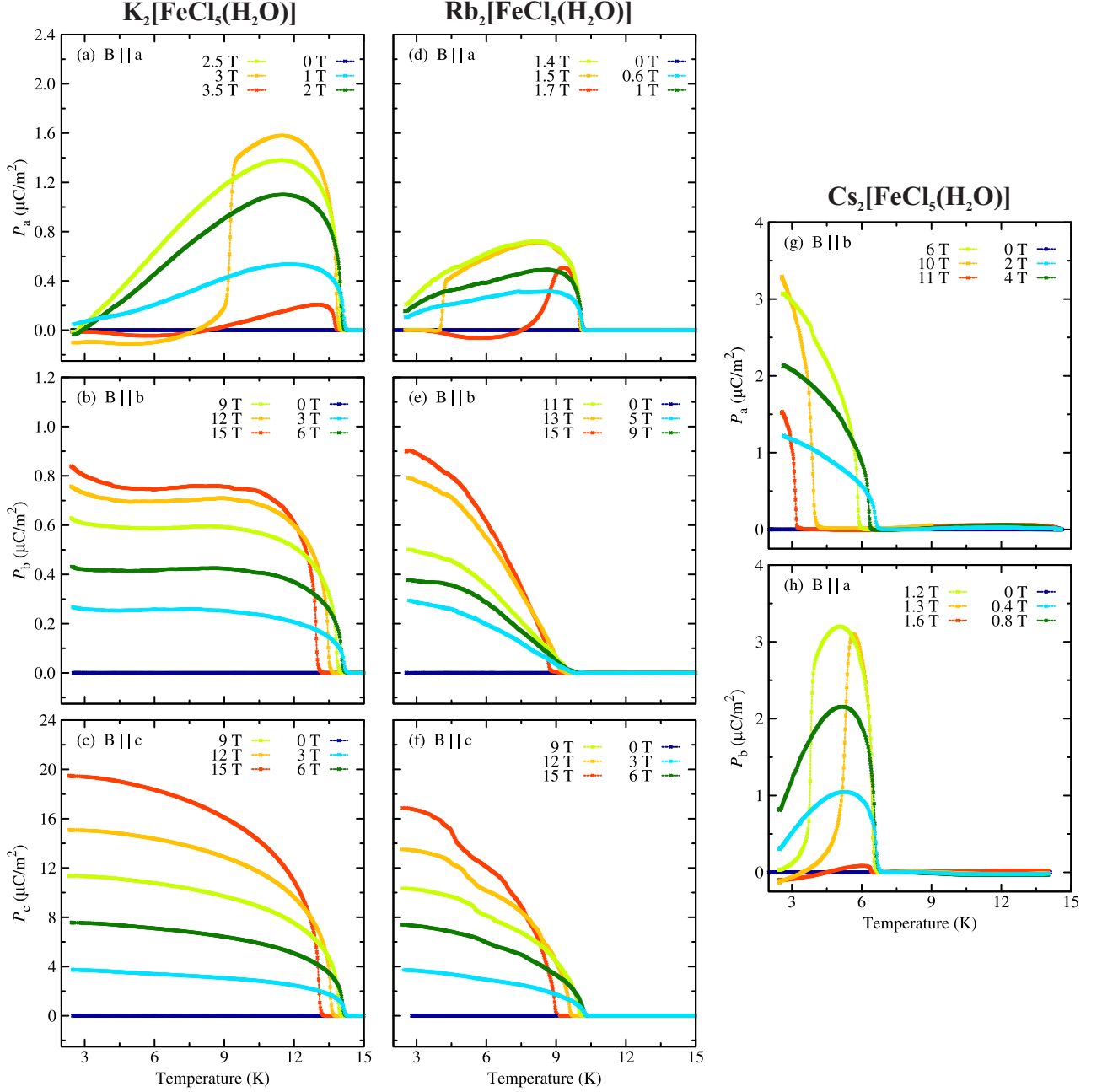


Figure 5.14: Temperature dependences of the electric polarization P_a , P_b and P_c of (a)-(c) $\text{K}_2[\text{FeCl}_5(\text{H}_2\text{O})]$, (d)-(f) $\text{Rb}_2[\text{FeCl}_5(\text{H}_2\text{O})]$ and (g)-(h) $\text{Cs}_2[\text{FeCl}_5(\text{H}_2\text{O})]$ for magnetic fields applied parallel to the a , b or c axis, respectively. The magnetic-field configurations, where no electric polarization is induced, are not presented here.

dependent dielectric constants ϵ_i^r ($i = a, b, c$) of $\text{K}_2[\text{FeCl}_5(\text{H}_2\text{O})]$ for \mathbf{B} parallel to a , b and c are displayed in figure 5.16. The zero-field curves show only faint kinks at T_N , but in finite magnetic fields, spiky anomalies occur at the transition temperatures, which grow in intensity with increasing magnetic field in all cases. For $\mathbf{B} \parallel a$, above the magnetic spin-flop field, the spiky anomaly

5.4 $A_2[\text{FeCl}_5(\text{H}_2\text{O})]$ with $A = \text{K}, \text{Rb}, \text{Cs}$

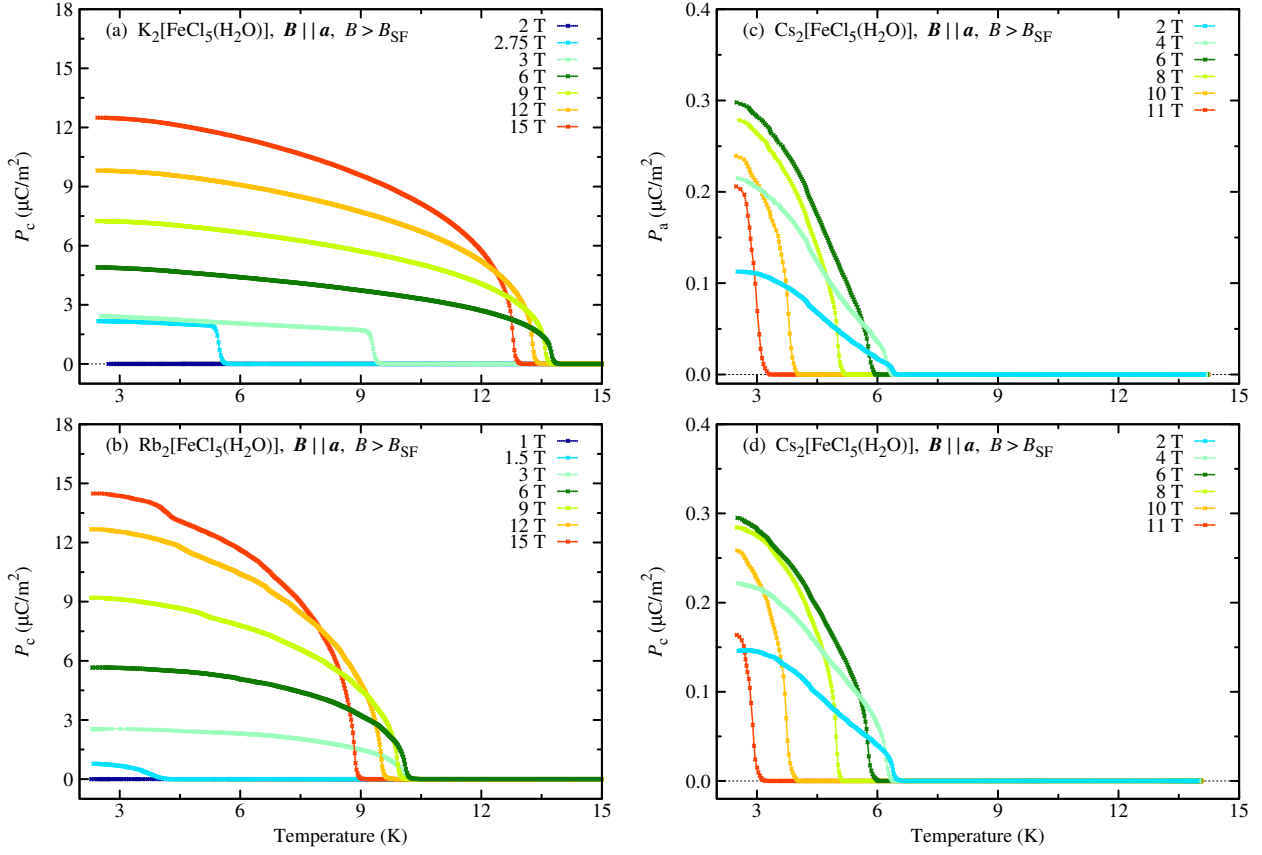


Figure 5.15: Temperature dependences of the electric polarization P_a and P_c of (a) $\text{K}_2[\text{FeCl}_5(\text{H}_2\text{O})]$, (b) $\text{Rb}_2[\text{FeCl}_5(\text{H}_2\text{O})]$ and (c)-(d) $\text{Cs}_2[\text{FeCl}_5(\text{H}_2\text{O})]$ for magnetic fields applied parallel to the a axis above the spin-flop transitions.

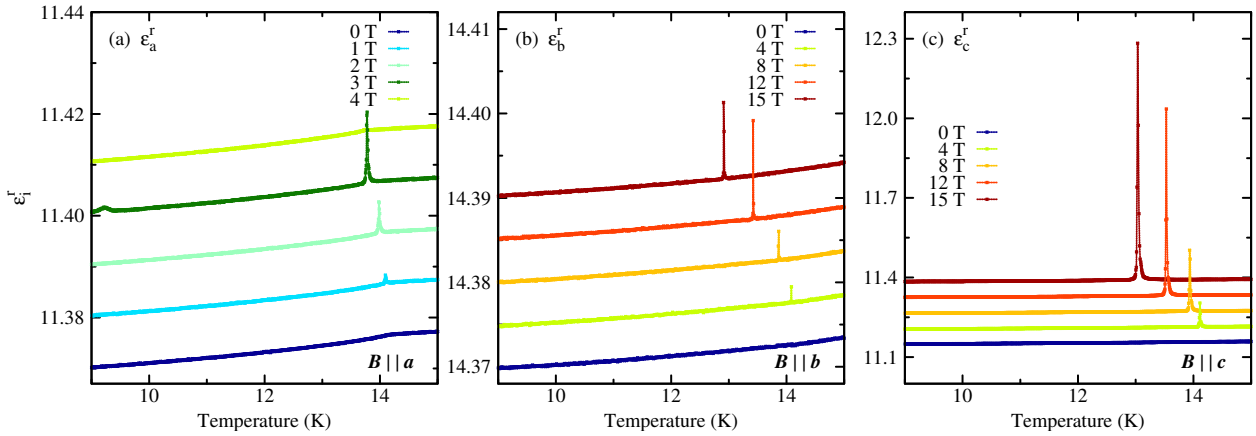


Figure 5.16: Representative temperature dependences of the longitudinal components of the dielectric tensor ϵ_i^r ($i = a, b, c$ from left to right) of $\text{K}_2[\text{FeCl}_5(\text{H}_2\text{O})]$ for different magnetic fields applied parallel to a , b or c . For clarity, with increasing field strength the curves are shifted with respect to each other by constant offsets of 0.01 in (a), 0.005 in (b) and 0.06 in (c).

disappears again, while for the other field directions the anomalies stay present up to the maximum field of 15 T. In the vicinity of the spin-flop field, a second anomaly occurs, which coincides with the suppression of the electric polarization component P_a .

5.4.3 Magnetolectric effect

For magnetic fields well below or above the spin-flop fields, the magnetic-field induced electric polarization in $A_2[\text{FeCl}_5(\text{H}_2\text{O})]$ with $A = \text{K}, \text{Rb}, \text{Cs}$ depends in all cases linearly on the magnetic-field strength. This indicates that all three compounds are linear magnetoelectrics. The linear field dependence of the electric polarization of all compounds is illustrated in figures 5.17 and 5.18, by plotting the components P_i^K , P_i^{Rb} and P_i^{Cs} ($i = a, b, c$) as functions of the magnetic field at representative temperatures. Linear fits to the magnetic-field dependent electric polarization data yield the linear magnetoelectric tensor components $\alpha_{ij}(T) = \partial\mu_0 P_i(T)/\partial B_j$ in SI units.

The linear magnetoelectric tensors of $\text{K}_2[\text{FeCl}_5(\text{H}_2\text{O})]$ and $\text{Rb}_2[\text{FeCl}_5(\text{H}_2\text{O})]$ have a diagonal form with the non-zero components α_{11} , α_{22} and α_{33} . This result is compatible with the magnetic point-group symmetry $m'm'm'$, determined by neutron-diffraction measurements [185, 186], see appendix G. The temperature dependences and absolute values of corresponding tensor components $\alpha_{ii}(T)$ of both compounds are very similar to each other, as can be seen in figure 5.19 (a), (d). Below the Néel temperatures $\alpha_{22}(T)$ and $\alpha_{33}(T)$ grow strongly and then saturate with decreasing temperature, while $\alpha_{11}(T)$ first reaches a broad maximum and finally approaches zero for $T \rightarrow 0$. In contrast to the K-based and Rb-based compound, $\text{Cs}_2[\text{FeCl}_5(\text{H}_2\text{O})]$ has only off-diagonal tensor components α_{21} and α_{12} . The component $\alpha_{21}(T)$ has an analogous temperature dependence as $\alpha_{11}^{\text{K,Rb}}(T)$ and the component $\alpha_{12}(T)$ behaves similar to $\alpha_{22}^{\text{K,Rb}}(T)$ and $\alpha_{33}^{\text{K,Rb}}(T)$, see figure 5.19 (g). The linear magnetoelectric tensors of $A_2[\text{FeCl}_5(\text{H}_2\text{O})]$ with $A = \text{K}, \text{Rb}, \text{Cs}$ calculated at representative temperatures are displayed in table 5.4.3.

The spin-flop transitions for $\mathbf{B}||\mathbf{a}$ lead to a modification of the magnetoelectric responses in all $A_2[\text{FeCl}_5(\text{H}_2\text{O})]$ compounds. For $A = \text{K}$ or Rb , the component α_{11} is suppressed and α_{31} occurs. For $A = \text{Cs}$, the component α_{21} is suppressed and α_{11} as well as α_{31} occur. Their temperature dependences are very similar to each other, see figures 5.19 (c), (f) and (i). The behaviour of the other tensor components in the spin-flop phases could not be determined because in the used experimental setup it was not possible to apply a constant magnetic field $B > B_{\text{SF}}$ parallel to \mathbf{a} , while applying a variable magnetic field parallel to \mathbf{b} or \mathbf{c} .

For collinear antiferromagnetic magnetoelectrics, the temperature dependences of the linear magnetoelectric tensor components for \mathbf{B} parallel ($\alpha_{||}$) and \mathbf{B} perpendicular (α_{\perp}) to the magnetic easy axis are characterized by the product of the corresponding magnetic susceptibilities $\chi_{||}(T)$ and $\chi_{\perp}(T)$ with the sublattice magnetization $\bar{S}(T)$ according to equation 2.22 in section 2.3.2.

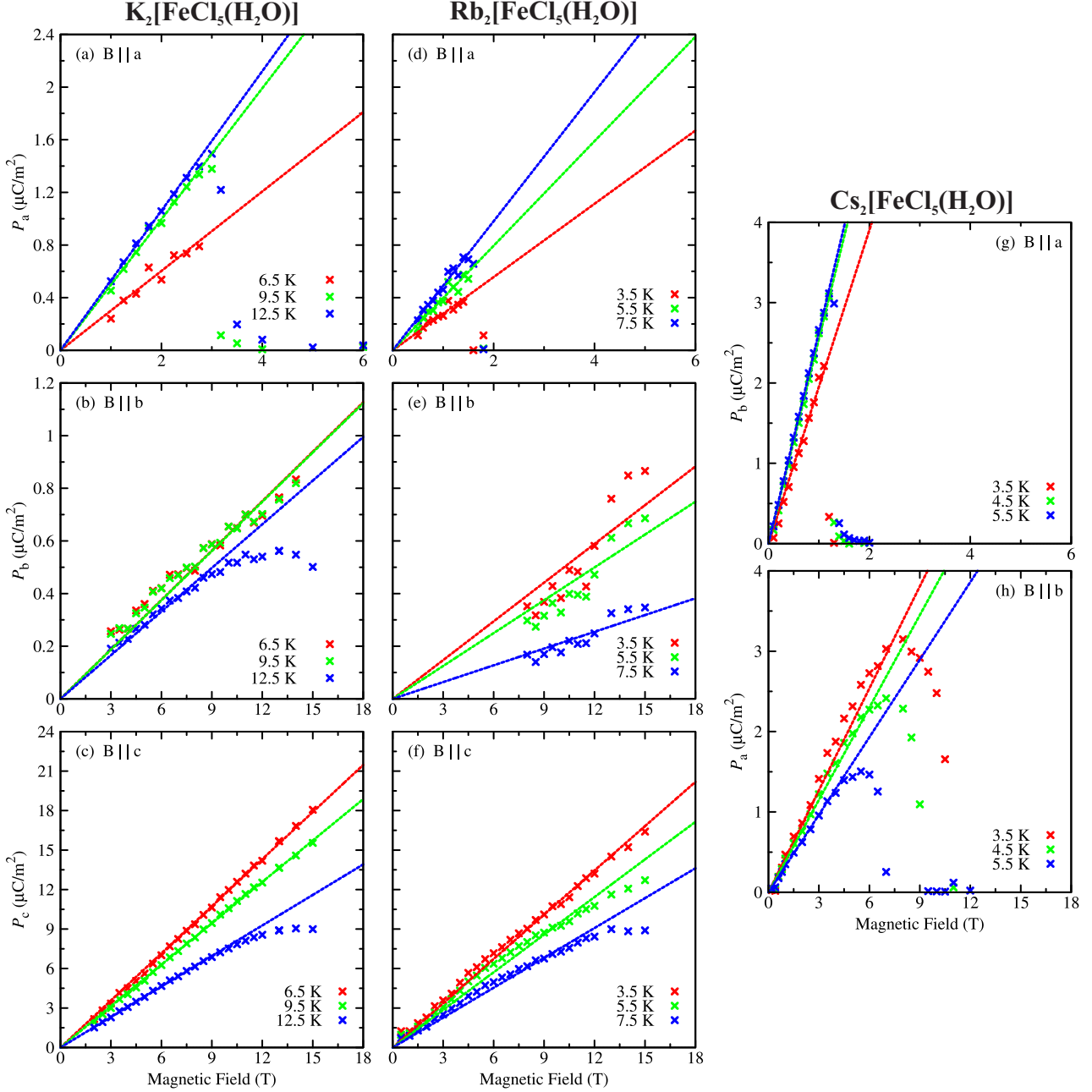


Figure 5.17: Magnetic-field dependences of the electric polarization of (a)-(c) $\text{K}_2[\text{FeCl}_5(\text{H}_2\text{O})]$, (d)-(f) $\text{Rb}_2[\text{FeCl}_5(\text{H}_2\text{O})]$ and (g)-(h) $\text{Cs}_2[\text{FeCl}_5(\text{H}_2\text{O})]$ at representative temperatures. The field-dependent data were obtained by resorting the temperature-dependent data of figure 5.14. The solid lines are linear fits to the data for small magnetic-field strengths. Note that in the case of $\text{Cs}_2[\text{FeCl}_5(\text{H}_2\text{O})]$ no electric polarization is induced for $B \parallel c$.

As is shown in figure 5.19 the determined temperature-dependent $\alpha_{ij}(T)$ well agree to the expected behaviour according to equation 2.22. For magnetic fields perpendicular to the magnetic easy axis ($B \parallel b$ or $B \parallel c$), the temperature dependences of the magnetoelectric responses are dominated by that of the sublattice magnetization \bar{S} because the corresponding magnetic susceptibil-

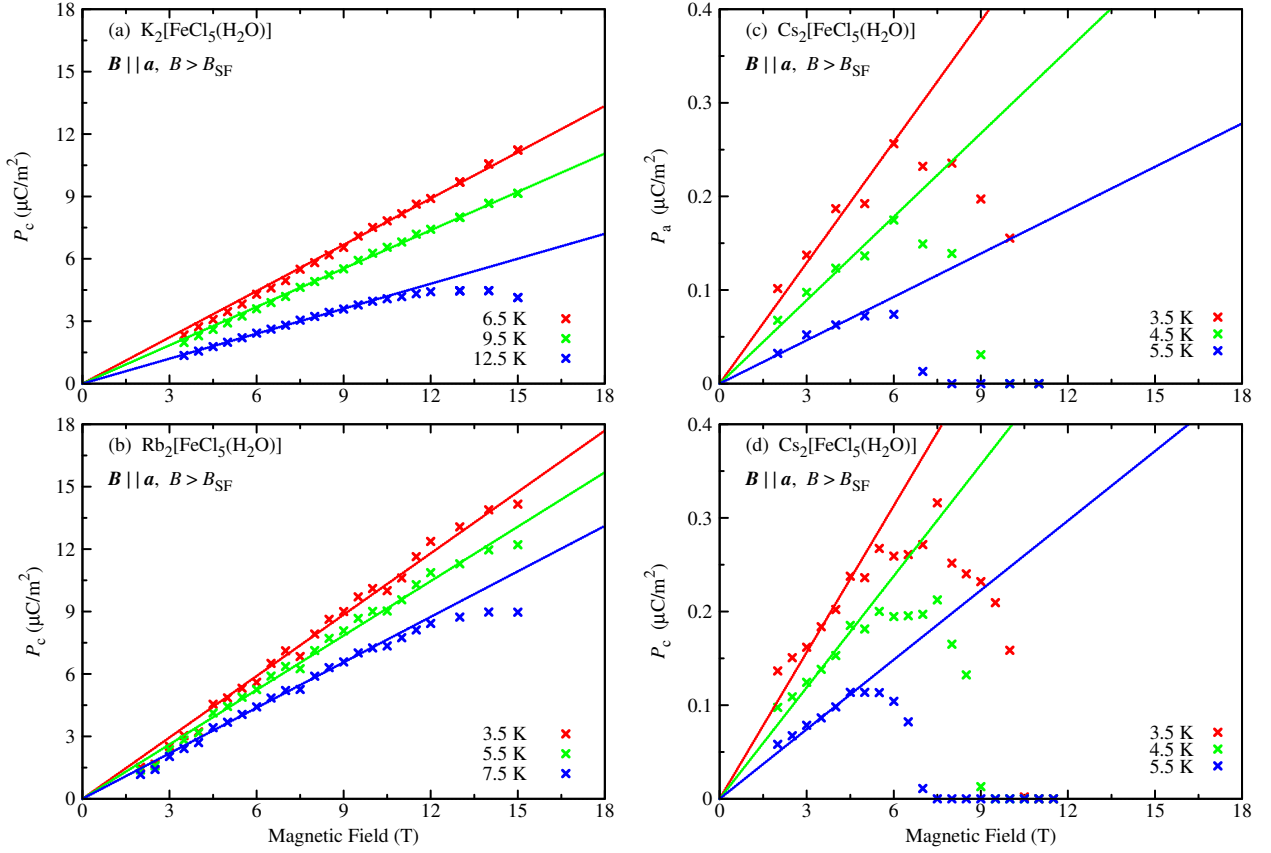


Figure 5.18: Magnetic-field dependences of the electric polarization of (a) $\text{K}_2[\text{FeCl}_5(\text{H}_2\text{O})]$, (b) $\text{Rb}_2[\text{FeCl}_5(\text{H}_2\text{O})]$ and (c)-(d) $\text{Cs}_2[\text{FeCl}_5(\text{H}_2\text{O})]$ at representative temperatures for applied magnetic fields along a above the spin-flop transition. The field-dependent data were obtained by resorting the temperature-dependent data of figure 5.15. The solid lines indicate linear fits to the data for small magnetic-field strengths.

ities stay nearly constant below T_N , see figure 5.13. Therefore, $\alpha_{22}(T)$, $\alpha_{33}(T)$ for the K-based and Rb-based compound and $\alpha_{12}(T)$ for $\text{Cs}_2[\text{FeCl}_5(\text{H}_2\text{O})]$ have the form of an order parameter. For magnetic fields parallel to the magnetic easy axis ($\mathbf{B} \parallel \mathbf{a}$), the temperature dependences of the magnetoelectric responses are dominated by the corresponding magnetic susceptibilities, which approach zero for $T \rightarrow 0$. Therefore, $\alpha_{11}(T)$ for the K-based and Rb-based compound and $\alpha_{21}(T)$ for $\text{Cs}_2[\text{FeCl}_5(\text{H}_2\text{O})]$ approach zero as well for $T \rightarrow 0$. The different temperature characteristics of the magnetoelectric responses are further illustrated in figures 5.19 (b), (e) and (h), where the ratios $\alpha_{\parallel}/\chi_{\parallel}$ and $\alpha_{\perp}/\chi_{\perp}$ are displayed.⁷ In most of the cases the expected temperature dependence of an order parameter is nicely reproduced. Partially, slight deviations occur in the low-temperature limit. These can be explained by problems in determining the accurate absolute values of the electric polarization from the results of pyroelectric-current measurements, when the respective

⁷For the calculation of the ratios α/χ , the magnetic volume susceptibilities in SI units $\chi^{\text{SI}} = 4\pi\chi^{\text{CGS,mol}}/V_{\text{mol}}$ are used.

5.4 $A_2[\text{FeCl}_5(\text{H}_2\text{O})]$ with $A = \text{K, Rb, Cs}$

compound	T (K)	$[\alpha_{ij}]_{\text{AF}}$ (ps/m)	$[\alpha_{ij}]_{\text{SF}}$ (ps/m)
$\text{K}_2[\text{FeCl}_5(\text{H}_2\text{O})]$	11 K	$\begin{bmatrix} 0.71 & \sim 0 & \sim 0 \\ \sim 0 & 0.08 & \sim 0 \\ \sim 0 & \sim 0 & 1.17 \end{bmatrix}$	$\begin{bmatrix} \sim 0 & - & - \\ \sim 0 & - & - \\ 0.71 & - & - \end{bmatrix}$
$\text{Rb}_2[\text{FeCl}_5(\text{H}_2\text{O})]$	8 K	$\begin{bmatrix} 0.63 & \sim 0 & \sim 0 \\ \sim 0 & 0.02 & \sim 0 \\ \sim 0 & \sim 0 & 0.98 \end{bmatrix}$	$\begin{bmatrix} \sim 0 & - & - \\ \sim 0 & - & - \\ 1.0 & - & - \end{bmatrix}$
$\text{Cs}_2[\text{FeCl}_5(\text{H}_2\text{O})]$	5 K	$\begin{bmatrix} \sim 0 & 0.45 & \sim 0 \\ 3.35 & \sim 0 & \sim 0 \\ \sim 0 & \sim 0 & \sim 0 \end{bmatrix}$	$\begin{bmatrix} 0.03 & - & - \\ \sim 0 & - & - \\ 0.02 & - & - \end{bmatrix}$

Table 5.3: Linear magnetoelectric tensors of $A_2[\text{FeCl}_5(\text{H}_2\text{O})]$ with $A = \text{K, Rb, Cs}$ at representative temperatures. The tensors in the right column refer to the spin-flop phases for $B > B_{\text{SF}}$ along \mathbf{a} , where only the components α_{i1} could be determined.

pyroelectric currents hardly exceed the background currents, see section 3.2.7.

As mentioned in the introduction, the magnetic structure of $\text{Cs}_2[\text{FeCl}_5(\text{H}_2\text{O})]$ is still unknown. With the knowledge of the anisotropy of the linear magnetoelectric effect of $\text{Cs}_2[\text{FeCl}_5(\text{H}_2\text{O})]$ it is, however, possible to deduce its magnetic space group by the following symmetry analysis.

Starting with the point-group symmetry $\frac{2}{m} \frac{2}{m} \frac{2}{m}$ for the prototypic, paramagnetic phase of $\text{Cs}_2[\text{FeCl}_5(\text{H}_2\text{O})]$, the only possible magnetic point groups, compatible with the form of the linear magnetoelectric tensor, are $mm2$, $2'mm'$, $2'2'2$ and mmm' , see appendix G. The magnetic-susceptibility measurements reveal that the spins are ordered antiferromagnetically below the Néel temperature with \mathbf{a} as the magnetic easy axis. In addition, the results of the dielectric investigations show that in the antiferromagnetically ordered phase no electric polarization occurs in zero magnetic field. Therefore, the two polar groups $mm2$ and $2'mm'$ can be (almost certainly) excluded, as well as the ferromagnetic group $2'2'2$. Hence, the only remaining possibility is the magnetic point group $mmm' \triangleq \frac{2'}{m} \frac{2'}{m} \frac{2'}{m}$. Including the information about the space group $Cmcm \triangleq C \frac{2}{m} \frac{2}{c} \frac{2}{m}$ of the room-temperature crystal structure of $\text{Cs}_2[\text{FeCl}_5(\text{H}_2\text{O})]$, the (only possible) magnetic space group for its linear magnetoelectric phase is $C \frac{2'}{m} \frac{2'}{c} \frac{2_1}{m'}$, which corresponds to the magnetic space group number 63.5.515 according to [187]. With this knowledge, a model for the magnetic structure of $\text{Cs}_2[\text{FeCl}_5(\text{H}_2\text{O})]$ can be derived. Starting with a spin at an arbitrary Fe site oriented along \mathbf{a} , the orientations of all the other spins within the structure follow by applying all the symmetry elements of the magnetic space group $C \frac{2'}{m} \frac{2'}{c} \frac{2_1}{m'}$. In figure 5.20 the resulting magnetic structure of $\text{Cs}_2[\text{FeCl}_5(\text{H}_2\text{O})]$ below $T_N = 6.8$ K is displayed for one unit cell. The spin direction alternates between $\pm \mathbf{a}$ along the zigzag chains of the $[\text{FeCl}_5(\text{H}_2\text{O})]^{2-}$ octahedra running along \mathbf{c} and the spins

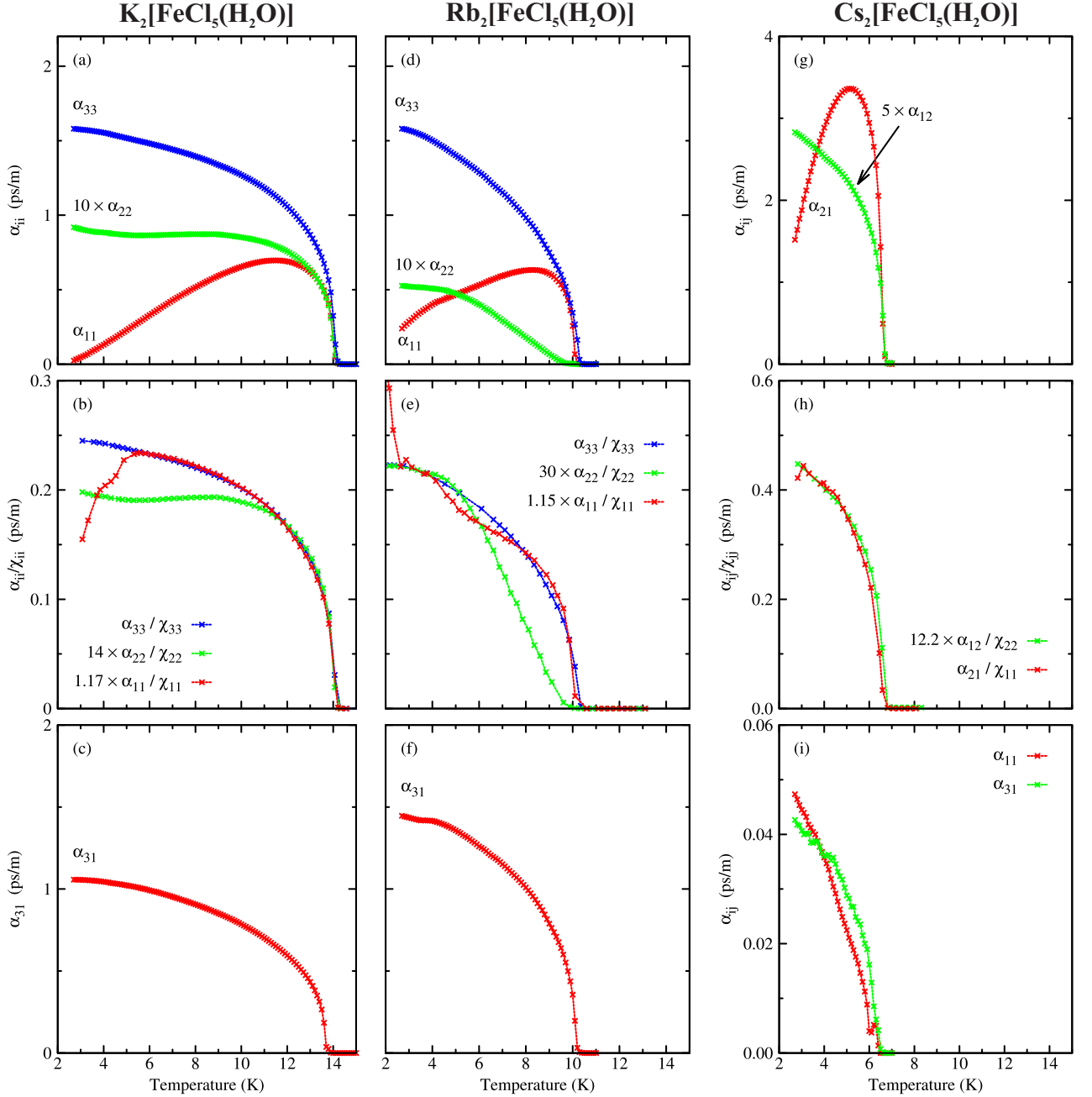


Figure 5.19: Magnetolectric properties of $A_2[\text{FeCl}_5(\text{H}_2\text{O})]$ with $A = \text{K}, \text{Rb}, \text{Cs}$. (a), (d), (g) Temperature dependences of the linear magnetolectric coefficients in the antiferromagnetic phases. (b), (e), (h) Temperature dependence of $\alpha_{\parallel}/\chi_{\parallel}$ for \mathbf{B} parallel to the magnetic easy axis and of $\alpha_{\perp}/\chi_{\perp}$ for \mathbf{B} perpendicular to the magnetic easy axis. (c), (f), (i) Temperature dependence of the linear magnetolectric coefficients in the spin-flop phases.

of neighbouring chains are in phase. Therefore, the magnetic structure of the Cs-based compound is of the same type as that of the K-based and Rb-based compounds. The direction of the AFM zigzag chains is equivalent in the $Pnma$ -type and $Cmcm$ -type structure, but the orientations of

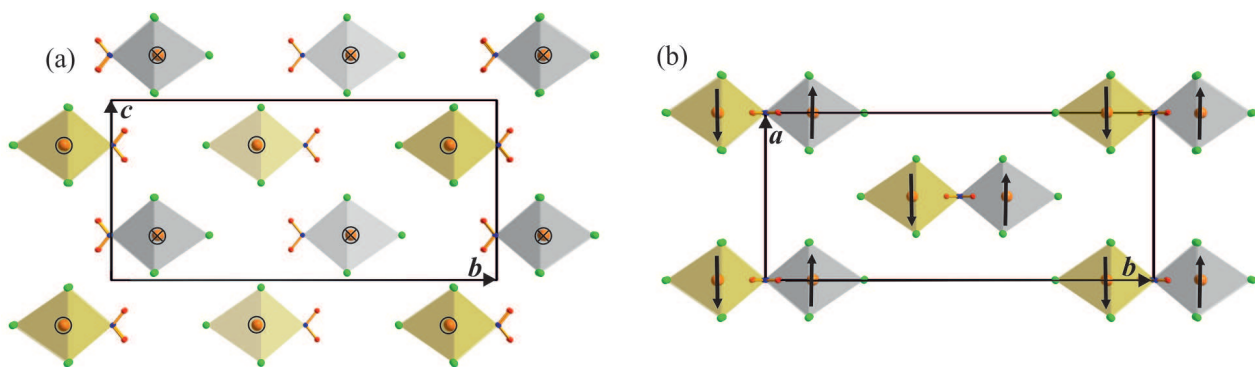


Figure 5.20: Magnetic structure of $\text{Cs}_2[\text{FeCl}_5(\text{H}_2\text{O})]$ below $T_N = 6.8 \text{ K}$, deduced from a symmetry analysis of its linear magnetoelectric tensor. The spin directions are along $\pm \mathbf{a}$ as indicated by \circ versus \times in the view along \mathbf{a} (left) and by arrows in the view along \mathbf{c} . Along the zigzag chains running along \mathbf{c} the spin direction alternates between $\pm \mathbf{a}$, whereas the spins of neighbouring chains are in phase.

the magnetic easy axes differ by 90° .

5.4.4 Phase diagrams and conclusion

The present investigations reveal that all compounds $A_2[\text{FeCl}_5(\text{H}_2\text{O})]$ with $A = \text{K}, \text{Rb}, \text{Cs}$ are linear magnetoelectrics. By means of their magnetic-field versus temperature phase diagrams for $\mathbf{B} \parallel \mathbf{a}$, their properties are summarized and compared in the following, see figure 5.21. The phase boundaries are based on the results of the dielectric investigations and the magnetic-susceptibility measurements. The three phase diagrams are very similar to each other. For each compound there exists a paramagnetic phase (PM), a linear magnetoelectric, antiferromagnetically ordered phase (AF, ME) and a linear magnetoelectric spin-flop phase (SF, ME). With increasing ionic radius of the alkali metal in the crystal structure ($r_{\text{Cs}} > r_{\text{Rb}} > r_{\text{K}}$), the zero-field transition temperature decreases from $T_N^{\text{K}} = 14.3 \text{ K}$ and $T_N^{\text{Rb}} = 10.2 \text{ K}$ to $T_N^{\text{Cs}} = 6.8 \text{ K}$. In the same way the magnetic spin-flop transition fields reduce from $B_{\text{SF}}^{\text{K}} = 3.5 \text{ T}$ and $B_{\text{SF}}^{\text{Rb}} = 1.5 \text{ T}$ to $B_{\text{SF}}^{\text{Cs}} = 1.2 \text{ T}$. The phase boundaries of the K-based and Rb-based compound hardly change with field, while that of the Cs-based compound is strongly bent towards lower temperatures for increasing magnetic-field strength. Figure 5.21 only displays the phase diagrams for \mathbf{B} parallel to \mathbf{a} because, apart from the absence of spin-flop transitions, the respective phase boundaries for \mathbf{B} parallel to \mathbf{b} and \mathbf{c} essentially coincide with the phase boundaries for \mathbf{B} parallel to \mathbf{a} for all three compounds.

The magnetic point group $m'm'm'$, determined for $\text{K}_2[\text{FeCl}_5(\text{D}_2\text{O})]$ and $\text{Rb}_2[\text{FeCl}_5(\text{D}_2\text{O})]$ via neutron scattering [185, 186] is consistent with the results of the present magnetoelectric investigations. For both compounds, the linear magnetoelectric tensor has a diagonal form with the components α_{11} , α_{22} and α_{33} . This tensor form would also allow the point-group symmetry 222

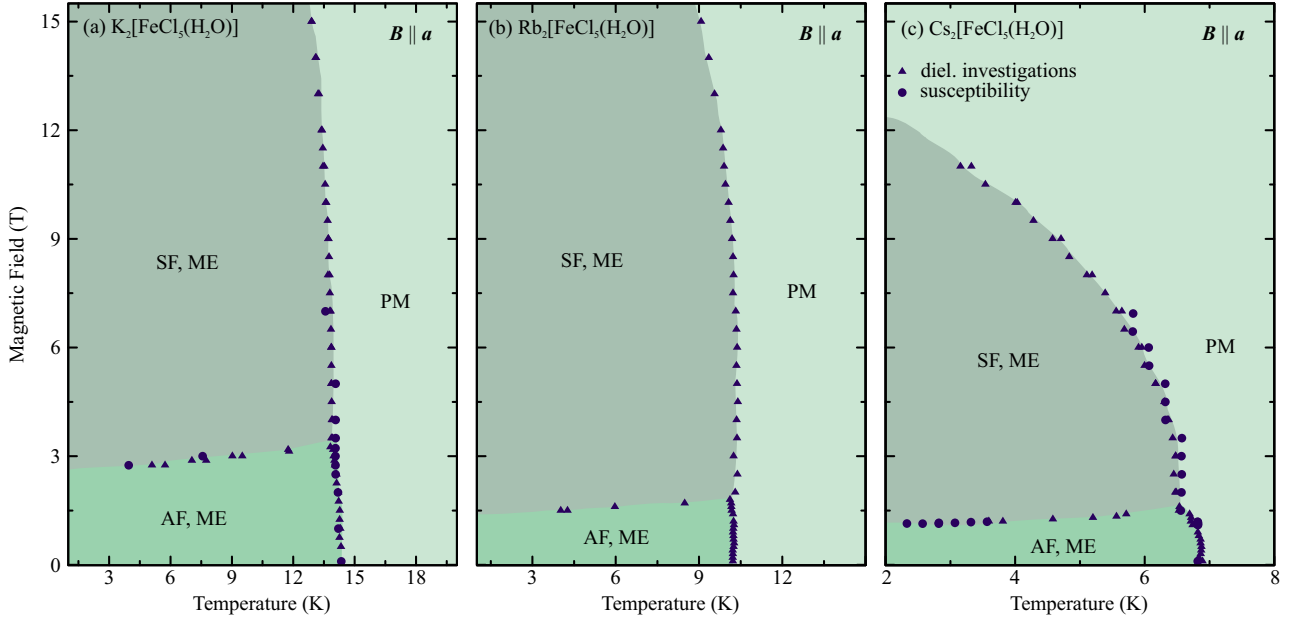


Figure 5.21: Magnetic-field versus temperature phase diagrams of $\text{K}_2[\text{FeCl}_5(\text{H}_2\text{O})]$, $\text{Rb}_2[\text{FeCl}_5(\text{H}_2\text{O})]$ and $\text{Cs}_2[\text{FeCl}_5(\text{H}_2\text{O})]$ for B parallel a . The vertical phase boundaries between the paramagnetic and antiferromagnetic phases for B parallel b and c coincide within the experimental uncertainty with the respective ones for B parallel a . The phase boundaries are based on the dielectric and magnetic measurements.

and $m'm'/2$. Because $m'm'/2$ is polar and no electric polarization is observed in zero magnetic field for both compounds, it can be excluded. The point group 222 however, is like $m'm'm'$ consistent with the results of the present study. For $\text{Cs}_2[\text{FeCl}_5(\text{H}_2\text{O})]$, the linear magnetoelectric tensor has only the off-diagonal elements α_{12} and α_{21} , which leads after a symmetry analysis to the magnetic point group mmm' and magnetic space group $C_{\frac{2'}{m} \frac{2'}{c} \frac{2_1}{m'}}$ for the magnetoelectric phase of this compound. Based on this result, the model shown in figure 5.20 is proposed for the magnetic structure of $\text{Cs}_2[\text{FeCl}_5(\text{H}_2\text{O})]$, which is of the same type as that of the K-based and Rb-based compound. However the orientations of the magnetic easy axes in both structure types are different.

Although the alkali-based compounds investigated in the present work are structurally closely related to $(\text{NH}_4)_2[\text{FeCl}_5(\text{H}_2\text{O})]$, their magnetic properties are less complex and consequently they are only linear magnetoelectrics. The spin structure of $(\text{NH}_4)_2[\text{FeCl}_5(\text{H}_2\text{O})]$ exhibits an XY anisotropy with a magnetic easy plane. Interestingly, this easy plane corresponds to the plane that is spanned by the two different orientations of the magnetic easy axes found in the K-based and Rb-based compound on the one hand and in the Cs-based compound on the other hand. Therefore, already slight crystal-chemical modifications within the erythrosiderite-type structure can change the orientation of the easy axes either by 90° or even transform the easy-axis anisotropy into an easy-plane anisotropy. The fact that the easy-plane anisotropy allows the occurrence of a spiral spin structure suggests that such spin spirals may induce the multiferroicity in $(\text{NH}_4)_2[\text{FeCl}_5(\text{H}_2\text{O})]$ via

the so-called inverse Dzyaloshinskii-Moriya mechanism [97].

Chapter 6

Explorative studies of potential multiferroic compounds

6.1 NaFe(WO₄)₂

6.1.1 Introduction

The discovery of spin-driven multiferroicity in MnWO₄ [14, 19–21] some years ago led to the search for other multiferroic materials in the tungstate family [14]. Especially NaFe(WO₄)₂ was investigated in more detail and the results of first dielectric measurements indicated that this compound could be another new multiferroic [14]. The crystal structure of NaFe(WO₄)₂ is a modification of the well-known MnWO₄ structure by a coupled substitution of Na⁺ and Fe³⁺ ions for the Mn²⁺ ions. NaFe(WO₄)₂ crystallizes in the monoclinic space group *P*2/*c* with the lattice parameters $a = 9.88 \text{ \AA}$, $b = 5.72 \text{ \AA}$, $c = 4.94 \text{ \AA}$ and $\beta = 90 \pm 0.5^\circ$ at room temperature [222]. The crystal structure consists of one-dimensional zigzag chains of edge-sharing [FeO₆] octahedra, [WO₆] octahedra and [NaO₆] octahedra running along the *c* axis, see figure 6.1 (a). The three different chain systems are arranged in neighbouring planes perpendicular to the *a* axis, leading to a layered structure with a sequence of [FeO₆]-[WO₆]-[NaO₆]-[WO₆] layers.

Although the distance between the [FeO₆] planes is rather large with about 10 Å, a three-dimensional collinear antiferromagnetic order sets in at about 4 K in NaFe(WO₄)₂ with the spins being oriented along the *a* axis [14, 223, 224]. The results of magnetic-susceptibility measurements indicate that the three-dimensional magnetic ordering is preceded at around 13 K by the onset of low-dimensional magnetic correlations [14]. In a first neutron-diffraction study in zero magnetic field [223] a commensurate propagation vector of $\mathbf{k} = (0.5, 0.5, 0.5)$ was found, while a second one [224] revealed a slightly incommensurate propagation vector $\mathbf{k}' = (0.5 + \delta, 0.5, 0.5 + \delta)$

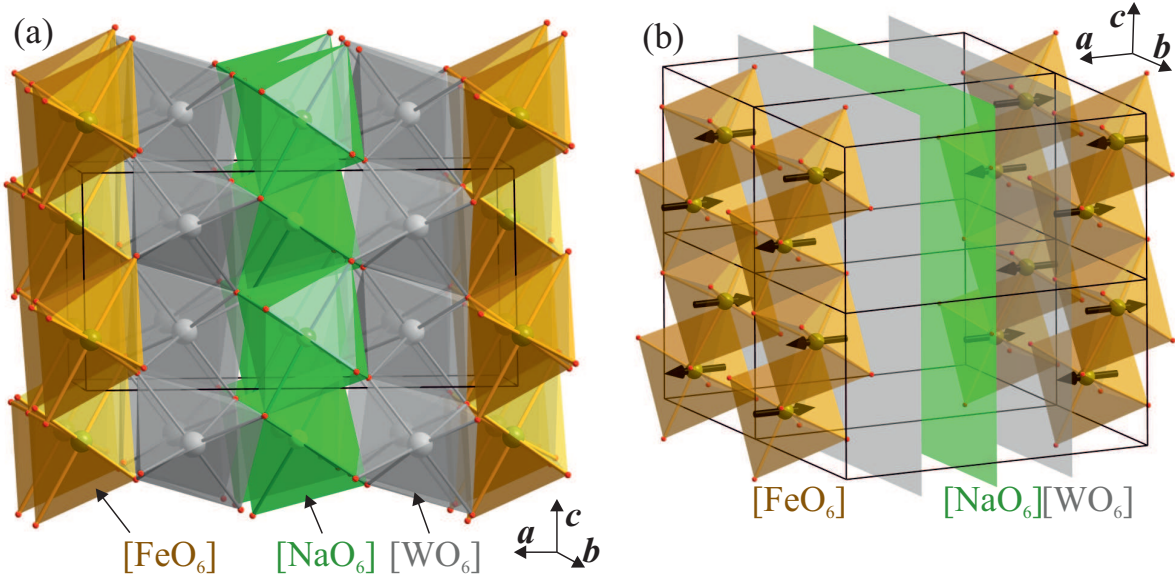


Figure 6.1: (a) Room-temperature crystal structure of $\text{NaFe}(\text{WO}_4)_2$ (b) Magnetic structure of $\text{NaFe}(\text{WO}_4)_2$ below 5 K.

with $\delta \approx 0.03$. According to this latter study a commensurate magnetic structure forms with $\mathbf{k} = (0.5, 0.5, 0.5)$ in finite magnetic fields above 1.5 T [224]. In figure 6.1 (b), the magnetic structure reported in [223] is displayed.

6.1.2 Experimental details

All crystals of $\text{NaFe}(\text{WO}_4)_2$ investigated in the present work were grown by Prof. Dr. P. Becker-Bohatý from high-temperature solution using a top-seeded solution-growth process (TSSG). A melt solution of the system $\text{Na}_2\text{WO}_4\text{-WO}_3$ was used. With the morphological faces as reference planes, oriented samples with faces perpendicular to $\mathbf{b} \times \mathbf{c}$, \mathbf{b} and \mathbf{c} were prepared.

The dielectric properties of $\text{NaFe}(\text{WO}_4)_2$ were investigated by performing pyroelectric-current measurements on different samples with faces perpendicular to $\mathbf{b} \times \mathbf{c}$, \mathbf{b} or \mathbf{c} . Because of the very low magnetic-ordering temperature of about 4 K, the standard setup with the variable temperature insert ($T_{\min} = 2$ K) could not be used for these measurements. Instead, a Heliox system was used, which expands the temperature range down to $\simeq 300$ mK. In this context, a new sample holder for dielectric investigations was engineered.¹ The results of the dielectric investigations reveal that $\text{NaFe}(\text{WO}_4)_2$ is neither multiferroic nor magnetoelectric. Small currents similar to those already reported in [14], which occurred below 4 K, could be attributed to frozen charge carriers. Thermal-expansion and magnetostriction measurements, which were also performed in a Heliox system for magnetic fields applied parallel to $\mathbf{b} \times \mathbf{c}$, \mathbf{b} or \mathbf{c} , reveal glass-like transitions below 4 K.² Based

¹For details, see section 3.2.6.

²All the thermal-expansion and magnetostriction measurements were performed by Y. Sanders.

on the results of the thermal-expansion and magnetostriction measurements, magnetic-field versus temperature phase diagrams are derived.

6.1.3 Thermal expansion and magnetostriction

In order to derive magnetic-field versus temperature phase diagrams of $\text{NaFe}(\text{WO}_4)_2$, a thermal-expansion and magnetostriction study along \mathbf{b} was performed for \mathbf{B} parallel to $\mathbf{b} \times \mathbf{c}$, \mathbf{b} or \mathbf{c} .² Figure 6.2 displays a representative selection of $\Delta L_b(T, \mathbf{B})/L_b^0$ curves measured as a function of increasing or decreasing temperature at constant magnetic fields. Problems with the temperature controller around 2 K caused perturbations in the corresponding $L_b(T, \mathbf{B})/L_b^0$ curves in some cases, which is typical for a heliox system because in this temperature regime the ^4He -dominated cooling changes to a ^3He -dominated cooling.

The down measurements show a rather strong continuous decrease of $\Delta L_b(T)/L_b^0$ between about 3 K and 2 K in zero magnetic field without the occurrence of any kink, see figure 6.2. In contrast, the up measurements exhibit two well-defined kinks at $\simeq 2$ K and $\simeq 3$ K, respectively, which indicate the presence of two different phase transitions at first sight. However, combining the informations about the up and down measurements leads to the following interpretation. During the cooling cycle a smeared, glass-like phase transition starts to emerge at $T_N \simeq 3$ K, which is not accomplished at lower temperatures (the transition process freezes). This transition can probably be attributed to the onset of the antiferromagnetic order, discussed in section 6.1.1. During the heating cycle the thermal energy grows again with increasing temperature until at $\simeq 2$ K it apparently suffices to accomplish the magnetic ordering, which causes the first kink. Finally, with further increasing temperature a transition from the magnetically ordered to the paramagnetic phase occurs at $\simeq 3$ K, which causes the second kink.

For small magnetic fields along \mathbf{b} , the glass-like transition stays present until above ~ 1.5 T it transforms to an ordinary second-order phase transition to the magnetically ordered phase. For 7 T and 11 T the corresponding spontaneous contractions are displayed in figure 6.2(b). Finally above 15 T, no transition at all occurs. The length changes for applied magnetic fields along $\mathbf{b} \times \mathbf{c}$ or \mathbf{c} have similar characteristics below $\simeq 4.5$ T as those in the low-field range for $\mathbf{B} \parallel \mathbf{b}$, indicating the occurrence of analogue glass-like transitions here, see figures 6.2(a) and (c). For higher magnetic fields along $\mathbf{b} \times \mathbf{c}$ or \mathbf{c} another type of transition emerges between $\simeq 4.5$ T and $\simeq 10.5$ T. The corresponding rather sharp length changes have a positive sign and show a weak temperature hysteresis. For even higher fields between $\simeq 10.5$ T and $\simeq 13.5$ T, the characteristics of the $\Delta L_b(T, \mathbf{B})/L_b^0$ curves change again. The hysteretic abrupt length changes disappear and instead well-defined kinks occur at lower temperatures. Finally, in the high-field limit no transitions at all emerge, such as for $\mathbf{B} \parallel \mathbf{b}$.

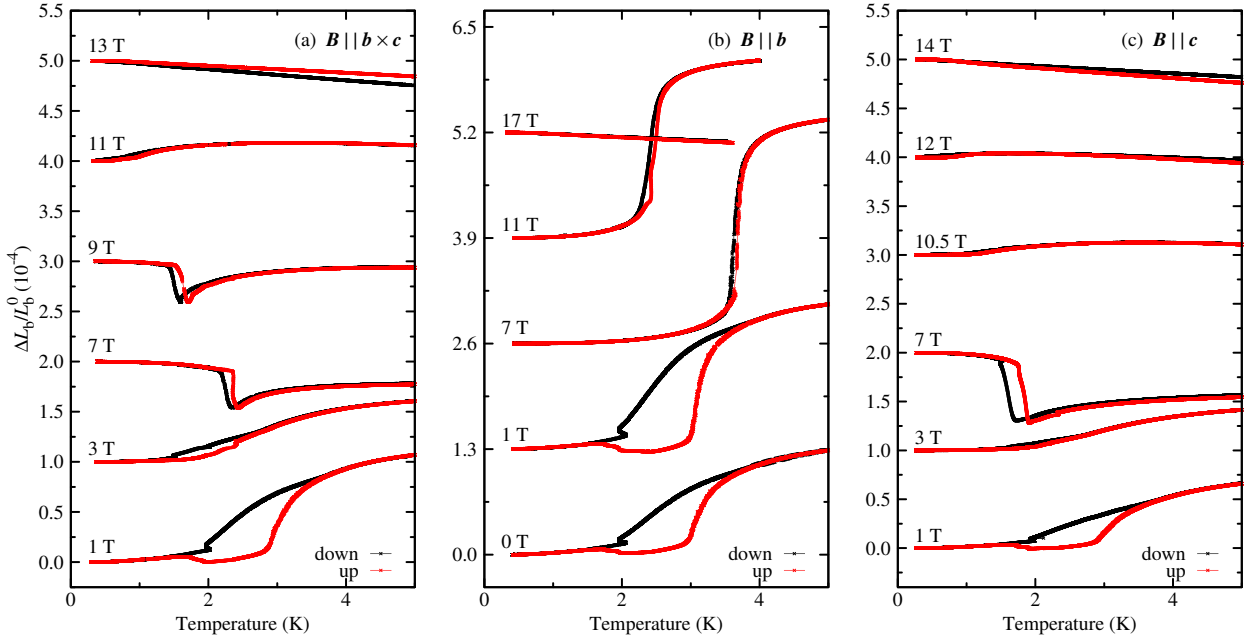


Figure 6.2: Thermal expansion of $\text{NaFe}(\text{WO}_4)_2$ along b for representative magnetic fields parallel to $b \times c$, b or c . For clarity, the curves are shifted with respect to each other with increasing field strengths by constant offsets of $1 \cdot 10^{-4}$ in (a), $1.3 \cdot 10^{-4}$ in (b) and by $1 \cdot 10^{-4}$ in (c). Measurements with increasing and decreasing temperature are plotted as red and black symbols, respectively.

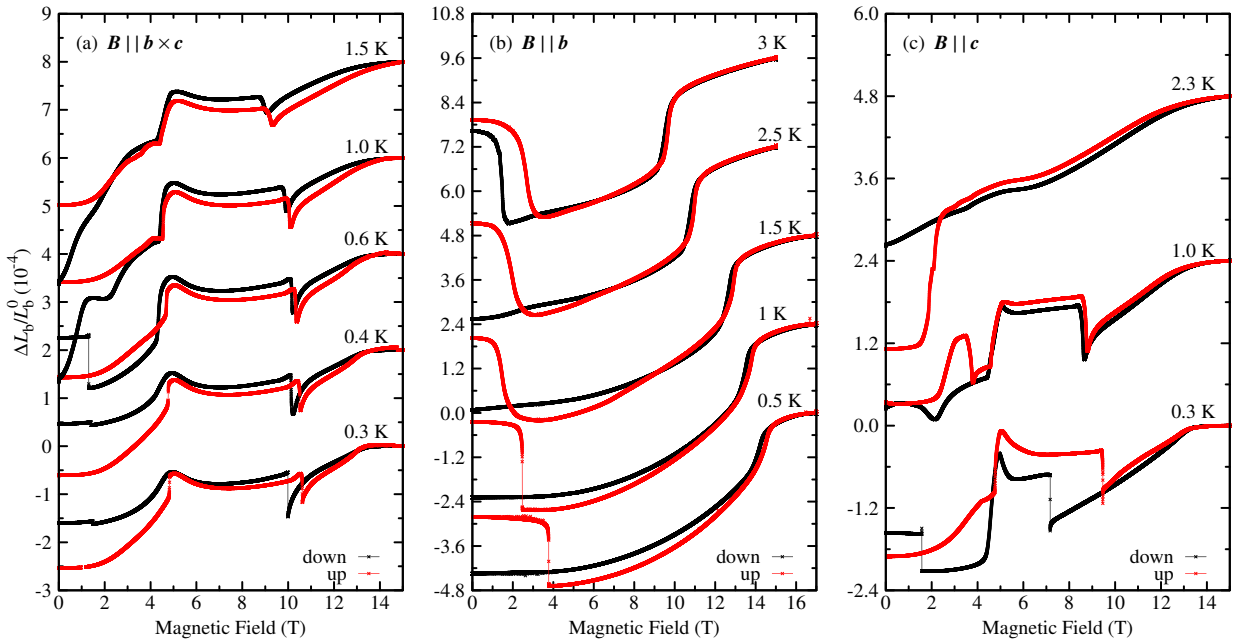


Figure 6.3: Magnetostriction of $\text{NaFe}(\text{WO}_4)_2$ along b for magnetic fields parallel to $b \times c$, b or c . For clarity, the curves are shifted with respect to each other with increasing temperature by constant offsets of $2 \cdot 10^{-4}$, $2.4 \cdot 10^{-4}$ and $2.4 \cdot 10^{-4}$ in (a), (b) and (c), respectively. Measurements with increasing and decreasing magnetic field are plotted as red and black symbols, respectively.

Figure 6.3 summarizes representative magnetostriction measurements along the b direction for magnetic fields applied parallel to $b \times c$, b or c . The magnetic-field dependent $\Delta L_b/L_b^0$ curves are very complex, especially for $B||b \times c$ or $B||c$. In some cases it is very difficult to interpret them. Therefore, the discussion will focus first on the simplest case for $B||b$. The initial phase at $\simeq 0.5$ K in zero magnetic field is the mixed, partially ordered phase discussed above in the context of figure 6.2 (b). With increasing field strength at about 4 T a sharp drop of $\Delta L_b/L_b^0$ arises indicating the completion of the frozen phase transition to the magnetically ordered phase, see figure 6.3 (b). Then, $\Delta L_b/L_b^0$ continuously grows until around 14 T a kink occurs, which suggests a transition to the paramagnetic phase. In the down measurement this kink is reproduced indicating a re-entrance in the magnetically ordered phase, which then extends down to zero magnetic field. With increasing temperature the principal characteristics of the observed length changes stay the same. The sharp drop of $\Delta L_b/L_b^0$ in the up measurements is shifted to lower field strength and slightly broadens. At 3 K finally, an abrupt length change is also visible in the down measurement at $\simeq 2$ T, indicating that the magnetically ordered phase is left again.

For $B||b \times c$ or $B||c$, the magnetic-field dependent $\Delta L_b/L_b^0$ curves show up to four different anomalies. One of them is only visible in the down curves, see figures 6.3 (a) and (c). This indicates the presence of two more phases compared to $B||b$. The initial phase for $B||b \times c$ at 0.3 K in zero magnetic field is again the mixed partially ordered phase, already discussed above. With increasing field strength $\Delta L_b/L_b^0$ continuously grows until at $\simeq 5$ T an abrupt positive length change takes place indicating a direct transition from the partially ordered phase to another magnetically ordered phase, see figure 6.3 (a). With further increasing field, $\Delta L_b/L_b^0$ stays nearly constant up to $\simeq 10.5$ T, where a sharp drop occurs indicating another phase transition. Finally, a kink emerges at about 13 T, which can probably be attributed to a transition to the paramagnetic phase. In the down measurement this kink is reproduced, while the anomaly at around $\simeq 10.5$ T is slightly shifted to a lower field strength, which proves a hysteretic behaviour of this transition. The anomaly at $\simeq 5$ T is broadened and finally below $\simeq 2$ T apparently another phase transition occurs, which could not be observed in the up measurement. With increasing temperature the characteristics of the transitions above $\simeq 4$ T stay essentially the same. The characteristics of the $\Delta L_b/L_b^0$ curves in the low-field regime, however, change in a way, which is difficult to interpret. For $B||c$ similar anomalies are observed as for $B||b \times c$, see figures 6.3 (a) and (c). As before, especially in the low-field regime the characteristics of the $\Delta L_b/L_b^0$ curves are difficult to interpret.

Based on the results of the thermal-expansion and magnetostriction measurements, magnetic-field versus temperature phase diagrams were derived, see figure 6.4. On temperature decrease in zero magnetic field, $\text{NaFe(WO}_4)_2$ undergoes a glass-like phase transition at $T_N \simeq 3$ K from its paramagnetic phase to a partially antiferromagnetically ordered mixed phase. The suppression of the complete magnetic ordering is probably caused by a freezing process. On a subsequent temper-

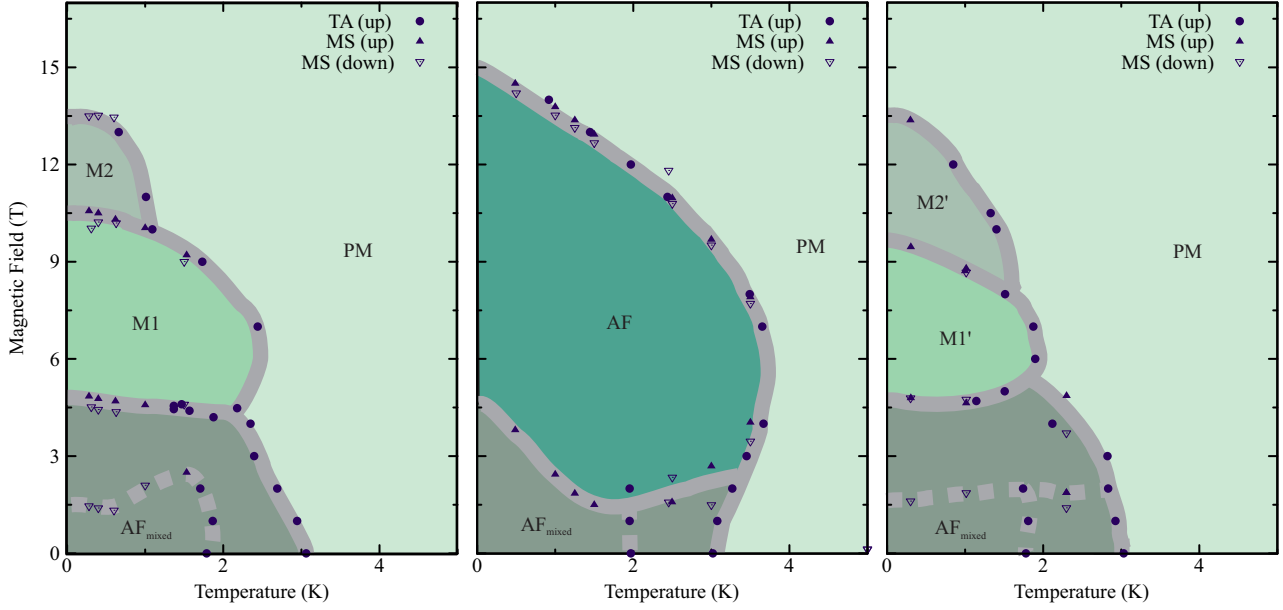


Figure 6.4: Magnetic-field versus temperature phase diagrams of $\text{NaFe}(\text{WO}_4)_2$ for magnetic fields applied parallel to $\mathbf{b} \times \mathbf{c}$, \mathbf{b} or \mathbf{c} . The phase boundaries are based on the anomalies of the thermal-expansion and magnetostriction curves.

ature or magnetic-field increase ($\mathbf{B} \parallel \mathbf{b}$) the magnetic ordering is accomplished above $\simeq 2$ K or $\simeq 1.5$ T, respectively, see figure 6.4 (b). The freezing of the magnetic ordering of $\text{NaFe}(\text{WO}_4)_2$ for low magnetic-field strengths and the completion of the ordering process in magnetic fields along \mathbf{b} for field strengths above $\simeq 1.5$ T could perhaps also explain the results of the neutron-diffraction studies, reported in literature [223, 224]. The slightly incommensurate propagation vector $\mathbf{k}' = (0.5 + \delta, 0.5, 0.5 + \delta)$ with $\delta \approx 0.03$, found in zero magnetic field, could perhaps be attributed to the frozen, mixed ordered phase and the commensurate vector $\mathbf{k} = (0.5, 0.5, 0.5)$ above 1.5 T to the complete magnetically ordered phase [224]. The fact that in the second study the commensurate propagation vector $\mathbf{k} = (0.5, 0.5, 0.5)$ was already observed in zero magnetic field [223] could reflect the strong history dependence of the low-temperature zero-field phase of $\text{NaFe}(\text{WO}_4)_2$.

In contrast to $\mathbf{B} \parallel \mathbf{b}$, an increase of magnetic fields applied along $\mathbf{b} \times \mathbf{c}$ or \mathbf{c} apparently does not lead to a completion of the magnetic ordering but causes transitions to other magnetically ordered phases (M1/M1') around 4.5 T, see figure 6.4 (a) and (c). With further increasing field strengths other transitions to differently ordered magnetic phases (M2/M2') seem to occur around 10.5 T. At about 13.5 T a transition to the paramagnetic phase occurs. Because of the very complex temperature and magnetic-field dependences of the thermal-expansion and magnetostriction measurements and their strong history dependence, the phase boundaries in figure 6.4 and the corresponding interpretations have to be considered with a lot of caution. It is necessary to perform much more

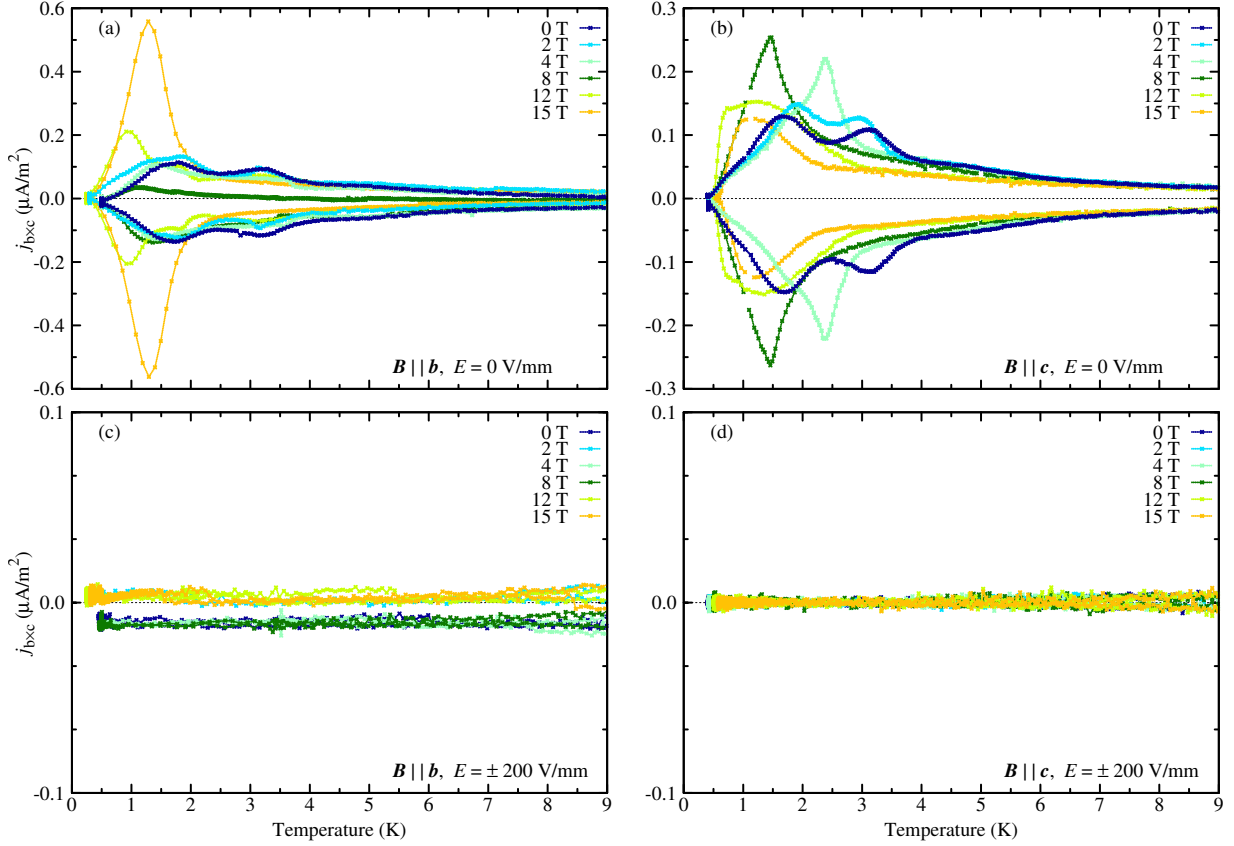


Figure 6.5: Pyroelectric-current densities of $\text{NaFe}(\text{WO}_4)_2$ along $b \times c$ recorded during heating and cooling cycles (top, bottom) for $B \parallel b$ (left) and $B \parallel c$ (right).

detailed investigations to corroborate the interpretations of this section.

6.1.4 Dielectric properties

The pyroelectric-current measurements of $\text{NaFe}(\text{WO}_4)_2$ along $b \times c$ and c are summarized in figures 6.5, 6.6 and 6.7. Because no currents were detected along b , the results of the measurements for this direction are not presented here.

In accordance to previous findings [14], a current flow could be detected in zero magnetic field along $b \times c$ with two maxima at about 2 K and 3 K during the heating cycles, see figures 6.5 (a) and (b). The sign of the current flow could be inverted by inverting the electric poling field during the preceding cooling cycles. However, no significant current flow was observed during the cooling cycles with applied electric poling fields, see figure 6.5 (c) and (d). This indicates that the detected currents during the heating cycles are not caused by the change of a spontaneous electric polarization as proposed in [14]. It is rather probable that charge carriers are frozen during the cooling cycles, which then cause a current flow during the heating cycles. For $B \parallel b$ and $B \parallel c$, the two

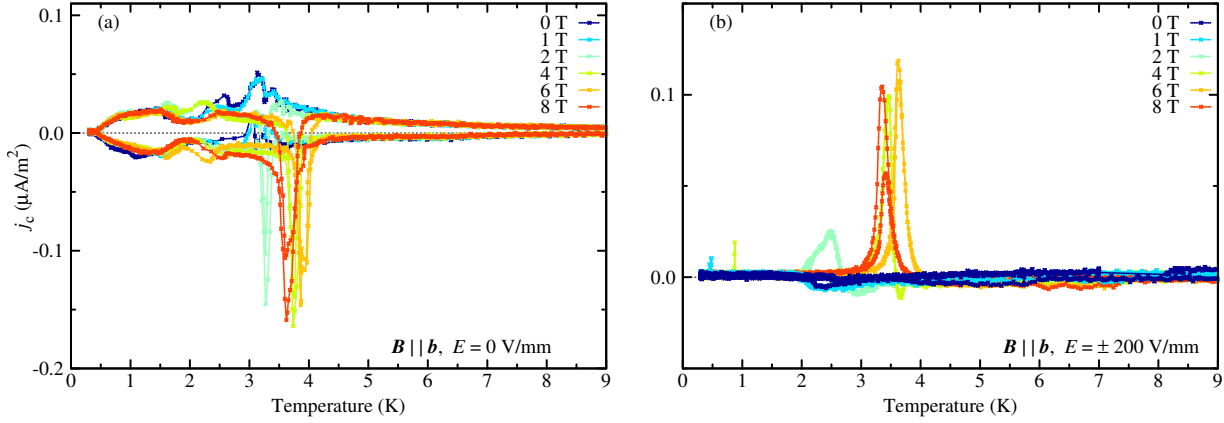


Figure 6.6: Former results of pyroelectric-current measurements of $\text{NaFe}(\text{WO}_4)_2$ along c for magnetic fields parallel to b , which were performed by S. Albiez and O. Heyer. (a) Current densities, recorded during (a) the heating cycles and (b) the cooling cycles.

current maxima converge with increasing field strength until only one maximum remains, which is shifted to lower temperatures with further increasing field strength, see figures 6.5 (a) and (b). All observed maxima coincide with anomalies of the thermal-expansion data of corresponding field directions. As in zero field no significant currents could be detected during the cooling cycles, see figure 6.5 (c) and (d). A reanalysis of the pyroelectric-current data of [14] proves that also in these measurements no significant currents emerged during the cooling cycles, which further supports the present interpretation.

Pyroelectric-current measurements along c , which were performed by S. Albiez and O. Heyer in applied magnetic fields along b , revealed the occurrence of current signals above 2 T with a maximum around 4 K, see figure 6.6. In contrast to the measurements along $b \times c$, these currents arose not only during the heating cycles, but also in applied electric poling fields during the cooling cycles. This indicates that they are probably not caused by the aforementioned freezing process. However, the sign of the emerging currents could not be inverted by inverting the electric poling field. Furthermore, the absolute values of the observed current maxima are not dependent on the magnetic-field strength within the experimental uncertainty. Therefore, the presence of a linear magnetoelectric effect can probably be excluded. In the present work, the pyroelectric-current measurements along c were repeated in applied magnetic fields along b and c using the same sample as in the investigations of S. Albiez and O. Heyer. However, the previous results could not be reproduced. No comparable currents were detected, see figure 6.7. During the cooling cycles no currents at all emerged and during the heating cycles only very small current signals were observed, which were independent from the magnetic-field strength.

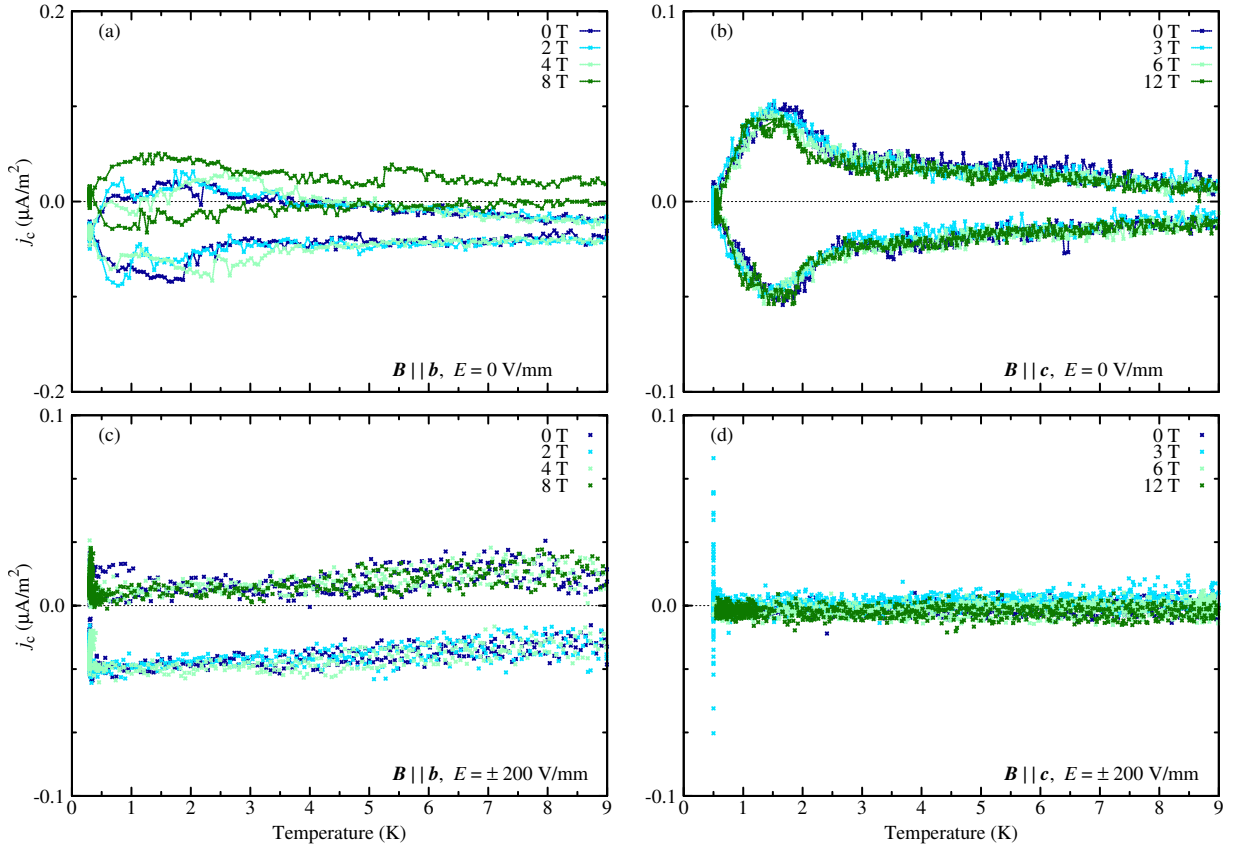


Figure 6.7: Pyroelectric-current densities of $\text{NaFe}(\text{WO}_4)_2$ along c recorded during heating and cooling cycles (top, bottom) for $B||b$ (left) and $B||c$ (right).

6.1.5 Conclusion

The thermal-expansion and magnetostriction measurements reveal that $\text{NaFe}(\text{WO}_4)_2$ undergoes at $\simeq 3$ K a glass-like transition to a probably mixed partially magnetically ordered phase. Previous results of magnetic-susceptibility measurements indicate that the three-dimensional magnetic ordering is preceded at around 13 K by the onset of low-dimensional magnetic correlations [14]. Based on the findings of a neutron-diffraction study, a collinear antiferromagnetic spin structure for temperatures below $\simeq 3$ K with the a axis as magnetic easy axis and a commensurate propagation vector of $\mathbf{k} = (0.5, 0.5, 0.5)$ was proposed [223]. In contrast, another study found a slightly incommensurate propagation vector $\mathbf{k}' = (0.5 + \delta, 0.5, 0.5 + \delta)$ with $\delta \approx 0.03$, which could perhaps be attributed to the frozen, mixed ordered phase [224]. The inconsistency of the two different neutron-diffraction studies could reflect the strong history dependence of the low-temperature zero-field phase of $\text{NaFe}(\text{WO}_4)_2$, which was observed during the thermal-expansion and magnetostriction measurements. With increasing field strength for $B||b$ a transition occurs at around 1.5 T, where the magnetic ordering is completed. For $B||b \times c$ and $B||c$, with increasing

field strength direct transitions from the mixed partially magnetically ordered phase in two other magnetically ordered phases occur.

The pyroelectric-current measurements prove that NaFe(WO₄)₂ is neither multiferroic nor linear magnetoelectric. The observed currents could be attributed to charge carriers frozen during the cooling cycles, which discharge during the subsequent heating cycles. Thus, apart from MnWO₄, up to date no other multiferroic material is known within the tungstate family.

6.2 CuBr₂

6.2.1 Introduction

The discovery of spin-driven multiferroicity in cupric chloride CuCl₂ some years ago [225, 226], which is an antiferromagnetic $S = 1/2$ chain compound ($T_N \simeq 24$ K), led to the search for multiferroicity in other related dihalide materials. In 2012, multiferroicity was also found in polycrystalline samples of CuBr₂ below $T_N \simeq 73.5$ K [13]. As CuCl₂, cupric bromide CuBr₂ is a $S = 1/2$ chain antiferromagnet. At room temperature it crystallizes in a distorted CdI_2 type structure with space group $C2/m$ and with the lattice parameters $a = 7.2096(5)$ Å, $b = 3.4742(2)$ Å, $c = 7.0475(6)$ Å and $\beta = 119.610(5)^\circ$ [227], see figure 6.8 (a). Ribbons of edge-sharing CuBr₄ squares are running along the b axis. Neighbouring ribbons are connected via longer Cu-Br bonds perpendicular to the ribbon planes leading to a layered structure with the layers being oriented parallel to the ab plane. Neutron-powder diffraction and magnetic-susceptibility measurements revealed at about 200 K the onset of one-dimensional magnetic correlations, proceeded below $T_N \simeq 73.5$ K by the occurrence of an incommensurate cycloidal spin structure propagating along the b axis and with the plane of the spin helix slightly inclined by an angle of 13° from the CuBr₄-ribbon planes [13, 228]. Therefore, a spontaneous electric polarization within the ac plane is expected according to equation 2.9 with $\mathbf{P} \propto \mathbf{e}_{ij} \times (\mathbf{S}^{(i)} \times \mathbf{S}^{(j)})$.

6.2.2 Experimental details

All crystals of CuBr₂ investigated in the present work were grown by Prof. Dr. L. Bohatý from a Cu-Br₂ solution at 40 °C. After typical growth periods of 6-8 weeks black, shiny single crystals with a tabular (001) morphology and dimensions up to about $30 \times 10 \times 2$ mm³ were obtained, see figure 6.8 (b). The CuBr₂ crystals are plastically deformable, hygroscopic and disintegrate in contact with a multitude of solvents. Because of their flexibility, a scalpel or a razor blade can be used for the preparation. A slight humidification of the blades with isopropanol helps to prevent the generation of plastic deformations. Metallizing the crystal surfaces with silver or gold electrodes by evaporation is difficult. It turned out that CuBr₂ attacks silver, gold but also other metals.

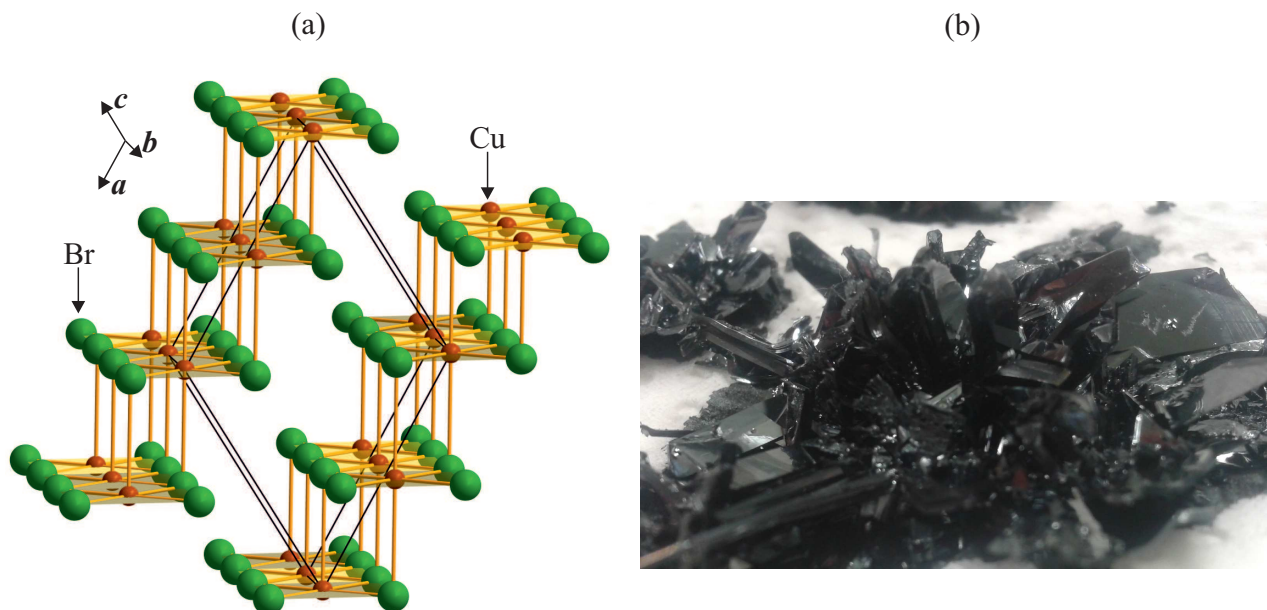


Figure 6.8: (a) Room-temperature crystal structure of CuBr_2 (b) Grown crystal of CuBr_2 .

Therefore, at the end graphite powder mixed with vacuum grease was used for the creation of the electrode areas.

CuBr_2 was characterized by dielectric investigations, which reveal the onset of ferroelectricity below $T_N \simeq 73.5 \text{ K}$ in agreement to [13].³ Because of the tabular morphology of CuBr_2 , the electric polarization and relative dielectric constant could only be investigated along (001). In order to sustain a single-domain state during the pyroelectric-current measurements, the electric poling field had to be applied both during the cooling and heating cycles, which indicates that the ferroelectric domains in CuBr_2 are metastable even at low temperatures far away from the transition temperature.

6.2.3 Dielectric properties

Figure 6.9 summarizes the temperature-dependent measurements of the electric polarization $P_{(001)}$ of CuBr_2 in magnetic fields applied parallel and perpendicular to the surface normal (001). The respective pyroelectric-current densities can be found in appendix E.5. $P_{(001)}$ emerges below $\simeq 73.5 \text{ K}$ in zero magnetic field and reaches at lower temperatures a maximum value of about $3 \mu\text{C}/\text{m}^2$, which is more than a factor of two smaller than the maximum polarization observed on polycrystalline samples of CuBr_2 [13]. This result is in accordance with the theoretical prediction based on the magnetic structure that the electric polarization is lying within the ac plane, see section 6.2.1. With increasing magnetic-field strength the electric polarization grows for both

³The dielectric investigations, presented here were performed by L. Andersen.

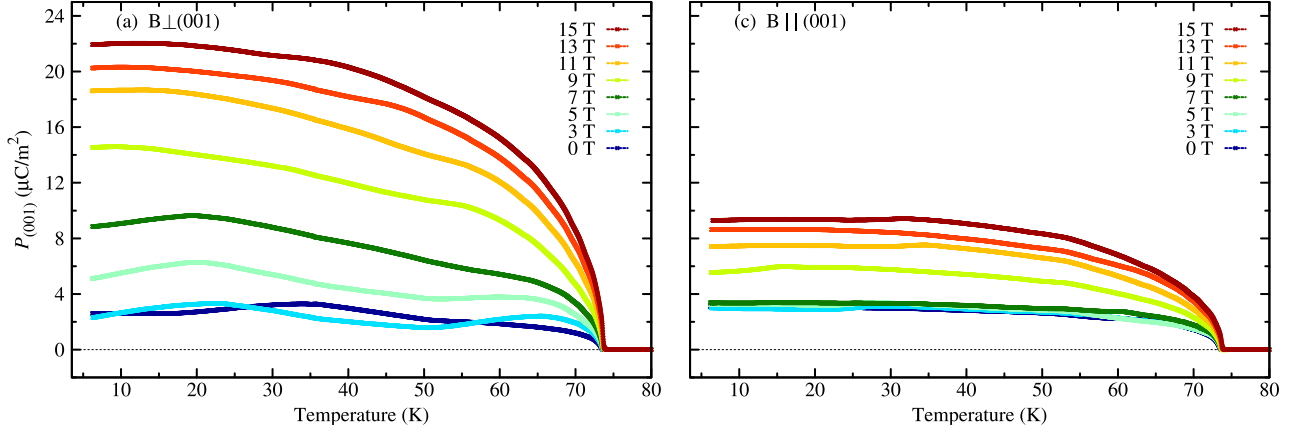


Figure 6.9: Temperature dependence of the spontaneous electric polarization of CuBr₂ along (001) for magnetic fields applied parallel (right) and perpendicular (left) to (001).

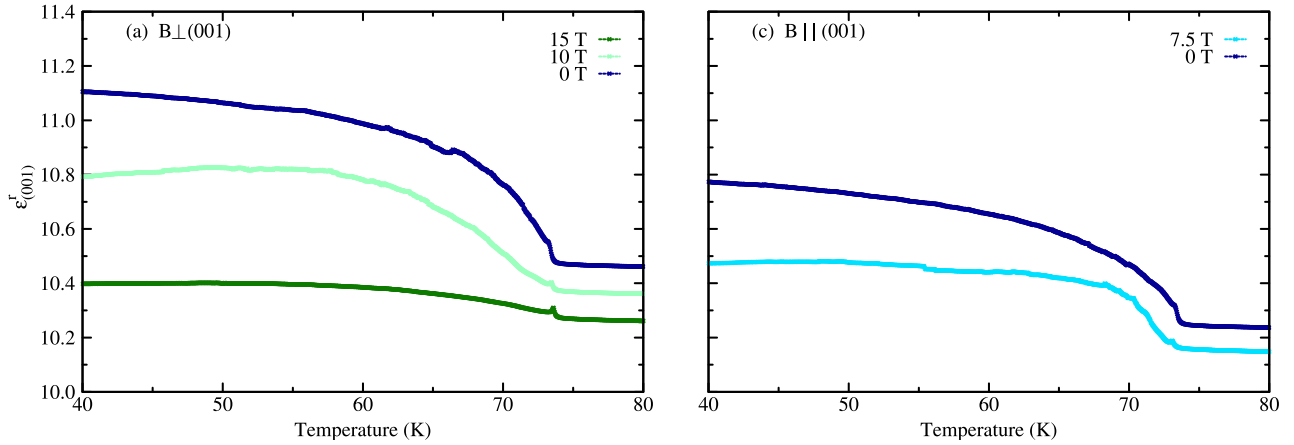


Figure 6.10: Temperature dependence of $\epsilon^r_{(001)}$ of CuBr₂ for (a) $B \perp (001)$ and (b) $B \parallel (001)$. The single curves are shifted by constant offsets of 0.1.

investigated field directions in accordance with the results reported in [13]. At 15 T the electric polarization reaches maximum values of about $10 \mu\text{C}/\text{m}^2$ and $22 \mu\text{C}/\text{m}^2$ for $B \parallel (001)$ and $B \perp (001)$, respectively.

The transition to the ferroelectric phase of CuBr₂ also causes distinct anomalies in the temperature dependences of the corresponding component of the dielectric tensor $\epsilon^r_{(001)}$ for magnetic fields applied parallel and perpendicular to (001), as can be seen in figure 6.10. At the transition temperature 73.5 K the dielectric constant shows a sharp rise in agreement to [13].

6.2.4 Conclusion

The dielectric investigations of CuBr₂ reveal the onset of a spontaneous electric polarization below $T_N \simeq 73.5 \text{ K}$ in accordance to [13], which is probably lying within the ac plane in zero magnetic

field. The investigated component along (001) grows with increasing field strength. No evidence was found during the investigations for a rotation of the electric polarization out of the ac plane in applied magnetic fields or the occurrence of further phase transitions. Because of the tabular morphology of the grown single crystals of CuBr_2 , the full anisotropy of its dielectric properties could not be investigated in the present work. In addition the CuBr_2 crystals are plastically deformable, hygroscopic and disintegrate in contact with a multitude of solvents and metals. Therefore, further investigations will be in any case very challenging.

6.3 $\text{Mn}_3\text{Al}_2(\text{GeO}_4)_3$

6.3.1 Introduction

At room temperature, the spessartite type garnet $\text{Mn}_3\text{Al}_2(\text{GeO}_4)_3$ crystallizes in a cubic structure with space group $Ia\bar{3}d$ and with the lattice constants $a = b = c = 11.894(2) \text{ \AA}$ [229]. It is isomorphous to its Si analogue $\text{Mn}_3\text{Al}_2(\text{SiO}_4)_3$, which occurs in nature as the mineral spessartite. Neutron powder-diffraction and magnetic-susceptibility in combination with specific-heat measurements revealed below $T_N \simeq 6.65 \text{ K}$ the onset of an antiferromagnetic ordering [229–231]. The magnetic structure below T_N can be described by the magnetic space group $R\bar{3}'c$ and forms spin vortices within the (111) planes with the spins being oriented parallel or antiparallel to $[2\bar{1}\bar{1}]$, $[\bar{1}2\bar{1}]$ or $[\bar{1}\bar{1}2]$ [229, 232]. The space group $R\bar{3}'c$ allows a perfectly antisymmetric linear magnetoelectric effect with the components $\alpha_{21} = -\alpha_{12}$, see appendix G. Since the antisymmetric part of the linear magnetoelectric effect can be related to the toroidal moment, this compound could be interesting for the search for fingerprints of toroidal order on the microscopic scale, which are distinct from the antiferromagnetic order, see section 2.4. In the literature no evidence was found for the occurrence of other phase transitions apart from the magnetic ordering at $T_N \simeq 6.65 \text{ K}$. Therefore, the onset of the magnetic ordering in $\text{Mn}_3\text{Al}_2(\text{GeO}_4)_3$ probably coincides with a ferroelastic transition with the species $m\bar{3}m1'F\bar{3}'m$. Therefore, $\text{Mn}_3\text{Al}_2(\text{GeO}_4)_3$ is probably a magnetoelastic multiferroic with four ferroelastic domain states.

6.3.2 Experimental details

The $\text{Mn}_3\text{Al}_2(\text{GeO}_4)_3$ crystals were grown by M. Groß in the laboratory of the FEE⁴, supervised by Dr. D. Rytz and Dr. habil. L. Ackermann. The starting composition of the growth melt was $3\text{MnO} + \text{Al}_2\text{O}_3 + 3\text{GeO}_2$ in a stoichiometric mixture. The crystals were grown using a top-seeded growth method in a crystal-puller furnace with resistance heater (TSG). An undoped YAG ($\text{Y}_3\text{Al}_2\text{Al}_3\text{O}_{12}$) rod with [111] orientation, serving as seed, was dipped into the melt at a temperature of 1376°C .

⁴Forschungsinstitut für mineralische und metallische Werkstoffe Edelsteine/Edelmetalle GmbH, Idar-Oberstein



Figure 6.11: Grown $\text{Mn}_3\text{Al}_2(\text{GeO}_4)_3$ crystal. The top surface is oriented along $[111]$.

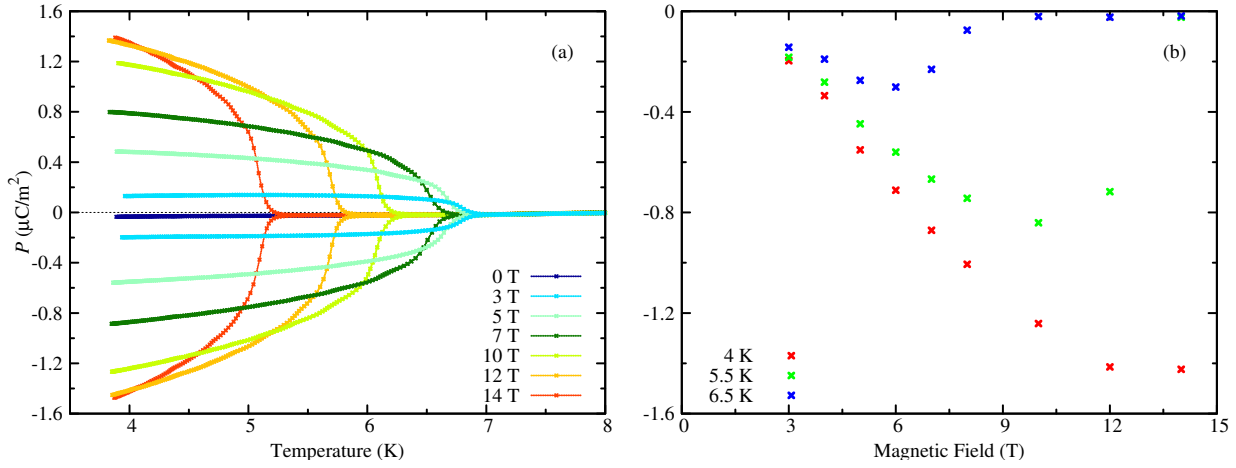


Figure 6.12: (a) Temperature dependence of the electric polarization of $\text{Mn}_3\text{Al}_2(\text{GeO}_4)_3$ along a general crystallographic direction (hkl) for a perpendicularly applied magnetic field. (b) Magnetic-field dependence of the electric polarization of $\text{Mn}_3\text{Al}_2(\text{GeO}_4)_3$ at representative temperatures.

The pulling was started after 7 hours from dipping with a seed-rotation rate of 5 rpm and with a pulling rate of 0.15 mm per hour. After a growth period of 23 hours a large single crystal with a weight of 42.34 g was obtained.

Some explorative dielectric investigations were performed on $\text{Mn}_3\text{Al}_2(\text{GeO}_4)_3$, which prove the presence of a linear magnetoelectric effect in this compound. Interestingly, the magnetoelectrically induced electric polarization seems to occur above a threshold field of about 1.5 T.

6.3.3 Dielectric properties

Figure 6.12 summarizes the results of the temperature-dependent measurements of the electric polarization of $\text{Mn}_3\text{Al}_2(\text{GeO}_4)_3$. The dielectric measurements were performed on a sample oriented along a general crystallographic direction (hkl) . The magnetic field was applied perpendicular to the measurement direction. In zero magnetic field no electric polarization occurs below $T_N \simeq 6.65$ K. Then above a threshold field of about 1.5 T an electric polarization arises, which grows linearly with increasing field strength, see figure 6.12(b). This indicates that $\text{Mn}_3\text{Al}_2(\text{GeO}_4)_3$ is a linear magnetoelectric as expected for the magnetic space group

$R\bar{3}'c$ [229, 232]. The observed threshold field is quite unusual for a linear magnetoelectric. Because the measurements were probably performed on a ferroelastic poly-domain sample, the presence of this threshold field should be considered, however, with some caution. For more detailed dielectric investigations, an appropriate way to pole the ferroelastic domains by clamping the samples under investigation should be found. However, due to the low transition temperature this will be a challenging task and the poling process should be additionally monitored with the help of a polarized-light microscope to check if a single-domain state is obtained.

6.4 Tb_3TaO_7

6.4.1 Introduction

Some years ago the crystal structures and magnetic properties of a series of rare earth tantalates $RE_3\text{TaO}_7$ ($RE = \text{La, Pr, Nd, Sm, Eu, Gd, Tb, Dy, Ho, Er, Tm, Yb, Lu}$) were investigated [233]. The results of temperature-dependent magnetic-susceptibility and specific-heat measurements indicate that the Nd and Tb compound undergo antiferromagnetic two-step transitions at $T_1^{\text{Nd}} = 2.6 \text{ K}$, $T_2^{\text{Nd}} = 2.1 \text{ K}$ and $T_1^{\text{Tb}} = 3.6 \text{ K}$, $T_2^{\text{Tb}} = 2.9 \text{ K}$, respectively. At room temperature, both compounds crystallize in the orthorhombic space group $C222_1$ [233]. For Ho_3TaO_7 , two different phases were found depending on the annealing process, one orthorhombic with space group $C222_1$ and one cubic with space group $Fm\bar{3}m$ [233]. Therefore, the orthorhombic phase of Ho_3TaO_7 is probably ferroelastic with the cubic phase as prototypic phase.

6.4.2 Experimental details

Because two-step magnetic transitions have often proven to coincide with the occurrence of multiferroicity, explorative pyroelectric-current measurements were performed on a polycrystalline sample of Tb_3TaO_7 , which was synthesized by Dr. M. Pelz in the laboratory of the FEE⁵. Tantalum oxide Ta_2O_5 and terbium sesquioxide Tb_2O_3 in a stoichiometric mixture were used as starting materials. After fusion in a rhenium crucible at temperatures above 2300°C polycrystalline Tb_3TaO_7 was obtained after a controlled cooling process, see figure 6.13 (a). Polarized-light microscopy at room temperature on polished thin sections of Tb_3TaO_7 reveals that its orthorhombic phase is apparently ferroelastic. The results of the pyroelectric-current measurements give first evidence for the occurrence of multiferroicity in Tb_3TaO_7 in a small temperature and magnetic-field window.

⁵Forschungsinstitut für mineralische und metallische Werkstoffe Edelsteine/Edelmetalle GmbH, Idar-Oberstein

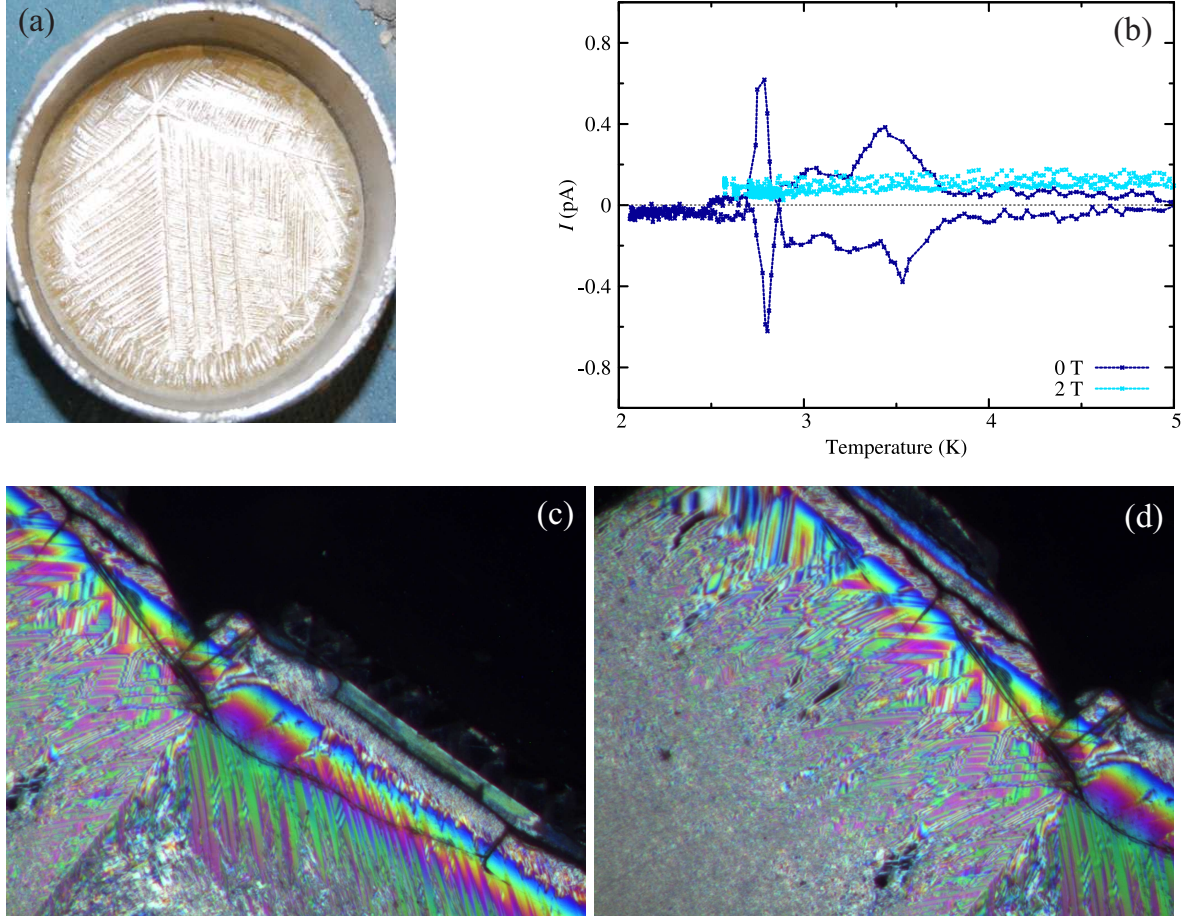


Figure 6.13: (a) Solidified, polycrystalline flux of Tb_3TaO_7 in a rhenium crucible. (b) Temperature dependence of the pyroelectric current of a polycrystalline sample of Tb_3TaO_7 in zero magnetic field and a field of 2 T. (c)-(d) Ferroelastic domains, observed in two different polished thin sections of polycrystalline Tb_3TaO_7 with a polarized-light microscope.

6.4.3 Results and discussion

The pyroelectric-current measurements are presented in figure 6.13 (b). In zero magnetic field a pyroelectric-current signal emerges between $T_2^{\text{Tb}} = 2.9$ K and $T_1^{\text{Tb}} = 3.6$ K, which can be inverted by reversing the electric poling field. This indicates the onset of an electric polarization coinciding with the occurrence of antiferromagnetic ordering below T_1^{Tb} . At the second magnetic transition at T_2^{Tb} the electric polarization is suppressed again. In magnetic fields perpendicular to the surface normal of the sample under investigation, no pyroelectric currents were detected, as is exemplified in figure 6.13 (b) for the case of 2 T.

The results of polarized-light microscopy at room temperature are displayed in figures 6.13 (c) and (d). A multitude of different ferroelastic domains with differently oriented domain walls is visible, indicating that the orthorhombic phase of Tb_3TaO_7 is ferroelastic. In analogy to Ho_3TaO_7 ,

which apparently undergoes a ferroelastic phase transition from cubic to orthorhombic in the high-temperature regime [233], a similar transition can be assumed to occur at even higher temperatures in Tb_3TaO_7 .

In conclusion, the present results of the pyroelectric-current measurements give first evidence for the occurrence of multiferroicity in Tb_3TaO_7 in a small temperature and magnetic-field window. The critical magnetic field for the suppression of the electric polarization has not been determined yet. More detailed dielectric investigations are needed on single crystals to better characterize the multiferroic properties of Tb_3TaO_7 . In addition, a ferroelastic phase transition from cubic to orthorhombic seems to occur in the high-temperature regime. The transition temperature is, however, not known yet and should be determined in high-temperature experiments.

Chapter 7

Summary

The objective of the present work was the search for new multiferroic and magnetoelectric crystals with strong magnetoelectric couplings and their basic characterization by investigating the dielectric and other thermodynamic properties. The used experimental environment for the dielectric investigations, that was already established by S. Jodlauk during his PhD thesis [14] was partially enlarged and improved. The construction of a sample holder for the HelioxVL sorption pumped ^3He insert extends the low-temperature limit of the experiments down to 0.3 K and the development of a new continuous-flow cryostat, operated with cold nitrogen gas extends the high-temperature limit up to 550 K.

The pyroxene family, which was established by S. Jodlauk as a class of multiferroic and linear magnetoelectric materials [14] was further studied in the present work. In this context, $\text{NaFeGe}_2\text{O}_6$ was characterized as first prototype multiferroic within the pyroxene family.¹ Multiferroicity arises at ~ 11.6 K with preceding AFM ordering at ~ 13 K. The electric polarization ($P \simeq 32 \mu\text{C}/\text{m}^2$) lies mainly within the ac plane with a small component along b . It can be strongly modified by magnetic fields. The general orientation of the electric polarization found in this work indicates the presence of a more complex spin structure as reported in [205–207] with a finite spin component along b within the ferroelectric phase I. In order to clarify the microscopic mechanisms leading to multiferroicity in $\text{NaFeGe}_2\text{O}_6$ and in order to resolve the inconsistencies discussed in section 4.4, more detailed information about the magnetic structure are needed. Therefore, as a future task neutron-diffraction experiments should be performed on single crystals of $\text{NaFeGe}_2\text{O}_6$. In addition, $\text{LiFeSi}_2\text{O}_6$ another member of the pyroxene family was reinvestigated. A detailed analysis of the anisotropy of the magnetoelectric effect of $\text{LiFeSi}_2\text{O}_6$ proved that all components of the linear magnetoelectric tensor are non-zero within the experimental uncertainty, apart from

¹Parallel to the investigations in the present work, multiferroicity in $\text{NaFeGe}_2\text{O}_6$ was also found by another research group in polycrystalline samples [12].

the component α_{22} . The electric polarization components $P_{b \times c}^{B_b}$, $P_b^{B_{b \times c}}$, $P_b^{B_c}$ and $P_c^{B_b}$, induced via the linear magnetoelectric effect, are one or two orders of magnitude smaller than $P_{b \times c}^{B_{b \times c}}$, $P_c^{B_{b \times c}}$, $P_{b \times c}^{B_c}$ and $P_c^{B_c}$. This result is in contradiction with the monoclinic space group $P2_1/c'$ proposed for the antiferromagnetic phase of $\text{LiFeSi}_2\text{O}_6$ in literature [204, 216] and indicates that $\text{LiFeSi}_2\text{O}_6$ actually transforms at $T_N \simeq 18.5$ K from the monoclinic space group $P2_1/c1'$ to the triclinic one $P\bar{1}'$. Because of the partly very weak magnetoelectric responses in $\text{LiFeSi}_2\text{O}_6$, an intensive analysis of parasitic currents generated by mismatched electrode areas was necessary to exclude parasitic effects as error sources. The analysis showed the importance of well-matched electrodes, especially in the case of only small pyroelectric or magnetoelectric effects, respectively. In addition, a simple model for the description of parasitic pyroelectric currents could be derived. Finally, a new phase was detected for magnetic fields parallel to c and investigated by thermal-expansion and magnetostriction measurements. Further examinations are needed to explain the observed discrepancies of the transition fields and temperatures detected in the dielectric investigations and thermal-expansion and magnetostriction measurements. In conclusion, the results of the present work show that the pyroxenes are still an interesting class of materials for further studies of multiferroicity and magnetoelectric coupling phenomena.

The erythrosiderite-type compounds $A_2[\text{FeCl}_5(\text{H}_2\text{O})]$ ($A = \text{K}, \text{Rb}, \text{Cs}, \text{NH}_4$) could be established as a new family of non-oxide multiferroic and linear magnetoelectric materials. Multiferroicity in $(\text{NH}_4)_2[\text{FeCl}_5(\text{H}_2\text{O})]$ arises at ~ 6.9 K, with preceding AFM ordering at ~ 7.3 K and a preceding structural ferroelastic phase transition at 79 K. While for low applied magnetic fields an electric polarization of about $3 \mu\text{C}/\text{m}^2$ is lying within the ab plane, it can be significantly enhanced and rotated to c for magnetic fields above about 5 T. The rather complex temperature versus magnetic-field phase diagrams of $(\text{NH}_4)_2[\text{FeCl}_5(\text{H}_2\text{O})]$ show several multiferroic/magnetoelectric phases, that differ in orientation and magnitude of the electric polarization and also in the orientation of the magnetic moments of iron. In order to characterize the different multiferroic/magnetoelectric phases of $(\text{NH}_4)_2[\text{FeCl}_5(\text{H}_2\text{O})]$ on the microscopic scale, and thus to enable an understanding of the underlying mechanism of multiferroicity of this compound, a detailed determination of the magnetic structure by means of neutron scattering is essential as a future investigation. However, because of the high content of hydrogen atoms (10 H per formula unit), this will require the use of the analogous deuterium compound $(\text{ND}_4)_2[\text{FeCl}_5(\text{D}_2\text{O})]$. Of course, a substantial influence of the isotope exchange on the relevant crystal properties is expected and will need a detailed investigation. Such studies could also help to clarify a possible influence of the system of hydrogen bonds on the phase transition at 79 K and on the mechanism of magnetoelectric multiferroicity in $(\text{NH}_4)_2[\text{FeCl}_5(\text{H}_2\text{O})]$. In contrast to $(\text{NH}_4)_2[\text{FeCl}_5(\text{H}_2\text{O})]$, the alkali-based compounds of the erythrosiderite-type family $A_2[\text{FeCl}_5(\text{H}_2\text{O})]$ are only linear magnetoelectrics. From the K-based to the Cs-based compound the transition temperature to the respective magnetoelectric phase de-

creases from $T_N^K = 14.3$ K and $T_N^{Rb} = 10.2$ K to $T_N^{Cs} = 6.8$ K. For all three compounds the complete magnetoelectric tensors and their temperature dependence were determined. A symmetry analysis of the linear magnetoelectric effect of $Cs_2[FeCl_5(H_2O)]$ allowed to derive a model for its magnetic structure with the magnetic space group $C'_{\frac{2'}{m} \frac{2'}{c} \frac{2_1}{m'}}$. At the moment mixed crystals $(NH_4)_{2-x}K_x[FeCl_5(H_2O)]$ are grown for a further investigation of the mechanisms leading to multiferroicity in pure $(NH_4)_2[FeCl_5(H_2O)]$. In addition, the examination of other members of the erythrosiderite-type family is planned for the future.

Detailed investigations of $NaFe(WO_4)_2$, which is a slight crystal-chemical modification of the well-known multiferroic compound $MnWO_4$ and a member of the tungstate family, revealed that the claim of multiferroicity in this material [14] is apparently wrong. Although a multitude of different phases were detected in the low-temperature limit and in applied magnetic fields, neither multiferroic nor magnetoelectric properties were found in this compound. More explorative work led to the discovery of magnetoelectric properties in some other compounds. With $CuBr_2$ a non-oxide multiferroic with a rather high transition temperature in the vicinity of the boiling point of liquid nitrogen was discovered and first dielectric investigations were performed.² Because of the tabular morphology of the single crystals of $CuBr_2$, the full anisotropy of its dielectric properties could not be determined in the present work. In addition, the $CuBr_2$ crystals are plastically deformable, hygroscopic and disintegrate in contact with a multitude of solvents and metals. Therefore, further investigations will be very challenging. With the spessartite-type garnet $Mn_3Al_2(GeO_4)_3$ a perfectly antisymmetric linear magnetoelectric material was found, which could be interesting for the study of the toroidal moment. Dielectric investigations on polycrystalline samples of Tb_3TaO_7 gave first evidence for multiferroicity in that compound in a small temperature interval between $T_2^{Tb} = 2.9$ K and $T_1^{Tb} = 3.6$ K. Furthermore, polarized-light microscopy revealed that the room-temperature phase of Tb_3TaO_7 is apparently ferroelastic.

²Parallel to the investigations in the present work, multiferroicity in $CuBr_2$ was also found by another research group in polycrystalline samples [13].

Appendix

A Tensor formalism for the description of macroscopic physical properties of crystals

Many macroscopic physical properties of crystals show a distinctive anisotropy and therefore cannot be described by scalar quantities but only by tensors in general. A tensor is defined via its transformation properties with respect to space-time coordinate transformations³ (mirroring, rotations, space inversion, time reversal). Four classes of tensors result $[t_{ij\dots q}]$ ⁴ [26, 161, 234]:

Polar c tensors:

$$t'_{ij\dots q} = R u_{ir} u_{js} \dots u_{qw} t_{rs\dots w} = (-1) u_{ir} u_{js} \dots u_{qw} t_{rs\dots w} \quad (1)$$

Axial c tensors:

$$t'_{ij\dots q} = R |u_{ij}| u_{ir} u_{js} \dots u_{qw} t_{rs\dots w} = (-1) |u_{ij}| u_{ir} u_{js} \dots u_{qw} t_{rs\dots w} \quad (2)$$

Polar i tensors:

$$t'_{ij\dots q} = R u_{ir} u_{js} \dots u_{qw} t_{rs\dots w} = (+1) u_{ir} u_{js} \dots u_{qw} t_{rs\dots w} \quad (3)$$

Axial i tensors:

$$t'_{ij\dots q} = R |u_{ij}| u_{ir} u_{js} \dots u_{qw} t_{rs\dots w} = (+1) |u_{ij}| u_{ir} u_{js} \dots u_{qw} t_{rs\dots w} \quad (4)$$

Here, (u_{ij}) designates a transformation matrix, which transforms a Cartesian coordinate system $\{e_i\}$ into another one $\{e'_i\}$, $|u_{ij}|$ stands for the determinant of (u_{ij}) and R is the time-reversal operator. A tensor $[t_{ij\dots q}]$ of the rank n has n indices and 3^n components.

³In the following only space-time coordinate transformations between Cartesian coordinate system are considered.

⁴Here, the Einstein-summation convention is applied.

The so-called crystal-physical principal system is a Cartesian coordinate system $\{e_i^H\}$, which serves as a reference system for crystal-physical tensor quantities. The Cartesian coordinate system is defined by a fixed relation to the crystallographic system $\{a_i\}$ [235].

$$e_3^H \parallel a_3, \quad e_2^H \parallel a_2^* = a_3 \times a_1, \quad e_1^H = e_2 \times e_3 \quad (5)$$

In non-polar crystals this definition is not unique. An additional definition of the positive-axes orientations is necessary. For that purpose, for example, the sign of special tensor components of the piezoelectric effect is used.

B Transformation properties of axial vectors

In figure 1, the transformation properties of axial vectors under application of different space-time symmetry operations are summarized.

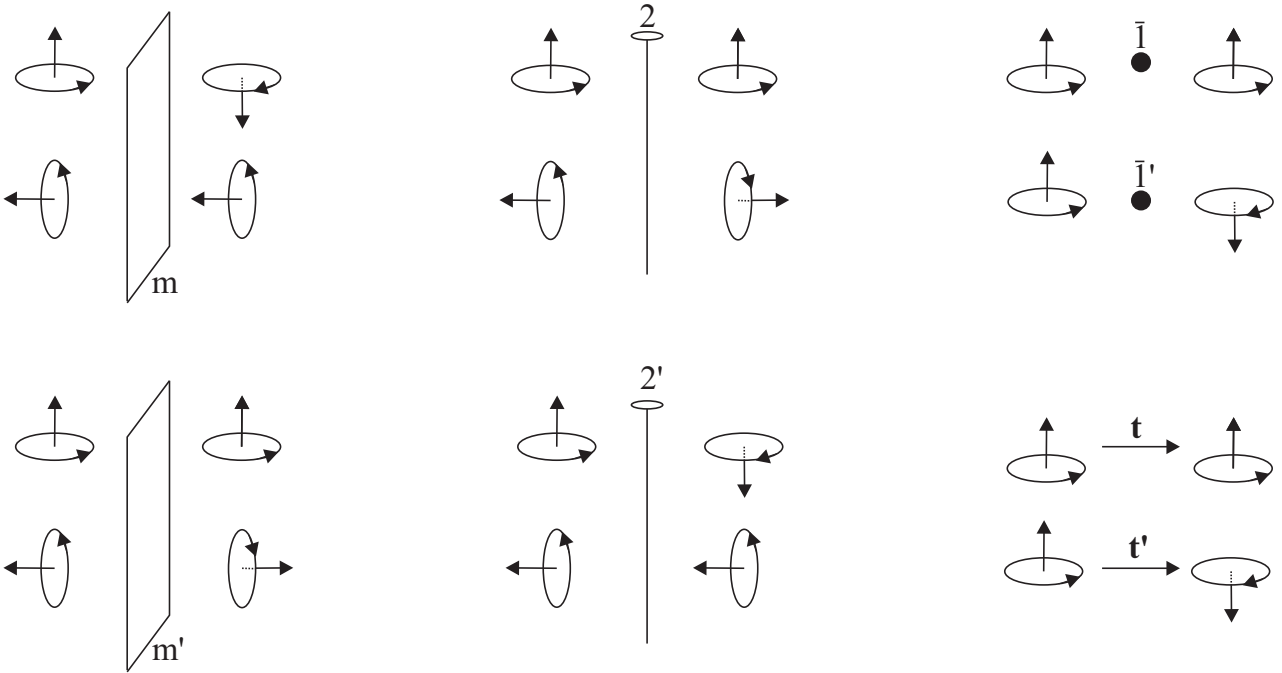


Figure 1: *Effects of different symmetry elements on axial vectors. Primed symmetry elements are combined with the time reversal operator. More information about transformation properties of axial vectors, as, e.g., magnetic moments can be found in [29].*

C Linear optical properties of crystals

The phase velocity of electromagnetic waves, propagating in non-cubic crystals depends on their polarization and propagation directions. An electromagnetic wave, entering in such crystals activates in general two linearly polarized modes with perpendicular oscillation directions. The two modes propagate with different phase velocities within the crystal because of two different active refractive indices. Therefore, the polarization of the corresponding wave is in general modified during the propagation through the crystal. The oscillation directions of the modes and their respective refractive indices as a function of their propagation direction (their wave vector \mathbf{k}) are represented by the so-called optical indicatrix, the representation surface of the inverse of the tensor of the relative permittivity $\epsilon_{ij}^{-1} x_i x_j = 1$.⁵ The indicatrix forms an ellipsoid with three mutually perpendicular principal axes oriented along $\mathbf{e}_1^0, \mathbf{e}_2^0$ and \mathbf{e}_3^0 . In this coordinate system, the optical dielectric impermeability tensor $[a_{ij}]$ has diagonal form and the components a_{ii}^0 on the diagonal correspond to the principal refractive indices n_i^2 . For an electromagnetic wave with wave vector \mathbf{k} in a general direction, the oscillation directions and the corresponding refractive indices of the two activated modes are obtained by intersecting the indicatrix with the plane perpendicular to \mathbf{k} . This leads to an elliptic section, where the orientation of the semi axes determines the oscillation directions of the activated modes and the lengths of the semi axes their refractive indices \tilde{n}_1 and \tilde{n}_2 . A direction, where the elliptic cross section of the indicatrix degenerates into a circle is called optical axis. In such a direction, the crystal seems to be isotropic because the active refractive indices are equal to each other. In the most general case of an indicatrix with three different principal axes $\mathbf{e}_1^0, \mathbf{e}_2^0$ and \mathbf{e}_3^0 with $n_1 < n_2 < n_3$, there are two optical axes in the plane perpendicular to \mathbf{e}_2^0 .

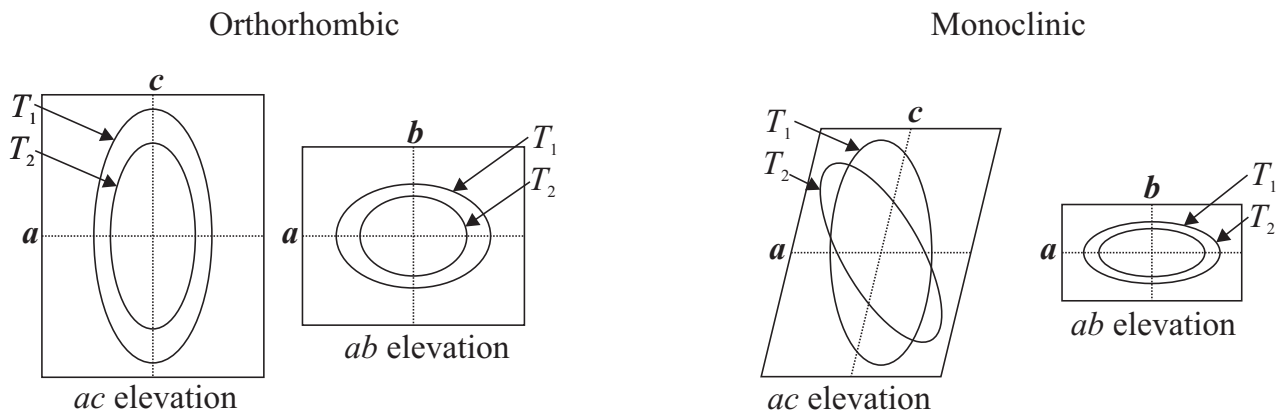


Figure 2: Orientation and temperature dispersion of the indicatrix in orthorhombic (left) and monoclinic (right) crystals.

For triclinic, monoclinic and orthorhombic symmetries the indicatrix forms a tri-axial ellipsoid.

⁵The inverse of the tensor of the relative permittivity $[\epsilon_{ij}^{-1}]$ corresponds to the so-called optical dielectric impermeability tensor $[a_{ij}]$ ($\epsilon_{ij}^{-1} x_i x_j = 1$ is equivalent to $a_{ij} x_i x_j = 1$).

While for orthorhombic symmetries all three principal semi-axes of the indicatrix e_1^0 , e_2^0 and e_3^0 are fixed to the crystallographic axes a , b and c , for monoclinic symmetries only one semi axis is fixed to the monoclinic b axis. In this case, the other two axes possess a rotational degree of freedom within the ac plane. The orientation and temperature dispersion of the indicatrix in orthorhombic and monoclinic crystals is illustrated in figure 2. For triclinic symmetries, all axes of the indicatrix are completely free. For trigonal, hexagonal and tetragonal crystals ($[a_{ij}]$ has only two independent components), the optical indicatrix forms an ellipsoid of rotation with the rotation axis of the ellipsoid being fixed by symmetry to the respective n -fold rotation axis ($3, \bar{3}, 4, \bar{4}, 6, \bar{6}$). Here, only one optical axis along the n -fold rotation axis exists. More details about the linear optical properties of crystals can be found, e.g., in [236].

D Continuous-flow cryostat for dielectric investigations in a temperature range of 100-580 K

D.1 The measuring apparatus

In the following the design and functionality of the continuous-flow cryostat will be discussed, which was engineered in the context of this work for dielectric investigations in the temperature range 100-580 K. Sectional views of the main part of the cryostat are displayed in figure 3. The sample chamber made out of brass has four access vacuum flanges. One hosts the sample wires (see (1) figure 3), one is for the thermometer wiring (see (4) figure 3), the third one contains two stainless steel capillary tubes fitted in the sample holder and serving as inlet pipes for the cold nitrogen gas (see (6) figure 3) and finally the fourth extra flange can be used for possible experimental add-ons of the cryostat. The vacuum flanges are closed by blind flanges with sockets (two four-pin thermometer sockets and two coaxial sockets, Lemo). The complete inner chamber of the cryostat can be evacuated to a pressure of approximately 6×10^{-3} mbar, in order to insulate it thermally from the environment. For the sample and thermometer wiring inside the cryostat 100 μm thin gold wires are used. The thermometer wires were melted into the contacts of the platinum thermometers with the help of a gas torch. They are electrically insulated from each other by inserting them into two four-wireway ceramic capillaries. The sample wires are fed through two other one-wireway ceramic capillaries. All the ceramic capillaries are fixed in the cryostat by thin Teflon discs. Cold nitrogen gas is generated with the help of a home-built evaporator insert in a liquid nitrogen storage vessel. Due to the pressure within the storage vessel, the nitrogen gas flows via an evacuated transfer tube through the stainless steel capillary tubes shown in figure 3 and the electrolytically gilded copper sample holder. One of the stainless steel capillary tubes of the sample holder is connected with the inner line of the transfer tube by a silicon flexible tube. The other stainless steel capillary tube is connected in the same way with an exhaust tube, which conducts the nitrogen gas out of the cryostat. The sample holder is fixed by a thin stainless steel ring and is electrically insulated from the cryostat itself by a Kapton foil. Below the sample holder in the bottom of the cryostat a fused silica glass window is fitted (see (11-13) in figure 3). Thus, the sample holder can be heated by radiation with a 250 W Halogen lamp. Samples and one of the platinum thermometers are fixed and thermally coupled to the sample holder by Cu-Be springs. The second thermometer is inserted into a bore hole at the side of the sample holder and delivers the temperature data for the temperature controller. The walls of the cryostat are cooled by a cooling water coil.

Between 100 K and 580 K a precise temperature control is achieved by two virtual LabVIEW PID controllers. They are integrated into a software, that is written in LabVIEW as well. One of

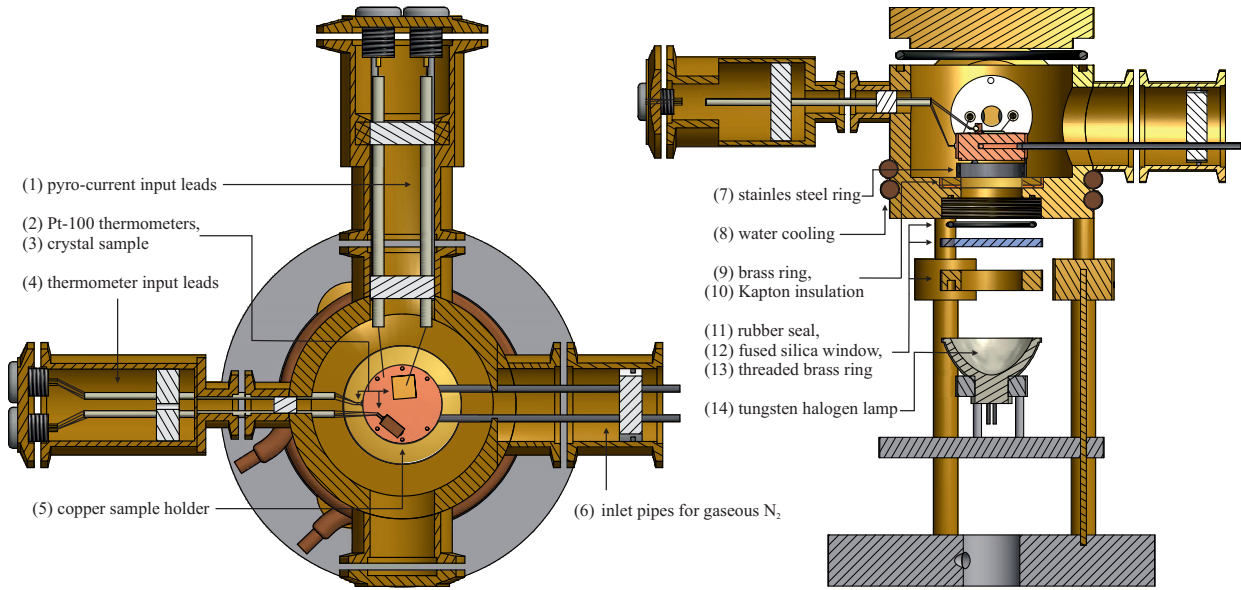


Figure 3: Sectional views of the continuous-flow cryostat for dielectric investigations in the temperature range 100-580 K.

the PID controllers controls the cooling power via a current source (Votcraft PPS-16005, power 360 W), which is wired to the nitrogen evaporator insert. The optimum PID settings during the cooling cycles turned out to be $K_p = -5$, $T_i = 1$ min and $T_d = 0$ min. During the heating-cycles the PID control of the cooling power is switched off and instead a constant heating power for the nitrogen evaporator of approx. 40 W is set. The second PID controller, which is linked to an additional current source (Agilent N5768A) connected to the 240 W halogen lamp, controls the heating power. In this case, for the heating cycles as well as the cooling cycles $K_p = 15$, $T_i = 1$ min and $T_d = 0$ min have proved to be ideal. It should be mentioned that the maximum achievable temperature is not limited by the power of the halogen lamp (at 580 K the maximum irradiated power amounts only to about 80% of the maximum possible power). The maximum achievable temperature is limited by the disintegration temperature of the Teflon discs, which are mounted in the access ports of the cryostat (all other components of the cryostat can stand much higher temperatures). If the Teflon discs were replaced by, e.g., ceramic discs, much higher temperatures could be achieved. The signal of the thermometers is recorded by two multimeters (Keithley 2000, Keithley 193A). For the pyroelectric measurements, a picoamperemeter (Keithley 6485) is used to short circuit the metallized sample surfaces. For the poling of the samples a high-voltage amplifier (Trek 2220, $U_{\max} = \pm 2$ kV) in connection with a function generator (Tektronix AFG 3022) is used. The measurements of the relative dielectric constant can be performed by a LCR-Meter (HP 4275A) at ten different test frequencies between 10 kHz and 10 MHz. In figure 4, the complete apparatus is

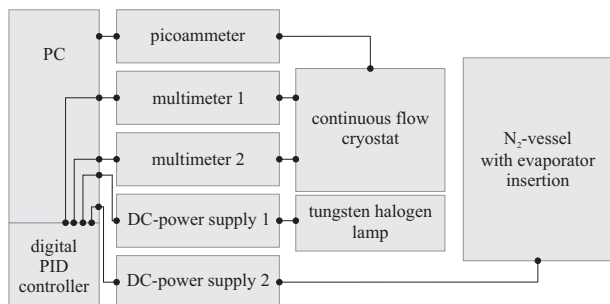


Figure 4: Schematic picture of the apparatus for the measurements of pyroelectric currents in the temperature range of 100-580 K.

shown schematically.

D.2 Measuring process

The measuring process of the dielectric investigations performed in the continuous-flow cryostat is in principle the same as that of the dielectric investigations at lower temperatures, see section 3.2.5. All the devices are connected to a computer via an IEEE-488-Bus. The LabVIEW software, including the two PID controllers is continuously recording data points (time, control temperature, sample temperature, current/capacity, the heating current of the halogen lamp and the heating current of the nitrogen evaporator) while the sample temperature is swept at rates between 1 K/min and 4 K/min. The time difference between two data points amounts typically to $\simeq 600$ ms.

D.3 Test measurements

During the master thesis of L. Andersen [155] the continuous-flow cryostat has been put into operation and was tested and improved by means of different well-known pyroelectrics and ferroelectrics. In addition, the pyroelectric properties of a multitude of monoclinic crystals were investigated. Here, exemplary results of the test measurements of the pyroelectrics $\text{Li}_2\text{SO}_4 \cdot \text{H}_2\text{O}$ and BiB_3O_6 are presented and discussed. For that purpose, the temperature dependences of the pyroelectric coefficient p_b of both compounds are shown in figure 5 (red data points)⁶. BiB_3O_6 and especially $\text{Li}_2\text{SO}_4 \cdot \text{H}_2\text{O}$ are well known in the literature and belong to the monoclinic point group 2 at room temperature. Among the known non-ferroelectric pyroelectrics $\text{Li}_2\text{SO}_4 \cdot \text{H}_2\text{O}$ exhibits one of the largest pyroelectric effects at room temperature, which has additionally a very strong temperature dependence [237–239]. In contrast, the pyroelectric effect of BiB_3O_6 above 150 K is nearly constant [153]. The temperature dependences of the pyroelectric coefficients reported in literature are included in figure 5 (black data points). Except of small deviations there is a very

⁶The pyroelectric coefficients illustrated in figure 5 were calculated from the measured pyroelectric currents with the help of equation 3.2 in section 3.2.1. The pyroelectric currents are not presented here.

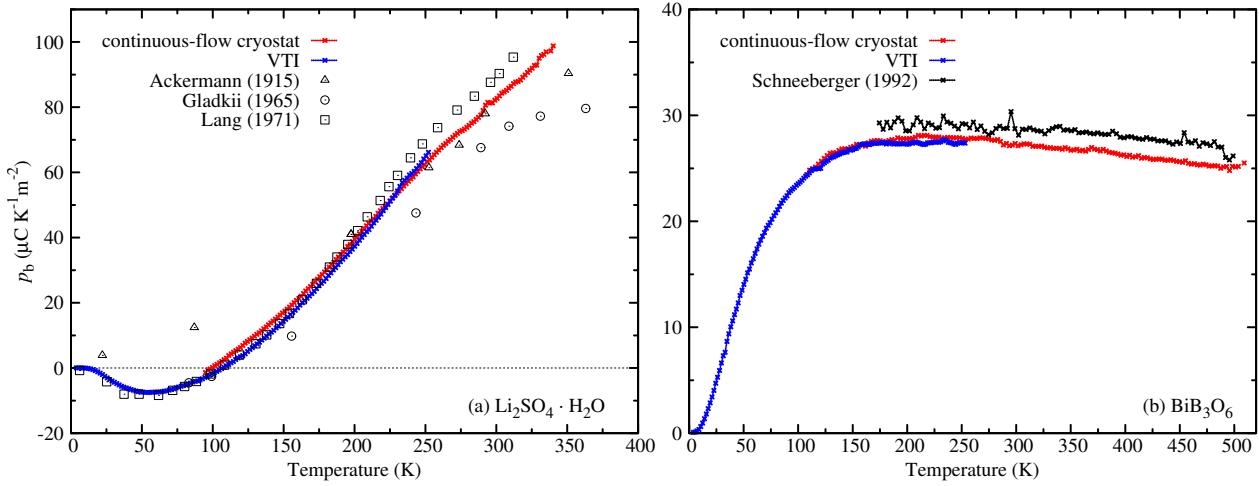


Figure 5: Temperature dependences of the pyroelectric coefficient p_b of the two pyroelectrics (a) $\text{Li}_2\text{SO}_4 \cdot \text{H}_2\text{O}$ and (b) BiB_3O_6 . Literature data from different authors (Ackermann [237], Gladkii [238], Lang [239], Schneeberger [153]) (black points) are compared with the data from measurements in the VTI (blue points) and with those from measurements in the continuous-flow cryostat (red points). There is an overall agreement between the different data sets.

good consistency between the test measurements and the data from the literature. For a further control, the pyroelectric effect of $\text{Li}_2\text{SO}_4 \cdot \text{H}_2\text{O}$ and BiB_3O_6 was investigated also at lower temperatures in the VTI between 4 K and 250 K, see blue data points in figure 5. Above 100 K they nicely reproduce the results of the test measurements in the continuous-flow cryostat.

It can be concluded that the continuous-flow cryostat, that was designed in this work, delivers reliable results in the case of the pyroelectric investigations of $\text{Li}_2\text{SO}_4 \cdot \text{H}_2\text{O}$ and BiB_3O_6 , which are consistent with the data from the literature and the results from the VTI measurements. Thus, the continuous-flow cryostat is suitable for pyroelectric-current measurements in the temperature range 100-580 K. Therefore, it could be used for dielectric investigations of multiferroic crystals at higher temperatures.

E Pyroelectric-current measurements

E.1 $\text{LiFeSi}_2\text{O}_6$

In figure 6, the temperature-dependent pyroelectric-current measurements of $\text{LiFeSi}_2\text{O}_6$ are presented. The data in figure 6 (g) and (i) are adopted from the PhD thesis of S. Jodlauk [14]. Some informations about the used samples are summarized in table 1. The sample jo1211' was used by S. Jodlauk. Its surfaces were metallized with conductive silver. All the other samples were metallized with silver electrodes by evaporation. In the sample ma1211, there was a preferred direction of the magnetic-field induced electric polarization. For poling voltages of an absolute value of 200 V, applied opposite to this preferred direction during the cooling processes, no single-domain state was obtained. In all other cases, the magnetic-field induced electric polarizations could be completely inverted, by cooling the samples from the paraelectric phase down to the magneto-electric phase with applied poling voltages of ± 200 V. For the measurement processes during the heating cycles, the electric poling voltages were removed. In figure 6 only the pyroelectric-current densities for one poling direction are presented.

In figure 7 (a), the temperature-dependent pyroelectric-current measurements, performed on sample ma1210 with not perfectly-matched electrode areas, for a magnetic field applied parallel to the c axis, are presented. In figure 7 (b) the temperature-dependent pyroelectric-current measurements, performed on the same sample in the same configuration, but with almost perfectly-matched electrode areas, are displayed. In the first case the magnetic-field induced current densities are about a factor of two larger, and for the two poling directions there exist a slight asymmetry. In addition, the anomalies occurring for magnetic fields above 6 T below 12 K in figure 7 (b) are only faintly visible in figure 7 (a). The reasons for that are analysed in section 4.3.4.

sample	A (mm ²)	d (mm)	e_A	e_B	B (T)	heating rate (K/min)
ma1211	15.2	0.62	(100)	(100), [010], [001]	0-14 T	4
ma1210	18.3	0.55	[010]	(100), [010], [001]	0-14 T	4
jo1211'	6	0.7	[001]	(100), [010], [001]	0-14 T	4
ma1211'	6.6	0.7	[001]	(100), [010], [001]	0-14 T	4

Table 1: Overview of the samples of $\text{LiFeSi}_2\text{O}_6$, used in the pyroelectric-current measurements, which are presented in figure 6. The sample jo1211' was used by S. Jodlauk for his measurements, already presented in his PhD thesis [14]. The sample-surface areas A , sample thicknesses d , surface normals e_A , directions of applied magnetic fields e_B , magnetic-field ranges and heating rates are specified.

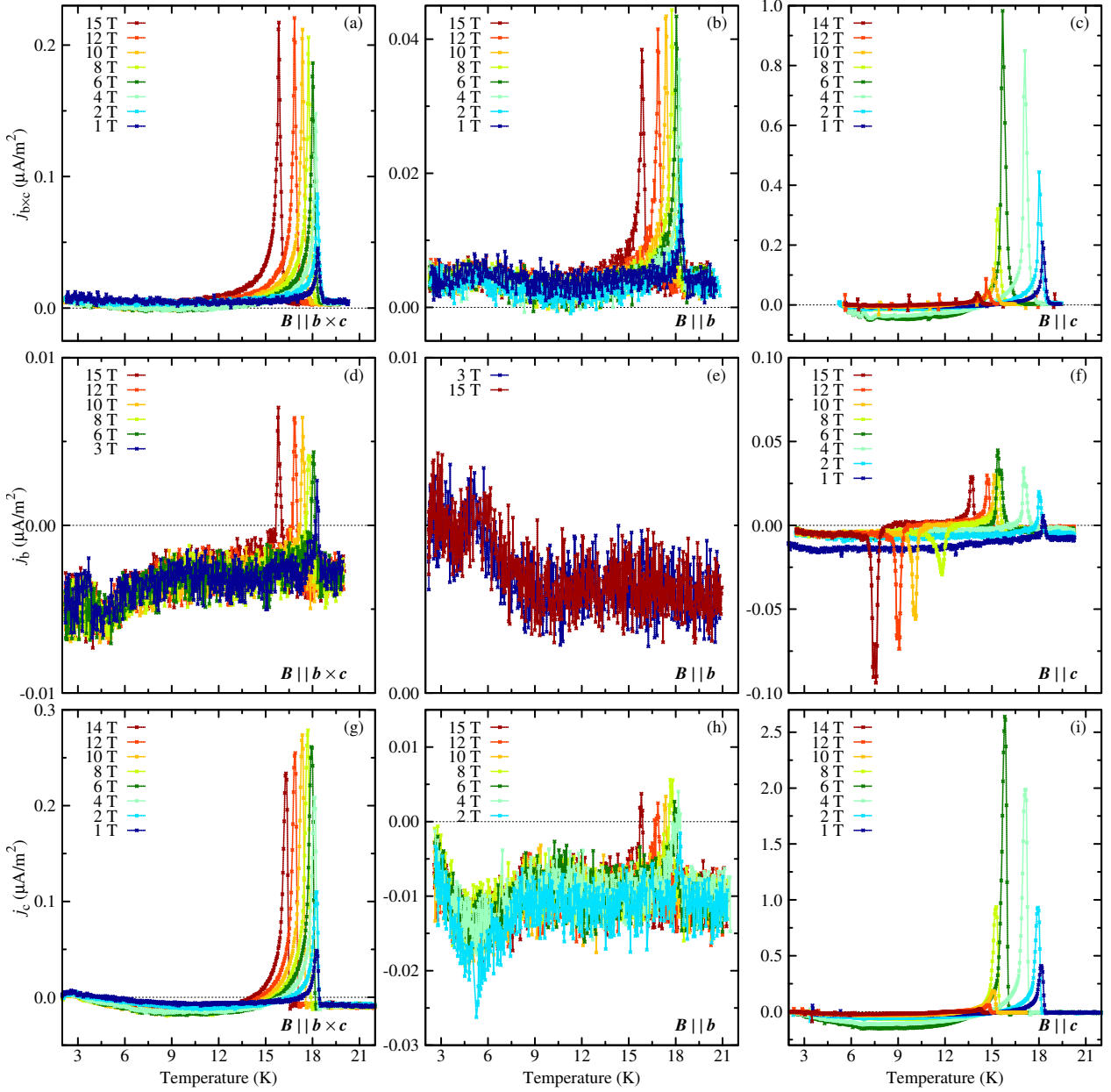


Figure 6: Temperature dependences of the pyroelectric-current densities $j_{b \times c}$, j_b and j_c (top to bottom) of $\text{LiFeSi}_2\text{O}_6$ for magnetic fields applied parallel to the $b \times c$, b or c axis (left to right). The pyroelectric-current densities for only one poling direction of the electric fields are presented. The used heating rates are displayed in table 1. The data in figure 6 (g) and (i) are adopted from the PhD thesis of S. Jodlauk [14].

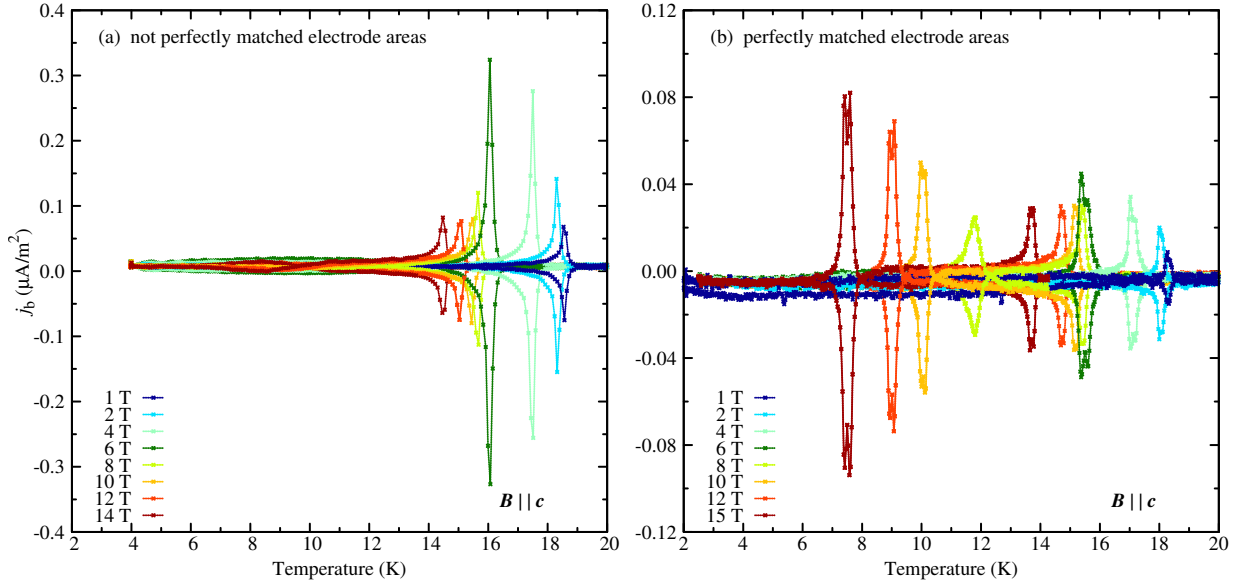


Figure 7: Temperature dependences of the pyroelectric-current density j_b of $\text{LiFeSi}_2\text{O}_6$ for a magnetic field applied parallel to the c axis. In the left panel, the results of the pyroelectric-current measurements, performed on sample ma1210 with not perfectly-matched electrode areas are displayed. In the right panel, the results of the pyroelectric-current measurements, performed on sample ma1210 with nearly perfectly-matched electrode areas are presented. The pyroelectric-current densities for both poling direction of the electric field are presented. The used heating rates are displayed in table 1.

E.2 $\text{NaFeGe}_2\text{O}_6$

In figure 8, the temperature-dependent pyroelectric-current measurements of $\text{NaFeGe}_2\text{O}_6$ are presented. Some informations about the used samples are summarized in table 2. They were metallized with conductive silver. In all cases, the measurements were performed on single-domain phases, which were obtained by cooling the samples from the paraelectric phase down to the ferroelectric phase with applied poling voltages of ± 200 V. For the measurement processes during the heating cycles, the electric poling voltages were removed.

sample	A (mm ²)	d (mm)	e_A	e_B	B (T)	heating rate (K/min)
ma1411	22.5	0.95	[010]	(100), [010], [001]	0-14 T	3
ma1412	35.6	0.85	(100)	(100), [010], [001]	0-14 T	3
ma1414	22.1	1.09	[001]	(100), [010], [001]	0-14 T	3

Table 2: Overview of the samples of $\text{NaFeGe}_2\text{O}_6$, used in the pyroelectric-current measurements, which are presented in figure 8. The sample-surface areas A , sample thicknesses d , surface normals e_A , directions of applied magnetic fields e_B , magnetic-field ranges and heating rates are specified.

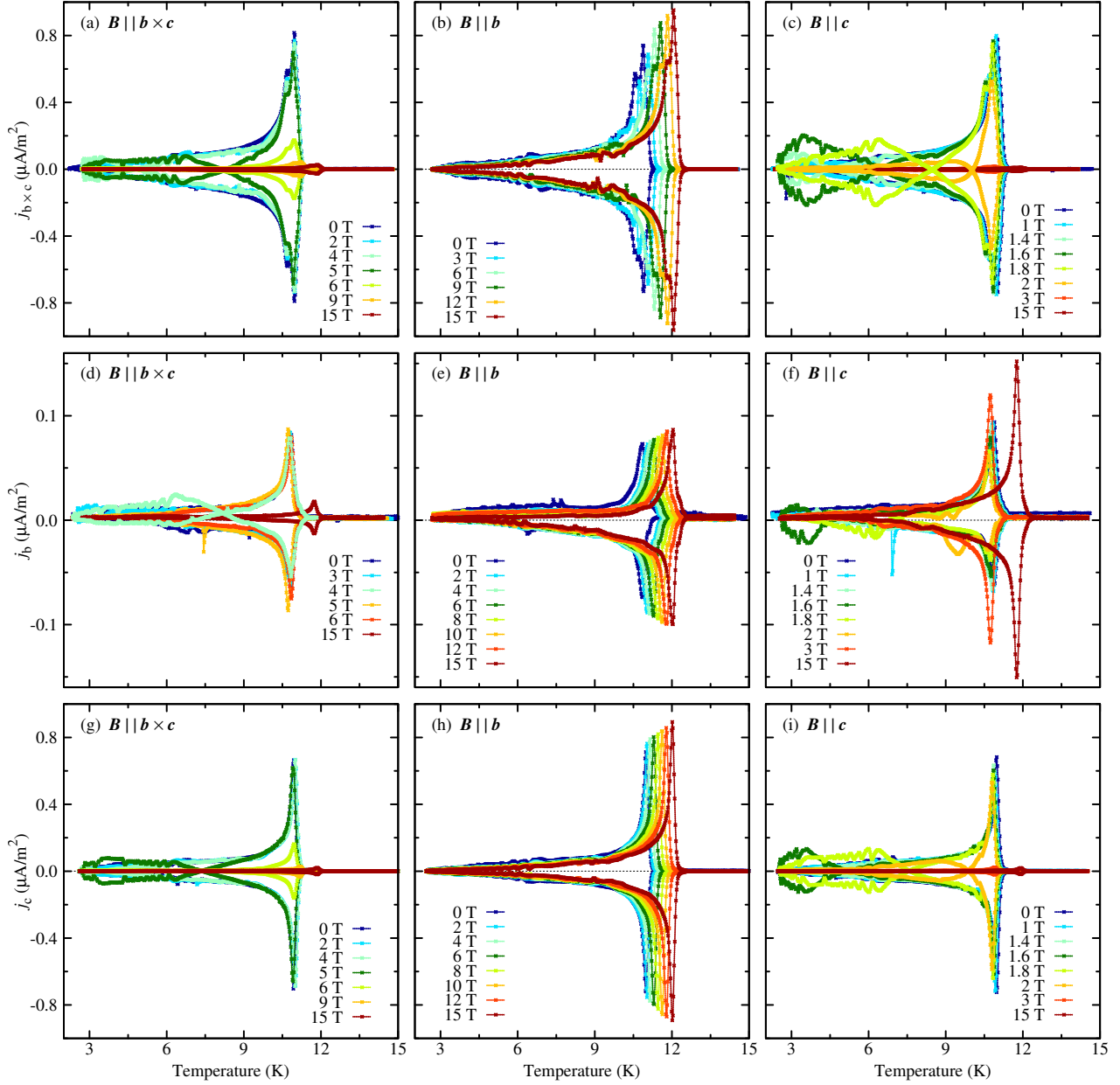


Figure 8: Temperature dependences of the pyroelectric-current densities $j_{b \times c}$, j_b and j_c (top to bottom) of NaFeGe₂O₆ for magnetic fields applied parallel to the $b \times c$, b or c axis (left to right). The pyroelectric-current densities for both poling directions of the electric fields are presented. The used heating rates are displayed in table 2.

E.3 $(\text{NH}_4)_2[\text{FeCl}_5(\text{H}_2\text{O})]$

In figure 9, the temperature-dependent pyroelectric-current measurements of $(\text{NH}_4)_2[\text{FeCl}_5(\text{H}_2\text{O})]$ are presented. Instead of pyroelectric currents, the pyroelectric-current densities $j = I/A$ are displayed. Some informations about the used samples are summarized in table 3. All the samples were metallized with silver electrodes by evaporation. In all cases, the measurements were performed on single-domain phases, which were obtained by cooling the samples from the paraelectric phase down to the ferroelectric phase with applied poling voltages of ± 200 V. For the measurement processes during the heating cycles, the electric poling voltages were removed.

In figure 10, the results of the magnetic-field dependent magnetoelectric-current measurements of $(\text{NH}_4)_2[\text{FeCl}_5(\text{H}_2\text{O})]$ at $T = 4.9$ K for applied magnetic fields parallel a and c are presented. In all cases, the measurements were performed on single-domain phases, which were obtained by cooling the samples from the paraelectric phase down to the ferroelectric phase with applied poling voltages of 200 V. For the measurement processes during the magnetic-field sweeps the electric poling voltages were not removed.

sample	A (mm ²)	d (mm)	e_A	e_B	B (T)	heating rate (K/min)
ma1262	26.8	1.14	[100]	[100], [010], [001]	0-14 T	3
ma1261	23.5	0.85	[010]	[100], [010], [001]	0-14 T	3
ma1260	37.4	1.02	[001]	[100]	0-12 T	1
ma1260	37.4	1.02	[001]	[100]	13-14 T	0.5
ma1250	29.2	0.96	[001]	[010]	0-14 T	3
ma1259	27.9	1.005	[001]	[001]	0-8 T	4
ma1259	27.9	1.005	[001]	[001]	9-12 T	2
ma1259	27.9	1.005	[001]	[001]	13-14 T	1

Table 3: Overview of samples of $(\text{NH}_4)_2[\text{FeCl}_5(\text{H}_2\text{O})]$, used in the pyroelectric- and magnetoelectric-current measurements, which are presented in figure 9 and 10. The respective sample-surface areas A , sample thicknesses d , surface normals e_A , directions of applied magnetic fields e_B , magnetic-field ranges and heating rates are specified.

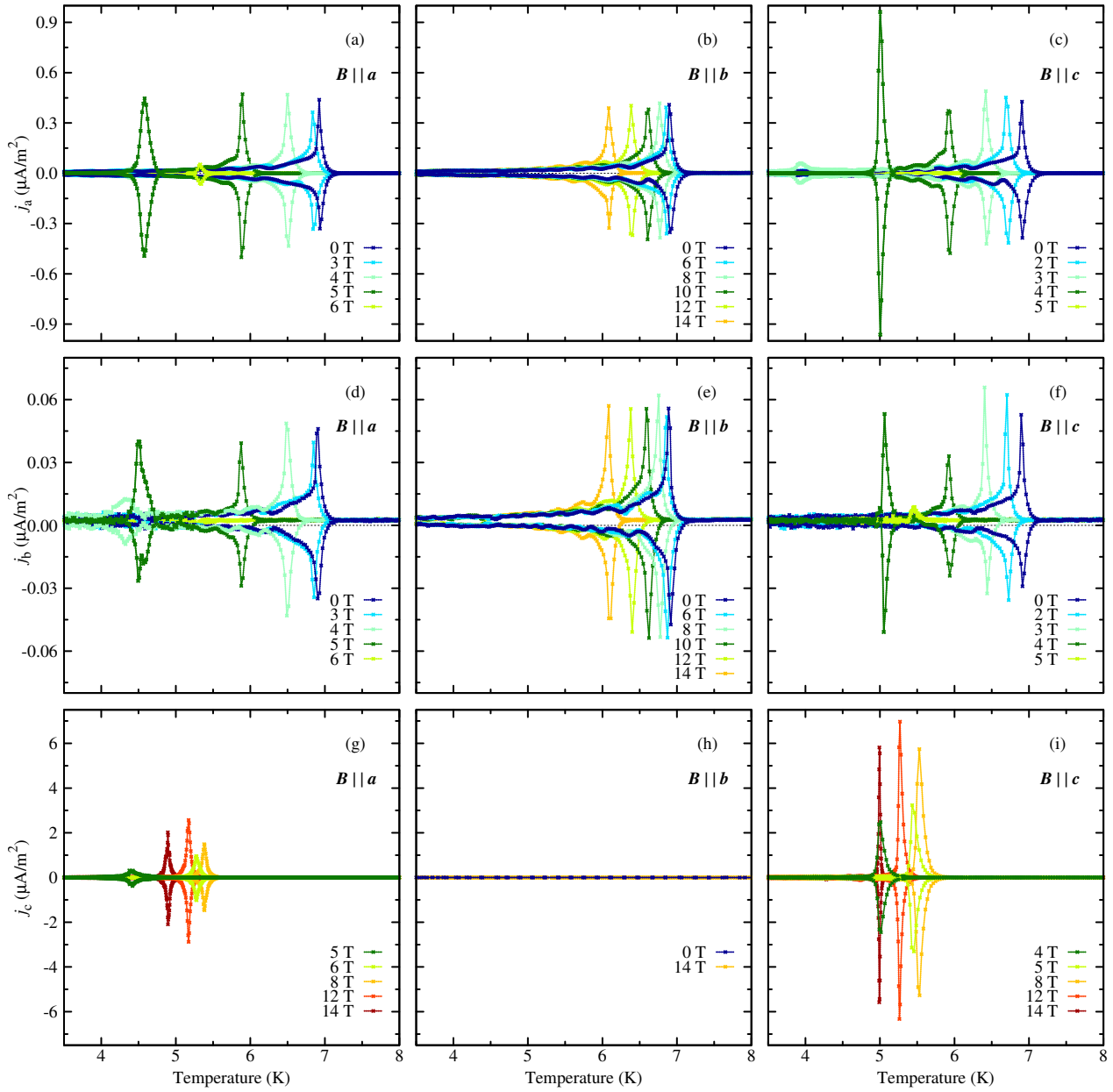


Figure 9: Temperature dependences of the pyroelectric-current densities j_a , j_b and j_c (top to bottom) of $(\text{NH}_4)_2[\text{FeCl}_5(\text{H}_2\text{O})]$ for magnetic fields applied parallel to the a , b or c axis (left to right). The pyroelectric-current densities for both poling directions of the electric fields are presented (current densities with positive and negative sign). The used heating rates are displayed in table 3. They range from 0.5 K/min to 4 K/min.

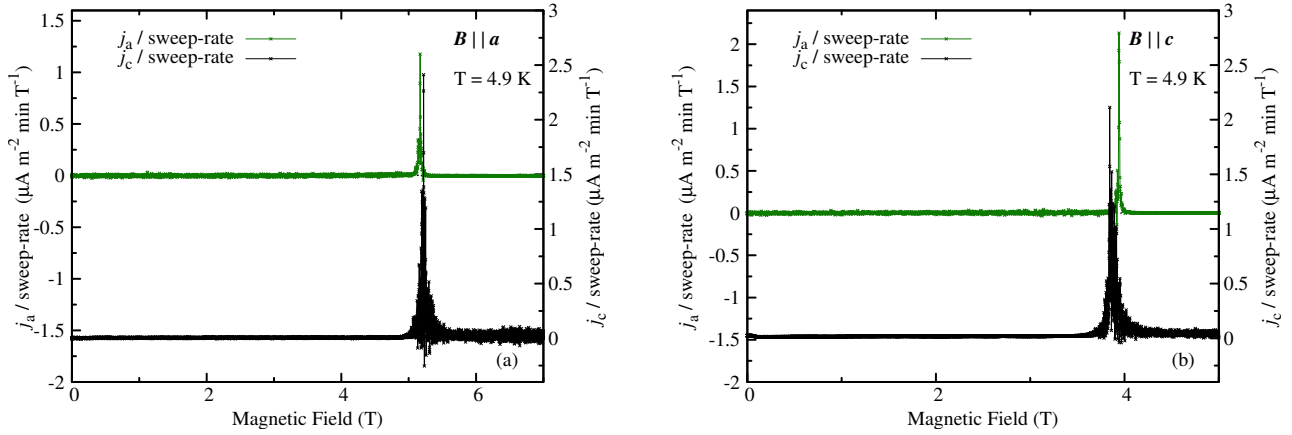


Figure 10: Magnetic-field dependences of the magnetoelectric-current densities j_a and j_c of $(\text{NH}_4)_2[\text{FeCl}_5(\text{H}_2\text{O})]$ for magnetic fields applied parallel to the a or c axis (left to right).

E.4 $\text{A}_2[\text{FeCl}_5(\text{H}_2\text{O})]$, ($A = \text{K, Rb, Cs}$)

In figures 11 and 12, the temperature-dependent pyroelectric-current measurements of $\text{K}_2[\text{FeCl}_5(\text{H}_2\text{O})]$, $\text{Rb}_2[\text{FeCl}_5(\text{H}_2\text{O})]$ and $\text{Cs}_2[\text{FeCl}_5(\text{H}_2\text{O})]$ are presented. Instead of pyroelectric currents, the pyroelectric-current densities are displayed. Some informations about the used samples are summarized in table 4. All the samples were metallized with silver electrodes by evaporation. In some cases there was a preferred direction of the magnetic-field induced electric polarization. For poling voltages of an absolute value of 200 V, applied opposite to these preferred directions during the cooling processes, no single-domain states were obtained. Only the pyroelectric-current densities along the preferred directions, which were measured on single-domain samples are presented.

sample	A (mm^2)	d (mm)	e_A	e_B	B (T)	heating rate (K/min)
ma1342, K	20.4	0.97	[100]	[100], [010], [001]	0-15 T	3
ma1343, K	17.21	1.15	[010]	[100], [010], [001]	0-15 T	3
ma1341, K	15.6	1.2	[001]	[100], [010], [001]	0-15 T	3
ma1337, Rb	14.4	1.07	[100]	[100], [010], [001]	0-15 T	3
ma1344, Rb	21.5	1.21	[010]	[100], [010], [001]	0-15 T	3
ma1338, Rb	19.3	1.2	[001]	[100], [010], [001]	0-15 T	3
ma1333, Cs	21.9	1.075	[100]	[100], [010], [001]	0-15 T	3
ma1331, Cs	18.2	1.06	[010]	[100], [010], [001]	0-15 T	3
ma1334, Cs	20.4	1.02	[001]	[100], [010], [001]	0-15 T	3

Table 4: Overview of samples of $\text{K}_2[\text{FeCl}_5(\text{H}_2\text{O})]$, $\text{Rb}_2[\text{FeCl}_5(\text{H}_2\text{O})]$ and $\text{Cs}_2[\text{FeCl}_5(\text{H}_2\text{O})]$, used in the pyroelectric-current measurements, which are presented in figure 11 and 12. The respective sample-surface areas A , sample thicknesses d , surface normals e_A , directions of applied magnetic fields e_B , magnetic-field ranges and heating rates are specified.

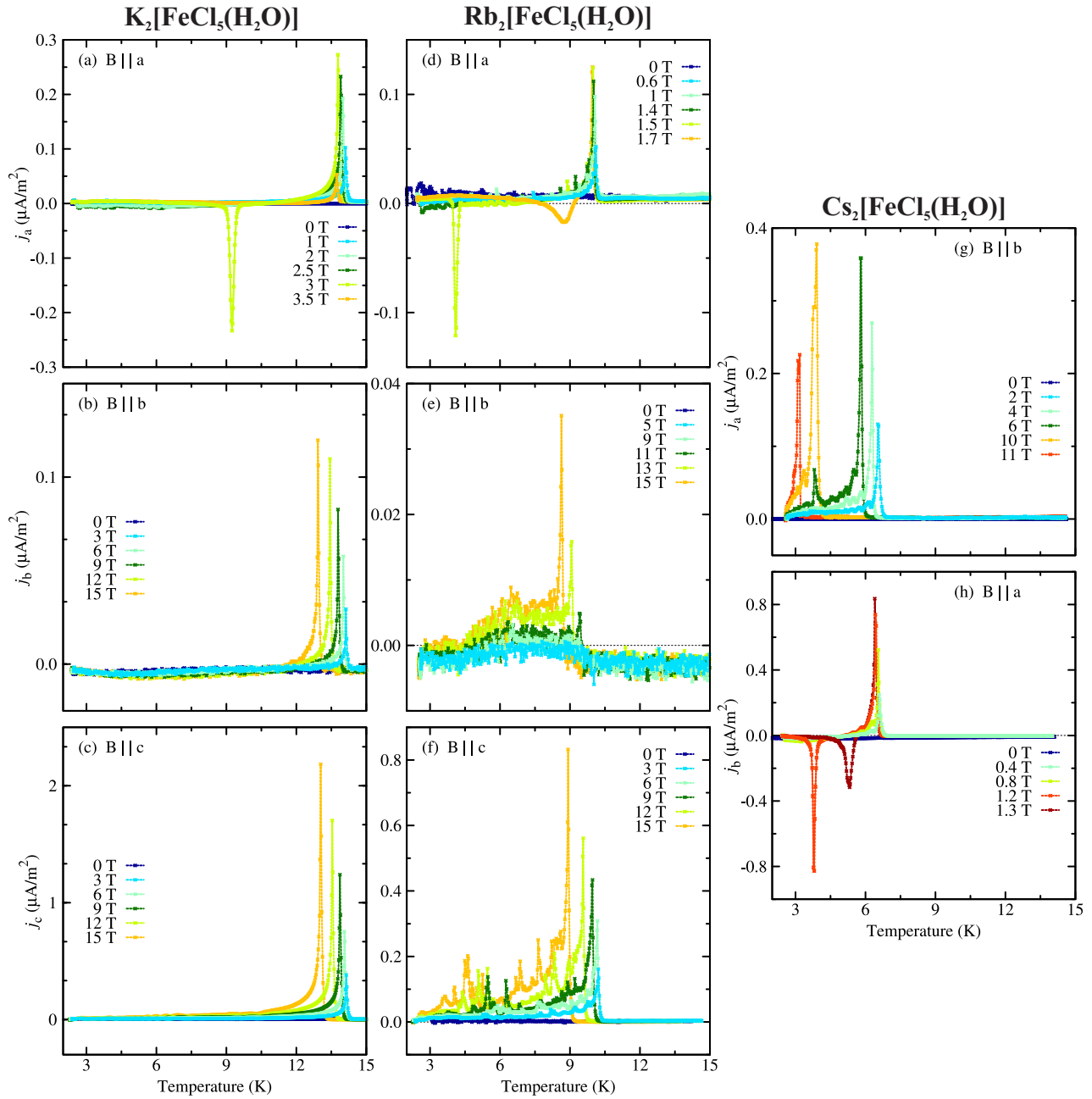


Figure 11: Temperature dependences of the pyroelectric-current densities j_a , j_b and j_c of $K_2[FeCl_5(H_2O)]$, $Rb_2[FeCl_5(H_2O)]$ and $Cs_2[FeCl_5(H_2O)]$ (top to bottom) for magnetic fields applied parallel to the a , b or c axis (left to right). The pyroelectric-current densities for the poling directions of the electric fields, parallel to the preferred directions of the magnetic-field induced electric polarization are presented. The used heating rate was 3 K/min.

In figure 12 the current densities in the spin-flop phases of $K_2[FeCl_5(H_2O)]$, $Rb_2[FeCl_5(H_2O)]$ and $Cs_2[FeCl_5(H_2O)]$ for applied magnetic fields along a are presented.

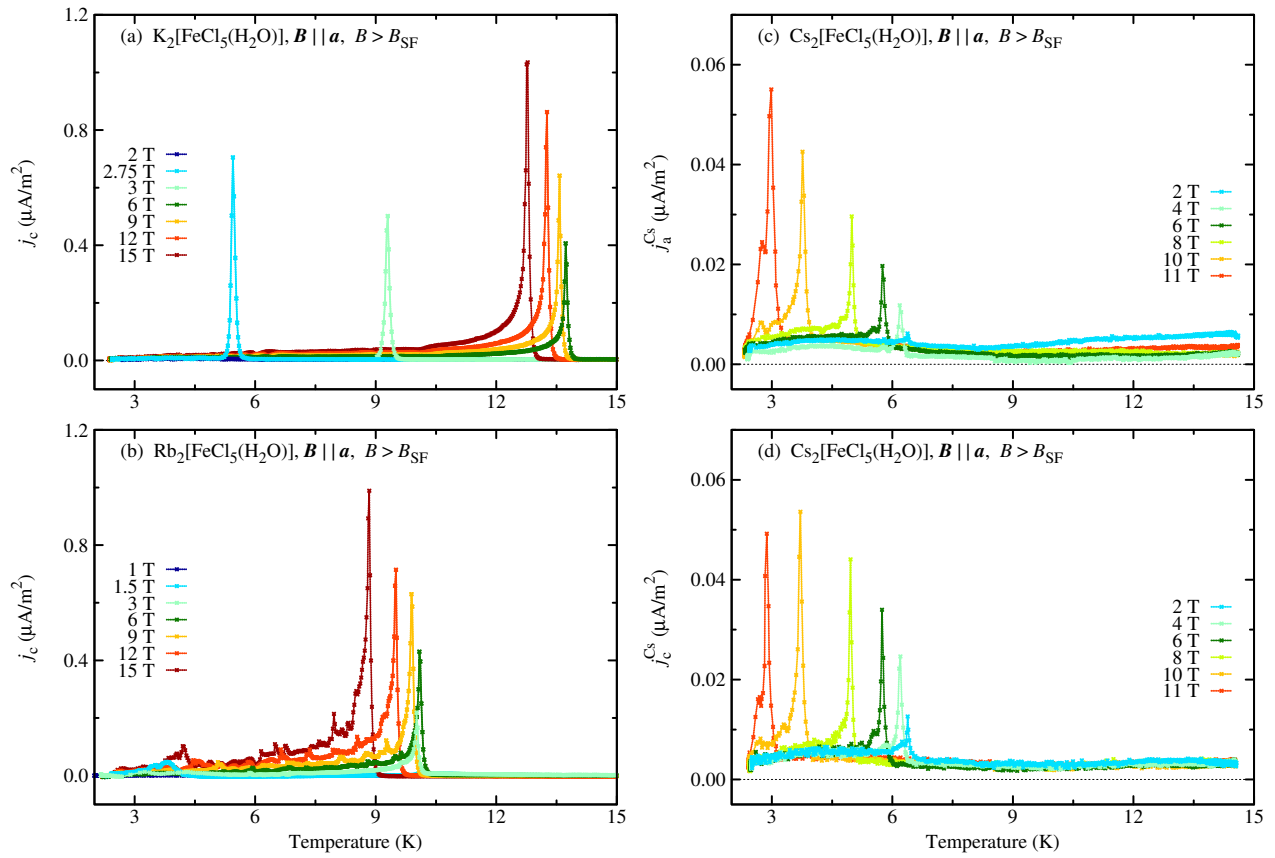


Figure 12: Temperature dependences of the pyroelectric-current densities j_a and j_c of $\text{K}_2[\text{FeCl}_5(\text{H}_2\text{O})]$, $\text{Rb}_2[\text{FeCl}_5(\text{H}_2\text{O})]$ and $\text{Cs}_2[\text{FeCl}_5(\text{H}_2\text{O})]$ for magnetic fields applied parallel to the a axis above the spin-flop fields. The pyroelectric-current densities for the poling directions of the electric fields, parallel to the preferred directions of the magnetic-field induced electric polarization are presented. The used heating rate was 3 K/min.

E.5 CuBr₂

In figure 13, the temperature-dependent pyroelectric-current measurements of CuBr₂ are presented. The investigated sample had a thickness of about 1 mm and was supplied with electrodes consisting of graphite powder mixed with vacuum grease. In all cases, the measurements were performed on single-domain phases, which were obtained by cooling the samples from the paraelectric phase down to the ferroelectric phase with an applied poling voltage of 200 V. For -200 V no single-domain state was obtained. For the measurement processes during the heating cycles, the electric poling fields were not removed.

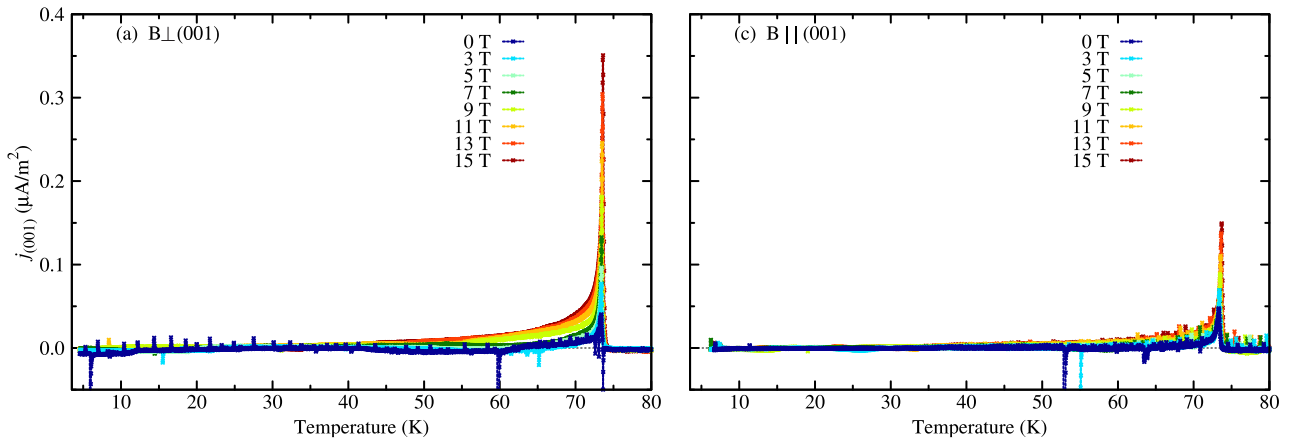


Figure 13: Temperature dependences of the pyroelectric-current density $j_{(001)}$ of CuBr₂ for magnetic fields applied parallel and perpendicular to (001). A heating rate of 3 K/min was used.

E.6 $\text{Mn}_3\text{Al}_2(\text{GeO}_4)_3$

In figure 14, the temperature-dependent pyroelectric-current measurements of $\text{Mn}_3\text{Al}_2(\text{GeO}_4)_3$ along a general direction (hkl) are presented. The magnetic field was applied perpendicular to the surface normal. The investigated sample had a thickness of about 1 mm and was metallized with conductive silver. In all cases, the measurements were performed on single-domain phases, which were obtained by cooling the samples from the paraelectric phase down to the ferroelectric phase with an applied poling voltage of ± 200 V. For the measurement processes during the heating cycles, the electric poling fields were removed.

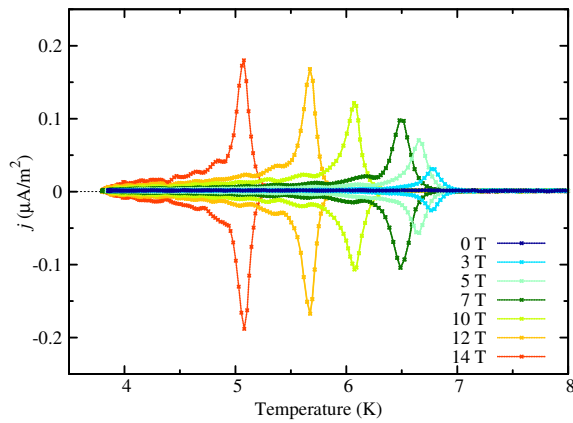


Figure 14: Temperature dependences of the pyroelectric-current density j of $\text{Mn}_3\text{Al}_2(\text{GeO}_4)_3$ along a general direction (hkl). The magnetic field was applied perpendicular to the surface normal. A heating rate of 3 K/min was used.

F Comparison of magnetic-susceptibility data of natural aegirine and synthetic NaFeSi₂O₆

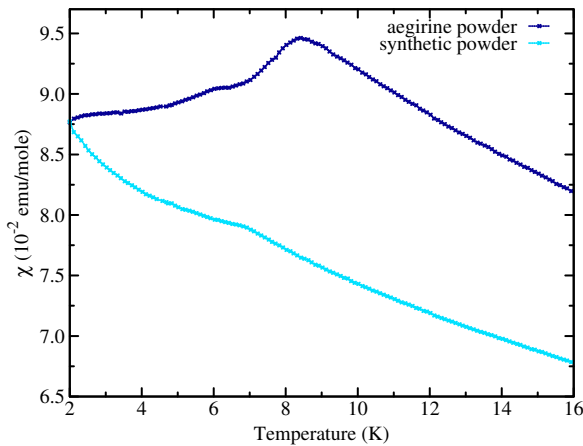


Figure 15: Comparison of magnetic-susceptibility data of polycrystalline, natural aegirine from Mount Malosa (Malawi) and polycrystalline, synthetic NaFeSi₂O₆. Both measurements were performed in an applied magnetic field of 0.1 T.

In figure 15, the magnetic-susceptibility measurements, performed on a polycrystalline powder sample of a natural aegirine⁷ and a synthetic polycrystalline powder sample⁸ of NaFeSi₂O₆ are presented. The applied magnetic field in both cases was 0.1 T. The magnetic susceptibility of the natural sample shows two anomalies at about 8 K and about 6 K, confirming the magnetic transition temperatures already reported in [14, 204], see figure 15. In contrast, the magnetic susceptibility of the synthetic sample shows only one anomaly at about 7 K in accordance with the results reported in [16]. Hence, the magnetic properties of synthetic NaFeSi₂O₆ are different from those of the natural aegirine with a complex composition, see also section 4.1. One may speculate that multiferroicity in the natural aegirine could be caused by the natural dopants present in that compound and that these drive the potentially only linear magnetoelectric synthetic NaFeSi₂O₆ to become multiferroic. However, a definite proof of this speculation is still missing because of the difficulties in growing large synthetic single crystals of NaFeSi₂O₆.

⁷The sample was taken from the same natural crystal from Mount Malosa (Malawi) of the composition Na_{1.04}Fe_{0.83}Ca_{0.04}Mn_{0.02}Al_{0.01}Ti_{0.08}Si₂O₆, already used in the PhD thesis of S. Jodlauk [14].

⁸The synthetic polycrystalline powder of NaFeSi₂O₆ was synthesized by crystallisation of a glass of stoichiometric composition at 800 °C by Prof. Dr. P. Becker.

G Symmetry aspects of magnetoelectric phenomena

G.1 Forms of the linear magnetoelectric tensor

$$\begin{aligned}
 \text{(A)} \quad 1, \bar{1}' & \begin{bmatrix} \alpha_{11} & \alpha_{12} & \alpha_{13} \\ \alpha_{21} & \alpha_{22} & \alpha_{23} \\ \alpha_{31} & \alpha_{32} & \alpha_{33} \end{bmatrix} \\
 \text{(B)} \quad 2, m', \frac{2}{m'} & \begin{bmatrix} \alpha_{11} & 0 & 0 \\ 0 & \alpha_{22} & \alpha_{23} \\ 0 & \alpha_{32} & \alpha_{33} \end{bmatrix}_x \quad \begin{bmatrix} \alpha_{11} & 0 & \alpha_{13} \\ 0 & \alpha_{22} & 0 \\ \alpha_{31} & 0 & \alpha_{33} \end{bmatrix}_y \quad \begin{bmatrix} \alpha_{11} & \alpha_{12} & 0 \\ \alpha_{21} & \alpha_{22} & 0 \\ 0 & 0 & \alpha_{33} \end{bmatrix}_z \\
 \text{(C)} \quad 2', m, \frac{2'}{m} & \begin{bmatrix} 0 & \alpha_{12} & \alpha_{13} \\ \alpha_{21} & 0 & 0 \\ \alpha_{31} & 0 & 0 \end{bmatrix}_x \quad \begin{bmatrix} 0 & \alpha_{12} & 0 \\ \alpha_{21} & 0 & \alpha_{23} \\ 0 & \alpha_{32} & 0 \end{bmatrix}_y \quad \begin{bmatrix} 0 & 0 & \alpha_{13} \\ 0 & 0 & \alpha_{23} \\ \alpha_{31} & \alpha_{32} & 0 \end{bmatrix}_z \\
 \text{(D)} \quad 222, m'm'2, (2m'm'), & \begin{bmatrix} \alpha_{11} & 0 & 0 \\ 0 & \alpha_{22} & 0 \\ 0 & 0 & \alpha_{33} \end{bmatrix} \\
 & (m'2m'), m'm'm' \\
 \text{(E}_1\text{)} \quad 2mm, 22'2', m'm2' & \begin{bmatrix} 0 & 0 & 0 \\ 0 & 0 & \alpha_{23} \\ 0 & \alpha_{32} & 0 \end{bmatrix} \\
 & (m'2'm), m'mm \\
 \text{(E}_2\text{)} \quad mm2, 2'2'2, 2'mm', & \begin{bmatrix} 0 & \alpha_{12} & 0 \\ \alpha_{21} & 0 & 0 \\ 0 & 0 & 0 \end{bmatrix} \\
 & (m2'm'), mmm' \\
 \text{(E}_3\text{)} \quad m2m, 2'22', mm'2', & \begin{bmatrix} 0 & 0 & \alpha_{13} \\ 0 & 0 & 0 \\ \alpha_{31} & 0 & 0 \end{bmatrix} \\
 & (2'm'm), mm'm
 \end{aligned}$$

Here, the 58 magnetic point groups are summarized, which allow the magnetoelectric effect including the corresponding tensor forms [118]. There are 31 magnetic point groups, for which the linear magnetoelectric tensor has not to be symmetric and which allow simultaneously the occurrence of a spontaneous toroidal moment. Under point **(B)** and **(C)** three different tensor forms are

given with the indices x, y, z depending on the setting of the respective point groups with respect to the crystal-physical reference system. The tensor forms with the index x correspond, for example, to the case when the twofold rotation axis is oriented parallel to x or when the mirror plane is perpendicular to x . The tensor forms under (\mathbf{E}_1) , (\mathbf{E}_2) and (\mathbf{E}_3) also differ only by the setting of the corresponding point groups. In all cases the point group symbols in brackets designate other settings of the respective point groups with the same tensor form.

$$(\mathbf{F}) \quad 4, \bar{4}', 4/m', 3, \bar{3}', 6, \bar{6}', 6/m' \quad \begin{bmatrix} \alpha_{11} & \alpha_{12} & 0 \\ -\alpha_{12} & \alpha_{11} & 0 \\ 0 & 0 & \alpha_{33} \end{bmatrix}$$

$$(\mathbf{G}) \quad \bar{4}, 4', 4'/m' \quad \begin{bmatrix} \alpha_{11} & \alpha_{12} & 0 \\ \alpha_{12} & -\alpha_{11} & 0 \\ 0 & 0 & 0 \end{bmatrix}$$

$$(\mathbf{H}) \quad 422, 4m'm', \bar{4}'2m', (\bar{4}'m'2), \\ 4/m'm'm', 32, 3m', \bar{3}'m', 622, \\ 6m'm', \bar{6}'m'2, (\bar{6}'2m'), 6/m'm'm' \quad \begin{bmatrix} \alpha_{11} & 0 & 0 \\ 0 & \alpha_{11} & 0 \\ 0 & 0 & \alpha_{33} \end{bmatrix}$$

$$(\mathbf{I}) \quad 4mm, 42'2', \bar{4}'2'm, (\bar{4}'m2') \\ 4/m'mm, 32', 3m, \bar{3}'m, 62'2', \\ 6mm, \bar{6}'m2', (\bar{6}'2'm), 6/m'mm \quad \begin{bmatrix} 0 & \alpha_{12} & 0 \\ -\alpha_{12} & 0 & 0 \\ 0 & 0 & 0 \end{bmatrix}$$

$$(\mathbf{J}) \quad \bar{4}2m, \bar{4}m'2', 4'22', 4'm'm, 4'/m'm'm \quad \begin{bmatrix} \alpha_{11} & 0 & 0 \\ 0 & -\alpha_{11} & 0 \\ 0 & 0 & 0 \end{bmatrix}$$

$$(\mathbf{K}) \quad 23, m'\bar{3}', 432, \bar{4}'3m', m'\bar{3}'m' \quad \begin{bmatrix} \alpha_{11} & 0 & 0 \\ 0 & \alpha_{11} & 0 \\ 0 & 0 & \alpha_{11} \end{bmatrix}$$

G.2 Magnetoelectric types of order

In tables 5 and 6, the 90 magnetic and 32 grey point groups are classified with respect to the allowed magnetoelectric-ordering phenomena.

Type	Type of ordering		Permitted terms of stored free enthalpy	Magnetic point groups		Number of magnetic point groups		
	magn.	el.		V_s not permitted	V_s permitted			
FEIV	D	P	$E \ o \ oo \ ooo \ EHH$	$[1'], [21'], [m1'], [mm21'], 41', 4mm1', 31', 3m1', 61', 6mm1'$		10	31	49
FEIII	\bar{M}	P	$E \ o \ oo \ HEE \ EHH$	$6', 6'mm'$		2		
FEII	\bar{M}	P	$E \ o \ EH \ HEE \ EHH$	$4', 4'mm'$	$[mm2], 4mm, 3m, 6mm$	6		
FEI/FMI	M	P	$E \ H \ EH \ HEE \ EHH$	$[\{m'm'2\}], 3m', 4m'm', 6m'm'$	$[\{1\}], [\{2\}], 3, 4, 6, [\{m\}], [\{2\}'], [\{m'\}], [\{mm'2'\}]$	13	31	
FMII	M	\bar{P}	$o \ H \ EH \ HEE \ EHH$	$\bar{4}, \bar{4}2'm'$	$\{2'2'2\}, 42'2', 32', 62'2'$	6		
FMIII	M	\bar{P}	$o \ H \ oo \ HEE \ EHH$	$\bar{6}, \bar{6}m'2'$		2		
FMIV	M	O	$o \ H \ oo \ HEE \ ooo$	$\{\bar{1}\}, \{2/m\}, \{2'/m'\}, \{m'm'm\}, 4/m, 4/mm'm', \bar{3}, \bar{3}m', 6/m, 6/mm'm'$		10		

Table 5: Classification of the 90 magnetic and 32 grey point groups according to different magnetoelectric types. Types of order: M = pyro-, ferro- or ferrimagnetic; P = pyro-, ferro- or ferrielectric; \bar{M} = antiferromagnetic; \bar{P} = antiferroelectric; D = diamagnetic, paramagnetic, antiferromagnetic; O = paraelectric, antiferroelectric. $\{\}$ weak ferromagnetism, $[\]$ weak ferroelectricity. V_s allowed means that the occurrence of a toroidal moment is symmetry allowed. Extracted from [25].

Type	Type of ordering		Permitted terms of stored free enthalpy	Magnetic point groups		Number of magnetic point groups		
	magn.	el.		V_s not permitted	V_s permitted			
AAI	\bar{M}	\bar{P}	$\circ \circ EH HEE EHH$	$222, 422, \bar{4}2m, 4'22', 4'2m', 32, 622, \bar{6}'m'2, 23, \bar{4}'3m'$	$\bar{4}', \bar{4}'2'm, \bar{6}', \bar{6}'m'2'$	14	73	
AAII	\bar{M}	\bar{P}	$\circ \circ \circ HEE EHH$	$\bar{6}m2, 6'2'2$		2		
AAIII	\bar{M}	\bar{P}	$\circ \circ EH \circ \circ \circ \circ \circ$	$m'm'm', 4'/m', 4'/m'm'm, 4/m'm'm', \bar{3}'m', 6/m'm'm', 432, m'3, m'3m'$	$\bar{1}', 2/m', 2'/m, mmm', 4/m', 4/m'mm, \bar{3}', \bar{3}'m, 6/m', 6/m'mm$	19		
AAIV	\bar{M}	O	$\circ \circ \circ HEE \circ \circ \circ$	$mmm, 4'/m, 4'/mmm, 4'/mmm', 6'/mmm, \bar{3}m, 6'/m', 6'/m'm'm, m3, m3m'$		10		
	\bar{M}	\bar{P}		$4'32'$		1		
AAV	\bar{M}	\bar{P}	$\circ \circ \circ \circ \circ EHH$	$\bar{4}3m$		1		
	D	\bar{P}		$2221', \bar{4}1', 4221', \bar{4}2m1', 6221', 321', \bar{6}1', \bar{6}m21', 231', \bar{4}3m1'$		10		
AAVI	\bar{M}	O	$\circ \circ \circ \circ \circ \circ \circ$	$m3m$		1		
	D	\bar{P}		$4321'$		1		
	\bar{M}	\bar{P}		$6'/m, 6'/mm'm, m'3m$		3		
	\bar{M}	\bar{P}		$\bar{1}1', 2/m1', mmm1', 4/m1', 4/mmm1', \bar{3}1', \bar{3}m1', 6/m1', 6/mmm1', m31', m3m1'$		11		
	D	O						

Table 6: Classification of the 90 magnetic and 32 grey point groups according to different magnetoelectric types. Types of order: M = pyro-, ferro- or ferrimagnetic; P = pyro-, ferro- or ferrielectric; \bar{M} = antiferromagnetic; \bar{P} = antiferroelectric; D = diamagnetic, paramagnetic, antiferromagnetic; O = paraelectric, antiferroelectric. $\{\}$ weak ferromagnetism, $[\]$ weak ferroelectricity. V_s allowed means that the occurrence of a toroidal moment is symmetry allowed. Extracted from [25].

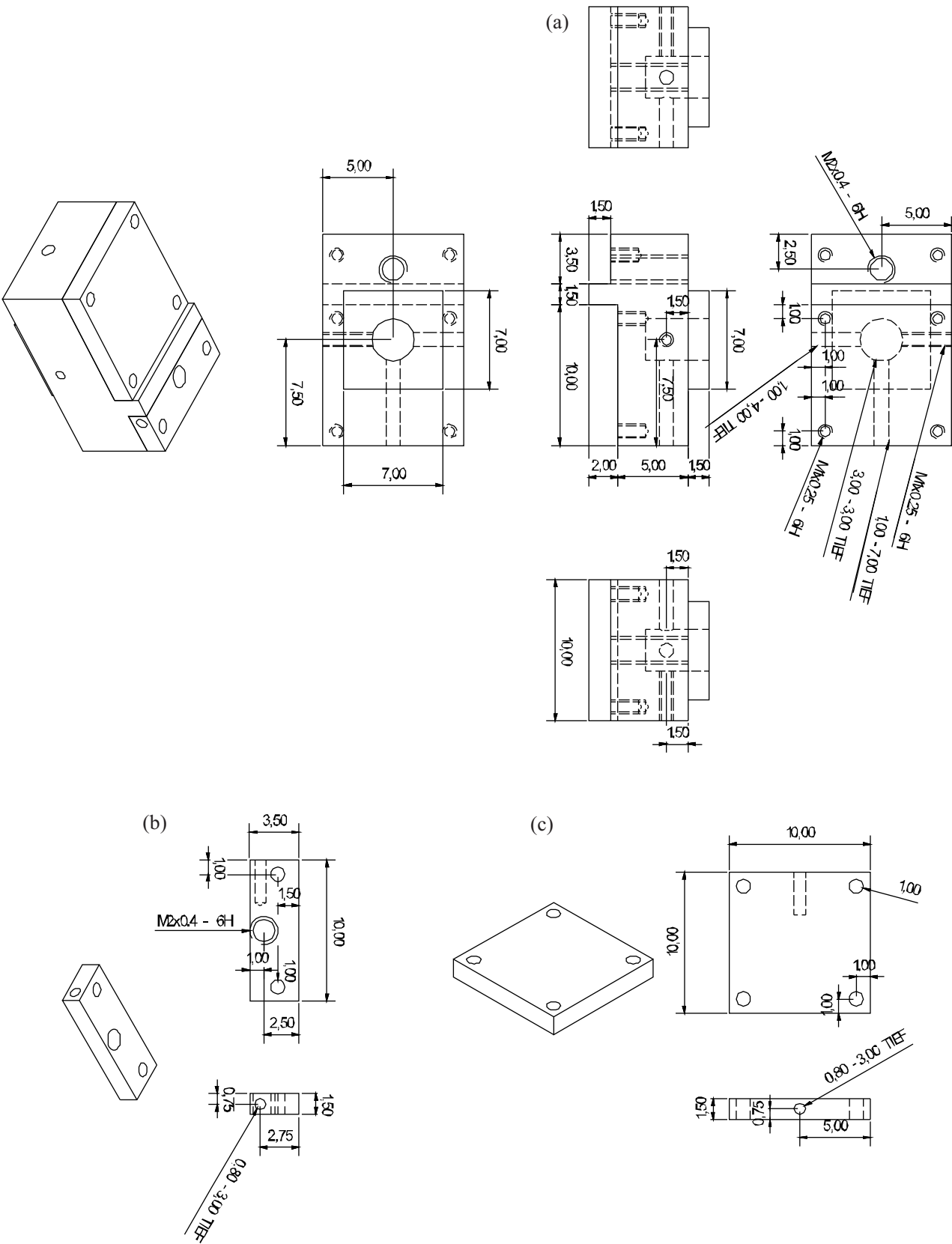


Figure 18: Sample holder: (a) Teflon body, (b)+(c) Copper electrode discs

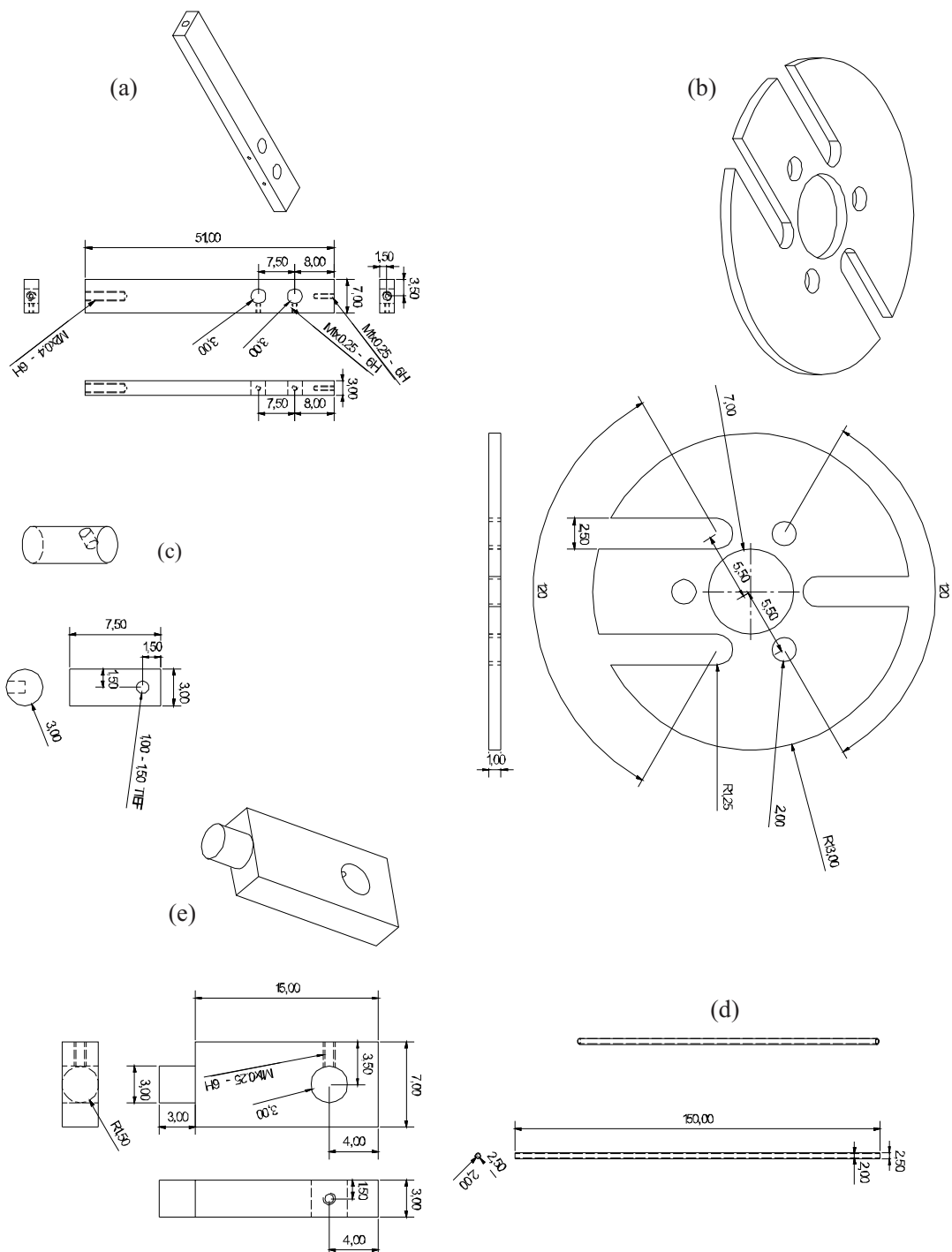


Figure 19: (a) Sample platform (b) Radiation shield (c) Copper pin for the attachment of the sample holder on the sample platform (d) Stainless steel capillary tube (e) Supplement to the sample platform.

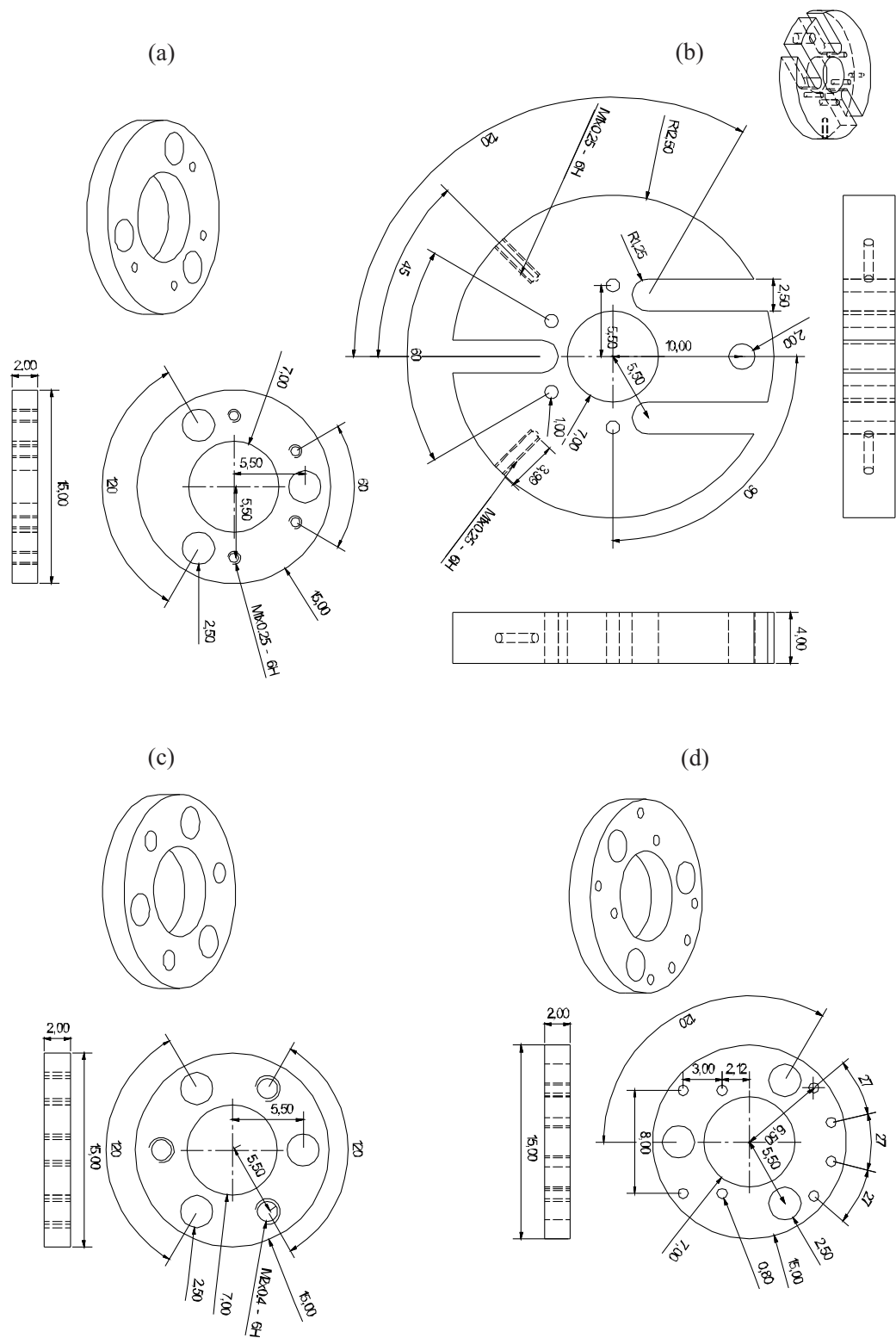


Figure 20: Different copper discs, which are linked to the stainless steel capillary tubes.

H.2 Continuous-flow cryostat

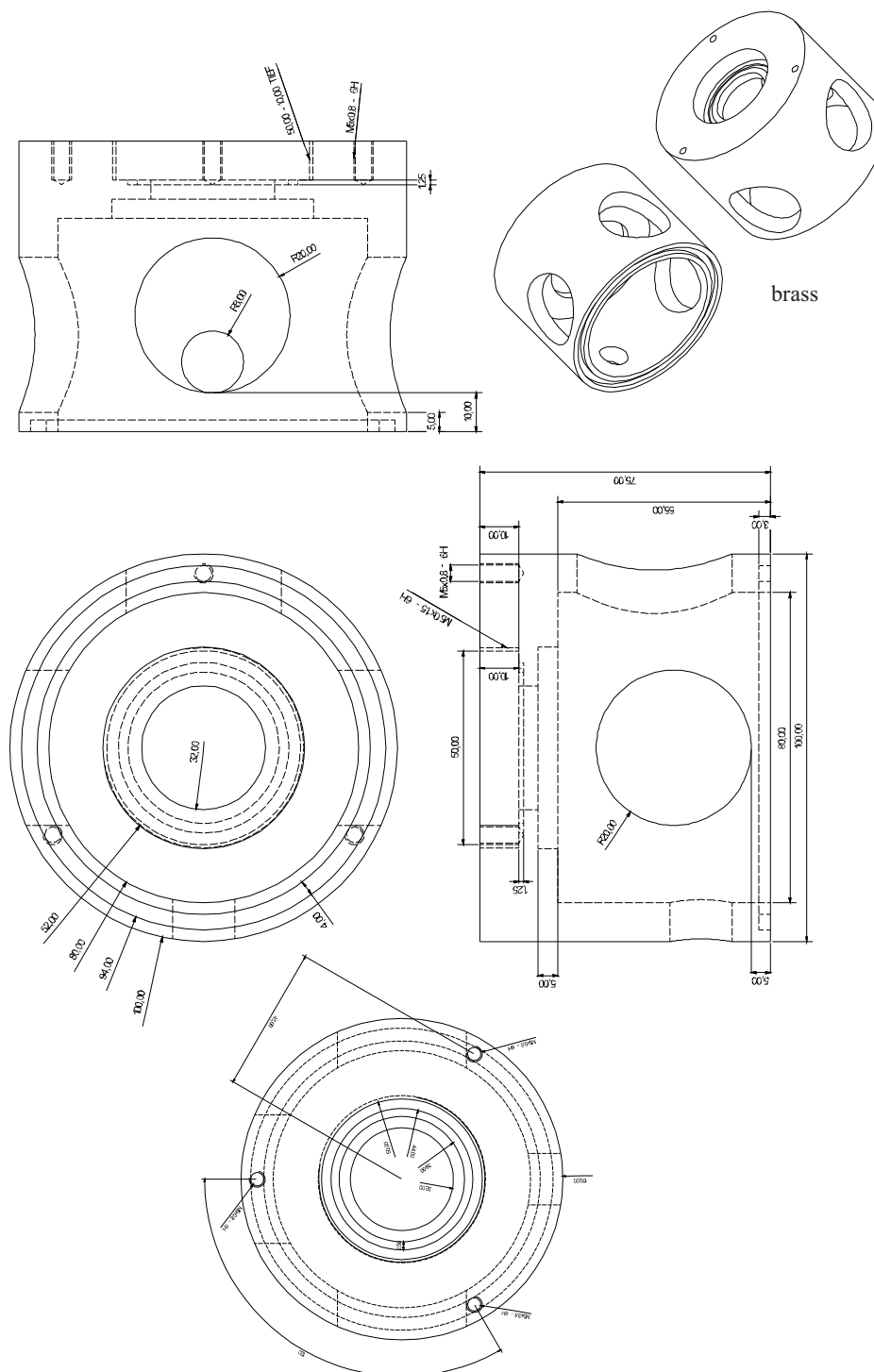


Figure 21: Main chamber of the continuous-flow cryostat, made of brass.

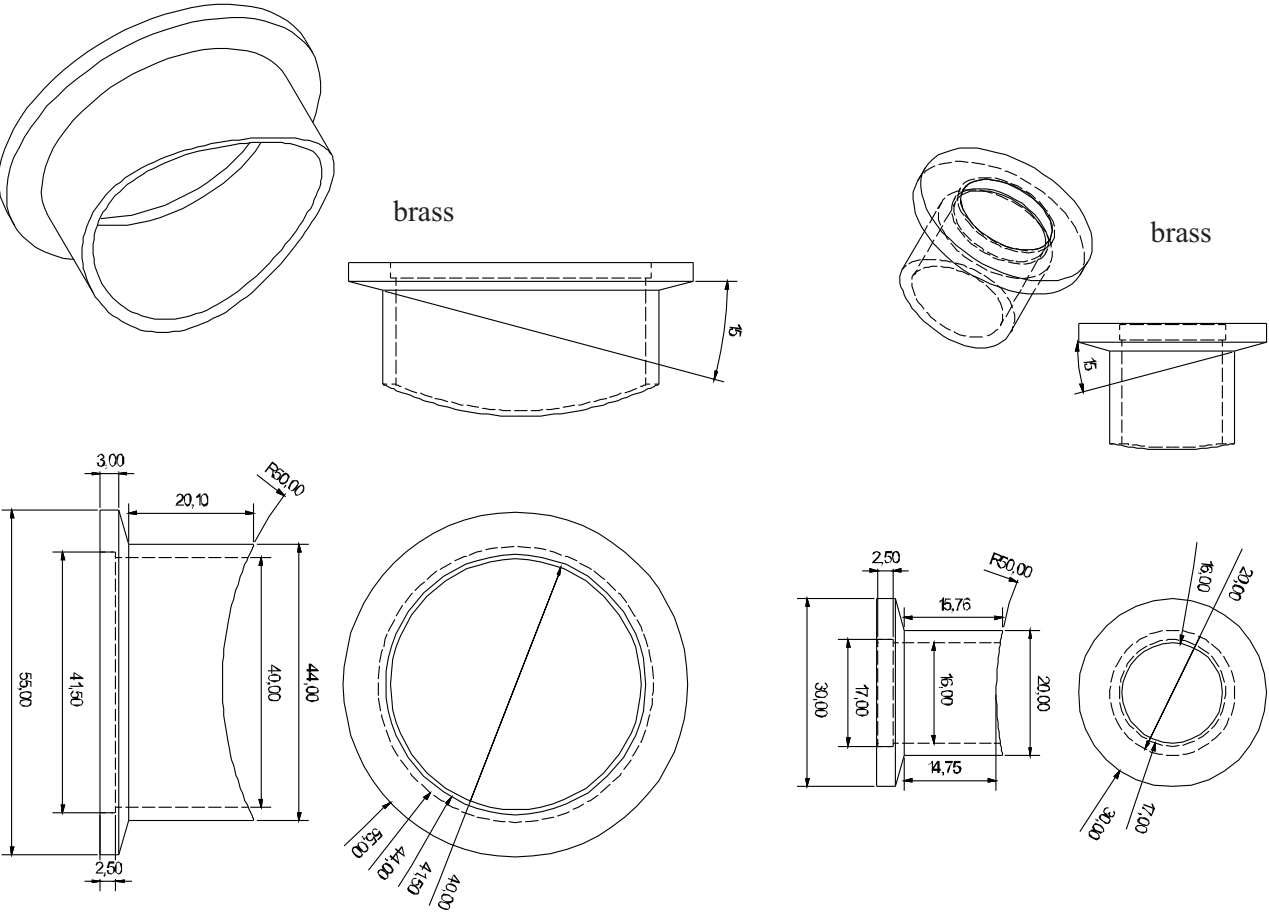


Figure 22: Vacuum flanges for the main chamber of the continuous-flow cryostat, made of brass.

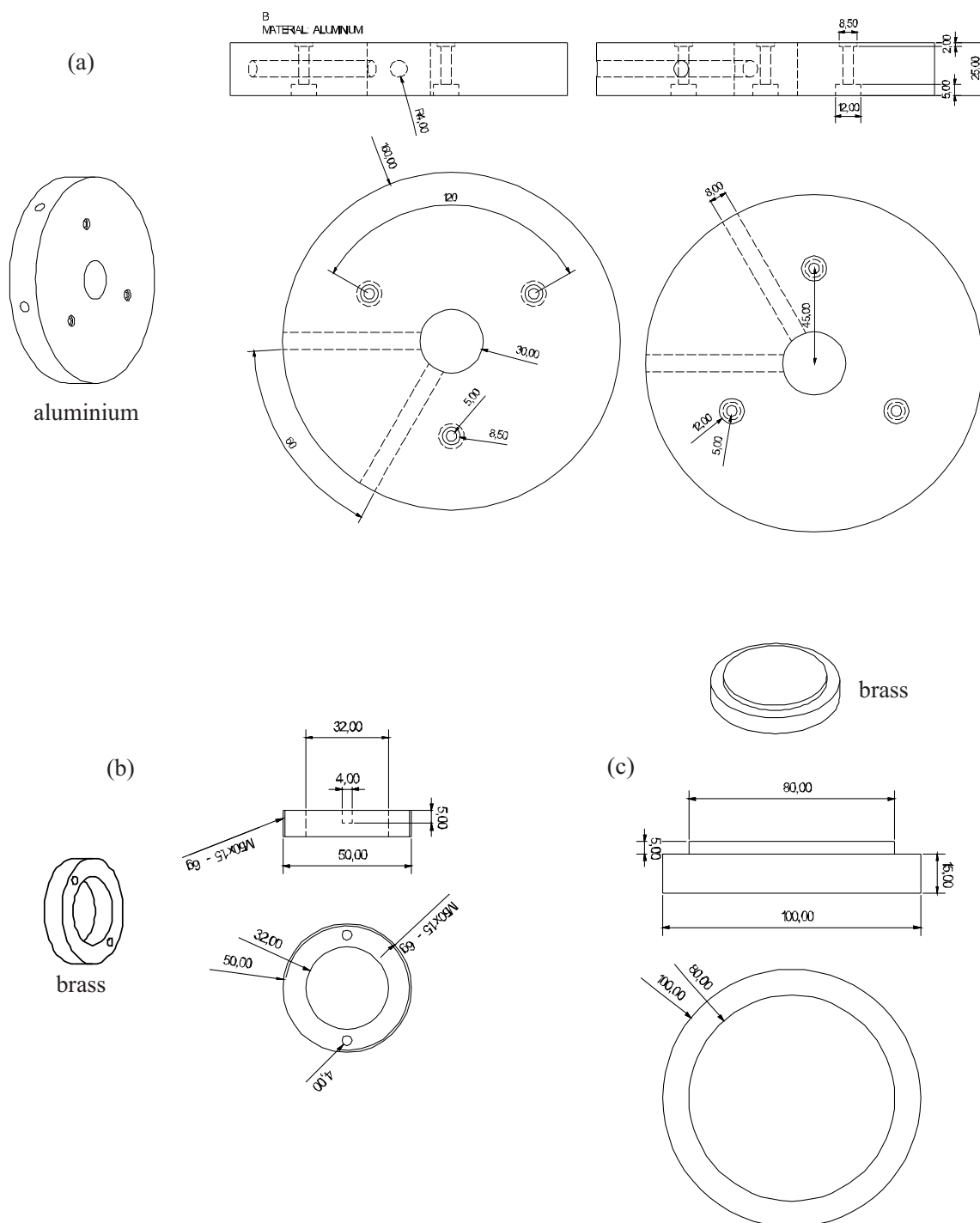


Figure 23: (a) Base plate of the continuous-flow cryostat, made of aluminium. (b) Threaded brass ring for the attachment of the fused silica window in the bottom of the main chamber of the continuous-flow cryostat. Cap of the main chamber of the continuous-flow cryostat, made of brass.

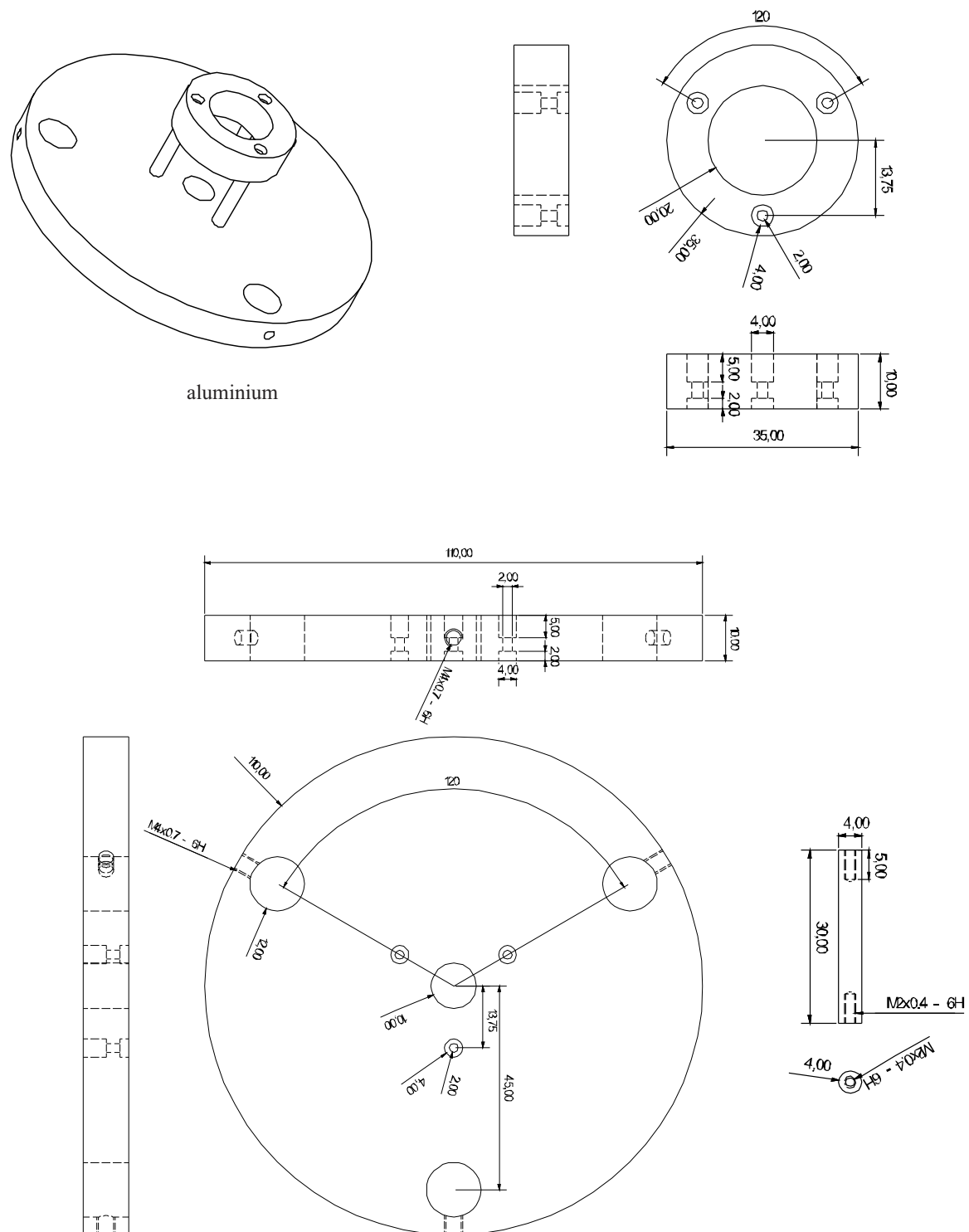


Figure 24: Carrier for the halogen lamp, made of aluminium.

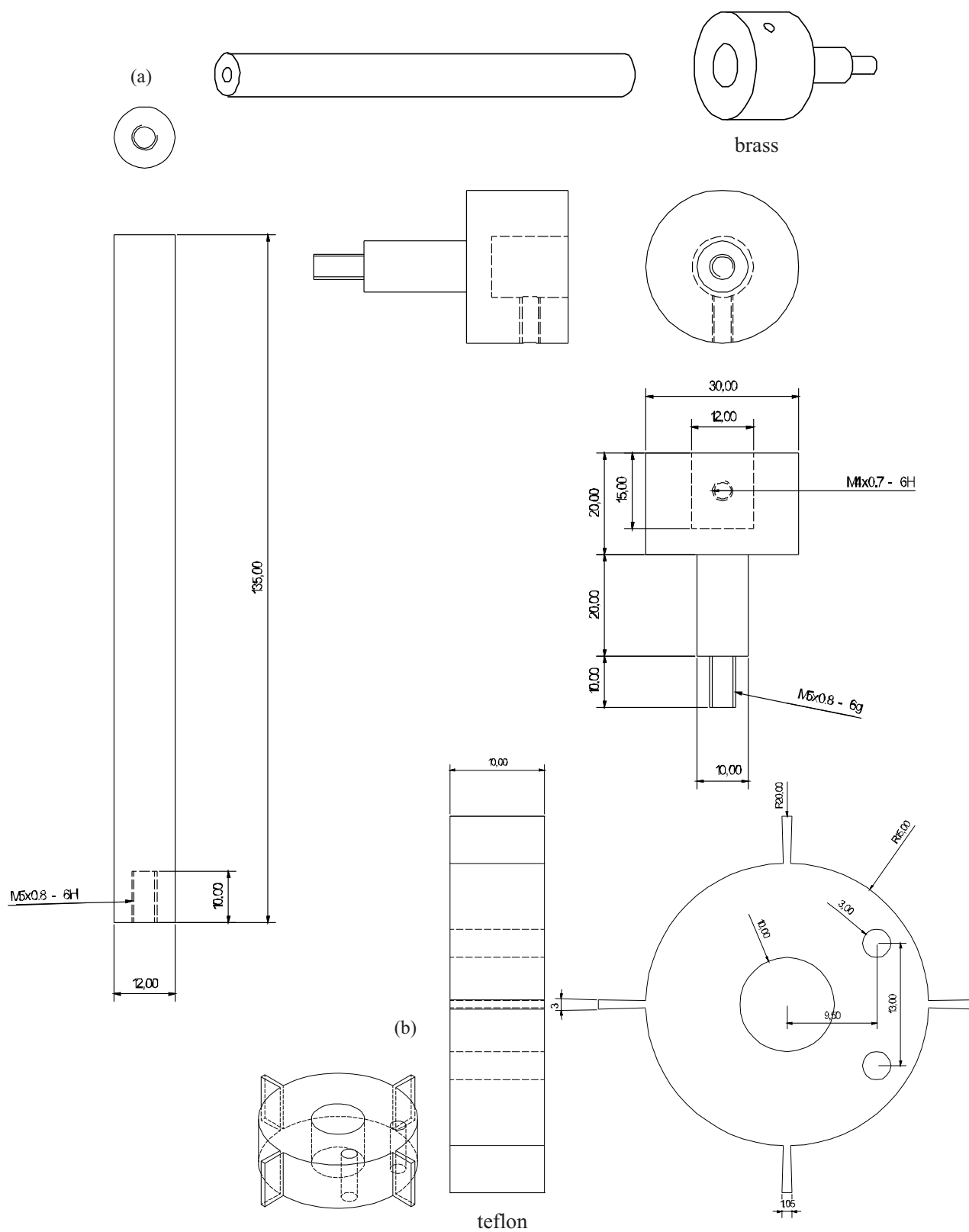


Figure 25: (a) Brass rods, on which the main chamber of the continuous-flow cryostat is mounted. (b) Teflon ring for the attachment of the stainless steel inlet pipes for the cold nitrogen gas within the cryostat.

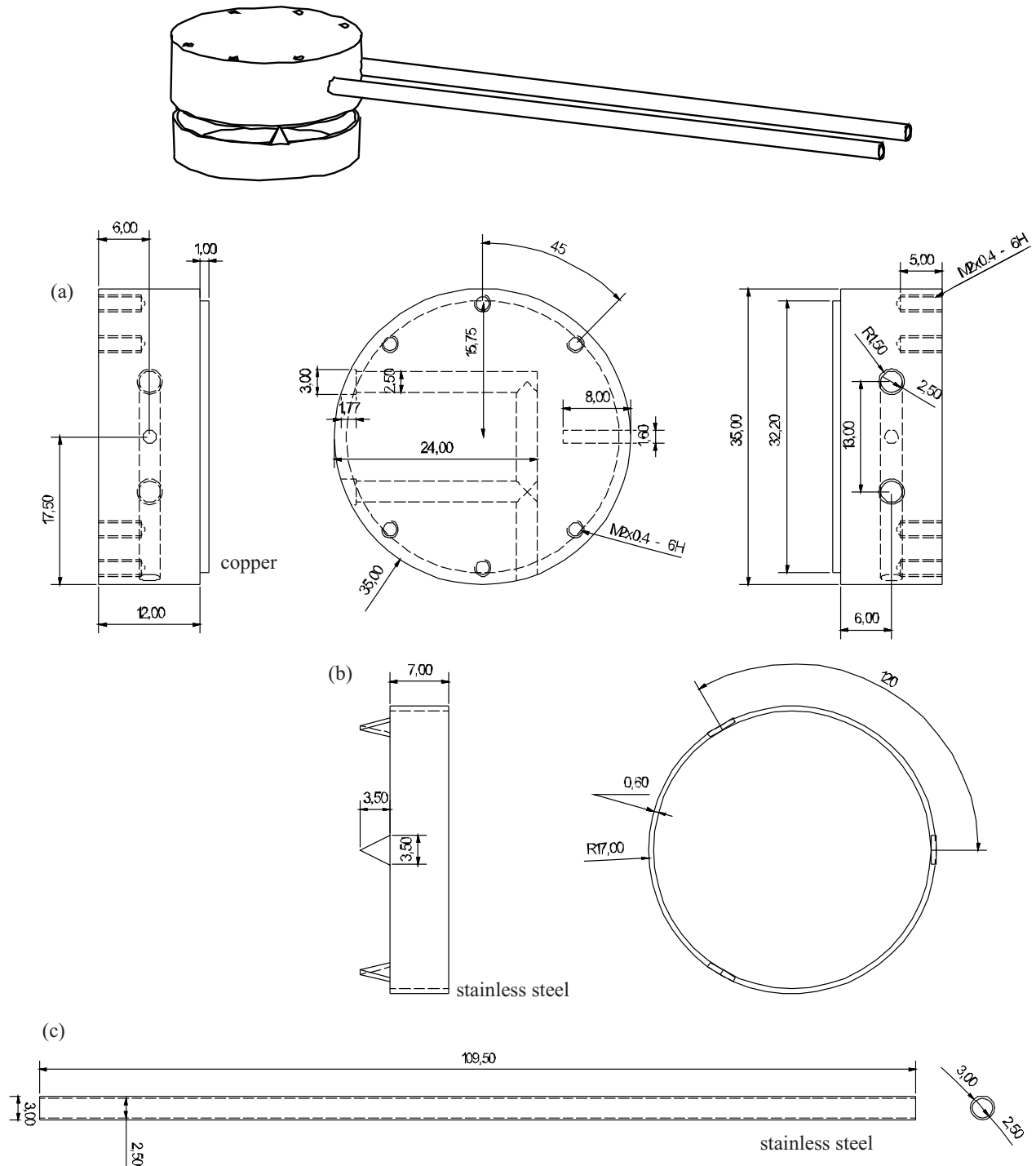


Figure 26: Sample holder consisting of a (a) copper cylinder, (b) a stainless steel ring and (c) two stainless steel capillary tubes.

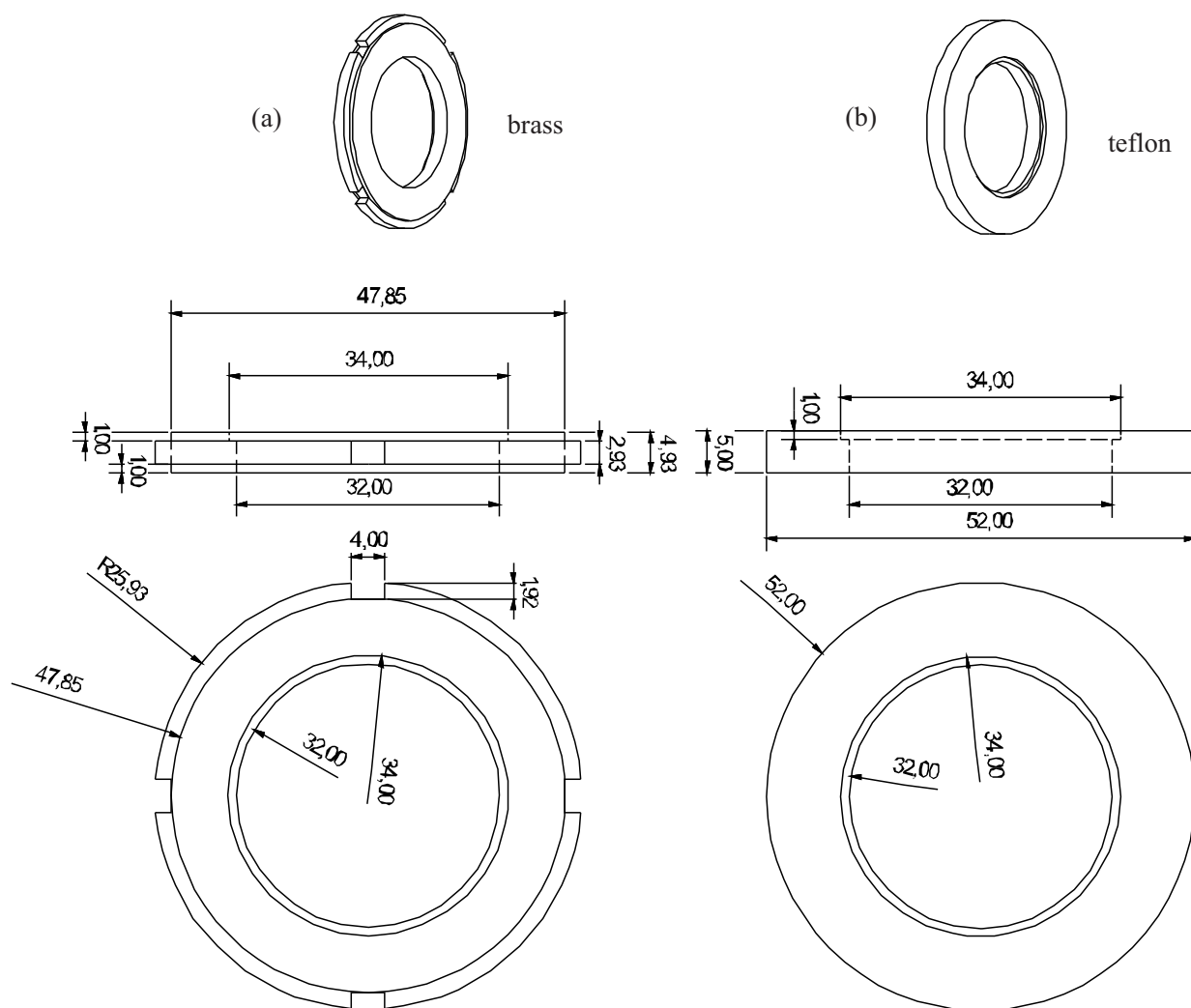


Figure 27: Insertion rings for the electric insulation of the sample holder from the rest of the cryostat.

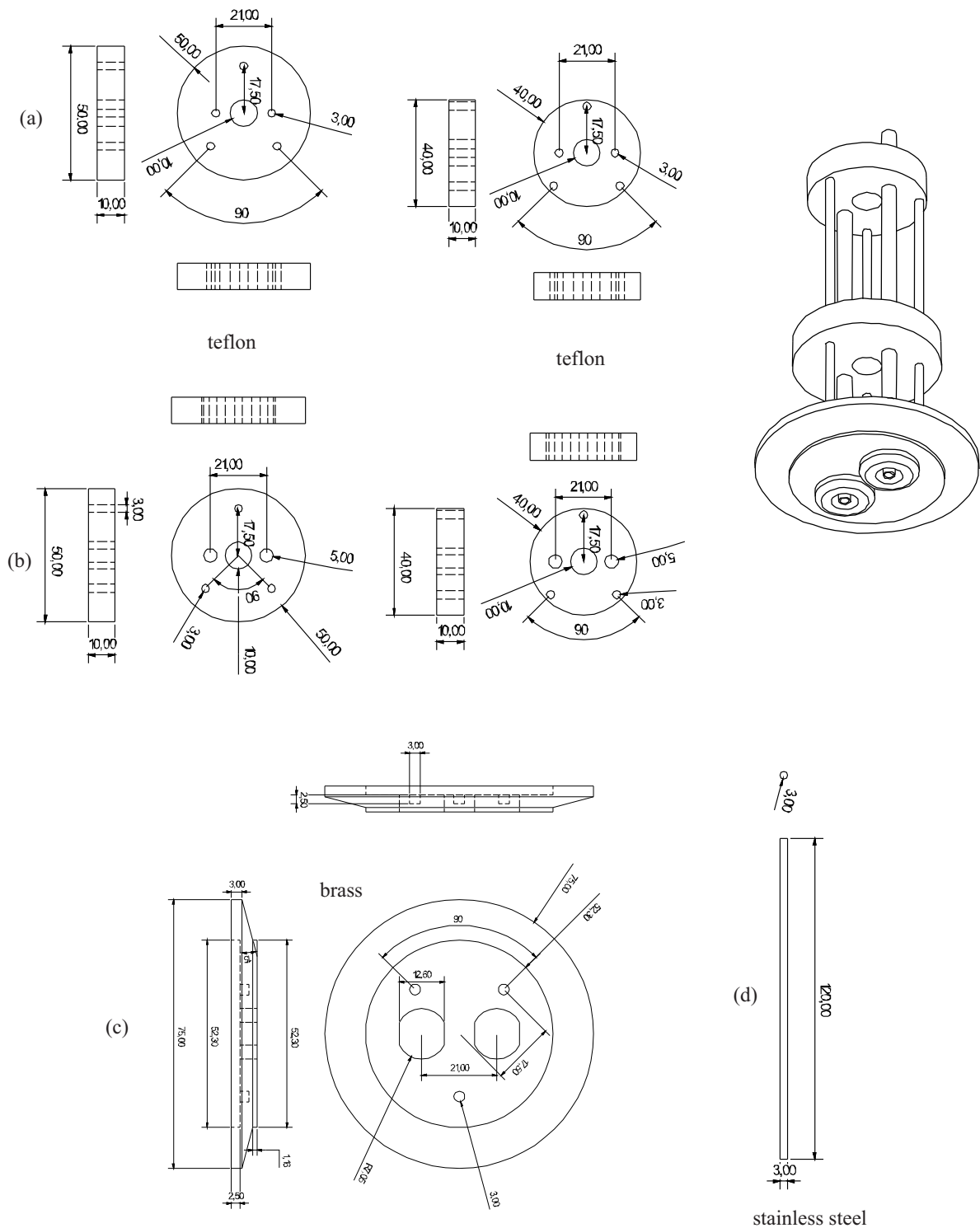


Figure 28: Feed through for the thermometer and sample wiring.

Bibliography

- [1] W. C. Röntgen. *Ann. Physik* **35**, 264 (1888)
- [2] P. Curie. *J. Physique* **3**, 393 (1894)
- [3] J. Curie and P. Curie. *B. Soc. Fr. Mineral.* **3**, 90 (1880)
- [4] D. N. Astrov. *Sov. Phys.-JETP* **11**, 708 (1960)
- [5] H. Schmid. *Int. J. Magnetism* **4**, 337 (1973)
- [6] S. Goshen, D. Mukamel, H. Shaked and S. Shtrikman. *J. Appl. Phys.* **40**, 1590 (1969)
- [7] S. Goshen, D. Mukamel, H. Shaked and S. Shtrikman. *Phys. Rev. B* **2**, 4679 (1970)
- [8] R. E. Newnham, J. J. Kramer, W. A. Schulze and L. E. Cross. *J. Appl. Phys.* **49**, 6088 (1978)
- [9] M. K. Wilkinson, D. E. Cox, B. C. Frazier, R. E. Newnham and R. P. Santoro. *J. Appl. Phys.* **40**, 1124 (1969)
- [10] T. Kimura, T. Goto, H. Shintani, K. Ishizaka, T. Arima and Y. Tokura. *Nature* **426**, 55 (2003)
- [11] K. F. Wang, J.-M. Liu and Z. F. Ren. *Adv. Phys.* **58**, 321 (2009)
- [12] I. Kim, B.-G. Jeon, D. Patil, S. Patil, G. Nénert and K. H. Kim. *J. Phys.: Condens. Matter* **24**, 306001 (2012)
- [13] L. Zhao, T.-L. Hung, C.-C. Li, Y.-Y. Chen, M.-K. Wu, R. K. Kremer, M. G. Banks, A. Simon, M.-H. Whangbo, C. Lee, J. S. Kim, I. Kim and K. H. Kim. *Adv. Mater.* **24**, 2469 (2012)
- [14] S. Jodlauk. PhD thesis, Universität zu Köln 2009
- [15] S. Jodlauk, P. Becker, J. A. Mydosh, D. I. Khomskii, T. Lorenz, S. V. Streltsov, D. C. Hezel and L. Bohatý. *J. Phys.: Condens. Matter* **19**, 432201 (2007)
- [16] P. J. Baker, H. J. Lewtas, S. J. Blandell, T. Lancaster, I. Franke, W. Hayes, F. L. Pratt, L. Bohatý and P. Becker. *Phys. Rev. B* **81**, 214403 (2010)
- [17] G. Nénert, I. Kim, M. Isobe, C. Ritter, A. N. Vasiliev, K. H. Kim and Y. Ueda. *Phys. Rev. B* **81**, 184408 (2010)

- [18] G. Nénert, M. Isobe, I. Kim, C. Ritter, C. V. Colin, A. N. Vasiliev, K. H. Kim and Y. Ueda. *Phys. Rev. B* **82**, 024429 (2010)
- [19] O. Heyer, N. Hollmann, I. Klassen, S. Jodlauk, L. Bohatý, P. Becker, J. A. Mydosh, T. Lorenz and D. I. Khomskii. *J. Phys.: Condens. Matter* **18**, L471 (2006)
- [20] K. Taniguchi, N. Abe, T. Takenobu, Y. Isawa and T. Arima. *Phys. Rev. Lett.* **97**, 097203 (2006)
- [21] A. H. Arkenbout, T. T. M. Palstra, T. Siegrist and T. Kimura. *Phys. Rev. B* **74**, 184431 (2001)
- [22] K. Aizu. *Phys. Rev. B* **2**, 754 (1970)
- [23] R. E. Newnham. *American Mineralogist* **59**, 906 (1974)
- [24] R. E. Newnham and L. E. Cross. *Ferroelectrics* **10**, 269 (1976)
- [25] H. Schmid. *J. Phys.: Condens. Matter* **20**, 434201 (2008)
- [26] R. R. Birss. *Symmetry and Magnetism* (Amsterdam, North-Holland Publishing Company) (1964)
- [27] E. Ascher. *Int. J. Magn.* **5**, 287 (1974)
- [28] N. V. Belov, N. N. Neronova, T. S. Smirnova. *Kristallografiya* **2**, 315 (1957) (Translation: *Soviet Phys. Cryst.* **32**, 311)
- [29] G. Donnay, L. M. Corliss, J. D. H. Donnay, N. Elliot and J. M. Hastings. *Phys. Rev.* **112**, 1917 (1958)
- [30] E. F. Bertaut. *Acta Cryst. A* **24**, 217 (1968)
- [31] E. F. Bertaut. *J. Phys. Colloques* **32**, 462 (1971)
- [32] W. Opechowski and T. Dreyfus. *Acta Cryst. A* **27**, 470 (1971)
- [33] H. Schmid. *Ferroelectrics* **162**, 317 (1994)
- [34] D. I. Khomskii. *J. Magn. Magn. Mater.* **306**, 1 (2006)
- [35] D. I. Khomskii. *Physics* **2**, 20 (2009)
- [36] H. Schmid. *Bull. Mater. Sci.* **17**, 1411 (1994)
- [37] H. Schmid. *Ferroelectrics* **221**, 9 (1999)
- [38] M. Adachi, Y. Akishige, T. Asahi, K. Deguchi, K. Gesi, K. Hasebe, T. Hikita, T. Ikeda and Y. Iwata. *Ferroelectrics and Related Substances: Oxides Part I: Perovskite-type Oxides and LiNbO₃ Family*, Landolt-Börnstein, New Series III/36A1, Herausgeber T. Mitsui, Y. Shiozaki and E. Nakamura (Berlin, Springer) (2001)

-
- [39] J. B. Goodenough, W. Gräper, F. Holtzberg, D. L. Huber, R.A. Lefever, J. M. Longo, T. R. McGuire and S. Methfessel. *Magnetic and Other Properties of Oxides and Related Compounds: Garnets and Perovskites*, Landolt-Börnstein, New Series III/12a, Herausgeber K. H. Hellwege and A.M. Hellwege (Berlin, Springer) (1978)
- [40] N. A. Hill. *J. Phys. Chem. B* **104**, 6694 (2000)
- [41] D.I. Khomskii. *Bull. Am. Phys. Soc. C* 21,002 (2001)
- [42] N. A. Hill. *Annu. Rev. Mater. Res.* **32**, 1 (2002)
- [43] R. E. Cohen. *Nature* **358**, 136 (1992)
- [44] R. E. Cohen and H. Krakauer. *Ferroelectrics* **136**, 65 (1992)
- [45] G. A. Smolenskii and V. A. Ioffe. Communication No. 71 *Colloque International du Magnétisme*, Grenoble (1958)
- [46] G. A. Smolenskii, A. I. Agranovskaya and V. A. Isupov. *Sov. Phys. Solid State* **1**, 149 (1959)
- [47] Yu. N. Venevtsev, V. N. Lyubimov, V. V. Ivanova and G. S. Zhdanov. *J. Phys. Colloques* **33**, C2-255 (1972)
- [48] G. A. Smolenskii and I. E. Chupis. *Sov. Phys. Usp.* **25**, 475 (1982)
- [49] Yu. N. Venevtsev, V. V. Gagulin and I. D. Zhitomirsky. *Ferroelectrics* **73**, 221 (1987)
- [50] Yu. N. Venevtsev, G. S. Zhdanov, S. P. Solovijev, Ye. V. Bezus, V. V. Ivanova, S. A. Fedulov and A. G. Kapyshev. *Kristallografiya* **5**, 620 (1960)
- [51] R. Seshadri and N. A. Hill. *Chem. Mater.* **13**, 2892 (2001)
- [52] G. Catalan and J. F. Fox. *Adv. Mater.* **21**, 2463 (2009)
- [53] R. T. Smith, G. D. Achenbach, R. Gerson and W. J. James. *J. Appl. Phys.* **39**, 70 (1968)
- [54] J. M. Moreau, C. Michel, R. Gerson and W. J. James. *J. Phys. Chem. Solids* **32**, 1315 (1971)
- [55] D. Lebeugle, D. Colson, A. Forget and M. Viret. *Appl. Phys. Lett.* **91**, 022907 (2007)
- [56] I. Sosnowska, T. Peterlin-Neumaier and E. Steichele. *J. Phys. C* **15**, 4835 (1982)
- [57] F. Sugawara, S. Iida, Y. Syono and S. Akimoto. *J. Phys. Soc. Jpn.* **25**, 1553 (1968)
- [58] T. Yokosawa, A. A. Belik, T. Asaka, K. Kimoto, E. Takayama-Muromachi and Y. Matsui. *Phys. Rev. B* **77**, 024111 (2008)
- [59] R. V. Shpanchenko, V. V. Chernaya, A. A. Tsirlin, P. S. Chizhov, D. E. Sklovsky, E. V. Antipov, E. P. Khlybov, V. Pomjakushin, A. M. Balagurov, J. E. Medvedeva, E. E. Kaul and C. Geibel. *Chem. Mater.* **16**, 3267 (2004)

- [60] A. Kumar, L. W. Martin, S. Denev, J. B. Kortright, Y. Suzuki, R. Ramesh and V. Gopalan. *Phys. Rev. B* **75**, 060101(R) (2007)
- [61] T. Zhao, A. Scholl, F. Zavaliche, K. Lee, M. Barry, A. Doran, M. P. Cruz, Y. H. Chu, C. Ederer, N. A. Spaldin, R. R. Das, D. M. Kim, S. H. Baek, C. B. Eom and R. Ramesh. *Nature Mater.* **5**, 823 (2006)
- [62] D. Lebeugle, D. Colson, A. Forget, M. Viret, A. M. Bataille and A. Gukasov. *Phys. Rev. Lett.* **100**, 227602 (2008)
- [63] S. Lee, W. Ratcliff, S.-W. Cheong and V. Kiryukhin. *Appl. Phys. Lett.* **92**, 192906 (2008)
- [64] J. Park, S.-H. Lee, S. Lee, F. Gozzo, H. Kimura, Y. Noda, Y. J. Choi, V. Kiryukhin, S.-W. Cheong, Y. Jo, E. S. Choi, L. Balicas, G. S. Jeon and J.-G. Park. *J. Phys. Soc. Jpn.* **80**, 114714 (2011)
- [65] F. Bertaut, F. Forrat and P. Fang. *C. R. Acad. Sci.* **256**, 1958 (1963)
- [66] T. Lottermoser, M. Fiebig, D. Fröhlich, S. Leute and K. Kohn. *J. Magn. Magn. Mater.* **226-230**, 1131 (2001)
- [67] T. Lottermoser, M. Fiebig, D. Fröhlich, S. Kallenbach and M. Maat. *Appl. Phys. B* **74**, 759 (2002)
- [68] B. B. van Aken, T. M. Palstra, A. Filippetti and N. A. Spaldin. *Nature Mater.* **3**, 164 (2004)
- [69] C. J. Fennie and K. M. Rabe. *Phys. Rev. B* **72**, 100103(R) (2005)
- [70] M. Fiebig, T. Lottermoser, T. Lonkai, A. V. Goltsev and R. V. Pisarev. *J. Magn. Magn. Mater.* **290-291**, 883 (2002)
- [71] M. Fiebig, T. Lottermoser, D. Fröhlich, A. V. Goltsev and R. V. Pisarev. *Nature* **419**, 818 (2002)
- [72] T. Lottermoser, T. Lonkai, U. Amann, D. Hohlwein, J. Ihringer and M. Fiebig. *Nature* **430**, 541 (2004)
- [73] C. Ederer and N. A. Spaldin. *Phys. Rev. B* **74**, 024102 (2006)
- [74] J. F. Scott. *Rep. Prog. Phys.* **42**, 1055 (1979)
- [75] E. Ascher, H. Schmid and D. Tar. *Solid State Commun.* **2**, 45 (1964)
- [76] H. Schmid, H. Rieder and E. Ascher. *Solid State Commun.* **3**, 327 (1965)
- [77] E. Ascher, H. Rieder, H. Schmid and H. Stössel. *J. Appl. Phys.* **37**, 1404 (1966)
- [78] J.-P. Rivéra and H. Schmid. *Ferroelectrics* **36**, 447 (1981)
- [79] D. V. Efremov, J. van den Brink and D. I. Khomskii. *Nature Mater.* **3**, 853 (2004)
- [80] J. van den Brink and D. I. Khomskii. *J. Phys.: Condens. Matter* **20**, 434217 (2008)

-
- [81] G. Giovannetti, S. Kumar, D. I. Khomskii, S. Picozzi and J. van den Brink. *Phys. Rev. Lett.* **103**, 156401 (2009)
- [82] K. Yamauchi, T. Fukushima and S. Picozzi. *Phys. Rev. B* **79**, 212404 (2009)
- [83] F. Schrettle, S. Krohns, P. Lunkenheimer, V. A. M. Brabers and A. Loidl. *Phys. Rev. B* **83**, 195109 (2011)
- [84] N. Ikeda, H. Ohsumi, K. Ohwada, K. Ishii, T. Inami, K. Kakurai, Y. Murakami, K. Yoshii, S. Mori, Y. Horibe and H. Kito. *Nature* **436**, 1136 (2005)
- [85] D. Niermann, F. Waschowski, J. de Groot, M. Angst and J. Hemberger. *Phys. Rev. Lett.* **109**, 016405 (2012)
- [86] A. Ruff, S. Krohns, F. Schrettle, V. Tsurkan, P. Lunkenheimer and A. Loidl. *Eur. Phys. J. B* **85**, 290 (2012)
- [87] G. A. Smolenskii, V. A. Bokov, V. A. Isupov, N. N. Krainik and G. H. Nedlin. *Helv. Phys. Acta* **41**, 1187 (1968)
- [88] Y. N. Venevtsev and V. V. Gagulin. *Ferroelectrics* **162**, 23 (1994)
- [89] M. Fiebig. *J. Phys. D: Appl. Phys.* **38**, R123 (2005)
- [90] M. Kenzelmann, A. B. Harris, S. Jonas, C. Broholm, J. Schefer, S. B. Kim, C. L. Zhang, S.-W. Cheong, O. P. Vajk and J. W. Lynn. *Phys. Rev. Lett.* **95**, 087206 (2005)
- [91] T. Kimura, J. C. Lashley and A. P. Ramirez. *Phys. Rev. B* **73**, 220401(R) (2006)
- [92] Y. J. Choi, H. T. Yi, S. Lee, Q. Huang, V. Kiryukhin and S.-W. Cheong. *Phys. Rev. Lett.* **100**, 047601 (2008)
- [93] H. Katsura, N. Nagaosa and A. V. Balatsky. *Phys. Rev. Lett.* **95**, 057205 (2005)
- [94] S. Picozzi, K. Yamauchi, B. Sanyal, I. A. Sergienko and E. Dagotto. *Phys. Rev. Lett.* **99**, 227201 (2007)
- [95] T. Arima. *J. Phys. Soc. Jpn.* **76**, 073702 (2007)
- [96] J. Hu. *Phys. Rev. Lett.* **100**, 077202 (2008)
- [97] I. A. Sergienko and E. Dagotto. *Phys. Rev. B* **73**, 094434 (2006)
- [98] H. J. Xiang, S.-H. Wei, M.-H. Whangbo and J. L. F. Da Silva. *Phys. Rev. Lett.* **101**, 037209 (2008)
- [99] A. Malashevich and D. Vanderbilt. *Phys. Rev. Lett.* **101**, 037210 (2008)
- [100] A. Malashevich and D. Vanderbilt. *Phys. Rev. B* **80**, 224407 (2009)
- [101] H. J. Xiang, P. S. Wang, M.-H. Whangbo and X. G. Gong. *Phys. Rev. B* **88**, 054404 (2013)

- [102] I. Dzyaloshinskii. *J. Phys. Chem. Solids* **4**, 241 (1958)
- [103] T. Moriya. *Phys. Rev.* **120**, 91 (1960)
- [104] S.-W. Cheong and M. Mostovoy. *Nature Mater.* **6**, 13 (2007)
- [105] I. E. Dzyaloshinskii. *Sov. Phys.-JETP* **10**, 628 (1959)
- [106] D. N. Astrov. *Sov. Phys.-JETP* **13**, 729 (1961)
- [107] V. J. Folen, G. T. Rado and E. W. Stalder. *Phys. Rev. Lett.* **6**, 607 (1961)
- [108] G. T. Rado and V. J. Folen. *Phys. Rev. Lett.* **7**, 310 (1961)
- [109] F. W. Hehl, Y. N. Obukhov, J.-P. Rivera and H. Schmid. *Phys. Rev. A* **77**, 022106 (2008)
- [110] S. L. Hou and N. Bloembergen. *Phys. Rev.* **138**, A1218 (1965)
- [111] M. J. Cardwell. *Phil. Mag.* **20**, 1087 (1969)
- [112] B. I. Al'shin and D. N. Astrov. *Sov. Phys.-JETP* **17**, 809 (1963)
- [113] G. T. Rado. *Phys. Rev. Lett.* **13**, 335 (1964)
- [114] A. S. Borovik-Romanov and H. Grimmer. *International Tables for Crystallography* Band D, Herausgeber A. Authier (Dordrecht/Boston/London, Kluwer Academic Publishers) (2003)
- [115] G. T. Rado and V. J. Folen. *J. Appl. Phys.* **33**, 1126 (1962)
- [116] H. Schmid. *Introduction to Complex Mediums for Optics and Electrodynamics: Magnetoelectric Effects in Insulating Magnetic Materials*, Herausgeber W. S. Weiglhofer and A. Lakhtakia (Washington, SPIE-The International Society for Optical Engineering) (2003)
- [117] J.-P. Rivera. *Eur. Phys. J. B* **71**, 299 (2009)
- [118] J.-P. Rivera. *Ferroelectrics* **161**, 165 (1994)
- [119] I. Dzyaloshinskii. *Soviet Phys.-JETP* **10**, 628 (1960)
- [120] E. Ascher. *Phil. Mag.* **17**, 149 (1968)
- [121] G. T. Rado. *Phys. Rev. B* **15**, 290 (1977)
- [122] H. Grimmer *Ferroelectrics* **161**, 181 (1994)
- [123] A. S. Bhalla and R. E. Newnham. *Phys. Stat. Sol. a* **58**, K19 (1980)
- [124] G. T. Rado. *Phys. Rev. Lett.* **6**, 609 (1961)
- [125] R. M. Hornreich and S. Shtrikman. *Phys. Rev.* **161**, 506 (1967)
- [126] H. Yatom and R. Englmann. *Phys. Rev.* **188**, 793 (1969)

-
- [127] O. F. de Alcantara Bonfim and G. A. Gehring. *Adv. in Phys.* **29**, 731 (1980)
- [128] G. A. Gehring. *Ferroelectrics* **161**, 275 (1994)
- [129] W. F. Brown, R. M. Hornreich and S. Shtrikman. *Phys. Rev.* **168**, 574 (1968)
- [130] H. Schmid. *Ferroelectrics* **252**, 41 (2001)
- [131] C. Ederer and N. A. Spaldin. *Phys. Rev. B* **76**, 214404 (2007)
- [132] N. A. Spaldin, M. Fiebig and M. Mostovoy. *J. Phys.: Condens. Matter* **20**, 434203 (2008)
- [133] N. A. Spaldin, M. Fechner, E. Bousquet, A. Balatsky and L. Nordström. *Phys. Rev. B* **88**, 094429 (2013)
- [134] K. Siratori, J. Akimitsu, E. Kita and M. Nishi. *J. Phys. Soc. Japan B* **48**, 1111 (1980)
- [135] K. Siratori and E. Kita. *J. Phys. Soc. Japan B* **48**, 1443 (1980)
- [136] D. B. Litvin. *Acta Cryst. A* **64**, 316 (2008)
- [137] B. van Aken, J.-P. Rivera, H. Schmid and M. Fiebig. *Nature* **449**, 702 (2007)
- [138] M. Baum, K. Schmalzl, P. Steffens, A. Hiess, L. P. Regnault, M. Meven, P. Becker, L. Bohatý and M. Braden. *Phys. Rev. B* **88**, 024414 (2013)
- [139] S. Jodlauk. Diploma thesis, Universität zu Köln 2005
- [140] J. Baier. Diploma thesis, Universität zu Köln 2002
- [141] M. Kriener. PhD thesis, Universität zu Köln 2005
- [142] H. Kierspel. PhD thesis, Universität zu Köln 1996
- [143] C. Hanebeck. Diploma thesis, Universität zu Köln 2002
- [144] S. Orbe. Diploma thesis, Universität zu Köln 2011
- [145] O. Breunig. Diploma thesis, Universität zu Köln 2011
- [146] G. Kolland. PhD thesis, Universität zu Köln 2013
- [147] O. Heyer. Diploma thesis, Universität zu Köln 2005
- [148] R. Pott. Diploma thesis, Universität zu Köln 1977
- [149] M. Seher. Diploma thesis, Universität zu Köln 2012
- [150] T. Lorenz. PhD thesis, Universität zu Köln 1998
- [151] R. Pott and R. Schefzyk. *J. Phys. E: Sci. Instrum.* **16**, 444 (1983)
- [152] G. Brändli and R. Griessen. *Cryogenics* **13**, 299 (1973)

- [153] H. Schneeberger. PhD thesis, Ludwig-Maximilians-Universität München 1992
- [154] E. Breidenbach. PhD thesis, Universität zu Köln 1996
- [155] L. P. L. Andersen. Master thesis, Universität zu Köln 2012
- [156] M. Schalenbach. Bachelor thesis, Universität zu Köln 2009
- [157] D. Brüning. Bachelor thesis, Universität zu Köln 2013
- [158] STOE and Cie GmbH 2011 *STOE WinXPOW* v.3.0.2.1
- [159] J. Brand. PhD thesis, Universität zu Köln 2013
- [160] H. Ulbrich. PhD thesis, Universität zu Köln 2012
- [161] S. Haussühl. *Kristallphysik* (Weinheim, Physik-Verlag GmbH) (1983)
- [162] R. L. Byer and C. B. Roundy. *Ferroelectrics* **3**, 333 (1972)
- [163] M. E. Lines and A. M. Glass. *Principles and applications of ferroelectric and related materials* (Oxford, Clarendon Press) (1977)
- [164] R. P. Lowndes and D. H. Martin. *Proc. Roy. Soc. A* **308**, 473 (1969)
- [165] C. Andeen, J. Fontanella and D. Schuele. *Rev. Sci. Instr.* **41**, 1573 (1970)
- [166] C. Andeen, J. Fontanella and D. Schuele. *Phys. Rev. B* **2**, 5068 (1970)
- [167] C. Andeen, J. Fontanella and D. Schuele. *J. Appl. Phys.* **42**, 2216 (1971)
- [168] P. Preu. PhD thesis, Universität zu Köln 1982
- [169] Keithley Model 6517A Electrometer User's Manual
- [170] C. Zobel. PhD thesis, Universität zu Köln 2002
- [171] Keithley Low Level Measurements Handbook (6th edition)
- [172] J. Luzón, J. Campo, F. Palacio, G. J. McIntyre and A. Millán. *Phys. Rev. B* **78**, 054414 (2008)
- [173] I. Lindqvist. *Ark. Kemi., Mineral. Geol.* **24**, 1 (1947)
- [174] A. Bellanca. *Period. Mineral.* **17**, 59 (1948)
- [175] B. N. Figgis, C. L. Raston, R. P. Sharma and A. H. White. *Aust. J. Chem.* **70**, 5161 (1977)
- [176] C. J. O'Connor, B. S. Deaver and E. Sinn. *J. Chem. Phys.* **70**, 5161 (1979)
- [177] J. E. Greedan, D. C. Hewitt, R. Faggiani and I. D. Brown. *Acta Cryst. B* **36**, 1927 (1980)
- [178] A. J. Schultz and R. L. Carlin. *Acta Cryst. B* **51**, 43 (1995)

-
- [179] D. Lacková, I. Ondrejčková and M. Koman. *Acta Chim. Slov.* **6**, 129 (2013)
- [180] J. N. McElearney and S. Merchant. *Inorg. Chem.* **17**, 1207 (1978)
- [181] J. A. Puértolas, R. Navarro, F. Palacio, J. Bartolomé, D. González and R. L. Carlin. *Phys. Rev. B* **31**, 516 (1985)
- [182] F. Palacio, A. Paduan-Filho and R. L. Carlin. *Phys. Rev. B* **21**, 296 (1980)
- [183] C. S. M. Partiti, A. Piccini and H. R. Rechenberg. *Solid State Commun.* **56**, 687 (1985)
- [184] C. S. M. Partiti, H. R. Rechenberg and J. P. Sanchez. *J. Phys. C: Solid State Phys.* **21**, 5825 (1988)
- [185] M. Gabás, F. Palacio, J. Rodríguez-Carvajal and D. Visser. *J. Phys.: Condens. Matter* **7**, 4725 (1995)
- [186] J. Campo, J. Luzón, F. Palacio, G. J. McIntyre, A. Millán and A. R. Wildes. *Phys. Rev. B* **78**, 054415 (2008)
- [187] D. B. Litvin *Acta Cryst. A* **64**, 419 (2008)
- [188] J. Chadwick and M. F. Thomas. *J. Phys. C: Solid State Phys.* **20**, 3979 (1987)
- [189] J. A. Puértolas, R. Navarro, F. Palacio, J. Bartolomé, D. González and R. L. Carlin. *Phys. Rev. B* **26**, 395 (1982)
- [190] M. Ackermann, D. Brüning, T. Lorenz, P. Becker and L. Bohatý. *New. J. Phys.* **15**, 123001 (2013)
- [191] R. L. Carlin, S. N. Bhatia and C. J. O'Connor. *J. Am. Chem. Soc.* **99**, 7728 (1977)
- [192] G. Giovannetti, S. Kumar, A. Stroppa, J. van den Brink, S. Picozzi and J. Lorenzana. *Phys. Rev. Lett.* **106**, 026401 (2011)
- [193] G. Jin, K. Cao, G.-C. Guo and L. He. *Phys. Rev. Lett.* **108**, 187205 (2012)
- [194] P. Tolédano, N. Leo, D. D. Khalyavin, L. C. Chapon, T. Hoffmann, D. Meier and M. Fiebig. *Phys. Rev. Lett.* **106**, 257601 (2011)
- [195] R. Villarreal, G. Quirion, M. L. Plumer, M. Poirier, T. Usui and T. Kimura. *Phys. Rev. Lett.* **109**, 167206 (2012)
- [196] G. Quirion and M. L. Plumer. *Phys. Rev. B* **87**, 174428 (2013)
- [197] A. P. Filho, F. Palacio and R. L. Carlin. *J. Physique Lett.* **39**, 279 (1978)
- [198] J. A. Johnson, C. E. Johnson and M. F. Thomas. *J. Phys. C: Solid State Phys.* **20**, 91 (1987)
- [199] W. A. Deer, R. A. Howie and J. Zussman *Single Chain Silicates*, Rock-Forming Minerals Vol. 2A, (London, Longman) (2001)

- [200] A. E. Ringwood. *Geochim. Cosmochim. Acta* **55**, 2083 (1991)
- [201] M. Cameron and J. J. Papike. *Am. Mineral.* **66**, 1 (1981)
- [202] G. J. Redhammer and G. Roth. *Z. Kristallogr.* **219**, 585 (2004)
- [203] R.M. Thompson, R. T. Downs and G. J. Redhammer. *Am. Mineral.* **90**, 1840 (2005)
- [204] M. Baum. PhD thesis, Universität zu Köln 2013
- [205] T. V. Drokina, G. A. Petrakovskii, L. Keller and J. Schefer. *J. Phys.: Conf. Ser.* **251**, 012016 (2010)
- [206] G. J. Redhammer, A. Senyshyn, M. Meven, G. Roth, S. Prinz, A. Pachler, G. Tippelt, C. Pietzonka, W. Treutmann, M. Hoelzel, B. Pedersen and G. Amthauer. *Phys. Chem. Minerals* **38**, 139 (2011)
- [207] T. V. Drokina, G. A. Petrakovskii, L. Keller, J. Schefer, A. D. Balaev, A. V. Kartashev and D. A. Ivanov. *JETP* **112**, 121 (2011)
- [208] G. J. Redhammer, G. Roth, W. Treutmann, M. Hoelzel, W. Paulus, G. André, C. Pietzonka and G. Amthauer. *J. Solid State Chem.* **182**, 2374 (2009)
- [209] G. Nénert, M. Isobe, C. Ritter, O. Isnard, A. N. Vasiliev and Y. Ueda. *Phys. Rev. B* **79**, 064416 (2009)
- [210] G. Nénert, C. Ritter, M. Isobe, O. Isnard, A. N. Vasiliev and Y. Ueda. *Phys. Rev. B* **80**, 024402 (2009)
- [211] G. J. Redhammer, G. Roth, A. Senyshyn, G. Tippelt and C. Pietzonka. *Z. Kristallogr.* **228**, 140 (2013)
- [212] E. Baum, W. Treutmann, M. Behruzi, W. Lottermoser and G. Amthauer. *Z. Kristallogr.* **183**, 273 (1988)
- [213] M. Behruzi, T. Hahn, C. T. Prewitt and K. Baldwin. *Acta Cryst. A* **40** (Suppl.), C-247 (1984)
- [214] F. Nestola, G. J. Redhammer, M. G. Pamato, L. Secco and A. D. Negro. *Am. Mineral.* **94**, 616 (2009)
- [215] G. J. Redhammer, F. Cámara, M. Alvaro, F. Nestola, G. Tippelt, S. Prinz, J. Simons, G. Roth and G. Amthauer. *Phys. Chem. Minerals* **37**, 685 (2010)
- [216] G. J. Redhammer, G. Roth, W. Treutmann, M. Hoelzel, W. Paulus, G. André, C. Pietzonka and G. Amthauer. *J. Solid State Chem.* **182**, 2374 (2009)
- [217] A. C. Komarek. PhD thesis, Universität zu Köln 2009
- [218] O. Ballet, J. Coey, G. Fillion, A. Ghose, A. Hewat and J. Regnard. *Phys. Chem. Minerals* **16**, 672 (1989)

-
- [219] T. V. Drokina, O. A. Bayukov, G. A. Petrakovskii, D. A. Velikanov, A. F. Bovina, G. N. Stepanov and D. A. Ivanov. *Phys. Solid State* **50**, 2141 (2008)
- [220] T. V. Drokina, O. A. Bayukov, G. A. Petrakovskii and D. A. Velikanov. *Bull. Russ. Acad. Sci. Phys.* **73**, 1054 (2009)
- [221] G. J. Redhammer, G. Roth, W. Paulus, G. André, W. Lottermoser, G. Amthauer, W. Treutmann and B. Koppelhuber-Bitschnau. *Phys. Chem. Minerals* **28**, 337 (2001)
- [222] P. V. Klevtsov and R. F. Klevtsova. *J. Solid State Chem.* **2**, 278 (1970)
- [223] L. Nyam-Ochir, H. Ehrenberg, A. Buchsteiner, A. Senyshyn, H. Fuess and D. Sangaa. *J. Magn. Magn. Mater.* **320**, 3251 (2008)
- [224] S. Holbein. Diploma thesis, Universität zu Köln 2011
- [225] M. G. Banks, R. K. Kremer, C. Hoch, A. Simon, B. Ouladdiaf, J.-M. Broto, H. Rakoto, C. Lee and M.-H. Whangbo. *Phys. Rev. B* **80**, 024404 (2009)
- [226] S. Seki, T. Kurumaji, S. Ishiwata, H. Matsui, H. Murakawa, Y. Tokunaga, Y. Kaneko, T. Hasegawa and Y. Tokura. *Phys. Rev. B* **82**, 064424 (2010)
- [227] O. Oeckler and A. Simon. *Z. Kristallogr. NCS* **215**, 13 (2000)
- [228] C. Lee, J. Liu, M.-H. Whangbo, H.-J. Koo, R. K. Kremer and A. Simon. *Phys. Rev. B* **86**, 060407(R) (2012)
- [229] W. Prandl. *Phys. Stat. Sol.* **B55**, K159 (1973)
- [230] R. Plumier. *Solid State Commun.* **12**, 109 (1973)
- [231] T. V. Valyanskaya, V. P. Plakhtii and V. I. Sokolov. *Sov. Phys. JETP* **43**, 1189 (1976)
- [232] A. Gukasov, V. P. Plakhty, B. Dorner, S. Y. Kokovin, V. N. Syromyatnikov, O. P. Smirnov and Y. P. Chernenkov. *J. Phys.: Condens. Matter* **11**, 2869 (1999)
- [233] M. Wakeshima, H. Nishimine and Y. Hinatsu. *J. Phys.: Condens. Matter* **16**, 4103 (2004)
- [234] J. F. Nye. *Physical Properties of Crystals* (Oxford, Oxford University Press) (1985)
- [235] *Standards on Piezoelectric Crystals, Proceedings of the IRE* **37**, 1378 (1949)
- [236] M. Born. *Optik, Ein Lehrbuch der optischen Lichttheorie* (Berlin, Heidelberg, New York; Springer) (1933)
- [237] W. Ackermann. *Ann. Physik* **46**, 197 (1915)
- [238] V. V. Gladkii and I. Zheludev. *Sov. Phys. Cryst.* **10**, 63 (1965)
- [239] S. B. Lang. *Phys. Rev. B* **4**, 3603 (1971)

Abstract

The present work is concerned with the search for new multiferroic or magnetoelectric crystals, with strong magnetoelectric couplings and their basic characterization by investigating the dielectric and other thermodynamic properties. The focus of the experimental work lies on two different classes of compounds, the pyroxenes AMX_2O_6 (A = mono- or divalent metal, M = di- or trivalent metal and X = tri- or tetravalent cation) and the erythrosiderite-type family $A_2[FeX_5(H_2O)]$ (A = alkali metal or ammonium ion, X = halide ion).

An analysis of the anisotropy of the linear magnetoelectric effect of $LiFeSi_2O_6$ by means of dielectric measurements and investigations with a polarized-light microscope reveal that the magnetic space group $P2_1/c'$ proposed in literature for its antiferromagnetic phase is actually wrong. The correct space group has to be instead $P\bar{1}'$. The multiferroic properties of $NaFeGe_2O_6$, the first prototype multiferroic within the pyroxene family, are characterized by dielectric investigations, magnetic-susceptibility, thermal-expansion and magnetostriction measurements on large single crystals. Ferroelectricity arises below $\simeq 11.6$ K within an antiferromagnetically ordered state ($T_N \simeq 13$ K). The corresponding electric polarization can be strongly modified by applying magnetic fields. Detailed magnetic-field versus temperature phase diagrams are derived.

$(NH_4)_2[FeCl_5(H_2O)]$ is classified as a new multiferroic material. The onset of ferroelectricity is found below $\simeq 6.9$ K within an antiferromagnetically ordered state ($T_N \simeq 7.25$ K). The corresponding electric polarization can drastically be influenced by applying magnetic fields. Based on measurements of pyroelectric currents, dielectric constants and magnetization the magnetoelectric, dielectric and magnetic properties of $(NH_4)_2[FeCl_5(H_2O)]$ are characterized. Combining these data with measurements of thermal expansion, magnetostriction and specific heat detailed magnetic-field versus temperature phase diagrams are derived. Depending on the direction of the magnetic field up to three different multiferroic phases are identified, which are separated by a magnetically ordered, but non-ferroelectric phase from the paramagnetic phase. Besides these low-temperature transitions, a ferroelastic phase transition at $\simeq 79$ K is observed and investigated. Three other members of the erythrosiderite-type family ($K_2[FeCl_5(H_2O)]$, $Rb_2[FeCl_5(H_2O)]$, $Cs_2[FeCl_5(H_2O)]$) are classified as linear magnetoelectric materials by means

of dielectric investigations and measurements of the magnetic susceptibility. From the K-based to the Cs-based compound the transition temperature to the respective magnetoelectric phase decreases from $T_N^K = 14.3$ K and $T_N^{Rb} = 10.2$ K to $T_N^{Cs} = 6.8$ K. For all three compounds the anisotropy and the temperature dependence of the linear magnetoelectric effect is analysed. Based on the anisotropy study of the magnetoelectric effect of $Cs_2[FeCl_5(H_2O)]$ a model for its unknown magnetic structure, described by the magnetic space group $C'_{\frac{2'}{m} \frac{2'}{c} \frac{2_1}{m'}}$, is developed.

Kurzzusammenfassung

Die vorliegende Arbeit befasst sich mit der Suche nach neuen multiferroischen und magnetoelektrischen Kristallen mit starker magnetoelektrischer Kopplung und ihrer grundlegenden Charakterisierung durch Untersuchungen ihrer dielektrischen und anderer thermodynamischer Eigenschaften. Der experimentelle Schwerpunkt der Arbeit liegt dabei auf zwei verschiedenen Kristallfamilien, den Pyroxenen AMX_2O_6 (A = mono- oder divalentes Metall, M = di- oder trivalentes Metall und X = tri- oder tetravalentes Kation) sowie den erythrosiderit-artigen Verbindungen $A_2[FeX_5(H_2O)]$ (A = Alkali Metall oder Ammonium Ion, X = Halogenid Ion).

Eine Analyse der Anisotropie des linear magnetoelektrischen Effekts von $LiFeSi_2O_6$ mit Hilfe dielektrischer sowie polarisationsmikroskopischer Untersuchungen ergibt, dass die in der Literatur vorgeschlagene magnetische Raumgruppe $P2_1/c'$ für seine antiferromagnetische Phase nicht korrekt sein kann. Die vorliegenden Ergebnisse sind nur kompatibel mit der triklinen Raumgruppe $P\bar{1}'$. Die multiferroischen Eigenschaften von $NaFeGe_2O_6$, dem ersten Prototyp-Multiferroikum unter den Pyroxenen, werden detailliert charakterisiert durch dielektrische Untersuchungen sowie Messungen der magnetischen Suszeptibilität, der thermischen Ausdehnung und der Magnetostraktion. Ferroelektrizität tritt unterhalb von $\simeq 11.6$ K in einer antiferromagnetisch geordneten Phase ($T_N \simeq 13$ K) auf. Die zugehörige spontane elektrische Polarisation lässt sich durch Magnetfelder beeinflussen. Es werden detaillierte B - T Phasendiagramme entwickelt.

$(NH_4)_2[FeCl_5(H_2O)]$ wird als ein neues Multiferroikum klassifiziert. Ferroelektrizität tritt unterhalb von $\simeq 6.9$ K in einer antiferromagnetisch geordneten Phase auf ($T_N \simeq 7.25$ K). Es besteht eine starke magnetoelektrische Kopplung, da sich die spontane elektrische Polarisation durch magnetische Felder stark modifizieren lässt. Die magnetischen, dielektrischen und magnetoelektrischen Eigenschaften von $(NH_4)_2[FeCl_5(H_2O)]$ werden durch dielektrische Untersuchungen sowie Messungen der Magnetisierung charakterisiert. In Kombination mit Messungen der thermischen Ausdehnung, Magnetostraktion sowie spezifischen Wärme, ergeben sich komplexe B - T Phasendiagramme. In Abhängigkeit von der Richtung des angelegten magnetischen Feldes können bis zu drei verschiedene multiferroische bzw. magnetoelektrische Phasen identifiziert werden, die durch eine magnetisch geordnete, nicht ferroelektrische Zwischenphase von der para-

magnetischen Phase getrennt sind. Neben diesen Tieftemperatur-Phasenumwandlungen wird bei $\simeq 79$ K eine ferroelastische Phasenumwandlung beobachtet und untersucht. Drei andere Mitglieder der Erythrosiderit-Familie ($\text{K}_2[\text{FeCl}_5(\text{H}_2\text{O})]$, $\text{Rb}_2[\text{FeCl}_5(\text{H}_2\text{O})]$ und $\text{Cs}_2[\text{FeCl}_5(\text{H}_2\text{O})]$) werden als lineare Magnetoelektrika klassifiziert und durch dielektrische Untersuchungen sowie Messungen der Magnetisierung charakterisiert. Von der Kalium- zur Rubidium-Verbindung nimmt die Übergangstemperatur zur jeweiligen magnetoelektrischen, antiferromagnetischen Phase von $T_N^K = 14.3$ K und $T_N^{\text{Rb}} = 10.2$ K zu $T_N^{\text{Cs}} = 6.8$ K hin ab. Für alle drei Verbindungen werden die Anisotropie sowie die Temperaturabhängigkeit des linear magnetoelektrischen Effekts detailliert untersucht und analysiert. Im Fall von $\text{Cs}_2[\text{FeCl}_5(\text{H}_2\text{O})]$ kann durch eine Symmetrieanalyse des linear magnetoelektrischen Effekts ein Modell für die unbekannte magnetische Struktur dieser Verbindung, beschrieben durch die magnetische Raumgruppe $C_{\frac{2'}{m} \frac{2'}{c} \frac{2_1}{m'}}$, hergeleitet werden.

Danksagung

Zum Abschluss meiner Arbeit möchte ich mich bei einigen Menschen bedanken, die mich während der letzten Jahre begleitet und unterstützt haben. Ganz besonderer Dank geht dabei an meinen Doktorvater Herrn Prof. Dr. Ladislav Bohatý, der mich mit seiner Begeisterung für die Wissenschaft insbesondere für die Kristallographie stets motiviert hat und mir ein großes Vorbild ist. In einer Vielzahl von Diskussionen und Gesprächen habe ich viel über Kristallographie und Kristallphysik gelernt und ohne seine Unzahl guter Ideen zu potentiell neuen Multiferroika und linearen Magnetoelektrika wäre diese Arbeit nicht möglich gewesen. Herzlich bedanken möchte ich mich außerdem auch bei Priv.-Doz. Dr. Thomas Lorenz, der mir die experimentelle Arbeit am II. Physikalischen Institut ermöglicht und mich während der letzten Jahre ebenfalls bestens betreut und unterstützt hat. Die unzähligen Diskussionen mit ihm waren sehr fruchtbar und haben diese Arbeit maßgeblich vorangetrieben. Auch hat er sich freundlicherweise bereit erklärt die Zweitbegutachtung meiner Arbeit zu übernehmen. Prof. Dr. Sanjay Mathur danke ich für die Bereitschaft den Vorsitz bei meiner Disputation zu übernehmen. Ich möchte mich auch bei Gerhard Kolland und Oliver Breunig bedanken, die mich zu Beginn meiner Arbeit in die verschiedenen Methoden der experimentellen Tieftemperaturphysik eingeführt haben und von denen ich über die Jahre sehr viel gelernt habe. Frau Prof. Dr. Petra Becker-Bohatý danke ich für die gute Zusammenarbeit und ihre Beharrlichkeit bei der komplizierten Züchtung von $\text{NaFeGe}_2\text{O}_6$. Außerdem möchte ich mich bei ihr bedanken für die Präparation einer Vielzahl von Kristallpräparaten, die Auswertung der Röntgen-Pulveraufnahmen von $(\text{NH}_4)_2[\text{FeCl}_5(\text{H}_2\text{O})]$ und die Einführung in die Polarisationsmikroskopie im Zusammenhang mit der Untersuchung von $\text{LiFeSi}_2\text{O}_6$ und $(\text{NH}_4)_2[\text{FeCl}_5(\text{H}_2\text{O})]$. Lionel Andersen möchte ich danken für die große Geduld bei der Verbesserung des in dieser Arbeit selbst konstruierten Durchflusskryostaten und die vielen durchgeführten Messungen vor allem auch gegen Ende dieser Arbeit. Ein großer Dank geht auch an Michael Groß und Dr. Daniel Rytz vom FEE, die freundlicherweise zwei große $\text{Mn}_3\text{Al}_2(\text{GeO}_4)_3$ Kristalle für diese Arbeit gezüchtet haben. Außerdem möchte ich mich bei Dr. Mark Pelz für die polykristalline Tb_3TaO_7 Probe bedanken, an der ich erste Pyrostrommessungen durchführen konnte.

Des weiteren möchte ich mich auch bei allen anderen Kollegen des Instituts für Kristallographie

sowie des II. Physikalischen Instituts für die schöne und erfolgreiche Zeit der letzten Jahre bedanken. Bei Herrn Prof. Dr. Mühlberg für nette Gespräche über Afrika und die USA, sowie für viele hilfreiche Tipps bei Latex- und gnuplot-Problemen. Bei Dr. Peter Held und Gunther Pillunat für die Hilfe bei Computer- und Netzwerkproblemen aller Art. Bei Marion Möllering und Steffi Seidel für die Hilfe bei organisatorischen und labortechnischen Problemen. Bei der feinmechanischen Werkstatt des II. Physikalischen Instituts für den Bau von Probenhaltern, Messeinsätzen und dem Durchflusskryostaten für dielektrische Messungen bei höheren Temperaturen. Bei Susanne Heijligen für die vielen Magnetisierungsmessungen mit dem SQUID-Magnetometer. Bei Dr. Harald Kierspel und Ralf Dommel für die hervorragende Heliumversorgung. Und schließlich bei allen aktuellen und ehemaligen Mitgliedern der Lorenz-Gruppe, sowie meinen Bürokollegen, insbesondere Michael Woll für viele nette Gespräche und eine gute Arbeitsatmosphäre.

Der größte Dank geht abschließend an meine Familie, die mich immer in allen Lebenslagen hervorragend unterstützt und gefördert hat und außerdem an meine Freundin Caro die mir immer wieder Mut zugesprochen hat, wenn ich mit meiner Arbeit nicht vorangekommen bin. Bei meinem Vater möchte ich mich nochmals gesondert bedanken für die Hilfe bei der Übersetzung eines Teils dieser Arbeit ins Englische, aber auch für die vielen anregenden und ermutigenden Gesprächen, die wir im Verlauf dieser Arbeit immer wieder hatten.

Publications and conference contributions

Publications:

M. Ackermann, D. Brüning, T. Lorenz, P. Becker and L. Bohatý

Thermodynamic properties of the new multiferroic material $(\text{NH}_4)_2[\text{FeCl}_5(\text{H}_2\text{O})]$

New J. Phys. **15**, 123001 (2013).

M. Ackermann, L. Andersen, T. Lorenz, L. Bohatý and P. Becker

Anisotropy study of multiferroicity in the pyroxene $\text{NaFeGe}_2\text{O}_6$

Submitted, *New J. Phys.*, (2014). arXiv:1408.6772

M. Ackermann, T. Lorenz, P. Becker and L. Bohatý

Magnetoelectric properties of $A_2[\text{FeCl}_5(\text{H}_2\text{O})]$ with $A = \text{K}, \text{Rb}, \text{Cs}$

Submitted, *J. Phys.: Condens. Matter*, (2014). arXiv:1408.3997

Conference contributions:

- 20th Annual Meeting of the German Crystallographic Society (DGK), München (2012)
Z. Kristallogr. Suppl. **32**, 52 (2012)
- SFB 608 Abschlussworkshop, Köln (2013)
- DPG-Frühjahrstagung der Sektion Kondensierte Materie, Regensburg (2013)
- 21th Annual Meeting of the German Crystallographic Society (DGK), Freiberg (2013)
Z. Kristallogr. Suppl. **33**, 102 (2013)
Z. Kristallogr. Suppl. **33**, 99 (2013)
- DPG-Frühjahrstagung der Sektion Kondensierte Materie, Dresden (2014)
- 22nd Annual Meeting of the German Crystallographic Society (DGK), Berlin (2014)
Z. Kristallogr. Suppl. **34**, 165 (2014)

Curriculum vitae

Name	Matthias Ackermann
Date of birth	16.06.1985
Place of birth	Göttingen
Marital status	unmarried
University studies	
Since Jun. 2011	PhD study in the group of Prof. Dr. Ladislav Bohatý at the Institut für Kristallographie, Universität zu Köln
11. May 2011	Diploma (Diplom-Physiker) at the Rheinische Friedrich-Wilhelms-Universität Bonn Title of diploma thesis: <i>Suspensionen von Lithiumniobat-Nanopartikeln: Untersuchung und Manipulation des Ausrichtungsverhaltens in elektrischen Feldern</i>
Oct. 2005 – May 2011	Study of physics at the Rheinische Friedrich-Wilhelms-Universität Bonn
Education	
1996–2005	Gymnasium an der Heinzenwies, Idar-Oberstein
1992–1996	Grundschule Göttschied, Idar-Oberstein

Offizielle Erklärung

Ich versichere, dass ich die von mir vorgelegte Dissertation selbstständig angefertigt, die benutzten Quellen und Hilfsmittel vollständig angegeben und die Stellen der Arbeit – einschließlich Tabellen, Karten und Abbildungen –, die anderen Werken im Wortlaut oder dem Sinn nach entnommen sind, in jedem Einzelfall als Entlehnung kenntlich gemacht habe; dass diese Dissertation noch keiner anderen Fakultät oder Universität zur Prüfung vorgelegen hat; dass sie – abgesehen von unten angegebenen Teilpublikationen – noch nicht veröffentlicht worden ist sowie, dass ich eine solche Veröffentlichung vor Abschluss des Promotionsverfahrens nicht vornehmen werde. Die Bestimmungen der Promotionsordnung sind mir bekannt. Die von mir vorgelegte Dissertation ist von Prof. Dr. Ladislav Bohatý betreut worden.

Köln, 04.08.2014, Matthias Ackermann

Teilpublikationen der vorliegenden Arbeit:

M. Ackermann, D. Brüning, T. Lorenz, P. Becker and L. Bohatý

Thermodynamic properties of the new multiferroic material $(\text{NH}_4)_2[\text{FeCl}_5(\text{H}_2\text{O})]$

New J. Phys. **15**, 123001 (2013).

M. Ackermann, L. Andersen, T. Lorenz, L. Bohatý and P. Becker

Anisotropy study of multiferroicity in the pyroxene $\text{NaFeGe}_2\text{O}_6$

Submitted, *New J. Phys.*, (2014). arXiv:1408.6772

M. Ackermann, T. Lorenz, P. Becker and L. Bohatý

Magnetoelectric properties of $A_2[\text{FeCl}_5(\text{H}_2\text{O})]$ with $A = \text{K}, \text{Rb}, \text{Cs}$

Submitted, *J. Phys.: Condens. Matter*, (2014). arXiv:1408.3997